INVESTIGATION OF THE KINEMATICS INVOLVED IN COMPTON SCATTERING AND HARD X-RAY PHOTOABSORPTION

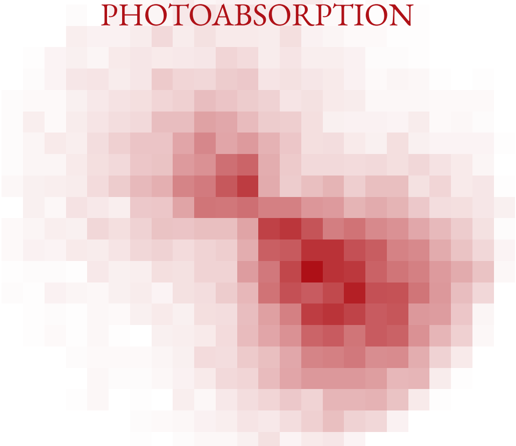

Dissertation
zur Erlangung des Doktorgrades
der Naturwissenschaften

vorgelegt beim Fachbereich Physik
der Johann Wolfgang Goethe-Universität
in Frankfurt am Main

von
Max Kircher
aus Ehringshausen

Frankfurt 2023
(D 30)

vom Fachbereich Physik der
Johann Wolfgang Goethe-Universität als Dissertation angenommen.

Dekan:	Prof. Dr. Roger Erb
Gutachter:	Prof. Dr. Reinhard Dörner Prof. Dr. Till Jahnke

Datum der Disputation: 10. Juli 2023

CONTENTS

I PREREQUISITES

II RESULTS

III CONCLUSIONS

ADDENDUM

List of Figures

LIST OF TABLES

Beginning and end seem synonyms
Impossible to trace and nevertheless infinite
There is always another horizon

A. L. N.

INTRODUCTION 1

We are standing on the shoulders of giants!—a phrase to emphasize that scientific progress is achieved not downright by one's own merits, but by building upon previous advancements and the knowledge of others. Indeed with absolute certainty, the knowledge I acquired throughout my studies of physics is absolutely unachievable if not for the works of swaths of scholars before me. As such, it is only natural to fall back on the wisdom of the giants-past and realize that many of the puzzles one comes across already kept even the giants wondering. Richard Feynman famously once claimed: "Nobody understands quantum mechanics!" and at the heart of it, quantum mechanics seems like a paradox dreamed up by nature. The double slit experiment proves the wave-like nature of light while at the same time, Compton scattering proves the particle-like nature of it—two seemingly exclusive properties:

How can something be a wave and a particle at the same time?

This work does not aim to answer this question. However, Compton scattering—more general, photon scattering—is such a fundamental phenomenon of quantum mechanics that the process itself is worth exploring on this fact alone. And it is somewhat puzzling that there are still fundamental questions to be answered, even though Compton scattering seems so basic in nature: A game of billiards with photons and electrons, so to speak. But while for billiards the dynamics have been formalized and observed, the complete kinematics of a Compton scattering event were not observed to this day—one hundred years after the first observation of the process itself!

Such an observation of the complete kinematics has been achieved in scope of this work and is presented in this thesis. It is not the sole achievement of this work. The rise of high-intensity fourth generation synchrotron machines enables a new approach in observing Compton scattering: using the cold-target recoil-ion momentum spectroscopy (COLTRIMS) technique. Instead of—as is historically the approach—detecting the energy of photons under fixed scattering angles, the COLTRIMS technique measures the momenta of the Compton electron(s) and the Compton ion(s) in coincidence, enabling an indirect measurement of the photon momentum by exploitation of the momentum conservation law. This way, a full solid detection angle of scattered photons is achievable, increasing the detection efficiency of the technique immensely. Using the COLTRIMS technique, Compton scattering was observed with soft and hard x rays on helium and molecular nitrogen, observing the aforementioned complete and fully differential dynamics of Compton scattering, investigating electron-electron correlations of helium and observing Compton scattering in a molecular frame of reference. Additionally to the investigation of Compton scattering, this work presents results on photoionization of molecular nitrogen in the hard x-ray regime, where the linear photon momentum significantly affects the momentum distributions of the photoelectron and the photoions.

This work most definitely does not topple the claim of Feynman, but it hopefully provides some insights into the fundamentals of the Compton scattering process.

A brief history of Compton scattering

Compton scattering—the inelastic scattering of a photon at an electron—in its simplest description seems not to be a complex problem: A photon scatters at a static electron; momentum and energy conservation determine the energy and momentum of the scattered photon for fixed scattering angles θ_γ. Under these assumptions, the wavelength shift was first quantified by Arthur H. Compton 1923 [Com23a] as $\Delta\lambda = \lambda_C(1 - \cos\theta_\gamma)$ (for electrons, the Compton wavelength λ_C has a value of 2.4×10^{-12} m), which earned him the Nobel price in 1927. The discovery spawned experimental and theoretical interest in the first half of the twentieth century, when the frameworks of quantum mechanics were developed. The differential cross section in angle was derived by Klein and Nishina in 1929 [Kle29], enabling a first experimental test of quantum electrodynamics. For fixed scattering angles, the wavelength shift is not sharp but broadened, a fact that was explained by DuMond in 1929 [DuM29] and is attributed to the momentum distribution of bound electrons (that is, non-static electrons). The broadening provides a definite and *direct* proof of a linear momentum of bound electrons, whereas previous spectroscopy only observed changes in energy (which is attributed to the dynamic nature of bound electrons, and thus only indirectly measures the linear electron momentum). Further, the measurements of DuMond of 1929 provide the first experimental evidence that electrons in metals follow Fermi-Dirac instead of Maxwell-Boltzmann statistics [Coo77]. In 1977, Cooper wrote in his excellent review [Coo77]: “physicists [...] need to be persuaded to consider their problems in momentum space rather than coordinate space.” and Compton scattering proves to be an excellent experimental tool for just that.

While many experiments investigating the electron momentum distributions of various elements were performed from the nineteen twenties up to

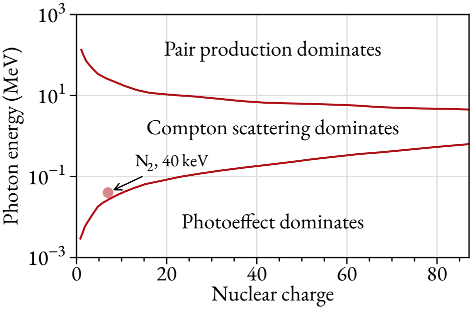

Figure 1.1: Relative regions of importance of photon/matter interactions. The boundaries (red lines) are obtained from [Cul89]. The dot marks the region where one of the measurements of this work was performed. (Taken from [Ber97].)

the beginning of the nineteen forties, those experiments were only performed by a select few surrounding DuMond and coworkers [Coo77]. Some examples of early works on Compton scattering can be found in References [Com23b; Jau25; Ros34; Blo34; Kap36]. An early review on the field of Compton scattering was given by DuMond in 1933 [DuM33].

In fact, experimental publications of Compton scattering practically ceased to exist in the following decades. The weakness of the Compton effect—it is about a million times weaker than photoionization at respective thresholds—stems the experimental success of observing the Compton effect. For instance, DuMond and Kirkpatrick measured the Compton profile (which relates to the momentum distribution of the bound electron) of helium in 1937, where the experiment took more than 2000 hours to complete [DuM37]! Further, the observation of Compton scattering by observing the Compton peak requires large initial photon energies. For once, the probability for Compton scattering increases for larger photon energies (see Figure 1.1). The detection method of early experiments requires photon energies large enough so that the Compton shift is detectable. The Compton shift is given by $\lambda_C = h/(mc)$, where h is the Planck constant, c is the vacuum speed of light, and m is the mass of the scatterer. For electrons, $\lambda_C = 2.4 \times 10^{-12}$ m. The initial photon wavelength needs to be of similar order of magnitude—that is, hard x rays and upward—for the Compton shift to be detectable.

Early photon detectors (typically ionization chambers or photosensitive film in conjunction with crystal spectrometers) had poor efficiency and resolution for high-energy photon detection and at the time, radioisotopes producing γ rays resulted in much lower fluxes than x-ray tubes, which are based on the radiative decay of excited atoms. Consequently, although higher photon energies were experimentally preferable, they were typically below about 25 keV. For instance, molybdenum Kα corresponds to 17.6 keV photons, silver Kα to 22.2 keV. This limits the elements that can be studied using Compton scattering and the heaviest element seriously studied was aluminum [Coo85]. This limitation was a limitation of theory, since low energy transfers (compared to the ionization threshold of the investigated system) cause the impulse approximation to fail. The impulse approximation assumes a free electron with a momentum distribution as if it was bound. Examples of theoretical and experimental studies of the failure of the impulse approximation can be found in References [Pla65; Eis70; Cur71; Wei77].

The development of solid state detectors at the beginning of the nineteen seventies improved on reliability, accuracy, and speed [Coo77], enabling the replacement of x-ray tubes by γ-ray sources and causing a resurgence of Compton scattering experimental work. A detailed review of these can be found in Reference [Kan92]. An overview of the theoretical work on Compton scattering is given in [Ber97].

The majority of the aforementioned work investigates the momentum distributions of electrons bound in various forms of matter by detecting the scattered photon. Measuring the scattered photon and Compton electron in coincidence $(\gamma, e\gamma)$ carries experimental difficulties which bedeviled the success of such early attempts. The coincidence technique for $(\gamma, e\gamma)$ experiments was already developed 1925 by Bothe and Geiger [Bot25] and more coincidence experiments were carried out thereafter (for example, see Reference [Cro50]), however, they were not able to resolve the influence of the initial momentum distribution on the emerging electron's trajectory. Poor energy resolution of the detectors and a multiple scattering of the Compton electrons within the target are attributed as causes for the failure [Kan92]. Around 1990, Rollason et al. and Bell et al. successfully performed $(\gamma, e\gamma)$ experiments using synchrotron radiation [Rol89; Bel90; Bel91], successfully showcasing the feasibility of $(\gamma, e\gamma)$ experiments as a mean to access the ground-state electron momentum density. However, studies where the ejected Compton electron is observed remain limited [Pra14].

Using synchrotron radiation as a photon source became viable in the nineteen seventies. Its advantages are superior resolution of the incident beam due to the low beam divergence and monochromatibility, as well as its energy tuneability [Coo85]. Modern synchrotron facilities offer sufficient photon fluxes even in the hard x-ray regime. Disadvantageous is the scale and cost of a synchrotron facility as compared to alternative x-ray or γ-ray sources.

For this thesis, Compton scattering at gas-phase targets was investigated. Due to the weakness of the effect, the low target density of gas-phase samples is of increasing nuisance, explaining the scarcity of experimental work with gas-phase samples. The aforementioned 2000-hour-long experiment by DuMond and Kirkpatrick [DuM37] with gas-phase helium emphasizes the consequence of combining a weak process with low target densities.

One goal of the here presented work was the observation of the complete kinematics of Compton scattering at helium, which required low initial photon energies, even further decreasing the cross section of the process. With these experimental parameters Samson et al. [Sam94] measured the relative Compton scattering cross section for helium with photon energies of 2.5 to 5.5 keV. The COLTRIMS technique was already utilized to measure the ratio of single to double ionization of helium by Spielberger et al. [Spi95; Spi96; Spi99]. However in all these experiments, no electron coincidences were observed.

Although the COLTRIMS technique was first utilized by Spielberger and coworkers almost thirty years ago to observe Compton scattering, it remained virtually unused for observing Compton scattering ever since. This is mostly attributed to the fact that for traditional electron momentum density studies, this particular experimental approach offers few advantages over more established techniques. While electron momentum densities can be obtained solely by measuring the Compton ions' momentum distribution [Kal04]— consequently removing the need for a coincident photon and electron detection— the low target densities intrinsic to the technique were a major restraint for it. Only the advancements of the COLTRIMS technique—in particular, the ability to detect ever increasing electron energies with sufficient resolution and efficiency—as well as the advancements of modern synchrotron machines make coincident detection of the Compton electron(s) and the Compton ion(s) feasible. This opens experimental access to some fundamental but unexplored aspects of Compton scattering, which this thesis aims to showcase.

PHOTOIONIZATION BY HARD X RAYS

Depending on the photon energy and the investigated element, Compton scattering is not the only relevant photon/matter interaction. For one of the measurements performed for this work, the initial photon energy was 40 keV and the target sample was molecular nitrogen. The dot in Figure 1.1 marks this region. There, as one can see, the photoeffect—the absorption of a photon by a system and the subsequent emission of an electron whose kinetic energy is the photon energy minus its binding energy, also referred to as photoionization in case single atoms or molecules are the target system—and Compton scattering are of similar relevance. Therefore, without necessitating a different experimental setup or even experimental run, Compton scattering and photoionization were observed *simultaneously*. The two effects are separable by the final momentum configuration of the Compton and photoions.

Photoionization is another fundamental effect of light/matter interaction. Its explanation by Einstein in 1905 [Ein05] was a step toward the formalization of quantum physics and it is the subject of innumerable scientific works. At low energies—that is, energies close to the binding energies of the absorbing electrons—it is of far greater magnitude than the Compton effect, warranting easier experimental access to its observation. Some aspects of photoionization, however, only become relevant in the soft to hard x-ray regime, decreasing the cross section for lighter elements to yet again experimentally challenging levels. For instance, the widely used dipole approximation, which effectively neglects the linear photon momentum, becomes invalid for increasing photon energies.

In scope of this work, a multitude of nondiple effects caused by the linear momentum of the photon have been observed.

STRUCTURE AND CONVENTIONS OF THIS THESIS

Part I introduces the necessary background in order to understand the experimental work. In it, a brief introduction of x-ray scattering and photoionization (Chapter 2), atoms and molecules as described in quantum mechanics (Chapter 3), the experimental techniques to observe the processes (Chapter 4), and the offline analysis performed (Chapter 5) is given.

Part II presents the multiple experimental results of this work and gives further explanations of the theoretical methods used specifically for the respective experiments. The concrete experimental parameters are given within the respective appendices of the chapters of Part II. Chapter 6 presents the kinematically complete measurement of Compton scattering at helium at $\hbar\omega = 2.1$ keV. Chapter 7 presents the results of Compton scattering at helium with $\hbar\omega = 40$ keV. Chapters 8 and 9 present the results of Compton scattering at and photoionization of molecular nitrogen, respectively.

A summary and outlook is given in Part III.

* * *

Throughout this thesis, vectors are typeset in bold italic letters while the vector's magnitude is typeset in italic ($|\boldsymbol{v}| = v$). A vector with a hat corresponds to a vector with a magnitude of unit-length one ($|\hat{\boldsymbol{v}}| = 1$). Multiplication of two variables is indicated explicitly by the "×" symbol or implicitly by no symbol, for example $c = a \times b = ab$. The center-dot is used for the dot product of two vectors $\{c = \boldsymbol{a} \cdot \boldsymbol{b} = ab\cos[\angle(\boldsymbol{a}, \boldsymbol{b})]\}$. Within the context of vector multiplication, the "×" symbol means the cross product of two vectors, for example, $\boldsymbol{c} = \boldsymbol{a} \times \boldsymbol{b}$.

Dream a little less, a little wiser

M. Andresakis

Part I

PREREQUISITES

2

INELASTIC X-RAY SCATTERING AND PHOTOABSORPTION

The present work investigates interactions of single photons (the projectiles) with single atoms or molecules (the targets). The gas-phase target is created by a supersonic gas expansion, the photons are created by synchrotron machines (the details of which are discussed in Chapter 4). In the experiments which were performed for this work, the kinematics of the light/matter interaction are investigated, in particular, the two light/matter interactions *photoabsorption* and *Compton scattering*.

In photoabsorption, the incident photon is absorbed by the atomic or molecular target and, if the photon energy is greater than the ionization threshold, a photoelectron is emitted which in the case of a single photon being absorbed is referred to as *one-photon* photoionization. Ionization by the absorption of multiple photons is referred to as *multi-photon* photoionization, for instance, ionization by a high-intensity laser field. In scope of this work, only the former process was investigated. Therefore, throughout this thesis, photoionization implicitly refers to one-photon photoionization unless explicitly stated otherwise. Photoabsorption is discussed in Section 2.3.

Compton scattering refers to inelastic scattering of photons at electrons. It is discussed in Section 2.4.

For both photoabsorption and Compton scattering, if the energy transfer is larger than the double-ionization threshold, the single interaction of one photon with the target system can lead to the emission of two electrons. This *one-photon double ionization* is discussed in Section 2.5.

2.1 LIGHT/MATTER INTERACTION

For any quantum system described by a Hamiltonian H, the stationary Schrödinger equation

$$H\Psi(\boldsymbol{r}) = E\Psi(\boldsymbol{r}) \tag{2.1}$$

determines the energy eigenstates Ψ of this system as well as the energies E corresponding to these states.

For a single particle interacting with mass m in an external potential $V(\boldsymbol{r})$, the Hamiltonian is given by

$$H = \frac{\boldsymbol{p}^2}{2m} + V(\boldsymbol{r})\,. \tag{2.2}$$

$\boldsymbol{p} = -\mathrm{i}\hbar(\partial/\partial x, \partial/\partial y, \partial/\partial z) \equiv -\mathrm{i}\hbar\boldsymbol{\nabla}$ is the momentum operator.

The interaction of an electromagnetic field of light is described by replacing the momentum operator $\boldsymbol{p}$ with $\boldsymbol{p}_{\text{field}} = \boldsymbol{p} - e\boldsymbol{A}$, where e is the magnitude of the electron charge and $\boldsymbol{A} = \boldsymbol{A}(\boldsymbol{r}, t)$ is the vector potential (see, for instance, Reference [Her17]). $\boldsymbol{A}$ is not an observable itself, only the electric field $\boldsymbol{E}$ and the magnetic flux $\boldsymbol{B}$ derived from $\boldsymbol{A}$ are observable. In absence of any additional external potentials, $\boldsymbol{E}$ and $\boldsymbol{B}$ are given by

$$\boldsymbol{E}(\boldsymbol{r}, t) = -\frac{\partial}{\partial t}\boldsymbol{A}(\boldsymbol{r}, t) \quad \text{and} \quad \boldsymbol{B}(\boldsymbol{r}, t) = \boldsymbol{\nabla} \times \boldsymbol{A}(\boldsymbol{r}, t)\,, \tag{2.3}$$

respectively.

One can choose an alternative form of $\boldsymbol{A}$, as long as the physical properties $\boldsymbol{E}$ and $\boldsymbol{B}$ are not changed. In one of these so-called gauges—the Coulomb gauge—$\boldsymbol{A}$ is chosen such that $\boldsymbol{\nabla} \cdot \boldsymbol{A} = 0$. Then, $\boldsymbol{p} \cdot \boldsymbol{A} = \boldsymbol{A} \cdot \boldsymbol{p}$.

Then, the Hamilton operator for the interaction of a classical electromagnetic field with an atom or molecule becomes

$$\begin{aligned} H &= \frac{\boldsymbol{p}_{\text{field}}^2}{2m_e} + V(\boldsymbol{r}) = \frac{\left(\boldsymbol{p} - e\boldsymbol{A}\right)^2}{2m_e} + V(\boldsymbol{r}) \\ &= \frac{\boldsymbol{p}^2}{2m_e} + V(\boldsymbol{r}) - \frac{e}{m_e}\boldsymbol{p} \cdot \boldsymbol{A} + \frac{e^2}{2m_e}\boldsymbol{A}^2\,, \end{aligned} \tag{2.4}$$

where the first two terms (henceforth called H_{sys}) correspond to the Hamiltonian given by the atomic or molecular system [or, if $V(\boldsymbol{r}) = 0$, the Hamiltonian of a free electron] and the last two terms correspond to the Hamiltonian

$$H_{\text{int}} = \frac{e}{m_e}\boldsymbol{p} \cdot \boldsymbol{A} + \frac{e^2}{2m_e}\boldsymbol{A}^2 \tag{2.5}$$

of the interaction of the field with the electron. m_e is the mass of the electron.

For the interaction of a photon with an atomic or molecular system, the contribution of H_{int} is small compared to H_{sys} and thus, the problem can be treated within the framework of perturbation theory (see next Section 2.2).

In the plane-wave representation of the photon field and within the Coulomb gauge, the vector potential $\boldsymbol{A}$ is expanded with respect to the photon wave vector $\boldsymbol{k}_\gamma$ [Åbe85]

$$\boldsymbol{A} \propto \sum_{\boldsymbol{k}_\gamma,\, q} \left(a_{\boldsymbol{k}_\gamma, q}\, \hat{\boldsymbol{e}}^{(q)}\, \mathrm{e}^{\mathrm{i}\boldsymbol{k}_\gamma \cdot \boldsymbol{r}} + a^\dagger_{\boldsymbol{k}_\gamma, q}\, \hat{\boldsymbol{e}}^{(q)^*}\, \mathrm{e}^{-\mathrm{i}\boldsymbol{k}_\gamma \cdot \boldsymbol{r}} \right)\,. \tag{2.6}$$

Here, $\hat{\boldsymbol{e}}^{(q)}$ ($q = \pm 1$) are the spherical unit vectors perpendicular to $\boldsymbol{k}_\gamma$ (that is, the direction of $\hat{\boldsymbol{e}}^{(q)}$ corresponds to the polarization vector direction $\boldsymbol{\varepsilon}$) and the expansion factors $a^\dagger_{\boldsymbol{k}_\gamma, q}$ and $a_{\boldsymbol{k}_\gamma, q}$ are the transverse-photon creation and destruction operators, respectively. Note that the photon momentum relates to the photon wave vector by $\boldsymbol{k}_\gamma = \boldsymbol{p}_\gamma / \hbar$. Within atomic units (see Appendix "Atomic units," Page 205), $\hbar = 1$ and thus, the photon wave vector equals the photon momentum, which is why throughout this work, $\boldsymbol{k}_\gamma$ is used to refer to the photon momentum.

2.2 Calculating cross sections

Ultimately, in the experimental approach presented in this work—the cold-target recoil-ion momentum-spectroscopy (COLTRIMS) technique, see Chapter 4—clicks-at-positions and times-of-clicks on the detector are measured. With the knowledge of the experimental parameters these translate to momenta of particles at reaction time and consequently to all derived observables, such as their energy, emission angles, et cetera. Thus, one detects experimental yields of a certain observable, that is, one counts how many times a certain value of an observable is measured during the experiment. Note that no absolute probabilities are measured, since this requires knowledge of many quantities not determined by the experiment, for example total number of photon/target interactions, or absolute detection efficiencies.

Depending on the observable, the experimental yield is directly linked to relative differential cross sections. An example is the singly differential cross section $\mathrm{d}\sigma / \mathrm{d}\theta_\gamma$ for Compton scattering, that is, the probability that a photon scatters with a given angle θ_γ. It is measured by the experimental setup by measuring the angular distribution of θ_γ. Since with the COLTRIMS technique momenta (and thus all derived quantities) of multiple reaction particles are measured in coincidence, one is not restricted to singly differential cross sections.

As we will see in this section, calculating cross sections—that is, the probability that a system transitions from an initial state $|i\rangle$ to a final state $|f\rangle$—requires knowledge of the initial and the final state of a system. Thus, measuring cross sections gives a direct test of theoretical models, which, in turn, gives insight into underlying principles. Note however that not all observed quantities of an experiment utilizing the COLTRIMS technique relate to cross sections. For instance, the momenta of helium ions produced by high-energy Compton scattering reflect the initial momentum distribution of the bound electron, which is connected to the initial electron wave function (see Section 2.4.1).

* * *

Transitioning from an initial to a final state is not time-independent and thus, the system is characterized by the time-dependent Schrödinger equation

$$H\Psi(\boldsymbol{r},t) = \mathrm{i}\hbar\frac{\partial\Psi(\boldsymbol{r},t)}{\partial t}\,, \tag{2.7}$$

with the Hamiltonian $H = H_{\mathrm{sys}} + H_{\mathrm{int}}(t)$. Since H_{int} is small compared to the total Hamiltonian, the Schrödinger equation can be solved within the framework of time-dependent perturbation theory. Within thereof, the system is split into an unperturbated—that is, a system with exact solutions—and a perturbated part. The photon/atom interaction is treated as a perturbation of the initial system. The goal of perturbation theory is to compute approximate wave functions of the perturbated system by starting with the exact wave functions of the unperturbated system. An exhaustive discussion of perturbation theory can be found in [Pal06].

Within the framework of perturbation theory, the transition rate from an unperturbated initial state $|i\rangle$ to an unperturbated final state $|f\rangle$ is given by

$$w_{i\to f} = \frac{2\pi}{\hbar}|M_{fi}|^2\delta(E_f - E_i)\,, \tag{2.8}$$

which is known as *Fermi's Golden Rule*. Here,

$$M_{fi} = \langle f|H_{\mathrm{int}}|i\rangle = \int \mathrm{d}^3\boldsymbol{r}\; \Psi_f^* H_{\mathrm{int}} \Psi_i \tag{2.9}$$

is the transition matrix element and $\Psi_{f/i}$ are the wave-function representations of the states $|f\rangle$ and $|i\rangle$ in space, respectively. The δ-function ensures energy conservation. Calculating transition rates (and thus, cross sections), requires knowledge of the initial and the final states as well as knowledge of the transition matrix element.

2.3 PHOTOABSORPTION

Photoabsorption is a first-order interaction of a photon with matter—that is, only the $\boldsymbol{p}\cdot\boldsymbol{A}$ term of H_{int} is relevant since the quadratic contribution of $\boldsymbol{A}$ introduces two-photon processes [Sta06]. Interpreting the expansion factors $a^{\dagger}_{\boldsymbol{k}_\gamma,q}$ and $a_{\boldsymbol{k}_\gamma,q}$ of Equation (2.6) as photon creation and destruction operators gives an intuitive explanation: the linear contribution of $\boldsymbol{A}$ can only emit (create) or absorb (destroy) a photon. The quadratic term contains the creation and destruction operators in second order, thus, photons can be absorbed and emitted at the same time.

For photoabsorption, the final electron energy is fixed by the initial photon energy, that is,

$$E_e = \hbar\omega - E_{\mathrm{bind}} \,, \tag{2.10}$$

where E_{bind} is the magnitude of the binding energy of the electron.

The transition rate given by Fermi's Golden Rule [Equation (2.8)] contains the expansion of $\boldsymbol{A}$ with respect to the photon wave vector $\boldsymbol{k}_\gamma$ [Equation (2.6)]. For photoabsorption, the δ-function of the transition rate collapses this sum, resulting in

$$w_{i\to f} \propto \langle f|\boldsymbol{p}\cdot\boldsymbol{\varepsilon}\,\mathrm{e}^{\mathrm{i}\boldsymbol{k}_\gamma\cdot\boldsymbol{r}}|i\rangle \,, \tag{2.11}$$

where $\boldsymbol{p}$ is the momentum operator and $\boldsymbol{\varepsilon}$ is the photon's polarization vector.

The term $\mathrm{e}^{\mathrm{i}\boldsymbol{k}_\gamma\cdot\boldsymbol{r}}$ can be Taylor expanded, that is,

$$\mathrm{e}^{\mathrm{i}\boldsymbol{k}_\gamma\cdot\boldsymbol{r}} = 1 + \mathrm{i}\boldsymbol{k}_\gamma\cdot\boldsymbol{r} + \frac{(\mathrm{i}\boldsymbol{k}_\gamma\cdot\boldsymbol{r})^2}{2!} + \ldots \,. \tag{2.12}$$

If the product of the photon momentum $\boldsymbol{k}_\gamma$ and the electron position $\boldsymbol{r}$ is small, Equation (2.12) can be approximated with unity, which is referred to as the *dipole approximation*. It will be discussed in more detail in Section 2.3.1.

To calculate the transition rate [Equation (2.11)], appropriate initial and final states, that is, solutions to the Schördinger equation $H_{\mathrm{sys}}\Psi(\boldsymbol{r}) = E\Psi(\boldsymbol{r})$, have to be chosen.

For the simplest case, a hydrogen-like system with one active electron in a Coulomb potential, analytical separable solutions

$$\Psi(\boldsymbol{r}) = Y_{\ell m}(\theta,\phi)R_\ell(r) \tag{2.13}$$

exist, with the spherical harmonics $Y_{\ell m}(\theta,\phi)$ describing the angular dependence of Ψ, and the solutions of the radial Schrödinger equation $R_\ell(r)$ describing the radial dependence. θ and ϕ are the polar and azimuth angle in spherical coordinates; ℓ and m are the orbital angular momentum and projection quantum numbers, respectively. For an extensive discussion of specific forms of $Y_{\ell m}(\theta,\phi)$ and $R_\ell(r)$, see, for example, References [Hil06] and [Gru22].

To choose a final-state wave function, the most simple case is given by a free particle without external potential [$V(\boldsymbol{r}) = 0$], that is, the interaction between residual photoion and the photoelectron is ignored. The Hamiltonian is then simply given by

$$H = \frac{\boldsymbol{p}^2}{2m_e}\,, \tag{2.14}$$

resulting in plane-wave solutions

$$\Psi_{k_e}(\boldsymbol{r}) \propto \mathrm{e}^{\mathrm{i}\boldsymbol{k}_e\cdot\boldsymbol{r}}\,, \tag{2.15}$$

with the wave vector of the electron $\boldsymbol{k}_e$. A plane wave can also be expressed as a superposition of partial waves $\Psi_{k_e\ell m}$

$$\mathrm{e}^{\mathrm{i}\boldsymbol{k}_e\cdot\boldsymbol{r}} = \sum_{\ell=0}^{\infty} \Psi_{k_e\ell m} = \sum_{\ell=0}^{\infty} \frac{\mathrm{i}^\ell}{\hbar}\sqrt{\frac{2m_e k_e}{\pi}}\, j_\ell(k_e r) Y_{\ell m}(\theta,\phi)\,, \tag{2.16}$$

with the spherical Bessel functions of the first kind $j_\ell(kr)$.

Describing the final-state electron wave function using plane waves assumes the *Born approximation* [Bor26]. It is valid if the energy of the outgoing photoelectron is large compared to the binding energy, but not yet relativistic ($E_\mathrm{bind} \ll E_e \ll 511\,\mathrm{keV} = m_e c^2$).

2.3.1 THE DIPOLE APPROXIMATION

As mentioned, the dipole approximation refers to the case where Equation (2.12) is truncated after the first term, corresponding to dipole transitions from initial to final states, while higher-order terms correspond to multipole transitions. For instance, quadrupole transitions correspond to the $\boldsymbol{k}_\gamma \cdot \boldsymbol{r}$ term.

For dipole transitions, the interaction operator H_int is proportional to $\boldsymbol{p}\cdot\boldsymbol{\varepsilon}$ and thus, the transition rate is proportional to $w_{i\to f} \propto \langle f|\boldsymbol{p}\cdot\boldsymbol{\varepsilon}|i\rangle$. Then, with the above approximations of a hydrogen-like system and a plane-wave photoelectron wave function, the total photoionization cross section reads

$$\sigma = \frac{256\pi\alpha a_0^2}{3}\left(\frac{E_H}{2}\right)^{7/2} \times \frac{Z^5}{n^3(\hbar\omega)^{7/2}}\,. \tag{2.17}$$

Here, α is the fine structure constant, Z is the atomic charge, n is the principle quantum number, a_0 is the Bohr radius, and E_H is the Hartree energy. Omitted here is an extensive derivation of Equation (2.17), which can be found, for example, in Chapter 5.5 of Reference [Her17].

Equation (2.17) shows the dependency of the ionization cross section on the atomic charge Z, the principle quantum number n, and the photon energy $\hbar\omega$. It increases significantly for higher Z, while dropping significantly for outer electronic shells (that is, increasing n) and increasing photon energy. This can qualitatively be understood by the following consideration: The photon momentum is small compared to the final electron momentum after the emission. Therefore, the final electron momentum has to be largely a consequence of the initial bound-state momentum, which is higher for inner atomic shells and for higher atomic charge Z. Consequently, increasing photon energies require yet higher bound-electron momentum components to couple effectively, thus, the cross section decreases.

The cross section given by Equation (2.17) is valid within the Born ($E_{\mathrm{bind}} \ll E_e \ll 511\,\mathrm{keV}$) and the hydrogen approximation. It best describes the total cross section for high photon energies, where it is dominated by the slope proportional to $(\hbar\omega)^{-7/2}$. It fails to accurately describe the total cross section close to the ionization threshold.

Within the dipole approximation and for randomly polarized light the differential cross section in photoelectron emission angle is [Coo69]

$$\frac{\mathrm{d}\sigma}{\mathrm{d}\Omega} = \frac{\sigma}{4\pi}\left[P_0(\cos\theta_{e,\gamma}) - \frac{\beta}{2}P_2(\cos\theta_{e,\gamma})\right] . \tag{2.18}$$

However, every measurement presented in this thesis was performed with linearly polarized light. Therefore, this section focuses on linear photon polarization. For linearly polarized light, the differential cross section reads [Coo69]

$$\frac{\mathrm{d}\sigma}{\mathrm{d}\Omega} = \frac{\sigma}{4\pi}\left[P_0(\cos\theta_{e,\varepsilon}) + \beta P_2(\cos\theta_{e,\varepsilon})\right] . \tag{2.19}$$

In Equations (2.18) and (2.19), σ is the angle integrated cross section [for instance, calculated by Equation (2.17)], β the asymmetry parameter, $\theta_{e,\gamma}$ the angle between the emission direction of the photoelectron and the photon momentum k_γ, $\theta_{e,\varepsilon}$ the angle between the emission direction of the photoelectron and the photon polarization axis, and P_ℓ the ℓth Legendre polynomial, namely,

$$P_0(\cos\theta) = 1\,, \tag{2.20}$$

$$P_2(\cos\theta) = \frac{1}{2}(3\cos^2\theta - 1)\,. \tag{2.21}$$

The range of the asymmetry parameter is $-1 \leq \beta \leq 2$. It can be theoretically calculated from the orbital angular momentum quantum number ℓ, the dipole radial integrals depending on the radial wave functions for bound and free electrons, and the phase shift between two partial waves characterized by $(\ell+1)$ and $(\ell-1)$ {see Equation (8) in [Coo69]}. The angular distribution for different values of β is shown in Figure 2.1A. For photoelectrons originating from an s-shell, $\beta = 2$.

2.3.2 BEYOND THE DIPOLE APPROXIMATION

The dipole approximation is valid for $\boldsymbol{k}_\gamma \cdot \boldsymbol{r} \ll 1$. One can interpret this as a constant light-phase over the whole atom, that is, the wavelength of the incident light is large compared to the atom. Typical atomic radii are of the order of 1 Å. The wavelength λ of, for example, 100 eV photons equals $\lambda = hc/E_\gamma \approx 125$ Å $\gg 1$ Å. With $k = 2\pi/\lambda$, $kr \approx 0.05 \ll 1$.

For increasing photon energy, more than pure dipole transitions become relevant. For instance, Grundmann et al. measured multiple non-dipole quadrupole effects—that is, effects forbidden in pure dipole transitions—in photoionization of helium already at photon energies of as low as 800 eV (see References [Gru18; Gru20b], or [Gru22]). The linear photon momentum $\boldsymbol{k}_\gamma$ alters the photoelectron emission patterns already at $\hbar\omega = 300$ eV for photoionization of helium, as seen in photoion and photoelectron emission patterns measured by Grundmann et al. [Gru20a] (note that in Reference [Gru20a], experimental data which is presented in Section 9.4 of this thesis is included as well). At $\hbar\omega = 300$ eV, $kr \approx 0.15$.

Alternatively, the dipole approximation breaks down if the spatial extent of the electronic shell is large—that is, $r \gg 1$ Å—for instance, in photoionization of excited atoms. This has been observed, for example, by Krässig et al. [Krä95].

J. Cooper [Coo90] proposed corrections to Equation (2.19) introduced by the $\boldsymbol{k}_\gamma \cdot \boldsymbol{r}$ term of Equation (2.12). Without the restriction to only dipole

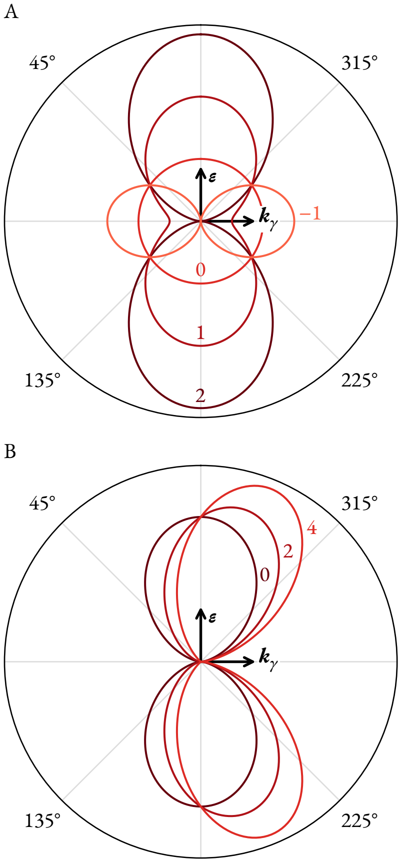

Figure 2.1: Electron angular distributions for linearly polarized light. A, Equation (2.19) for different values of β (numbers). The distributions are rotationally symmetric around the polarization axis. B, Equation (2.24) for $\beta = 2, \delta = 0, \phi_{e,\gamma} = 0$, and different values of γ (numbers). In both panels, the upward pointing arrow indicates the direction of the photon polarization $\boldsymbol{\varepsilon}$, the forward pointing arrow the direction of the photon momentum $\boldsymbol{k}_\gamma$.

transitions, the singly differential cross section is given by

$$\frac{\mathrm{d}\sigma}{\mathrm{d}\Omega} = \sum_{\ell} A_\ell P_\ell(\cos\theta_{e,\gamma}) \,. \tag{2.22}$$

Whereas for dipole transitions, only expansion factors A_0 and A_2 are non-zero, the inclusion of multipole transitions introduced by $\boldsymbol{k}_\gamma \cdot \boldsymbol{r}$ results in

$$\frac{\mathrm{d}\sigma}{\mathrm{d}\Omega} = \sum_{\ell=0}^{3} A_\ell P_\ell(\cos\theta_{e,\gamma}) \,, \tag{2.23}$$

which becomes

$$\begin{aligned}\frac{d\sigma}{d\Omega} = \frac{\sigma}{4\pi}\biggl[1 + \frac{\beta}{2}(3\cos^2\theta_{e,\varepsilon} - 1) \\ + (\gamma\cos^2\theta_{e,\varepsilon} + \delta)\sin\theta_{e,\varepsilon}\cos\phi_{e,\gamma}\biggr]\,,\end{aligned} \tag{2.24}$$

where $\delta = A_1 + A_3$ and $\gamma = -5A_3$, and $\phi_{e,\gamma}$ is the electron azimuth angle with respect to the photon direction. The electric-dipole/electric-quadrupole interference is represented by γ; δ is the magnetic-electric-dipole term. Figure 2.1b shows the photoelectron angular distributions for different values of γ. One can see that $\gamma \neq 0$ introduces forward/backward asymmetries with respect to the photon momentum $\boldsymbol{k}_\gamma$.

Derevianko et al. theoretically studied the corrections to the dipole photoelectron angular distribution [Equation (2.19)] due to the $\boldsymbol{k}_\gamma \cdot \boldsymbol{r}$ and the $\boldsymbol{k}_\gamma^2 \cdot \boldsymbol{r}^2$ terms of Equation (2.12) [Der99]. The $\boldsymbol{k}_\gamma^2 \cdot \boldsymbol{r}^2$ corrections are characterized by parameters λ, μ and ν, and $\Delta\beta$, a correction to the dipole asymmetry parameter β, with

$$\begin{aligned}\frac{d\sigma}{d\Omega} = \frac{\sigma}{4\pi}\bigl[1 &+ (\beta + \Delta\beta)P_2(\cos\theta_{e,\varepsilon}) \\ &+ (\gamma\cos\theta_{e,\varepsilon} + \delta)\sin\theta_{e,\varepsilon}\cos\phi_{e,\varepsilon} \\ &+ \lambda P_2(\cos\theta_{e,\varepsilon})\cos 2\phi_{e,\varepsilon} + \mu\cos 2\phi_{e,\varepsilon} \\ &+ \nu(1 + \cos 2\phi_{e,\varepsilon})P_4(\cos\theta_{e,\varepsilon})\bigr]\,,\end{aligned} \tag{2.25}$$

where the relation $\lambda + \mu + \nu = 0$ holds and P_4 is given by

$$P_4(\cos\theta) = \frac{1}{2}(35\cos^4\theta - 30\cos^2\theta + 3)\,. \tag{2.26}$$

[Note that in Equation (2.25), λ and ν are not the photon wavelength or the photon frequency; the symbols λ, μ, and ν are chosen to comply with literature standards.]

At 40 keV photon energy (the photon energy used in parts of this work), the photon wave length is 0.3 Å, smaller than the spatial extent of the atom of $r \approx 1$ Å, and thus, to accurately describe the $\exp i\boldsymbol{k}_\gamma \cdot \boldsymbol{r}$ term of the interaction operator, the inclusion of only a few terms of the Taylor expansion [Equation (2.12)] is not sufficient. In Section 9.3 of Chapter 9, electron angular distributions in the molecular frame of nitrogen at $\hbar\omega = 40$ keV are presented. In the theoretical calculations, to account for the $\exp i\boldsymbol{k}_\gamma \cdot \boldsymbol{r}$ term sufficiently, $\exp i\boldsymbol{k}_\gamma \cdot \boldsymbol{r}$ was expanded in partial waves [Equation (2.16), Page 16], including partial waves with quantum numbers $\ell \leq 90$ and $|m| \leq 6$.

2.4 COMPTON SCATTERING

Multiple effects of photon scattering have been described in the literature. The following (non-exhaustive) list gives an overview of the most common scattering processes.

Rayleigh scattering refers to elastic scattering of photons at small particles; that is, only an angular deflection of the photon without energy loss occurs. It is sometimes referred to as coherent scattering because of a fixed phase relationship between incident and scattered waves [Coo77].

Raman scattering refers to inelastic scattering at matter where no electrons are emitted; that is, the internal electronic configuration of the scatterer-system changes. Since inelastic scattering always involves energy loss of the scattered photon, the incident and the scattered photon waves are always incoherent.

Thomson scattering refers to elastic scattering of photons at electrons. It is the low-energy limit of Compton scattering.

Compton scattering refers to inelastic scattering of photons at free electrons, or in the case of electrons bound in matter, the case where at least one electron is emitted.

The term Compton scattering is furthermore used in different research fields. For instance, *stimulated* Compton scattering refers to a resonance of the Compton scattering process if in a two-color photon field, the electron absorbs the higher-frequency photon of the two-color field and emits the lower-frequency photon (see for example, [Bac14]). If the electron is bound in matter and the energy difference between the two photon fields is smaller than the ionization threshold, this is referred to as stimulated Raman scattering, as has been measured by Eichmann et al. [Eic20]. *Electron-Compton* scattering, also called *atomic momentum spectroscopy*, is another scientific field, however, it does not refer to photons but electrons scattering off matter. Electron-Compton scattering can be used to investigates intramolecular atomic motion [Vos01], analogously to using Compton scattering as a tool for electron momentum spectroscopy, that is, investigating the momentum distributions of bound electrons (more details will be discussed later in this section).

The main focus of this section (and the sole focus of experimental results for inelastic scattering presented in this thesis) is Compton scattering. In its simplest form, Compton scattering describes a photon scattering at a free electron at rest, the geometry of which is depicted in Figure 2.2. It was first

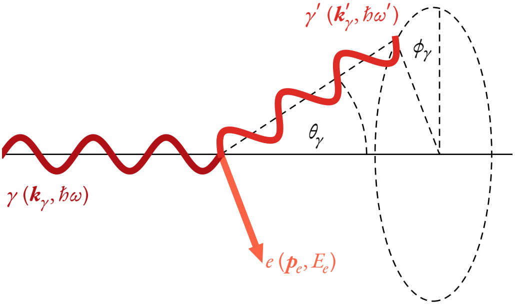

FIGURE 2.2: Principle sketch of Compton scattering with the polar angle θ_γ and the azimuth angle ϕ_γ.

explained by A. Compton in 1923 [Com23a], where he observed the scattering of photons at light elements and where he explained the wavelength-shift $\varDelta\lambda \equiv \lambda - \lambda'$. Qualitatively, the scattering of x rays and the wavelength shift was previously observed by J. Gray in 1920 [Gra20].

In the Compton reaction

$$\gamma + e \rightarrow \gamma' + e \,, \tag{2.27}$$

the initial photon momentum is $\boldsymbol{k}_\gamma$, the momentum of the scattered photon is $\boldsymbol{k}'_\gamma$, with respective energies $\omega = E_\gamma / \hbar$ and $\omega' = E_{\gamma'} / \hbar$. The incoming and outgoing photon's polarization vectors are $\boldsymbol{\varepsilon}$ and $\boldsymbol{\varepsilon}'$, respectively. The final momentum of the electron is $\boldsymbol{p}_e$, its energy is E_e. The photon scattering angle is θ_γ.

For Compton scattering at a free electron at rest, momentum and relativistic energy conservation—that is,

$$\boldsymbol{k}_\gamma = \boldsymbol{k}'_\gamma + \boldsymbol{p}_e \,, \tag{2.28}$$

$$\hbar\omega + m_e c^2 = \hbar\omega' + \sqrt{p_e^2 c^2 + m_e^2 c^4} \tag{2.29}$$

—result in a change of the photon wavelength

$$\varDelta\lambda = \frac{h}{m_e c}(1 - \cos\theta_\gamma) \tag{2.30}$$

which corresponds to an energy of the outgoing photon of

$$\hbar\omega_C \equiv \hbar\omega' = \frac{\hbar\omega}{1 + \hbar\omega(1 - \cos\theta_\gamma)/(m_e c^2)} \tag{2.31}$$

and the final momentum of the electron of

$$\boldsymbol{p}_e = \boldsymbol{k}_\gamma - \boldsymbol{k}'_\gamma \equiv \boldsymbol{Q}\,, \tag{2.32}$$

with the momentum transfer $\boldsymbol{Q}$. For this case, the differential cross section for Compton scattering is [Hei54]

$$\left(\frac{\mathrm{d}\sigma}{\mathrm{d}\Omega'}\right)_{\mathrm{KN}} = \frac{r_0}{4}\left(\frac{\omega'}{\omega}\right)^2\left(\frac{\omega'}{\omega} + \frac{\omega}{\omega'} - 2 + 4\cos^2\Theta\right)\,, \tag{2.33}$$

where the angle Θ is the angle between the polarization of the incident and the scattered photon, that is, $\cos\Theta = \boldsymbol{\varepsilon}\cdot\boldsymbol{\varepsilon}'$. r_0 is the classical electron radius. Equation (2.33) gives the differential cross section for an incident photon with energy $\hbar\omega$ and polarization $\boldsymbol{\varepsilon}$ scattering into the solid angle $\mathrm{d}\Omega = \mathrm{d}\cos\theta_\gamma \mathrm{d}\phi_\gamma$ with energy $\hbar\omega'$ and polarization $\boldsymbol{\varepsilon}'$. It represents the Klein-Nishina cross section, deduced 1929 by Klein and Nishina [Kle29], and is the result of a fully relativistic treatment of Compton scattering in the framework of quantum electrodynamics.

In case of unpolarized initial radiation, Equation (2.33) becomes [Hei54]

$$\left(\frac{\mathrm{d}\sigma}{\mathrm{d}\Omega'}\right)_{\mathrm{KN}} = \frac{r_0^2}{2}\left(\frac{\omega'}{\omega}\right)^2\left(\frac{\omega'}{\omega} + \frac{\omega}{\omega'} - \sin^2\theta_\gamma\right)\,. \tag{2.34}$$

Some angular distributions of θ_γ resulting from the Klein-Nishina formula (2.34) and different initial photon energies are shown in Figure 2.3a.

It is noteworthy that for polarized primary radiation and for small scattering angles, the scattered radiation remains completely polarized while for large scattering angles, the scattered radiation is unpolarized. Further, in Figure 2.3a, one can see that for small scattering angles, the Klein-Nishina cross section is identical to the low-energy—that is, non-relativistic—limit, shown by the dashed line. In the low-energy limit, $k_\gamma \ll m_e c^2$, and Equation (2.34) becomes

$$\left(\frac{\mathrm{d}\sigma}{\mathrm{d}\Omega'}\right)_{\mathrm{Th}} = \frac{r_0^2}{2}\left(1 + \cos^2\theta_\gamma\right)\,. \tag{2.35}$$

Equation (2.35) is known as the Thomson cross section, which corresponds to coherent scattering of light, where $k'_\gamma = k_\gamma$. It is independent of the energy of the incident photon. It represents the classical limit of scattering of radiation and can be deduced without any reference to quantum mechanics.

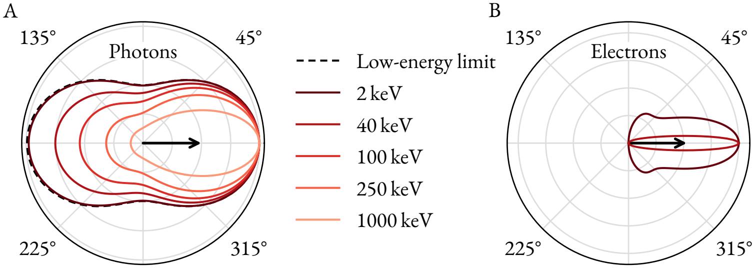

Figure 2.3: Angular distributions of photons (A) and electrons (B) corresponding to the Klein-Nishina cross section, that is, Equations (2.34) and (2.37), respectively. The solid lines correspond to different initial photon energies (see legend). The arrows indicate the direction of the initial photon. The dashed line in A is the low-energy limit, that is, Equation (2.35). In B, only the distributions for $\hbar\omega = 2$ and 40 keV are shown and both distributions are normalized to their maximum.

For a more comprehensive examination as well as a deduction of the Klein-Nishina cross section, the reader is referred to Reference [Hei54].

With the COLTRIMS technique, the scattered photon is not directly detected, but, instead, the recoiling electron. In the approximation that the electron is free and at rest, one can express the differential cross section (2.34) in terms of the electron recoil angle $\theta_e = \arccos(\boldsymbol{p}_e \cdot \boldsymbol{k}_\gamma)$ via Equations (2.30) to (2.32). It yields the expression

$$\frac{\mathrm{d}\sigma}{\mathrm{d}\Omega_e} = 4r_0^2 \frac{(1+\beta)^2 \cos\theta_e}{(1+2\beta+\beta^2\sin^2\theta_e)^2} \times T \tag{2.36}$$

with

$$T = 1 + \frac{2\beta^2\cos^4\theta_e}{[1+2\beta+\beta^2\sin^2\theta_e][1+\beta(\beta+2)\sin^2\theta_e]} - \frac{2(1+\beta)^2\sin^2\theta_e\cos^2\theta_e}{[1+\beta(\beta+2)\sin^2\theta_e]^2} \tag{2.37}$$

and $\beta = k_\gamma/(m_e c^2)$. It is visualized in Figure 2.3B.

In a more general approach to photon scattering, the interaction operator H_{int} [Equation (2.5), Page 12] leads to the well-known Kramers-Heisenberg-

Waller (KHW) matrix element [Kra25; Wal29]

$$
\begin{aligned}
M_{\mathrm{KHW}} = (\boldsymbol{\varepsilon}\cdot\boldsymbol{\varepsilon}'^{*})\langle f|\mathrm{e}^{\mathrm{i}\boldsymbol{Q}\cdot\boldsymbol{r}}|i\rangle \\
- \sum_{n} \frac{\langle f|\mathrm{e}^{-\mathrm{i}\boldsymbol{k}'_{\gamma}\cdot\boldsymbol{r}}(\boldsymbol{\varepsilon}'^{*}\cdot\boldsymbol{p})|n\rangle\langle n|\mathrm{e}^{\mathrm{i}\boldsymbol{k}_{\gamma}\cdot\boldsymbol{r}}(\boldsymbol{\varepsilon}\cdot\boldsymbol{p})|i\rangle}{E_n-(E_i+\omega+\mathrm{i}\varepsilon)} \\
- \sum_{n} \frac{\langle f|\mathrm{e}^{-\mathrm{i}\boldsymbol{k}_{\gamma}\cdot\boldsymbol{r}}(\boldsymbol{\varepsilon}\cdot\boldsymbol{p})|n\rangle\langle n|\mathrm{e}^{\mathrm{i}\boldsymbol{k}'_{\gamma}\cdot\boldsymbol{r}}(\boldsymbol{\varepsilon}'^{*}\cdot\boldsymbol{p})|i\rangle}{E_n-(E_i-\omega')}\,.
\end{aligned}
\tag{2.38}
$$

Here, $|f\rangle$, $|i\rangle$, and $|n\rangle$ are the final, the initial, and intermediate states, respectively, which are solutions to the Schrödinger equation within the independent-particle approximation. The sum over the intermediate states is a sum over a complete set of intermediate states, including occupied orbitals of the initial atomic configuration [Ber93]. The first term in Equation (2.38) corresponds to the $\boldsymbol{A}^2$ term of Equation (2.5), the other two terms to the $\boldsymbol{p}\cdot\boldsymbol{A}$ term evaluated in second-order perturbation theory. E_i is the binding energy of the electron in state $|i\rangle$, E_n the energy of the intermediate states. Note that when unpolarized photons are used, one must sum over all final polarization directions $\boldsymbol{\varepsilon}'$ and average over the initial polarization $\boldsymbol{\varepsilon}$.

Figure 2.4 shows various schematic spectral features of inelastic photon scattering with subsequent ionization of the scatterer-system—that is, the Compton spectrum—resulting from calculations based on Equation (2.38).

The infrared divergence for $\hbar\omega' \to 0$ [region (i)]—which is unambiguously predicted by theory, but has not yet been experimentally confirmed despite several attempts [Cha06]—is a consequence of quantum electrodynamics, which predicts a diverging amount of soft scattered photons (that is, photons with $\hbar\omega' \to 0$). For the infrared divergence, the $\boldsymbol{p}\cdot\boldsymbol{A}$ term of H_{int} is dominant [Pra10].

It is not possible to observe the infrared divergence using the COLTRIMS technique, since not the scattered photon is detected but instead, the ejected

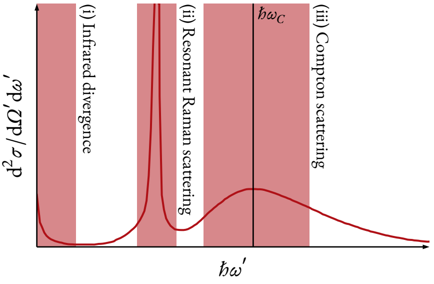

Figure 2.4: Schematic representation of the energy spectrum of inelastically scattered photons (adapted from [Ber93]).

Compton electron. For soft scattered photons the energy of the electron is indistinguishably close to the electron energy resulting from ionization by photoabsorption.

The Compton spectrum of Figure 2.4 shows resonant behavior for characteristic x-ray energies. The resonances appear at scattered photon energies $\hbar\omega'$ that match the downward transition energy from a higher state of the initial electron configuration to a lower state thereof, where the lower state may be occupied or unoccupied. Since the resonant behavior mimics that of Raman scattering—as in, the cross section is enhanced for energies matching the energetic separation of atomic subshells—it is referred to as resonant Raman scattering, or sometimes Raman-Compton scattering. Opposed to pure Raman scattering, an electron is emitted. Resonant Raman scattering is an effect of the $\boldsymbol{p} \cdot \boldsymbol{A}$ term of the interaction Hamiltonian. Bergstrom et al. predict it, for example, for Compton scattering at the L_2-subshell of carbon (see Figure 15 in [Ber93]), and it has been observed by C. Sparks [Spa74]. Noteworthily, the position of the resonance peak does not depend on the initial photon energy or the scattering angle [Ber97].

A broadened Compton peak around the Compton line $\hbar\omega_C$ corresponds to Compton scattering dominated by the $\boldsymbol{A}^2$ term of the interaction Hamiltonian. ω_C is given by Equation (2.31).

Equation (2.38) includes transitions where final and initial state are identical ($|f\rangle = |i\rangle$). If the energy of the scattered photon is the same as the incoming photon ($\omega' = \omega$), this corresponds to Rayleigh (elastic) scattering. In case of inelastic scattering, the photon loses energy in the scattering process and the internal structure of the target atom changes, that is, $\omega' \neq \omega$ and $|f\rangle \neq |i\rangle$. Conventionally, Raman scattering refers to the case where no electron is emitted and Compton scattering to the case where at least one electron is emitted. Note that in Figure 2.4, Raman scattering is not included.

With the COLTRIMS technique, the Compton electrons instead of the scattered photons are observed. For fixed scattering angles, the electron's energy distribution correlates to the spectrum shown in Figure 2.4, since the energy of the electron is given by $E_e = \hbar\omega - \hbar\omega' - E_{\text{bind}}$, where E_{bind} is the binding energy of the electron.

2.4.1 IMPULSE AND A^2 APPROXIMATION

According to the Klein-Nishina formula, the spectrum of Figure 2.4 would have solely a sharp line at $\omega' = \omega_C$, which is experimentally not observed. J. DuMond [DuM29] was the first to explain the broadened feature. He relates the broadening to the momentum density of the bound electron. This forms the most widely used approximation for Compton scattering, the *impulse approximation*. The impulse approximation assumes Compton scattering to happen at a free electron, where the binding is only considered insofar that the momentum distribution of the electron is given by the bound-state momentum distribution and the energy of the scattered photon is broadened in a Doppler-like fashion. It proved to be a valid approximation in the case that the width of the bound electron momentum distribution is much smaller than the momentum transfer Q. Its limits will be discussed in the next Section 2.4.1.1.

Within the impulse approximation, the final electron is described by a plane wave. Only considering the $\boldsymbol{A}^2$ term of Equation (2.38) the doubly differential cross section for nonrelativistic Compton scattering is given by [Big75]

$$\frac{\mathrm{d}^2\sigma}{\mathrm{d}\Omega'\mathrm{d}\omega'} = \left(\frac{\mathrm{d}\sigma}{\mathrm{d}\Omega'}\right)_{\mathrm{Th}} \frac{\omega}{\omega'}\frac{m_e}{k} J(q) \,. \tag{2.39}$$

Here, $(\mathrm{d}\sigma/\mathrm{d}\Omega')_{\mathrm{Th}}$ is the Thomson cross section [Equation (2.35)] and $J(q)$ is the Compton profile. It relates the momentum distribution $\rho(p)$ of the electron in the target atom with the Doppler-broadened Compton peak. The momentum distribution relates to the coordinate-space electron wave function $\Psi(\boldsymbol{r})$ via

$$\rho(\boldsymbol{p}) = |\Psi(\boldsymbol{p})|^2 \,, \tag{2.40}$$

where $\Psi(\boldsymbol{p})$ is the Fourier transform of $\Psi(\boldsymbol{r})$. q is the projection of the bound-electron momentum onto the photon momentum $\boldsymbol{k}_\gamma$. In case of a spherically symmetric momentum distribution and within the nonrelativistic impulse approximation, $J(q)$ is given by

$$J(q) = \frac{1}{2}\int_q^\infty \mathrm{d}p\, p \rho(p) \,. \tag{2.41}$$

Integration of Equation (2.39) over the final photon energies ω' yields the singly differential cross section, commonly written in terms of the incoherent scattering function $S(Q)$ [Ber93]

$$\left(\frac{\mathrm{d}\sigma}{\mathrm{d}\Omega'}\right)_{\mathrm{A}^2} = \left(\frac{\mathrm{d}\sigma}{\mathrm{d}\Omega'}\right)_{\mathrm{KN}} \times S(Q) \,. \tag{2.42}$$

Note that $S(Q)$ can be calculated without explicit reference to Compton scattering. It is the probability that the bound electron is emitted to the continuum if the bound-state wave function is shifted in momentum space by the amount Q. For instance, incoherent scattering functions are calculated by Hubbell et al. [Hub75], which already give a qualitative prediction of Compton scattering as measured in the presented work (see Chapter 6).

To derive Equation (2.39), only the $\boldsymbol{A}^2$ term of the KHW matrix element [Equation (2.38)] is considered, that is, the $\boldsymbol{p} \cdot \boldsymbol{A}$ term of the interaction operator H_{int} is ignored. This is referred to as the *A^2 approximation*. The ratio of $\boldsymbol{p} \cdot \boldsymbol{A}$ to the $\boldsymbol{A}^2$ term approaches zero roughly as $(\omega - \omega')/\omega$ [Åbe85]. The measurements performed for this work utilized photons with $\hbar\omega = 2.1$ and $\hbar\omega = 40$ keV. At $\hbar\omega = 2.1$ keV, the majority of electrons resulting from ionization of helium by Compton scattering have an energy of up to 50 eV (see Chapter 6). Then, the maximum energy loss of the photon is about 74.6 eV, resulting in a ratio $(\omega - \omega')/\omega = 0.035$ and thus, the contribution of the $\boldsymbol{p} \cdot \boldsymbol{A}$ is neglectable. At $\hbar\omega = 40$ keV the energy loss of the photon corresponding to Equation (2.31) (Page 22) is up to about 5 keV, resulting in a ratio of about 0.125. In the experiment (see Chapters 7 and 8), however, only Compton electrons with up to 1.3 keV could be detected. In that case, the ratio $(\omega - \omega')/\omega$ is about 0.04 [for Compton scattering at $\mathrm{N}(1s)$] or 0.03 [for Compton scattering at $\mathrm{N}(2s)$].

Equation (2.42) gives an interpretation of the Compton scattering process within the A^2 approximation. Within it, the singly differential cross section is given by the Klein-Nishina cross section times a correction factor $S(Q)$, given by the incoherent scattering function. That is, one can picture the Compton scattering process on bound electrons in two steps. First, the photon scatters at the bound electron as if it was free. The bound-electron momentum distribution and the binding of the electron are condensed in the incoherent scattering function $S(Q)$, so in the second step, the cross section for scattering at free electrons is corrected by $S(Q)$. Note that for Compton scattering at a free electron, only the $\boldsymbol{A}^2$ term of H_{int} contributes, since the $\boldsymbol{p} \cdot \boldsymbol{A}$ term of Equation (2.38) vanishes [Eis70; Pra10].

2.4.1.1 LIMITS OF THE IMPULSE AND THE A^2 APPROXIMATION

As mentioned above, the impulse approximation is valid in the case that the momentum transfer is much larger than p_0, that is, $p_0/Q \ll 1$, where p_0 corresponds to the width of the bound-state electron momentum distribution $\rho(p)$.

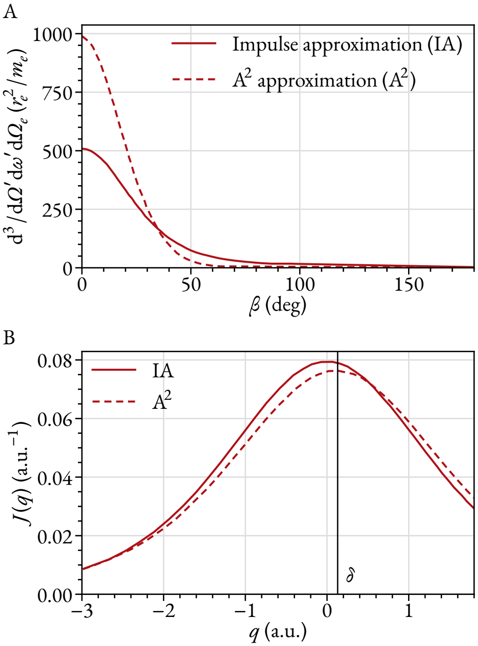

Figure 2.5: Comparison of impulse and A^2 approximation calculations. A, Triply differential cross section of photons Compton scattering at the beryllium K-shell as a function of the angle β (see main text). The incoming photon energy is $\hbar\omega = 10$ keV, the energy of the scattered photon is $\hbar\omega' = 9.66$ keV, and the scattering angle is $\theta_\gamma = 140°$. B, Compton profile for fixed $p_0/Q = 0.54$ for a beryllium K-shell electron in a hydrogenic model. The maximum of the A^2 approximation distribution is shifted by an amount δ, as marked by the vertical line. (Obtained from [Pra10].)

As Pratt et al. [Pra10] show, this assumption is generally too restrictive. While indeed they show that for triply differential cross sections the impulse approximation is only valid for the case that $p_0/Q \ll 1$, for the doubly differential cross section, calculations within the impulse approximation and calculations within the A^2 approximation do not show large discrepancies even for $p_0/Q = 0.54$ (which is approximately in the order of unity).

This can be seen in Figure 2.5. In Panel A, the triply differential cross section in photon scattering angle, scattered-photon energy and the solid angle of the electron emission direction are calculated within the impulse and the A^2 approximations. The angle β is the angle between electron momentum $\boldsymbol{p}_e$ and momentum transfer $\boldsymbol{Q}$.

These large discrepancies disappear after integration over the electron emission direction, that is, going from the triply differential cross section to the doubly differential cross section. This can be observed in Figure 2.5B. There, the Compton profile for beryllium K-shell electrons—calculated within the impulse and A^2 approximation, respectively, and with $p_0/Q = 0.54$—is shown. The biggest discrepancy is a shift δ of the maximum for the A^2 approximation calculations. The overall shape, however, is very well described by the calculations within the impulse approximation. Compensating for the shift δ and renormalizing both curves of Figure 2.5B to their respective maximum qualitatively demonstrates this, as is shows in Figure 6 of Reference [Pra10].

Bachau and Dieng performed calculations for initial photon energies of 2.18 keV Compton scattering at helium, emphasizing the contributions of the $\boldsymbol{p} \cdot \boldsymbol{A}$ term to the scattering cross section [Bac21]. They find that for small scattering angles the $\boldsymbol{p} \cdot \boldsymbol{A}$ term significantly contributes to the electron energy distribution, whereas for scattering angles of $\theta_\gamma = 10°$, the distributions are dominated by the $\boldsymbol{A}^2$ term. The authors chose the initial photon energy close to the photon energy of the low-energy Compton scattering experiment of this thesis. However, they investigated small scattering angles, which are experimentally not accessible due to the decreased cross section of this region, as will be discussed in Chapter 6. For the region of large momentum transfers (that is, large scattering angles) presented there, the findings of Bachau and Dieng back up the assumption that the A^2 approximation is valid.

Typically, cross sections for photon scattering angles and scattered-photon energies are calculated. In the work presented here, not the scattered photon is detected, but instead the Compton ion(s) and Compton electron(s) are detected in coincidence. Thus, the discrepancies of the fully differential cross sections obtained within the impulse approximation are generally too large to be applicable to quantitatively describe the experimental findings, and full A^2 approximation calculations are necessary unless $p_0/Q \ll 1$. For instance, to describe the experimental findings presented in Chapter 6 or Chapter 7, fully differential cross sections were calculated.

2.4.1.2 CALCULATING CROSS SECTIONS WITHIN THE A^2 APPROXIMATION

Throughout this work, all theoretical considerations and calculations are within the A^2 approximation.

The Klein-Nishina formula and other expressions laid out above give the singly differential cross section in photon scattering angle. From these, already a lot can be learned about the underlying internal structures of the scatterer-target atoms, and typically, in Compton scattering experiments, the scattered photons are measured, sometimes in coincidence with electrons [Coo85].

As mentioned, the experimental approach of this work observes Compton scattering in terms of Compton ion and Compton electron coincidence detection. This approach requires interaction-free Compton targets, which means a target in the gas phase is necessary. The low target densities of gas targets combined with the small cross sections of Compton scattering make this approach experimentally challenging and experiments on Compton scattering in means of ion and/or electron detection rare [Pra14]. Some examples following this approach are given in References [Sam94; Spi95; Spi96; Spi99; Kal04].

To calculate higher differential cross sections—for example, cross sections in electron emission angle or electron energy—within the A^2 approximation, in principle Equation (2.8) (Page 14) has to be solved. The matrix transition element M_{fi} is given by the Kramers-Heisenberg-Waller matrix element [Equation (2.38), Page 25] where, within the A^2 approximation, only the first term is considered. Appropriate initial and final states $|i\rangle$ and $|f\rangle$ have to be chosen.

A more detailed description for each theoretical approach utilized to describe the experimental data of this work is given in Chapters 6 and 7, where the results of two of the Compton scattering experiments performed are presented. They were published in References [Kir20] and [Kir22].

2.5 One-photon double ionization

In Compton scattering or photoabsorption, if the energy transfer onto the atom or molecule is larger than the double ionization threshold, double ionization—that is, the emission of two electrons—is possible. (For helium, the double ionization threshold is $E_{\text{bind}}^{++} = 79$ eV, the single ionization threshold is $E_{\text{bind}}^{+} = 24.6\,\text{eV}$). One-photon double ionization refers to the case, where the emission of both electrons is caused by only one interaction with the initial photon. In this section, two mechanisms which result in double ionization will be introduced: *shakeoff* and *knockout*.

Both of these mechanisms are the result of electron-electron correlations. In Section 2.3, photoabsorption specifically in hydrogen-like atoms and within the Born approximation was discussed and thus, electron-electron correlations in the initial state (hydrogen-like atoms) as well as the final state (Born approximation) were ignored.

One-photon double ionization is studied extensively within the dipole approximation (see, for example, Reference [Bri99] for a topical review), where the two mechanisms, shakeoff and knockout, emerge. The processes are visualized in the Feynman diagrams shown in Figure 2.6.

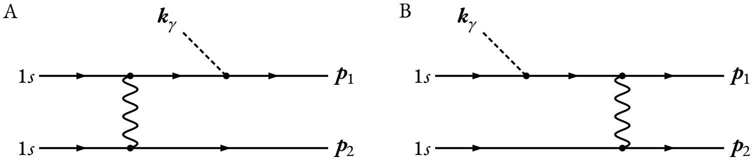

Shakeoff

Knockout

Figure 2.6: Feynman diagrams for the shakeoff (A) and the knockout (B) mechanisms for photoabsorption. For Compton scattering, another photon line $\boldsymbol{k}'_\gamma$ for the outgoing photon would be added (see Figure 7.1, Page 108). In each panel, a Feynman diagram with permutations of lines $\boldsymbol{p}_1$ and $\boldsymbol{p}_2$ (the final momenta of Electron 1 and 2, respectively) are omitted. (Taken from [Amu75].)

The knockout (also called two-step-one) mechanism can be visualized classically. In the first step, Electron 1 is emitted. In the second step, it interacts with Electron 2, causing it to be emitted as well, closely relating the process to electron-impact ionization. Thus, knockout refers to one-photon double ionization due to final-state interaction, and therefore, is not present within the Born approximation. The knockout process is dominant for low energies of Electron 1, since the energy of the first electron determines the interaction time. A high-energy electron escapes the atomic system faster than a low-energy electron, resulting in a shorter interaction time. Knockout at sufficiently large energy leads to a preferred angle of 90° between the electrons.

The shakeoff mechanism lacks a classical interpretation. As seen in Figure 2.6A, double ionization by shakeoff is the result of electron-electron correlations in the initial state, that is, before the interaction with the photon. Due to the interaction of both electrons with each other, only the total energy of the two-electron system is defined by the energy eigenstates, since energy can be shared between the two electrons. With this, shakeoff can be understood in the following picture: due to initial-state interaction, Electron 1 shares energy with Electron 2, virtually ionizing the system. Then, Electron 1 absorbs a photon, ensuring total energy conservation, and both electrons are ionized. Another way of interpreting the mechanism—which motivates the name *shake*off—is as follows: Electron 1 is removed abruptly from the system (by some ionization process), thus, the electronic eigenstates change abruptly from the old eigenstates of the two-electron system to the new eigenstates of a one-electron system. The remaining Electron 2 is still in the (old) eigenstates of the two-electron system which differ from the one-electron states. Therefore, the wave function of Electron 2 now has an overlap with bound as well as continuum states, and thus, a certain probability exists that

Electron 2 is emitted—that it is "shaken off."

Shakeoff as a double-ionization mechanism is favored for high energies of Electron 1, and eventually, the probability for shakeoff double-ionization becomes independent of Electron 1's energy. Given the decreasing probability to double ionize by knockout, the ratio of double to single ionization $R = \sigma^{++}/\sigma^{+}$ eventually becomes constant [Spi99]. This can be well understood from the two mechanisms as described above: For increasing energies of the first electron, the Born approximation ($E_{\text{bind}} \ll E_{e1} \ll m_e c^2$) is valid, that is, due to the practically instantaneous removal of the first electron, no final-state electron-electron interaction remains and thus, the knockout probability drops to zero. However, shakeoff is a result of initial-state electron-electron correlations, which are not changed by an increasing final energy of Electron 1. Therefore the shakeoff probability eventually becomes constant. Spielberger et al. measured the ratio R of helium at different photon energies and separated for Compton scattering and photoionization [Spi95; Spi96; Spi99]. At high energies, they find the ratio R_C for Compton scattering to be about 1%. This is different from the shakeoff probability for photoionization, which is 1.67% [And94; Spi95].

Amusia et al. predicted a third mechanism for one-photon double ionization that is forbidden within the dipole approximation, as it is purely the result of a quadrupole transition [Amu75]. Schöffler et al. confirmed the existence of the process [Sch13]. It is not relevant for the presented work. For an extensive study of the process, the reader is referred to [Gru22].

Another one-projectile double ionization process is the two-step-two mechanism, where the projectile interacts with each electron separately and independently. Obviously, for photoabsorption this process is impossible, however, the process may be relevant for collision physics with charged particles as projectiles. It is irrelevant for Compton scattering. Although the photon which scattered at Electron 1 can scatter at Electron 2 as well, the cross section for this "double" Compton scattering is incredibly small.

ATOMIC AND MOLECULAR SYSTEMS 3

In the scope of this work, helium and nitrogen were investigated. Under normal conditions, helium is the most fundamental atomic system (the competitor, hydrogen, exists under normal conditions as molecular hydrogen H_2). For this reason, it was chosen as a benchmark target for a kinematically complete, fully differential measurement of Compton scattering (see Chapter 6). Further, it is the most basic two-electron system, which makes it the ideal target to investigate electron-correlation effects, as has been done in the second experiment carried out for this work (see Chapter 7). In the following Section 3.1, the helium atom is briefly introduced from the view of quantum mechanics.

Expanding the investigations from atomic to molecular systems, N_2 was chosen as the target (see Chapters 8 and 9). Therefore, a basic introduction into molecules in quantum mechanics is given in Section 3.2, with the nitrogen molecule, specifically, being discussed in Section 3.2.4.

3.1 THE HELIUM ATOM

The helium atom has two electrons, and thus, calculating the energy levels for helium requires solving the Schrödinger equation

$$(H_1 + H_2 + V_{e,e})\Psi(\boldsymbol{r}_1, \boldsymbol{r}_2) = E\Psi(\boldsymbol{r}_1, \boldsymbol{r}_2)\,, \tag{3.1}$$

with the Hamiltonians H_1 and H_2 describing Electrons 1 and 2, respectively, and $V_{e,e}$ describing the repulsion of both electrons. That is,

$$H_{i=1,2} = \frac{\boldsymbol{p}_i^2}{2m_e} - \frac{2e^2}{4\pi\varepsilon_0 r_i}\,, \qquad V_{e,e} = \frac{e^2}{4\pi\varepsilon_0 r_{12}}\,, \tag{3.2}$$

with the vacuum permitivity ε_0, $r_{12} = |\boldsymbol{r}_{12}| = |\boldsymbol{r}_1 - \boldsymbol{r}_2|$, and the momentum operator for each electron $\boldsymbol{p}_{1,2} = -i\hbar\boldsymbol{\nabla}_{1,2}$. In Equation (3.1), already the approximation that the helium nucleus remains static at the coordinate origin is used and thus, its kinetic energy is zero. The approximation is based on the fact that the helium nucleus mass is several thousand times larger than the electron mass.

Unless stated otherwise, the following equations are given in atomic units (see Appendix "Atomic units," Page 205), in which $e = \hbar = m_e = 4\pi\varepsilon_0 = 1$.

A first approximation to solve the Schrödinger equation (3.1) is to not treat the electron-electron interaction explicitly, but to solve the problem for each electron individually while including the electron-electron interaction only effectively by introducing an effective Coulomb potential with $Z_{\text{eff}} = Z - S$. The electron-electron repulsion is then not included directly but by one of the electrons screening the Coulomb potential of the helium nucleus for the other. $S = 1$ corresponds to a complete screening of the Coulomb potential by one electron, $S < 1$ corresponds to partial screening.

Then, the wave function $\Psi(\boldsymbol{r}_1, \boldsymbol{r}_2)$ can be factorized

$$\Psi(\boldsymbol{r}_1, \boldsymbol{r}_2) = \psi(\boldsymbol{r}_1)\psi(\boldsymbol{r}_2)\,, \tag{3.3}$$

and two separate Schrödinger equations

$$\left(-\frac{\boldsymbol{\nabla}_1^2}{2} - \frac{Z}{r_1}\right)\psi_1(\boldsymbol{r}_1) = E_1\psi(\boldsymbol{r}_1)\,, \tag{3.4}$$

$$\left(-\frac{\boldsymbol{\nabla}_2^2}{2} - \frac{Z-S}{r_2}\right)\psi_2(\boldsymbol{r}_2) = E_2\psi(\boldsymbol{r}_2) \tag{3.5}$$

have to be solved. Here, Electron 1 within the Coulomb potential of $Z = 2$ screens the Coulomb potential for Electron 2. Equations (3.4) and (3.5) are the Schrödinger equations for the hydrogen-like atoms and can be solved exactly. The ground-state energy of helium is then

$$E_{\text{He}} = -\frac{Z^2}{2}E_H - \frac{(Z-S)^2}{2}E_H\,, \tag{3.6}$$

with the Hartree energy $E_H = 2 \times 13.6$ eV. For $S = 0.656$, the experimental value of $E_{\text{He}} = -2.9$ a.u. $= -79$ eV is reproduced [Dem16]. Note, for $S = 0$, that is, the electron-electron repulsion is ignored completely, E_{He} becomes -4 a.u., which is about 36% larger than the experimental value; the presence of two electrons effectively reduces the double ionization threshold.

Moving on from this very simplistic approach to calculate the energy levels of helium, a different approach is to calculate the energy levels and wave functions of helium using the Ritz principle: a variational method to solve the eigenvalue problem of the Schrödinger equation (3.1). For the helium atom, this approach has been first used by E. Hylleraas [Hyl28] to get helium wave functions. In the following section, I will introduce the principals of this approach.

3.1.1 Hylleraas-type wave functions

The variational Ritz principle is an important tool to determine ground-state energies in quantum mechanics by providing a method of finding an approximate ground-state wave function. It states that the energy obtained from an arbitrary trial wave function is an upper bound of the true ground state energy. Thus, the optimal trial wave function is found by minimizing the energy obtained from it. In case of a two-electron system, it follows [Her17]

$$E = \min \frac{\langle \Psi | H | \Psi \rangle}{\langle \Psi | \Psi \rangle} \tag{3.7}$$

with the trial wave function

$$|\Psi\rangle = \int \mathrm{d}^3 \boldsymbol{r}\, \Psi(\boldsymbol{r}) \quad \text{and} \quad \Psi(\boldsymbol{r}) = \sum_{\mu} c_\mu \psi_\mu(\boldsymbol{r}_1, \boldsymbol{r}_2)\,. \tag{3.8}$$

Here, $\boldsymbol{r}$ is the complete configuration space of both electrons, and c_μ is the coefficient that must be varied to achieve the minimal energy. ψ_μ are appropriately chosen wave functions.

E. Hylleraas was first to choose an appropriate trial wave function $\Psi(\boldsymbol{r})$ for helium [Hyl28]. Expanding the factorized wave function of Equation (3.3) by a wave function depending on the distance of both electrons to each other, he got [Hyl29]

$$\Psi(\boldsymbol{r}_1, \boldsymbol{r}_2) = \psi(\boldsymbol{r}_1)\psi(\boldsymbol{r}_2)\psi_{12}(\boldsymbol{r}_{12}). \tag{3.9}$$

Choosing $\psi(\boldsymbol{r}) = \exp -kr$, expanding $\psi_{12}(\boldsymbol{r}_{12})$, and introducing the coordinates $s = r_1 + r_2$, $t = r_2 - r_1$, and $u = r_{12}$, he got

$$\Psi(s,t,u) = \mathrm{e}^{-ks} \sum_{\alpha,\beta,\gamma} c_{\alpha,2\beta,\gamma}\, s^{\alpha} t^{2\beta} u^{\gamma}\,, \tag{3.10}$$

where k and $c_{\alpha,2\beta,\gamma}$ have to be varied to achieve minimal energy. Wave functions of the form (3.10) are referred to as Hylleraas-type wave functions. [Note, E. Hylleraas used the approach given by Equation (3.9) in his earlier publication of 1928, but improved upon it in his publication of 1929 shortly after, where the form given by Equation (3.10) achieved higher accuracy with fewer parameters necessary than his earlier approach.]

Stewart and Webb recalculated the values for the parameters N, k, and c_1 to c_5 using a five parameter Hylleraas-type wave function of form

$$\Psi(s,t,u) = N\mathrm{e}^{-ks}\left(1 + kc_1 u + k^2 c_2 t^2 + kc_3 s + c_4 k^2 s^2 + c_5 k^2 u^2\right)\,. \tag{3.11}$$

The parameters are listed in Reference [Ste63]. Note that Equation (3.11) was already used in his publication from 1929 by E. Hylleraas [Hyl29]. The ground-state energy resulting from Equation (3.11) is $E_{\mathrm{He}} = -2.903\,32$ a.u., which is already very close to the experimental value of $E_{\mathrm{He}}^{\mathrm{exp}} = -2.903\,72$ a.u. Modern calculations based on Hylleraas-type wave functions—including corrections due to the Lamb shift, the finite size of the helium nucleus, and more—achieve even better agreement with experimental values. For instance, a relative accuracy of 10^{-7} is achievable [Her17].

The wave function $\Psi(s, t, u)$ does not describe two independent electrons but two correlated ones, which is apparent since Ψ depends explicitly on s, t, and u—coordinates that always depend on *both* electron positions within the helium atom. However, it is difficult to connect the variational parameters $c_{\alpha,2\beta,\gamma}$ to physical properties of the two-electron system, as opposed to a one-electron hydrogen-like wave function $\Psi(\boldsymbol{r}) = Y_{\ell m}(\vartheta, \varphi)R_{\ell}(r)$ [see Equation (2.13), Page 15], where ℓ and m directly relate to the orbital angular momentum and the projection of the orbital angular momentum onto the quantization axis, respectively.

3.2 Molecules in quantum mechanics

Two or more atoms bound together are called molecules. The atomic nuclei repel each other, the bond is the result of the electronic orbitals interacting with each other. Different types of bonds exist, such as covalent bonds, ionic bonds, metallic bonds, hydrogen bonds, and molecular bonds due to the Van-der-Waals force. The prominent covalent bond is the result of "electron sharing," that is, the electrons are not characterized by atomic but molecular orbitals. The covalent bond is responsible for the formation of molecular nitrogen (N_2): each nitrogen atom "shares" three of its electrons with the other, resulting in a "closed" valence orbital (which would be eight electrons in the atomic-nitrogen L shell) for both atoms.

In this section, the necessary basics of molecular physics in quantum dynamics for an understanding of the nitrogen molecule are introduced. Since only molecular nitrogen and no other molecules were investigated in scope of this work, only a description of homonuclear diatomic molecules will be given. For a much more extensive introduction into molecular physics in quantum mechanics, the reader is referred to References [Wel20] or [Her10].

3.2.1 Born-Oppenheimer approximation

To describe a single atom within the frameworks of quantum mechanics, it is sufficient to neglect the nuclear motion (since the electron mass m_e is much smaller than the mass of the nucleus, and thus, the kinetic energy of the nucleus in the center-of-mass system can be approximated as zero). This is not the case anymore for molecular systems. A good description of a molecule has to include the motion of the nuclei explicitly to account for vibrational and rotational motions of the system.

Thus, the complete time-independent Schrödinger equation

$$H\Psi_{\mathrm{mol}}(\boldsymbol{r},\boldsymbol{R}) = E\Psi_{\mathrm{mol}}(\boldsymbol{r},\boldsymbol{R})\,, \tag{3.12}$$

has to include the kinetic energies of the atomic nuclei and the electrons (H_A and H_e, respectively), the Coulomb interaction of the nuclei with each other ($V_{A,A}$), the Coulomb interaction of the electrons with the nuclei ($V_{A,e}$), and the electron-electron interaction ($V_{e,e}$).

In Equation (3.12), $\boldsymbol{R} \equiv \boldsymbol{R}_\beta - \boldsymbol{R}_\alpha$. $\boldsymbol{R}_\alpha$ and $\boldsymbol{R}_\beta$ are the position vectors of the (identical) atomic nuclei, respectively. $\boldsymbol{r}$ denotes the coordinates of all electrons [$\boldsymbol{r} = (\boldsymbol{r}_1, \boldsymbol{r}_2, \dots, \boldsymbol{r}_N)$]. H is of form

$$H = H_A(\boldsymbol{R}) + H_e(\boldsymbol{r}) + V_{e,A}(\boldsymbol{r},\boldsymbol{R}) + V_{e,e}(\boldsymbol{r}) + V_{A,A}(\boldsymbol{R})\,. \tag{3.13}$$

Expanding the single terms of H emphasizes the complexity of the molecular Hamiltonian, even in the example of a homonuclear diatomic molecule [Yar06]:

$$\begin{aligned} H = &-\frac{\boldsymbol{\nabla}_R^2}{2\mu} - \sum_{i=1}^{N} \frac{\boldsymbol{\nabla}_{r_i}^2}{2} \\ &-\sum_{i=1}^{N} \frac{Z}{|\boldsymbol{r}_i - \boldsymbol{R}_\alpha|} - \sum_{i=1}^{N} \frac{Z}{|\boldsymbol{r}_i - \boldsymbol{R}_\beta|} + \sum_{i=1}^{N} \sum_{k=i}^{k<i} \frac{1}{|\boldsymbol{r}_i - \boldsymbol{r}_k|} + \frac{Z^2}{R} \end{aligned} \tag{3.14}$$

Here, $\mu = m_\alpha m_\beta / (m_\alpha + m_\beta) = m/2$ is the reduced mass and Z the charge of Atoms α and β. [Equation (3.14) is given in atomic units, as will be the following equations, unless stated otherwise.] Since $m \approx 10^3$ to 10^5 a.u. $\gg$ 1 a.u., the nuclear motion is much slower than the motion of the electrons, which is the basis for the *Born-Oppenheimer* approximation.

Since the electronic configuration of the molecule changes basically instantaneously in the time-frame of nuclear motion, the electronic motion is considered to be independent of the nuclear motion. Then, to describe the electronic configuration, the electron wave function does only depend parametrically on the internuclear distances $\boldsymbol{R}$. That is, one has to solve the time-independent Schrödinger equation for the electrons separately in a rigid mesh given by the nuclei. Then, a solution $\Psi^n_{\text{mol}}(\boldsymbol{r},\boldsymbol{R})$ can be expressed as the product of the wave function $\chi(\boldsymbol{R})$ of the nuclei and electronic wave function $\phi_n(\boldsymbol{r};\boldsymbol{R})$ (which only depends parametrically on $\boldsymbol{R}$) that is, $\Psi^n_{\text{mol}}(\boldsymbol{r},\boldsymbol{R}) = \chi(\boldsymbol{R})\phi_n(\boldsymbol{r};\boldsymbol{R})$. Choosing the $\phi_n(\boldsymbol{r};\boldsymbol{R})$ appropriately, $\Psi_{\text{mol}}(\boldsymbol{r},\boldsymbol{R})$ can be expanded as

$$\Psi_{\text{mol}}(\boldsymbol{r},\boldsymbol{R}) = \sum_n \chi_n(\boldsymbol{R})\phi_n(\boldsymbol{r};\boldsymbol{R})\,. \tag{3.15}$$

Equation (3.15) is a complete description of the molecular system, as long as the electronic wave functions $\phi_n(\boldsymbol{r};\boldsymbol{R})$ are chosen such that they describe a complete set of orthonormal functions, that is,

$$\langle\phi_n|\phi_m\rangle = \int \mathrm{d}^3\boldsymbol{r}\,\phi_n^*(\boldsymbol{r};\boldsymbol{R})\phi_m(\boldsymbol{r};\boldsymbol{R}) = \delta_{nm}\,, \tag{3.16}$$

with the Kronecker-Delta function

$$\delta_{nm} \equiv \begin{cases} 1 & (n = m) \\ 0 & (n \neq m) \end{cases}\,. \tag{3.17}$$

Then, the electronic Schrödinger equation in a rigid molecule of fixed $\boldsymbol{R}$ (that is, the nuclei are motionless) becomes

$$H_e\phi_n(\boldsymbol{r};\boldsymbol{R}) = E_n^R\phi_n(\boldsymbol{r};\boldsymbol{R})\,, \tag{3.18}$$

with the electronic Hamiltonian

$$H_e = H - H_A\,, \tag{3.19}$$

explicitly,

$$\begin{aligned} H_e = &-\sum_{i=1}^{N}\frac{\boldsymbol{\nabla}^2_{r_i}}{2} - \sum_{i=1}^{N}\frac{Z}{|\boldsymbol{r}_i - \boldsymbol{R}_\alpha|} \\ &- \sum_{i=1}^{N}\frac{Z}{|\boldsymbol{r}_i - \boldsymbol{R}_\beta|} + \sum_{i\neq k}\frac{1}{|\boldsymbol{r}_i - \boldsymbol{r}_k|} + \frac{Z^2}{R}\,, \end{aligned} \tag{3.20}$$

which has to be solved for each relevant $\boldsymbol{R}$ (what constitutes as "relevant $\boldsymbol{R}$" has to be chosen appropriately depending on the investigated system), resulting in the electronic energies E_n^R.

Assuming the electronic wave functions $\phi_n(\boldsymbol{r};\boldsymbol{R})$ are known, one can write down the complete Schrödinger equation for the molecule as [Her10]

$$
\begin{aligned}
H\phi_n(\boldsymbol{r},\boldsymbol{R})\chi(\boldsymbol{R}) &= E\phi_n(\boldsymbol{r};\boldsymbol{R})\chi(\boldsymbol{R}) \\
-\frac{\boldsymbol{\nabla}_R^2}{2\mu}\phi_n(\boldsymbol{r};\boldsymbol{R})\chi(\boldsymbol{R}) + H_e\phi_n(\boldsymbol{r};\boldsymbol{R})\chi(\boldsymbol{R}) &= E\phi_n(\boldsymbol{r};\boldsymbol{R})\chi(\boldsymbol{R})\,,
\end{aligned}
\tag{3.21}
$$

where E is the total energy of the molecule. With the product rule for differentiation, Equation (3.18), and some rearranging, Equation (3.21) becomes

$$
-\phi_n\left(\frac{\boldsymbol{\nabla}_R^2}{2\mu}\chi\right) + E_n^R\phi_n\chi - \chi\left(\frac{\boldsymbol{\nabla}_R^2}{2\mu}\phi_n\right) + \frac{1}{\mu}(\boldsymbol{\nabla}_R\phi_n)(\boldsymbol{\nabla}_R\chi) = E\phi_n\chi\,. \tag{3.22}
$$

The Born-Oppenheimer approximation assumes that $\boldsymbol{\nabla}_R\phi_n$ is neglectable. Thus, the last two terms of the left side of Equation (3.22) vanish. This effectively means that the movement of the nuclei affect the electronic wave functions ϕ_n only in a neglectable manner.

With this approximation, the Schrödinger equation for the nuclear motion becomes (for a derivation, see Reference [Her10])

$$
-\frac{\boldsymbol{\nabla}_R^2}{2\mu}\chi(\boldsymbol{R}) + E_n^R\chi(\boldsymbol{R}) = E\chi(\boldsymbol{R}) \tag{3.23}
$$

and thus, the Hamiltonian for the nuclear motion is given by

$$
H_A = -\frac{\boldsymbol{\nabla}_R^2}{2\mu} + E_n^R\,, \tag{3.24}
$$

that is, the nuclear motion is within a potential $E_n^R = E_n^R(\boldsymbol{R}) \equiv V(\boldsymbol{R})$ which is given by the electronic Schrödinger equation. By solving the electronic Schrödinger equation for all relevant $\boldsymbol{R}$, one can determine the potential energy curves of molecules or, in case of a molecule with more than two atoms, the potential energy surface.

3.2.2 LINEAR COMBINATION OF ATOMIC ORBITALS

How does one determine the electronic molecular orbitals? One method is to start with atomic orbitals, the principles of which will be discussed in the following (again, in the example of a homonuclear diatomic molecule).

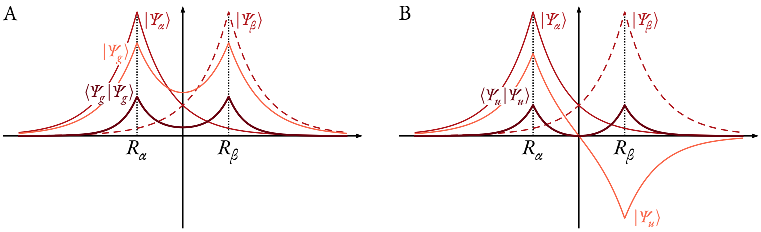

FIGURE 3.1: Schematic representation of a linear combination of two atomic orbitals $|\Psi_\alpha\rangle$ and $|\Psi_\beta\rangle$, where A refers to Equation (3.27) and B to Equation (3.28). (Adapted from [Her10].)

The atomic states $|\Psi_\alpha\rangle$ and $|\Psi_\beta\rangle$ for two (identical) atoms are given by the Schrödinger equations for each atom

$$H|\Psi_\alpha\rangle = E_A|\Psi_\alpha\rangle\,, \tag{3.25}$$

$$H|\Psi_\beta\rangle = E_A|\Psi_\beta\rangle\,. \tag{3.26}$$

If the two atoms are in proximity to each other, the electronic orbitals start to overlap. Using the principle of a linear combination of atomic orbitals, the new state is given by either additive or subtractive combination of the atomic states

$$|\Psi_g\rangle = \frac{1}{\sqrt{2}}\left(|\Psi_\alpha\rangle + |\Psi_\beta\rangle\right)\,, \tag{3.27}$$

$$|\Psi_u\rangle = \frac{1}{\sqrt{2}}\left(|\Psi_\alpha\rangle - |\Psi_\beta\rangle\right)\,, \tag{3.28}$$

which is illustrated in Figure 3.1. Indices g and u refer to *gerade* and *ungerade* states, which, in turn, refer to the parity of the two states. Parity describes the behavior of a wave function under inversion of space.

As can be seen in the two panels of Figure 3.1, the gerade combination of the two atomic orbitals results in an increased probability of electrons between the two atoms positioned at R_α and R_β, respectively. Thus, in one case, an increased probability of electrons between the molecules reduces the repulsion of the atomic nuclei, while in the other case, the lack of electrons leaves the nuclei to experience the full extent of their repulsion. Hence, the gerade state $|\Psi_g\rangle$ is binding and the ungerade state $|\Psi_u\rangle$ is anti-binding. That means, the energy of the molecule $E_{g/u}$ is decreased or increased compared to the atomic energy E_A, that is, $E_{g/u} = E_A \mp \varDelta E_{g/u}$.

In a more general approach, combining two orbitals of two atoms α and β—characterized by $|\psi_\alpha\rangle$ and $|\psi_\beta\rangle$, respectively—one gets the "test" wave function

$$|\Psi\rangle = c_\alpha|\psi_\alpha\rangle + c_\beta|\psi_\beta\rangle\,, \tag{3.29}$$

The best coefficients $c_{\alpha/\beta}$ are determined using the variational principle (see Section 3.1.1), that is, the energy

$$\epsilon = \frac{\langle\Psi|H|\Psi\rangle}{\langle\Psi|\Psi\rangle} \tag{3.30}$$

has to be minimized. Using Equation (3.29) in Equation (3.30), one gets [Her10]

$$\epsilon = \frac{\sum_{i=\alpha,\beta}\sum_{k=\alpha,\beta} c_i^* c_k H_{ik}}{\sum_{i=\alpha,\beta}\sum_{k=\alpha,\beta} c_i^* c_k S_{ik}}\,, \tag{3.31}$$

where

$$H_{ik} = \langle\psi_i|H|\psi_k\rangle = \int \mathrm{d}\boldsymbol{r}\,\psi_i^* H \psi_k \tag{3.32}$$

are the *exchange integrals*,

$$S_{ik} = \langle\psi_i|\psi_k\rangle = \int \mathrm{d}\boldsymbol{r}\,\psi_i^* \psi_k \tag{3.33}$$

the *overlap integrals*, and

$$H_{ii} = \langle\psi_i|H|\psi_i\rangle = \int \mathrm{d}\boldsymbol{r}\,\psi_i^* H \psi_i \tag{3.34}$$

the *Coulomb integrals*. Note that $S_{ii} = 1$, since the atomic orbitals are normalized to 1. The condition that $\epsilon = \epsilon(c_i)$ needs to be minimal constitutes $\partial\epsilon/\partial c_i^* = 0$, leading to the linear system of equations

$$\begin{array}{rcrcl} (H_{\alpha\alpha} - 1)c_\alpha & + & (H_{\alpha\beta} - S_{\alpha\beta})c_\beta & = & 0\,, \\ (H_{\beta\alpha} - S_{\beta\alpha})c_\alpha & + & (H_{\beta\beta} - 1)c_\beta & = & 0\,, \end{array} \tag{3.35}$$

which can be solved to get the optimal values for c_α and c_β.

As apparent from Equations (3.32) to (3.34), molecular orbitals have multiple centers, and thus, it is not possible anymore to separate the electronic wave function into radial and angular parts. Hence, the atomic angular momentum quantum number ℓ is not a good quantum number for the molecular system any more.

In case of a homonuclear diatomic molecule (such as N_2), the projection of ℓ onto the molecular axis is still conserved and thus, the atomic projection quantum number m is still a descriptive quantum number of the molecular system. Since the sign of m does not influence the total energy, the relevant molecular projection quantum number is $\lambda = |m|$ [Her10]. In homonuclear diatomic molecules, λ replaces the atomic quantum number ℓ and, analogously to the the atomic nomenclature s, p, d, ... for orbitals, one uses σ, π, δ, ... for molecular orbitals. For molecules with multiple electrons, one uses the capital Greek letters Σ, Π, Δ, ... for the projection of the total angular momentum, characterized by the quantum number Λ.

This leads to the common nomenclature for the total electronic configuration of a molecule

$$X^{2S+1}\Lambda^{+/-}_{g/u}\,, \tag{3.36}$$

where X refers to the total energy (typically X for the ground state and A, B, C, ... for increasing energies), $2S+1$ gives the multiplicity of the system with a total spin S. The subscripts g or u refer to gerade or ungerade symmetry, respectively, that is, the behavior of the wave function under inversion of space. For gerade states, $\Psi(\boldsymbol{r}) = \Psi(-\boldsymbol{r})$, and for ungerade states, $\Psi(\boldsymbol{r}) = -\Psi(-\boldsymbol{r})$. Superscripts + or − indicate the behavior of the wave function when mirrored at a plane which contains the two atomic nuclei, similar to g or u.

A molecular orbital with σ symmetry is binding for gerade parity and antibinding for ungerade parity, while an orbital with π symmetry has the opposite property.

3.2.3 Potential energy curves of molecules

The positively charged atomic nuclei Coulomb-repel each other, while the electrons screen the Coulomb potential of the nuclei. With these two properties, one can already determine some qualitative features of a molecular potential curve (again, discussed in the homonuclear diatomic example): For very large distances $R \rightarrow \infty$, the potential should tend asymptotically to zero, since there is no interaction between the two atoms. (The only interaction that does not require an overlap of the atomic electron orbitals is the Van-der-Waals force, which is proportional to R^{-6}). If the atoms are closer to each other, they will only form a bond if the electronic orbitals overlap, that is, there is an increased probability for electrons between the atoms (screening

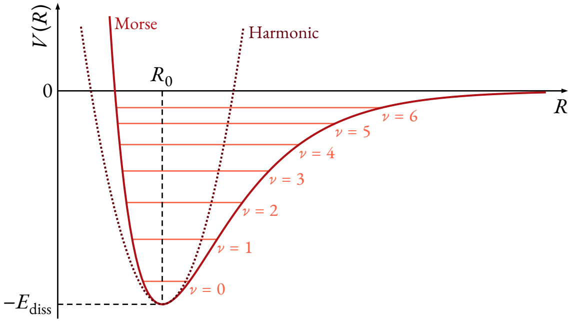

FIGURE 3.2: Morse potential [Equation (3.37)] with different energy levels E_ν [Equation (3.38)] and harmonic potential.

their positive charge). Then, at this intermediate distance, a molecule can form and the potential should be smaller than zero. For very small distances $R \to 0$, the two nuclei, which are assumed as point-like charges, repel each other and the potential should tend to infinity.

As discussed in the previous section, solving the electronic Schrödinger equation (3.18) and subsequently determining the potential $V(\boldsymbol{R})$ for all relevant $\boldsymbol{R}$ is necessary to describe the molecular system quantum-mechanically. However, the resulting potential is (generally) difficult to compute and the nuclear motion within that potential is (generally) not analytically solvable. To circumvent this problem, P. Morse proposed a potential of form [Mor29]

$$V(R) = E_{\text{diss}} \left(\mathrm{e}^{-2a(R-R_0)} - 2\mathrm{e}^{a(R-R_0)} \right) , \tag{3.37}$$

—now called Morse potential—which features the properties laid out above and is shown in Figure 3.2. In Equation (3.37), E_{diss} is the dissociation energy of the molecule, R_0 the position of the potential minimum, and a a parameter describing the “width” of the potential. For the Morse potential, the nuclear Schrödinger equation (3.23) can be solved analytically, resulting in the energy levels for the different vibrational states ν

$$E_\nu = -E_{\text{diss}} + \hbar\omega_0 \left(\nu + \frac{1}{2} \right) - \frac{\hbar^2 \omega_0^2}{4E_{\text{diss}}} \left(\nu + \frac{1}{2} \right)^2 , \tag{3.38}$$

with

$$\omega_0 = a\sqrt{2E_{\text{diss}}/\mu} \, . \tag{3.39}$$

Equation (3.38) shows that even in the ground state ($\nu = 0$), the nuclei are in motion. Analogously to the quantum-mechanic harmonic oscillator, a minimum ground-state energy $E_0 \neq 0$ exists, a fact determined by the

Heisenberg uncertainty principle. In Figure 3.2, the potential curve for a harmonic oscillator is shown as well. Of course, for large distances R, the harmonic potential is a bad model to describe a molecular potential (since V tends to infinity instead of vanishing). However, the harmonic oscillator can often be used to determine ground-state energy levels of molecules.

3.2.4 Properties of molecular nitrogen

Under standard temperature and pressure, atomic nitrogen bonds to the diatomic N_2 molecule. N_2 is the most abundant gas of the earth's atmosphere and is one of the most thoroughly investigated molecules. An extensive review of the spectrum of molecular nitrogen is given in [Lof77].

The electronic configuration of atomic nitrogen is $(1s)^2(2s)^2(2p)^3$. These atomic orbitals combine to the molecular orbitals of molecular nitrogen, resulting in the electronic configuration

$$(1\sigma_g)^2(1\sigma_u)^2(2\sigma_g)^2(2\sigma_u)^2(1\pi_u)^4(3\sigma_g)^2 \tag{3.40}$$

of the N_2 ground state $X\,{}^1\Sigma_g^+$ [Gil65]. N_2 has a triple bond (that is, the six electrons of the $1\pi_u$ and $3\sigma_g$ orbitals are responsible for the bond).

Figure 3.3 shows the formation of molecular orbitals from the atomic ones. The $1\sigma_g$ and $1\sigma_u$ molecular orbitals are almost unchanged compared to the atomic $1s$ orbital. They are, however, not completely degenerate. The ionization threshold for $1\sigma_u$ and $1\sigma_g$ were found to be 409.82 and 409.93 eV, respectively [Ala05]. The experiment performed for this thesis were not able to resolve the energy splitting of 110 meV, and thus, the atomic ionization

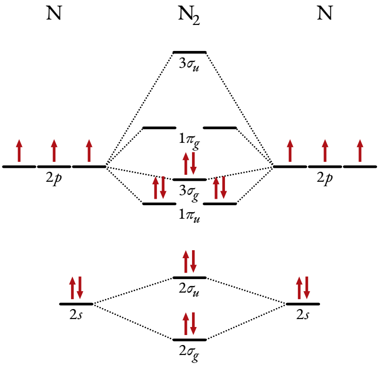

Figure 3.3: Formation of the molecular orbitals of N_2 from the atomic orbitals of nitrogen. The $1\sigma_{g/u}$ orbitals are omitted, since they are nearly identical to the atomic ones. The arrows represent electrons with spin up/down.

threshold for $N(1s)$ of 409.9 eV was used throughout. The minuscule energy splitting of the $1\sigma_s$ and $1\sigma_u$ orbitals, however, have peculiar consequences. Some studies thereof can be found in References [Her01; Rol05; Sem10].

In this work, valence-shell and core-shell ionization of N_2 was observed. The ground-state electronic configuration of the valence shell of N_2^+ is $(1\pi_u)^4(3\sigma_g)^1; X\,^2\Sigma_g^+$. A summary of the electronic configurations of the N_2^+ can be found in Reference [Gil65]. However, the state of the N_2^+ molecule is not resolved by the experiment performed for this work. Core-shell ionization of N_2 result in the hole-states $(1\sigma_u)^{-1}$ or $(1\sigma_g)^{-1}$, which eventually relax onto an unstable N_2^{2+} state via Auger decay. The average lifetime of the whole state is about 6.5 fs [Kem96].

The average bond length is 1.0977 Å for N_2 and 1.0744 and 1.0799 Å for $N_2^+(1\sigma_u)^{-1}$ and $N_2^+(1\sigma_g)^{-1}$, respectively [Eha06].

4 EXPERIMENTAL TECHNIQUES

The goal of this work is to investigate the complete kinematics of a Compton reaction at high (40 keV) and low (2.1 keV) photon energies. To achieve this goal, the momenta of the involved reaction particles have to be measured. This requires a different approach than that of a more "standard" Compton scattering experiment. Typically, Compton scattering is observed for photons scattering at matter in the solid phase, which compensates for the low cross section of the process. However, if one is interested in not only the kinematics of the electrons but the resulting ions as well, one needs to move to a target in gas phase to extract these electrons and ions without further interaction with other particles onto a detection system. Therefore, the first step of the experimental setup is to prepare a gas target with high-enough density to counter the low cross section of Compton scattering. The gas target has to be cooled and localized to achieve sufficient momentum resolution.

Second, a Compton reaction has to be induced. Modern synchrotron machines are able to achieve photon fluxes high enough to make experiments with targets of the above conditions (gas-phase, cold, and localized) feasible. For instance, with a photon flux of 10^{15} photons/s, a target area density of 10^{11} particles/cm^2, and a Compton scattering cross section of 10^{-24} cm^2, one can expect reaction rates of about 100 events per second, enough to collect sufficient statistics within days (instead of weeks) of data acquisition.

Third, the reaction must be observed. In particular, the momenta of the reaction particles must be measured, that is, the particles have to be guided to a detection system.

Cold-target recoil-ion momentum spectroscopy (COLTRIMS) combines these three parts. Within an electric and magnetic field, the cold gas target is crossed at ninety degree angle with synchrotron light. In this interaction region the reaction is induced. The electromagnetic fields guide the electrons and ions toward two detectors. Measuring the positions-of-impact and the times-of-flight of electrons and ions in coincidence, one can determine the three-dimensional momenta at reaction time on an event-by-event basis.

The creation of synchrotron radiation is discussed in Section 4.1, the target preparation in Section 4.2.1, the spectrometer in Section 4.2.2, and the detection system in Section 4.2.3. Since multiple COLTRIMS setups at two different beam lines were used, detailed experimental parameters will be provided in the respective appendices of Part II: Results.

For an extensive read on the COLTRIMS technique, the reader is referred to Reference [Kas20] (focusing on the experimental setup) or Reference [Ull03] (reporting on experimental findings from using the COLTRIMS technique).

4.1 SYNCHROTRON RADIATION

A synchrotron is a ring accelerator, where charged particles are forced on a circular orbit with bending magnets. The particles are accelerated one or multiple times per evolution. The strength of the magnetic fields created by the bending magnets has to be synchronized with the increasing energy of the accelerating particles, giving name to the *synchrotron* accelerator.

A basic property of charged particles is that they emit energy in form of photons while being accelerated. What is a hindrance in particle acceleration may be deliberately exploited for creating light sources. Special types of apparatus, namely wigglers or undulators, are employed to create synchrotron light. There, electrons are forced on wave-like trajectories with alternating magnetic fields.

One property of synchrotron light is particularly useful: the energy of the emitted photon depends, in part, on the strength of the acceleration. Due to this fact it is possible to adjust the energy of the photon, enabling the use of a wide range from terahertz up to soft or even hard x-ray photons for experimental purposes. This wide range of available energies makes photons in many cases an advantageous particle to manipulate and investigate matter. Modern synchrotron machines offer high-intensity x-ray beams, high energy resolution, and adjustable photon polarization. They utilize one ore multiple undulators to create synchrotron light in conjunction with monochromators to select narrow energy bandwidths. Synchrotron machines offer high brilliance beams. Brilliance describes the optical quality of a beam. It is defined as the number of photons $\mathit{\Delta} N$ per time t, area A, solid angle $\mathit{\Delta\Omega}$, and within a small wavelength band $\mathit{\Delta}\lambda/\lambda$

$$B = \frac{\mathit{\Delta} N}{t \cdot A \cdot \mathit{\Delta\Omega} \cdot \mathit{\Delta}\lambda/\lambda}\,. \tag{4.1}$$

It quantifies the photon flux per solid angle, area and wavelength band and, additionally, it defines the maximum focusability of a beam. Typically, synchrotron radiation is focused down to an area of 10^{-2} mm^{-2}, which is exceptionally well collimated compared to alternative light sources [Her17].

Synchrotron radiation is a special case of bremsstrahlung. For a particle with velocity close to the speed of light c, energy E, rest mass m_0, and charge q, the power it emits due to being accelerated onto a curve with radius r is

FIGURE 4.1: Angular distribution of emitted synchrotron radiation for different velocities with $\boldsymbol{v} \parallel \boldsymbol{a}$. The distribution is rotationally symmetric around the $\boldsymbol{a}$ vector. For bigger velocities v, the distribution bends towards the $\boldsymbol{v}$ direction. (From [Dem09].)

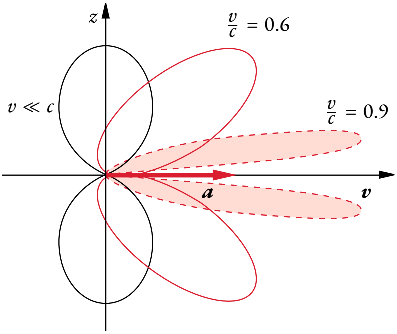

given by [Bet04]:

$$P = \frac{2}{3}\frac{cq^2}{r^2}\left(\frac{E}{m_0c^2}\right)^4 . \tag{4.2}$$

Note that the power is proportional to $1/m_0^4$. The mass ratio of proton-to-electron is about $m_p/m_e \approx 1836$, hence the power an accelerated electron emits is about 9×10^{14} times bigger than that of a proton. Because of this fact, synchrotron light facilities use electrons to create the synchrotron light. It is also important to emphasize that the above equation is for particles with a velocity v close to the speed of light. An accelerated particle with $v \ll c$ emits light perpendicular to the acceleration with a dipole distribution (see Figure 4.1). Only for highly relativistic particles will the majority of the emitted power point in forward direction [Dem09].

4.1.1 WIGGLERS AND UNDULATORS

The intensity of emitted light from one bending magnet is relatively small. To increase the intensity, synchrotron machines use the aforementioned magnetic structures: wigglers or undulators (see Figure 4.2A). Here, alternating magnetic poles create a magnetic field which forces electrons on a wiggling trajectory (giving rise to the name *wiggler*), where the electrons emit synchrotron light at each vertex. The difference between a wiggler and an undulator is in principle its compactness. In an undulator, smaller magnetic fields are employed, but the number of alternating magnetic poles is higher and therefore, the geometry of the electron trajectories is tighter. Whereas in a wiggler each light cone shines individually, the denser structure of an undulator creates an overlap of the light emitted at the different vertices.

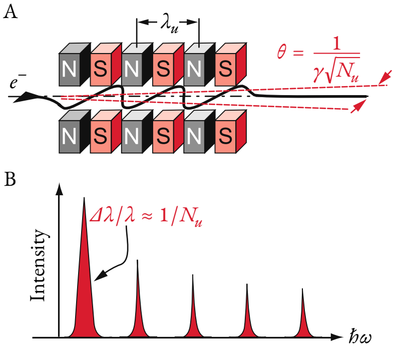

Figure 4.2: Principle sketch of an undulator and its typical frequency spectrum. A, Schematic of the undulator with N_u (here, $N_u = 3$) alternating periodic magnetic poles. B, Typical spectrum of an undulator with the different (odd) harmonics. (From [Dem09].)

Due to this overlap, light from the different vertices constructively and destructively interferes, creating different frequency bands of partially coherent synchrotron light, which in turn have much higher brilliance than respective light from a wiggler. The wavelength for the different resonant modes are given by the undulator equation [Her17]

$$\lambda_r = \frac{\lambda_u}{2\gamma}\left(1 + K^2 + \gamma^2\theta^2\right) , \tag{4.3}$$

where K is the dimensionless undulator parameter

$$K = \frac{eB\lambda_u}{2\pi m_e c} , \tag{4.4}$$

λ_u is the undulator wavelength (see Figure 4.2A), $\gamma = (1 - v^2/c^2)^{-1/2}$, B is the strength of the magnetic field of one undulator magnet, and $\theta \ll 1°$ is the angle of emission. Equation (4.3) shows an energy dependency of the synchrotron light on the undulator wavelength λ_u, the undulator parameter K, and, peculiarly, on the emission angle θ. The parameter K also gives a quantitative distinction for undulators and wigglers: for undulators, $K \leq 1$; for wigglers, $K \gg 1$. Examining Equation (4.3) further shows that higher harmonics $\omega_n = n\omega_r$, with $\omega_r = c/(2\pi\lambda_r)$ and uneven $n = 2j + 1$, are emitted. The fundamental $j = 0$ is dominant, as shown in Figure 4.2B. Synchrotron machines utilizing undulators as radiation source are also called third (or fourth) generation synchrotron machines.

The light emitted by an undulator setup is linearly polarized. The partially coherent nature of the emitted light enables the generation of arbitrarily polarized light if two successive undulators with a 90° coaxial orientation to each other are employed. The first undulator produces horizontally polarized light and the second one vertically polarized light. Changing the phase-correlation between the two undulators enables the generation of arbitrarily oriented linearly, elliptically, or left- or right-handed circularly polarized light. The phase-correlation is changed with another bending magnet pair—the modulator—behind each undulator unit [Kim84].

A different method to achieve different light polarization is to not use multiple undulators in sequence, but to manipulate the electrons within one undulator onto a gyrating trajectory, achieving a high-intensity light beam with well-defined polarization. For example, the variable polarization xuv beam line p04 at petra iii, Hamburg, Germany, utilizes an apple-2 (advanced planar polarization light emitter) undulator, capable of circularly and linearly (horizontal, vertical, or rotating) polarized light [Vie13].

At id31 of the esrf, Grenoble, France, an in-vacuum cryo-cooled undulator with a 14.5 mm period is used. It provides a photon energy range of 20 to 150 keV with 99% linear horizontal polarization. The total length of the beam line from the light source (the undulator) to the sample is about 125 m.

The electrons in the synchrotron storage ring are packed in bunches. Each electron bunch creates an x-ray flash. Depending on the number of bunches in the ring, the fill pattern, operation is classified differently. *Multi-bunch* operation refers to many electron bunches in the ring, typically with a separation of a few nanoseconds, resulting in x-ray pulses every few nanoseconds. In *single-bunch* operation, only one electron package is stored in the ring. The time spacing of the x-ray pulses then depends on the orbital period of the single electron package within the ring. Many synchrotron facilities have an in-between operation, where a few electron bunches are stored in the ring with bunch spacings of tens to a few hundreds of nanoseconds. For time-of-flight measurements such as coltrims, the bunch spacing typically needs to exceed the longest time-of-flight of the reaction electrons, since otherwise the x-ray pulse which induced the reaction can not be identified and the times-of-flight of the reaction particles can not be accurately determined (see Section 5.1). For the experiments performed for this work, the operation modes were 40-bunch operation at petra iii and 16-bunch operation at esrf, resulting in a photon bunch spacing of 192 and 176 ns, respectively.

4.1.2 MANIPULATING ENERGIES OF X-RAY BEAMS

Undulators (and wigglers) emit a broad spectrum of energies. Most experiments, however, need a fixed photon energy. Monochromators within the beam line select the desired energy band from the initial x-ray beam of the undulator. They use the energy-dependent diffraction of light to achieve this. The simplest setup would be a prism and an exit slit, where the prism unfolds the different energies of the source in angle and the exit slit selects the desired energy. Modern synchrotron light sources require more elaborate setups to accommodate the demands for the optical elements, for example, transmission, energy resolution, or heat dispersion.

Figure 4.3 shows an overview of beam line P04 of the PETRA III synchrotron. Here, monochromatizing is achieved with the plane-mirror and plane-grating unit, and the exit slit unit, where the plane mirror M_2 is a pre-mirror and the varied line-space (VLS) plane grating focuses the beam onto the exit slits.

With this setup, beam line P04 can operate in yet a different mode: pink beam mode. Instead of monochromatizing the x-ray beam using the aforementioned configuration, the x-ray beam from the undulator gap is reflected at the VLS grating with a grazing angle. In this setup, the pre-mirror and grating reflect the zeroth order onto the exit slits, and thus, effectively no selection of the photon energy is done. The photon energy is primarily the result of the undulator gap. Pink beam operation can achieve an x-ray flux multiple orders of magnitude higher than that of a monochromatic beam. Especially for processes with very low cross sections, pink beam operation can result in the

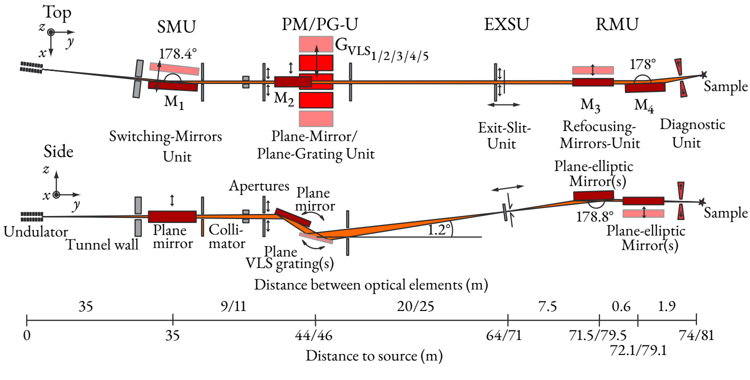

FIGURE 4.3: Schematic layout of beam line P04 at PETRA III (from [Vie13]).

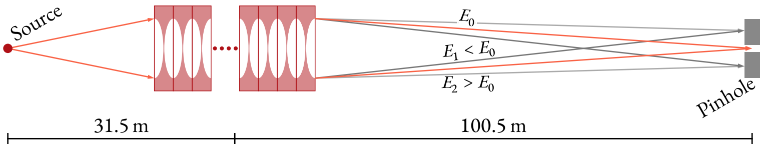

FIGURE 4.4: Principle of an x-ray transfocator. The concrete distances from the lenses to the source and the pinhole depend on the beam line. The values in the figure correspond to the distances at ID31 of the ESRF, Grenoble.

necessary x-ray flux to enable the measurement of significant statistics within feasible integration times, as long as the process under investigation does not require maximum energy resolution (which is the case for the Compton-scattering processes investigated in this work). At beam line P04, a photon flux of about 5×10^{14} photons/s was achieved for the low-energy Compton scattering experiment (see Chapter 6). This value was estimated using the total Compton scattering cross section $\sigma_{\text{tot}} \approx 0.2 \times 10^{-24}\,\text{cm}^2$ for helium with $\hbar\omega = 2.1$ keV, a target area density of about $\rho \approx 5.5 \times 10^{11}$ atoms/cm^2, a detection efficiency of $\epsilon_{\text{det}} \approx 50\%$, and the number of recorded Compton events N during the integration time t, that is,

$$\text{Photons/s} = \frac{N}{\rho \epsilon_{\text{det}} \sigma_{\text{tot}} t} . \tag{4.5}$$

Beam line ID31 of the ESRF, Grenoble, France, uses a different form of monochromator. Here, instead of grating mirrors, a variable number of compound refractive lenses focuses the x-ray source onto a pinhole, a setup referred to as *x-ray transfocators* [Vau11], the principle of which is sketched in Figure 4.4. Depending on the number of lenses, the energy-dependent focal length changes. Thus, it is possible to focus the desired photon energy onto the pinhole, cutting out other energies. Using this setup, beam line ID31 can achieve a photon flux of about 8×10^{15} photons/s at an energy resolution of $\Delta E/E = 1.1\%$ during 16-electron-bunch operation of the synchrotron.

4.1.3 SUPPRESSION OF LOW-ENERGY PHOTONS

Especially for Compton scattering experiments using the COLTRIMS technique another important aspect of synchrotron beam lines has to be considered: Ions produced by Compton scattering have much smaller ion momenta compared to photoionization. This, however, is only true if there are no low-energy photons within the beam. Photoionization by such low-

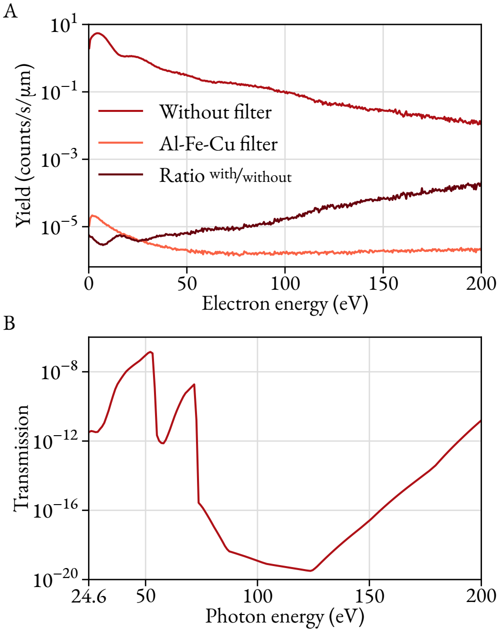

Figure 4.5: The effect of the foil filters in the beam line. A, Measured electron rates with and without filters. The rates are weighted by the beam-line exit-slit opening. B, Theoretical photon transmission through 980 nm of aluminum, 144 nm of copper, and 153 nm of iron. The theoretical data in B is based on Reference [Hen93].

energy photons would result in small ion momenta as well, but have a much larger cross section compared to Compton scattering (about 10^6 times larger). Hence, it is crucially important to filter out low-energy photons. At beam line P04 of the PETRA III synchrotron, small metal-foil filters, namely 980 nm of aluminum, 144 nm of copper, and 153 nm of iron, were installed within the beam. The effectiveness of the foil filters is demonstrated in Figures 4.5 and 4.6. In Figure 4.5A, the electron detection rates with $E_e < 200$ eV with and without filter-installments are shown. The detection rate is weighted by the opening of the beam line exit slits. To keep detection rates at a sustainable level, the exit slits were narrowed to 10 µm during the measurement without the filters. The exit slits were opened to 400 µm for the measurement with the filters. The ratio of the two rates is also shown in the panel. One can see a suppression of low-energy electrons by four to six orders of magnitude for electrons below 50 eV, which is the energy of the majority of Compton electrons produced by Compton scattering at helium with $\hbar\omega = 2.1$ keV. Since Compton electrons are in both distributions, this suppression must be due to the removal of low-energy photons within the synchrotron beam.

Figure 4.5B shows the theoretical photon transmission through the foil

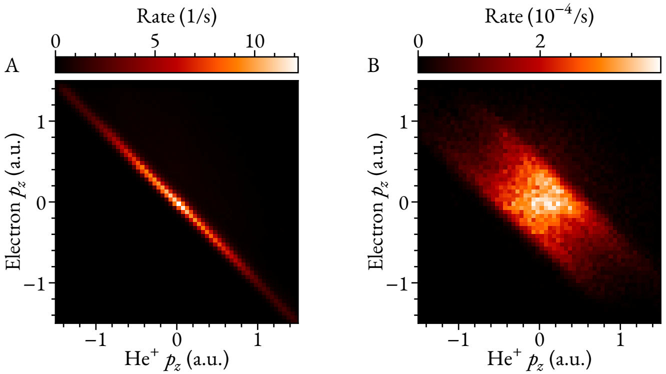

FIGURE 4.6: Comparison of the ion and electron coincidence with the foil filter setup and without. Displayed are the z component of the He$^+$ ion momenta in coincidence with the z component of the electron momenta without (A) and with (B) foil filters in the beam line. The color scale depicts the detection rate.

filters. The data was obtained from Reference [Hen93]. The transmission through the foil filters is many orders of magnitude smaller, which is not reflected in the measurement. However, to measure a suppression better than, for example, 10^{-6}, the signal-to-background ratio would need to be 10^6. This is not achieved in the present experiment.

Figure 4.6 shows an even stronger proof that no low-energy photons are within the incoming beam. In photoabsorption, the only particles in the final state are the electron and the He$^+$ ion. Hence, they must fulfill momentum conservation, that is, the sum of each component p_x, p_y, and p_z of the electron and the ion momenta equals zero, respectively. In a coincidence plot of electrons and ions, this is visible as a downward-diagonal sharp line, such as is visible in Figure 4.6A. In contrast, no such line is visible in Figure 4.6B. In Panel A, no foil filters are installed within the photon beam. In Panel B, the foil filters are present. Comparing the rates shown via the color scale of the figures, it is obvious that in Panel B, the sum momentum of the electron and the ion is not zero. Hence, with installed foil filters, photoabsorption is not the ionizing process and the low-momentum He$^+$ ions result from Compton scattering.

At beam line ID31 at ESRF an argon-gas absorber unit was installed, removing low-energy photons. The unit is necessary to prevent overheating of the optical elements of the beam line and therefore cannot be removed. Thus, no comparison of a filtered beam line setup with an unfiltered one is possible. (Note that after an upgrade of the ESRF synchrotron, 2019, the argon absorber unit of beam line ID31 was replaced by a solid titanium filter [Drn22])

4.2 COLD-TARGET RECOIL-ION MOMENTUM SPECTROSCOPY

The setup consists of three principal components. An atomic or molecular target is created by a supersonic gas expansion (1) and crossed with a projectile beam within the reaction chamber (2), inducing a reaction. In this work, the projectile beam is synchrotron light. The ion(s) and electron(s) of the reaction are then detected (3). Within a COLTRIMS spectrometer, electric and magnetic fields guide the particles towards two microchannel-plate detectors with delay-line anodes [Jag02]. The positions-of-impact and times-of-flight enable a reconstruction of the initial momenta at reaction time. Since the particles must not interact with any other particles after the reaction until they are detected, the experiment must be performed in an ultra-high vacuum.

Multiple differentially pumped vacuum sections ensure that the poor vacuum of the expansion stage—the stage where the supersonic gas-jet expansion takes place—does not destroy the ultra-high vacuum of the reaction chamber—the chamber housing the spectrometer in which the gas jet is crossed with the synchrotron beam. The gas target is prepared in a two-stage expansion chamber. These two stages are separated by a skimmer. A second skimmer separates the two-stage expansion chamber from the reaction chamber. Most of the gas target is unaffected by the synchrotron beam and will be dumped in a two-stage, differentially pumped jet dump, ensuring the ultra-high vacuum of the reaction chamber is not destroyed by back-flowing gas. Typical pressures within the different components are listed in Table 4.1.

The experimental parameters of the three different beam times that were carried out for this work are listed in the respective appendices of Part II, concretely, in Tables 6.1, 7.1 and 8.1 on Pages 105, 133 and 155.

TABLE 4.1: Typical pressures in millibar of the different vacuum components of a COLTRIMS setup with supersonic gas jet.

Fore-vacuum (Expansions)	Expansion 1	Expansion 2	Reaction chamber	Dump 1	Dump 2
10^{-1}	10^{-3}	10^{-6}	10^{-9}	10^{-9}	10^{-7}

4.2.1 SUPERSONIC GAS JET

The initial momenta of the target particles have to be smaller than the required momentum resolution of the experiment. Under normal conditions—that is, a temperature of $T = 300$ K and a atmospheric pressure of 1 bar—an atomic gas has internal energy of $E = {}^3\!/_2\, k_B T \approx 37$ meV (k_B being the Boltzman constant). For helium atoms, this is about 4.5 a.u. momentum, much higher than the required momentum resolution of most experiments. Hence, the target gas has to be cooled.

In the COLTRIMS setup, the gas target is cooled using a supersonic gas expansion. In such an expansion the gas is adiabatically expanding from a high-pressure (p_0) region into a low-pressure (p_b) region through a small orifice. The randomly oriented momenta of the gas particles align along the expansion direction, that is, the enthalpy of the gas is transformed into directional movement, given by

$$\frac{f}{2} k_B T_0 + k_B T_0 = \frac{f+2}{2} k_B T_0 = \frac{1}{2} m v^2 \,. \tag{4.6}$$

Here, T_0 is the temperature of the particles before expansion (that is, the temperature of the nozzle), f are the degrees of freedom of the gas particles, m is the particle mass, and v the velocity after expansion. Ideally, the relative motion of atoms within such a jet would be zero: the gas jet would have an internal temperature of $T \to 0$ K. Figure 4.7 shows a sketch of a microscopic point of view of the particles' velocities within and behind the nozzle. Only those particles with velocities in forward direction are able to "escape" through the orifice. Other particles collide within the gas until their velocities match and are able to escape without further interaction with other particles. The region behind the nozzle where no interaction of particles is present is called the zone of silence. If there was a perfect vacuum into which the gas expands, this zone of silence would have no boundaries and expand to infinity.

Of course, a real gas expansion does not have these ideal conditions. For real gases (not ideal gases), Equation (4.6) is an approximation only. Furthermore, for a perfect supersonic gas expansion the backing pressure p_b in the expansion

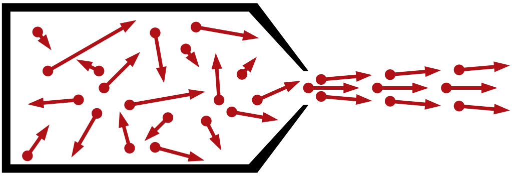

FIGURE 4.7: Molecular velocities before and after expansion through a nozzle (adapted from [Lev81]).

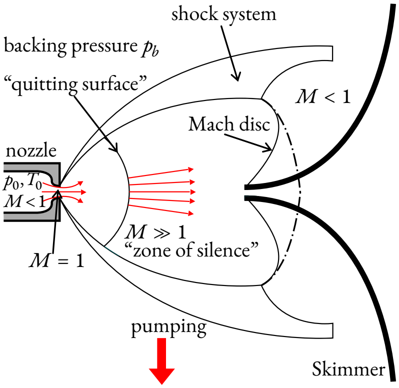

FIGURE 4.8: Schematic diagram of a typical supersonic gas epxansion (adapted from [Bar12]).

chamber had to be zero. Given that $p_b \neq 0$, a supersonic gas expansion only is possible, if the difference in the pressures p_0 and p_b is big enough for the gas to be accelerated to the speed of sound at the nozzle orifice. This condition is met if the pressure ratio surpasses the critical value

$$\frac{p_0}{p_b} = \left(\frac{\gamma+1}{2}\right)^{\frac{\gamma}{\gamma-1}} , \tag{4.7}$$

with $\gamma = c_p/c_V$, where c_p and c_V are the specific heat capacities at constant pressure and constant volume, respectively. For real gases, the critical ratio at which a supersonic gas expansion is possible is $p_0/p_b \gtrsim 2.1$ [Hoh02]. Under such conditions, the structure of the gas expansion is complex, as sketched in Figure 4.8. As seen in the figure, the structure is separated into regions with different values for the Mach number M, which is the particles' velocity relative to the speed of sound. Within the zone of silence, $M \gg 1$, that is, the gas particles are faster than the speed of sound. As such, the jet is independent of the surrounding conditions, since information within a gas only travels with the speed of sound. The zone of silence is limited by the compression waves in the shock system, resulting from interaction with the residual gas.

The length x_m of the zone of silence, that is, the distance of the Mach disk from the orifice is of particular interest. If a skimmer (a small cone-shaped aperture) is introduced into this region, the cold, supersonic particle beam of the expansion can be extracted. x_m is typically given in units of the nozzle orifice diameter d [Hoh02]:

$$\frac{x_m}{d} = \frac{2}{3}\sqrt{\frac{p_0}{p_b}} . \tag{4.8}$$

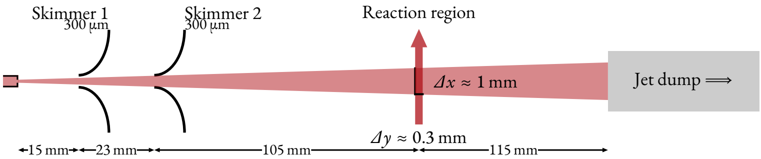

Figure 4.9: Sketch of the jet system. Two skimmers define the geometry of the jet. The reaction region is defined by the overlap of the jet and the x-ray beam. Δx is given by the width of the jet, Δy by the width of the x-ray beam focus.

The length x_m depends on the pressure ratio p_0/p_b. Higher backing pressures p_b result in a smaller zone of silence, since more collisions of the expanding gas with the residual gas take place.

Not only are the velocities of the jet particles matched by a supersonic expansion, inelastic collisions due to the expansion also result in rotational and vibrational cooling. This is of particular importance for experiments with molecules, where the additional degrees of freedom must be reduced.

The temperature T_{jet} of the supersonic jet can be approximated by [Mil88]

$$T_{\text{jet}} \approx \left(\frac{f}{2} + 1\right) \frac{T_0}{S^2} , \tag{4.9}$$

introducing the speed ratio S. The speed ratio is defined as the ratio of the mean velocity to the width of the velocity distribution:

$$S \equiv \frac{2\sqrt{\ln 2}\,\langle v \rangle}{\Delta v} . \tag{4.10}$$

Hence, the speed ratio gives a classification of the quality of the jet. A higher speed ratio means a cooler jet. Calculating actual jet velocities and determining the speed ratio using Equation (4.9) is complicated. In practice, the speed ratio is measured experimentally, as done, for example, in Reference [Bru02]. There, the speed ratio for helium was measured at different nozzle temperatures. This results in possible jet temperatures T_{jet} of only a few millikelvin. For helium, in the low-energy Compton scattering experiment of this work, the speed ratio was estimated to be about 150. In the high-energy experiment, it was estimated to be 200. This corresponds to a momentum resolution of $\Delta p \approx 0.04$ and $\Delta p \approx 0.03$ a.u., respectively, for detected helium ions with $p = 2$ a.u.

The transversal momentum component of the jet is defined by the experimental setup, sketched in Figure 4.9. The second skimmer geometrically defines the width of the jet at the reaction region, and thus limits the

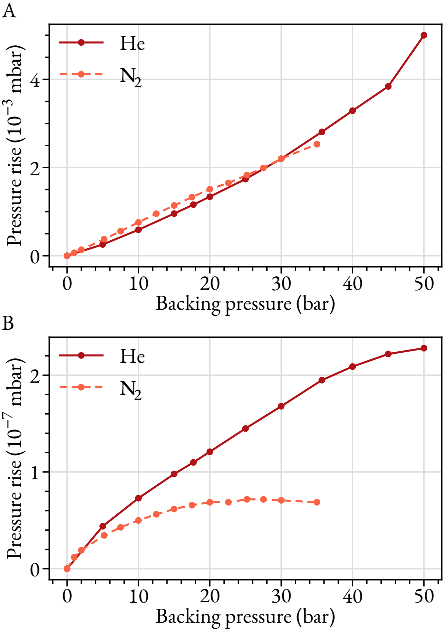

Figure 4.10: Jet curves for helium and N_2. A, Pressure rise in the first expansion chamber. B, Pressure rise in the second jet dump. The values are the readout of the ion gauge located at the respective vacuum chamber. The expansion chamber was pumped by an Edwards STP-iX3006 turbomolecular pump. The jet dump chamber was pumped by a Pfeiffer HiPace300.

maximum transversal momentum the jet particles have. The longitudinal momentum is given by the mean velocity $\langle v \rangle$. Further, the finite width Δx of the jet results in a finite reaction volume. This means that the location of the reaction is not a point source, which leads to another uncertainty in the measured momenta along this direction. Those errors can be compensated by the spectrometer design by using an electrostatic lens (in $\Delta x/\Delta y$ direction) or by time-of-flight-focusing geometries (Δz), as will be discussed in the next section. In the experiments for this work, the width of the jet was about 1 mm at the interaction region. The geometry of the jet setup is shown in Figure 4.9.

A jet curve characterizes the gas jet of a COLTRIMS setup well. There, the pressures in the different vacuum stages are measured for different backing pressures. In particular, the rise in pressure in the last vacuum stage where the jet is dumped characterizes the jet quality, from which the target density at the target can be estimated. Figure 4.10 shows the jet curves of the COLTRIMS obtained during the preparations for the beam times performed at the ESRF, Grenoble.

4.2.2 SPECTROMETER

The spectrometer is housed within the reaction chamber of the COLTRIMS setup. There, the ultra-high vacuum is necessary to ensure that the reaction particles are able to reach the detectors without any interaction with residual gas and, more importantly, the background signal caused by the interaction of residual gas atoms with the initial photon beam is minimal. The reaction chamber is separated by a skimmer with an opening of 0.3 mm from the two expansion stages and with a thin tube between reaction chamber and beam dumps.

The electric and magnetic fields of the spectrometer are created by stacked copper plates and a set of Helmholtz coils, respectively. The geometry of the spectrometer and the electric and magnetic field strengths are customizable to fit the specific requirements of an experimental goal. The copper plates are squared with a circular cutout big enough to ensure enough space for the reaction particles to reach the detector surface. Each copper plate has a constant electric potential, due to electric voltage being applied at each end of the spectrometer. The voltage drops over set resistors connecting each subsequent copper plate.

The Helmholtz coils create a homogeneous magnetic field throughout the reaction chamber. For the employed COLTRIMS setups of this work, they were about 1.7 m in diameter. The reaction chamber of the COLTRIMS setup is placed at the center axis of the Helmholtz coil. To correct the effect of surrounding magnetic fields, for instance, the earth's magnetic field, two smaller sets of Helmholtz coils—one set horizontally, the other set vertically oriented—are employed.

The electric field created by the copper plates guides the electrons and ions toward their respective detector. Due to the large mass of the reaction ions the influence of the magnetic field on them is minimal. At most, for very long ion times-of-flight, the ion's trajectory is bend slightly by a few degrees, which can be corrected in the offline analysis by virtually rotating the ion detector. The influence of the magnetic field on the electrons, however, is crucial for a typical COLTRIMS experiment. It forces the electrons onto a gyrating trajectory, enabling the detection of high-energy electrons with a large momentum perpendicular to the detection plane that otherwise could not be projected onto the finite detection surface. However, the gyrating trajectory returns back to the spectrometer center axis where the electrons originated. The distance from the point where an electron returns to the center axis to the interaction region is determined by the electron's momentum component parallel to the magnetic field (that is, the component in time-of-flight direction). If the electron hits the detector at this distance, the momentum uncertainty within the detection plane is infinite, since, independent of the electron's momentum components within the detection plane, it hits the detector at the same location. The frequency of the electron returning to the spectrometer center axis increases with raising magnetic fields and thus, the times-of-flight where the momentum uncertainty within the detection plane becomes infinite increases. This limits the maximum electron energy a COLTRIMS setup is able to feasibly detect. Hence, it was not possible to detect all Compton electrons of the experiments performed with high-energy photons ($\hbar\omega = 40$ keV, which results in Compton electrons with an energy of up to about 5 keV). The employed spectrometers of this work were able to detect electrons ranging from up to 30 eV to up to 500 eV with full solid angle. Since multiple spectrometers were employed for the experiments performed for this work, the details are listed in the respective chapters of Part II.

Due to expansion of the supersonic jet and the finite focus size of the synchrotron light, the reaction electrons and ions do not originate from a point source. This translates to a finite momentum resolution: two particles with identical momenta have different points-of-impact and times-of-flight depending on where exactly they originate in the reaction region.

The finite size of the reaction region can be corrected by the electric fields of the spectrometer. To compensate for the finite size in time-of-flight direction, the spectrometer is divided into acceleration and drift regions. If the length of the drift region is twice the length of the acceleration region, the time-of-flight difference between two particles—where one originates closer toward and the other farther away from the detector—is compensated. This geometry is called Wiley-McLaren geometry [Wil55]. Thin metal meshes are used to separate regions with different electric fields within the spectrometer. The transmission of such meshes ranges from 40 to 80%.

The finite target size within the detection plane (perpendicular to the time-of-flight direction) can be compensated by employing an electrostatic lens. The inhomogeneous electric field required for creating an electrostatic lens is achieved by increasing the resistance between two subsequent copper plates of the spectrometer. While using an electrostatic lens, the simple two-to-one ratio of the Wiley-McLaren geometry does not achieve time-of-flight focusing. Further, the usage of an electrostatic lens in combination with magnetic fields makes the momentum reconstruction unpractical. However, since ions are mostly unaffected by the magnetic fields, an electrostatic lens in conjunction with a time-of-flight geometry for an increased momentum resolution of the ions is common, while for electron detection, electrostatic lenses are less common. If only very low-energy electrons that do not require additional magnetic fields have to be detected, electrostatic lenses are employed for electrons as well, as has been done, for example, in Reference [Leb02].

For this work, a combination of electrostatic lenses and time-of-flight geometries were used. The details thereof are provided in the appendices of Chapters 6 to 9. A sketch of each spectrometer employed can be found in Figures 6.18, 7.17 and 8.13 on Pages 104, 132 and 155.

4.2.3 Microchannel-plate detector with delay-line anode

The reaction electrons and ions are projected by the spectrometer onto a microchannel-plate detector with delay-line anode [Jag02]. The microchannel-plate (MCP) amplifies the signal of the single electrons and ions high enough to be detected by a delay-line anode—while keeping the position-of-impact information intact.

A MCP is a roughly 1 mm thick glass wafer interspersed with small channels of diameters ranging from 5 to 25 μm. The channels are tilted by about 15° with respect to the surface normal. The surface of the waver has a metallic coating while the channels have high resistance, separating the electrodes created by the metallic coating on either side of the wafer. The total resistance of typical MCPs are some tens of megaohms. Applying a voltage to either surface of the wafer creates an electric field within the channels. Then, particles with sufficient energy hitting the inside of a channel extract secondary electrons, which, due to the electric field, are accelerated back to the channel walls, resulting in even more electrons being extracted. At high-enough voltages applied to the MCP (about 1 to 3 kV), this creates an avalanche of secondary electrons. Thus, a single MCP can multiply single-incident particles by a factor of up to tens of thousands. To further increase the amplification, two MCPs are used in succession in a so-called *Chevron* stack, where the two MCPs are oriented to each other such that the inclinations of their respective channels are opposite.

The transparency of a MCP is about 50%, automatically cutting the detection efficiency of a MCP-detector in about half. To counter this problem, so-called “funnel”-MCPs were developed. Here, the opening for each channel is widened in fashion of a funnel, increasing the active surface of a MCP to up to 90%, greatly increasing the detection efficiency. This is of special interest in multi-coincidence experiments. For instance, in a five-fold coincidence, using a funnel MCP compared to a “traditional” one, one can increase the detection efficiency up to 24 times [Feh18].

The electron avalanche exits the MCP and is projected onto the delay-line anode by an electric field. A delay-line anode is a long wire. The electron avalanche induces a signal on the wire which propagates to each end of it. The difference in arrival time at each end depends on the position-of-impact along the wire. Using at least two non-parallel wires, one can detect the position-of-impact within the detection plane. Using three layers of wires, with a mutual angle of 60% between each layer—as has been done for all detectors used in the present work—increases the redundancy of the information provided by the detector, which increases its multi-hit capability. Such delay-line anode detectors are referred to as *Hexanode* [RDek].

4.2.4 Signal processing and data acquisition

The times-of-flight and positions-of-impact have to be recorded for all reaction particles in coincidence in order to determine the three-dimensional momenta at reaction time on an event-by-event basis.

For the times-of-flight, a reference signal is necessary. For this, a *bunchmarker* signal is used, which has to be provided by the synchrotron ring, marking the times of the electron bunches within the undulator.

The signals of the MCPs and delay-line anodes resemble Gaussian shapes and have to be digitized to be fed into a computer. The signals have a magnitude of a few millivolts and durations of a few nanoseconds.

First, the high-frequency signals are out-coupled at vacuum-qualified feedthroughs. Then, the original signal is amplified by fast amplifiers to voltages of about 1.5 V. A constant-fraction discriminator (CFD) is used to determine the timing of the analogue signal. The NIM (nuclear instrumentation module standard) output of the CFD is fed into a time-to-digital converter (TDC) which records the times of all signals: a reference bunchmarker signal, the signal at each end of each anode layer of each detector, and the MCP signals of each detector.

The data is stored in *listmode* format using the data acquisition software COBOLD [CoB]. Rather than being written in a continuous stream, the data acquisition is triggered by a chosen trigger signal, for instance, by the ion-MCP signal. Upon a detected trigger signal, all signals in a given range before and after the trigger signal (specified by the experimentalist) are stored as a single event and thus, ideally, all detected particles of each event originate from the same photoreaction.

DATA ANALYSIS 5

The raw data of a typical cold-target recoil-ion momentum-spectroscopy (COLTRIMS) experiment are timing signals (stored as *listmode* files). In a first step, these need to be translated to positions-of-impact and times-of-flight of the reaction particles. From these deduced values and together with the experimental values such as electric and magnetic fields and spectrometer geometry, the three-dimensional momenta at reaction time—and consequently, all deduced physical observables—are determined.

For this procedure, the in-house developed software *lmf2root* (Version 3, developed by A. Czasch and T. Jahnke) is used. The initial steps of the software analysis are generally identical for different COLTRIMS experiments. They include a calibration of the microchannel-plate (MCP) delay-line anode detector as well as the subsequent calibration of the electric and the magnetic fields and the spectrometer geometry. The present chapter will introduce these procedures.

5.1 RECONSTRUCTING POSITIONS-OF-IMPACT AND TIMES-OF-FLIGHT

First, the positions-of-impact have to be reconstructed from the recorded arrival times of the signals at the anode-layer ends. For each layer, the position along the anode is given by the difference of the arrival times

$$u = s_u \times (t_{u1} - t_{u2}) \; . \tag{5.1}$$

The scaling factor s_u accounts for the signal propagation speed on the anode wire and its length. It is typically given in millimeter per nanosecond. t_{u1} and t_{u2} correspond to the signal arrival times at either end of the anode [RDek].

For a Hexanode detector (see Section 4.2.3), three different coordinates u, v, w connected to the three different layers of a Hexanode yield positions-of-impact along their respective anode. Transforming from the Hexanode coordinate frame (u, v, w) to the laboratory frame (x, y) results in a detection redundancy which can be used to increase the multi-hit capacity of the anode [Jag02]. The redundancy also enables the reconstruction of positions-of-impact where not all signal arrival times are recorded.

Depending on the observed process, different methods to determine times-of-flight are used. In this work, two different methods were used. In the experiments utilizing synchrotron light, the times-of-flight are determined in reference to a *bunchmarker* signal, which is a timing signal referencing the times of the electron bunches of the synchrotron storage ring. If—as was the case in all experiments performed for this work—the electron times-of-flight are always shorter than the bunchmarker spacing, the time-of-flight of an electron, TOF_e, is calculated via

$$\text{TOF}_e = \text{mod}(t_e - t_{\text{BM}}, \mathit{\Delta} t_{\text{BM}}) + t_0 \,. \tag{5.2}$$

Here, t_e is the signal time of the electron MCP, t_{BM} any recorded bunchmarker signal, and $\mathit{\Delta} t_{\text{BM}}$ the time-spacing between two bunchmarker signals. The modulo function returns the remainder of the division of $t_e - t_{\text{BM}}$ by $\mathit{\Delta} t_{\text{BM}}$ which, ideally, corresponds to the time-of-flight of the detected electron. Since signal processing by the different electronics delays recording times with respect to the bunchmarker signals, an offset t_0 has to be added in the time-of-flight calculation. Additionally, this removes the need of the bunchmarker signal to correspond to the exact time of the photon pulse arriving at the reaction region. Only a exact bunchmarker-spacing $\mathit{\Delta} t_{\text{BM}}$ is necessary to accurately determine the electron's time-of-flight.

The offset t_0 has to be determined experimentally by recording a so-called *wiggle* run. For this, a constant magnetic field is applied in the spectrometer. The electric field is scanned while electrons are measured. The magnetic field causes the electrons to return to their original position (nodes) within the detection plane after a fixed time t_g (see, for example, Figure 6.15a, Page 102). The scanned electric field causes different times-of-flight of the electron and thus, multiple nodes are recorded. The first node has to be recorded at electron times-of-flight of $\text{TOF}_e = t_g$, and thus, t_0 can be determined.

The time-of-flight of the ion is calculated in reference to the electron time-of-flight, that is,

$$\text{TOF}_{\text{ion}} = t_{\text{ion}} - t_e + \text{TOF}_e \,, \tag{5.3}$$

where t_{ion} is the recorded ion-detector MCP-signal time.

In parts of this work, an ion-collision experiment was performed for calibration purposes. In this case, the times-of-flight are calculated differently. In addition to an electron and a ion detector, a projectile detector is used. The projectile time-of-flight from the reaction region to the projectile detector is approximately constant. Because of this, the times-of-flights of the ions and the electrons are calculated in reference to the projectile times-of-flight, that is,

$$\text{TOF}_{e/\text{ion}} = t_{e/\text{ion}} - t_{\text{P}} + t_0 \,, \tag{5.4}$$

where t_0 also accounts for the time-of-flight of the projectile (as well as the finite offset given by the electronics) and t_P is the recorded projectile signal time.

5.2 Reconstructing particle momenta

All electrons measured for this work were guided by electric (E) and magnetic (B) fields onto the detector. From the electron's positions-of-impact x_e and y_e and the times-of-flight $\textsc{tof}_e$, the equations of motion yield

$$p_{e,x} = m_e \frac{bx_e - ay_e}{a^2 + b^2}\,, \quad p_{e,y} = m_e \frac{-bx_e - by_e}{a^2 + b^2} \tag{5.5}$$

for the electron momenta components along the detection plane, with

$$a = \frac{1 - \cos(\omega \times \textsc{tof}_e)}{\omega}\,, \quad b = \frac{\sin(\omega \times \textsc{tof}_e)}{\omega}\,, \quad \omega = \frac{eB}{m}\,. \tag{5.6}$$

In the case of a homogeneous electric field within the spectrometer—that is, no drift region for time-of-flight focusing is used—the electron momentum in z direction calculates via

$$p_{e,z} = m_e \left(\frac{l}{\textsc{tof}_e} - \frac{1}{2} \frac{eE}{m_e} \times \textsc{tof}_e \right)\,, \tag{5.7}$$

where l is the length of the acceleration region.

Equation (5.7) is not valid for multiple electric fields within the electron side of the spectrometer. For two different regions—for instance, an acceleration region and a drift region—analytical expressions for $p_{e,z}$ exist (see Reference [Fou03]), however in practice, a Newton method is used to solve the equations of motion.

Due to their large mass, ions are generally not affected by the magnetic field, simplifying the reconstruction of ion momenta. At most, for spectrometer geometries involving very long ion arms, the ion trajectory is rotated by a few degrees compared to the case of no magnetic field, which can be compensated by virtually rotating the ion detector in the offline analysis.

For the case that the spectrometer does not contain lenses, the x and y component of the ion momenta simply become

$$p_{\mathrm{ion},x} = \frac{x_\mathrm{ion}}{\textsc{tof}_\mathrm{ion}} \times m_\mathrm{ion}\,, \quad p_{\mathrm{ion},y} = \frac{y_\mathrm{ion}}{\textsc{tof}_\mathrm{ion}} \times m_\mathrm{ion}\,. \tag{5.8}$$

The ion-momentum z component is calculated using a linear approximation [Sch02], where

$$p_{\mathrm{ion},z} = q_{\mathrm{ion}} E \times (\mathrm{TOF}_0 - \mathrm{TOF}_{\mathrm{ion}}) \,. \tag{5.9}$$

Here, TOF_0 is the time-of-flight of ions with $p_{\mathrm{ion},z} = 0$, which is—given the case of an ion distribution that is symmetric in z direction, as is the case for all experiments performed for this work—the center of the ion time-of-flight distribution. q_{ion} is the ion's charge.

5.3 Detector and spectrometer calibrations

Due to non-linearities of the anode wires, the signal travel time to either end depends on where along the wire the signal was created, causing the detector image to not correspond to the physical size of the MCP. Further, the scaling factors $s_{u/v/w}$ of Equation (5.1) have to be determined.

The detector calibration is performed by an automated routine of the lmf2root program. It exploits the fact that the total signal runtime

$$t_{\mathrm{sum}} = t_{i1} + t_{i2} \quad (i = u, v, w) \tag{5.10}$$

on an anode wire is constant. The scaling factors $s_{u/v/w}$ are chosen such that the detector image matches the physical size of the used MCPs. However, individual stretch factors for the x and y direction are used to ensure that the detector accurately images the momenta of the reaction. These stretch factors are determined in conjunction with the calibrations for the electric field.

The electromagnetic fields of the spectrometer and its geometries are calibrated using appropriate measurements. Which particular type of calibration measurement is employed depends on the experimental parameters, for example, the maximum detectable particle energy or the energy range of the synchrotron light. For this work, different calibration measurements were used, which are discussed in the respective appendices of Part II: Results.

The magnetic field is calibrated by recording an aforementioned wiggle run. The gyration period t_g depends on the strength of the magnetic field. Thus, by measurement of t_g one can determine the magnetic field strength.

The geometry of the spectrometer and the electric field is calibrated in multiple ways. For the low-energy Compton scattering experiment performed at beam line P04 of the PETRA III synchrotron, DESY, electrons and ions with known energies were created from argon and helium targets, respectively (see Section 6.A, Page 101). For the experiment investigating helium double ionization by Compton scattering, performed at beam line ID31 of the ESRF, an ion-atom collision experiment was performed. In particular, single and double electron capture and autoionization processes were observed (see Section 7.B, Page 123). For high-energy Compton scattering at and photoionization of N_2, measured at beam line ID31 as well, the kinetic energy release of the N^+/N^+ Coulomb explosion was used for calibration (see Section 8.B, Page 152).

They may say nothing to be found
In the center of everywhere

Lori S.

Part II

RESULTS

LOW-ENERGY COMPTON SCATTERING

6

Arthur H. Compton derived the formulas for photon scattering at an electron assuming it to be free and at rest. Following momentum and energy conservation, the energy of the scattered photon $\hbar\omega'$ is given by

$$\hbar\omega' = \frac{\hbar\omega}{1 + \hbar\omega(1 - \cos\theta_\gamma)/(m_e c^2)} \tag{6.1}$$

with the scattering angle θ_γ. Evidently, since there are no other particles involved, the energy of the electron after the scattering process is simply $E_e = \hbar(\omega - \omega')$. In this approximation, the maximum energy transfer onto the electron is for back-scattering processes, that is, $\cos(\theta_\gamma = 180°) = -1$. Thus,

$$\begin{aligned} E_{e,\mathrm{max}} &= \hbar\omega - \hbar\omega'(\theta_\gamma = 180°) \\ &= \hbar\omega - \frac{\hbar\omega}{1 + 2\hbar\omega/(m_e c^2)} = \frac{\hbar\omega}{1 + m_e c^2/(2\hbar\omega)} \,. \end{aligned} \tag{6.2}$$

Compton-scattering experiments typically investigate systems in which the electron is bound in an atom and hence, the initial assumption of an electron which is free and at rest is invalid. A first correction to this assumption was proposed by J. DuMond [DuM29]. If $E_{e,\mathrm{max}}$ is much larger than the binding energy E_bind of the electron, one can correctly describe the process as scattering of a photon at a free electron with a momentum distribution given by the bound-state momentum distribution. The energy of the scattered photon is then broadened due to the momentum distribution of the scatterer-electron, since in the rest system of the electron, the wavelength (and thus the frequency and energy) of the scattering photon is Doppler-shifted. This is referred to as the impulse approximation (see Section 2.4.1, Page 26).

Naturally, a question arises: What happens in an energy regime where this condition $E_{e,\mathrm{max}} \gg E_\mathrm{bind}$ is not valid?

To this end, a photon energy of 2.1 keV was chosen to investigate ionization of helium by Compton scattering. The binding energy of a helium-1*s* electron is 24.6 eV, whereas an initial photon energy of 2.1 keV corresponds to a maximum energy transfer onto the electron [Equation (6.2)] of 17.1 eV, well below the binding energy.

A $\hbar\omega = 2.1$ keV circularly polarized photon beam produced at beam line P04 of the PETRA III synchrotron at DESY, Hamburg, Germany was crossed with a helium supersonic gas jet within the spectrometer of a cold-target recoil-ion momentum spectroscopy (COLTRIMS) setup. The momenta of the He$^+$ ion and the Compton electron are measured and, exploiting momentum conservation, the momentum of the scattered photon ($\boldsymbol{k}'_\gamma$) is calculated. The energy and momentum balance of the observed ionization process read

$$\hbar\omega = \hbar\omega' + E_{\mathrm{bind}} + E_e + E_{\mathrm{He}^+} \,, \quad \boldsymbol{k}_\gamma = \boldsymbol{k}'_\gamma + \boldsymbol{p}_e + \boldsymbol{p}_{\mathrm{He}^+} \,, \tag{6.3}$$

respectively. Due to the large mass of the helium ion, its kinetic energy $E_{\mathrm{He}^+} = \boldsymbol{p}^2_{\mathrm{He}^+} / (2m_{\mathrm{He}^+})$ can be neglected. Furthermore, the electron energies are only a few electronvolts and the ionization threshold of helium is small. Hence, the photon energy after and before the interaction is almost unchanged, that is,

$$\frac{\omega'}{\omega} \equiv t = 1 - \frac{E_{\mathrm{bind}} + E_e + E_{\mathrm{He}^+}}{\hbar\omega} \approx 1 \,. \tag{6.4}$$

Figure 6.1 shows the momenta in the laboratory frame of the electrons, He$^+$ ions and scattered photons. If the photon would scatter at a free electron at rest, the scattered photons and electrons would end up on the surface of a sphere, as indicated by the circles in Figures 6.1A and 6.1G. In reality, this is not a perfect sphere, since the photon loses energy in the scattering process (so the radius to the surface decreases for large scattering angles, that is, in Panels A and G, the circle would not extent perfectly to $2k$ and $-k$, respectively). As discussed in the context of Equation (6.4), for the chosen photon energy the deviation is neglectable. Because of a finite experimental resolution, the experimentally measured momentum of the photon is broad and not perfectly located on the sphere's surface. The deviation of the electron distribution compared to the indicated sphere in Figure 6.1A is much more drastic and has much deeper implications. They result from a complete breakdown of the impulse approximation. For the electron distributions in Figures 6.1A and 6.1B, two distinct features are already visible: a forward lobe and a smaller backward lobe, with an apparent minimum in-between. The forward lobe will be referred to as the binary peak and the backward lobe as the recoil peak, for reasons that will become obvious.

The broadness of the photon momentum $k'_{\gamma,\mathrm{raw}}$ can be corrected. Using the aforementioned approximation that $k'_\gamma = k_\gamma$, the magnitude of $\boldsymbol{k}'_{\gamma,\mathrm{raw}}$ can be scaled while keeping its direction:

$$\boldsymbol{k}'_\gamma = \frac{k_\gamma}{k'_{\gamma,\mathrm{raw}}} \, \boldsymbol{k}'_{\gamma,\mathrm{raw}} \,. \tag{6.5}$$

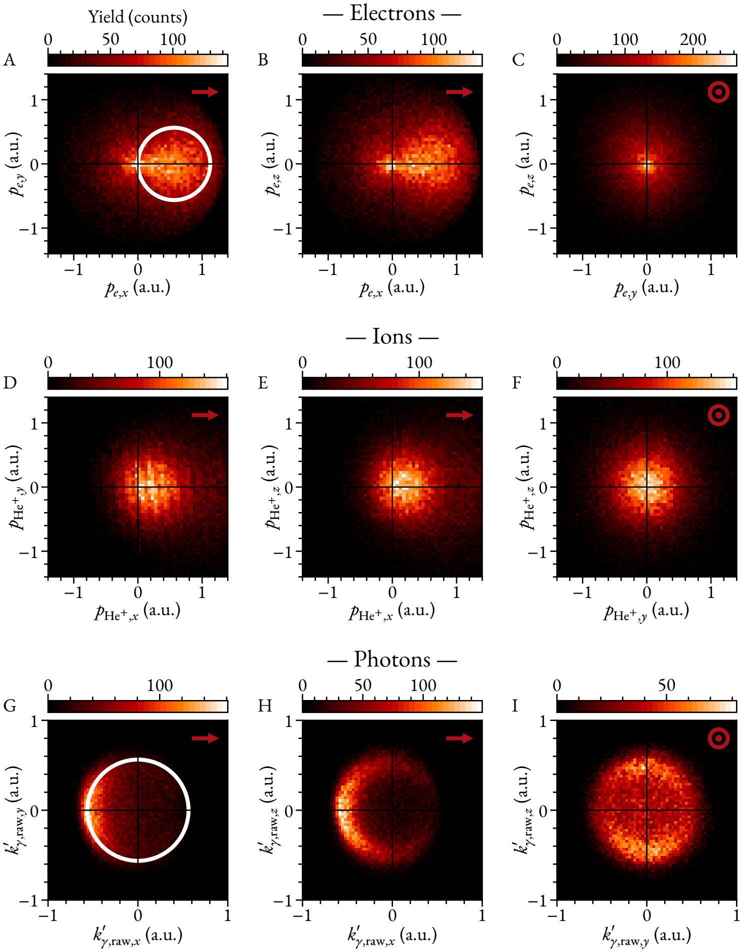

Figure 6.1: Electron (A–C), ion (D–F), and photon (G–I) momenta in the laboratory frame resulting from Compton scattering at helium with $\hbar\omega = 2.1$ keV. The direction of the incoming photon is indicated in the top right corner of each panel, respectively. See main text for an explanation of the circles in A and G. The vertical stripes in D carry no physical meaning but are an artifact of the detection method.

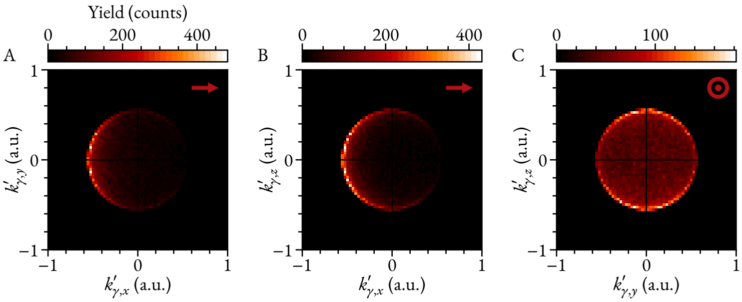

Figure 6.2: Scaled photon momenta from Figures 6.1G to 6.1I such that $k'_\gamma = k_\gamma$. The direction of the incoming photon is indicated in the top right corner of each panel, respectively.

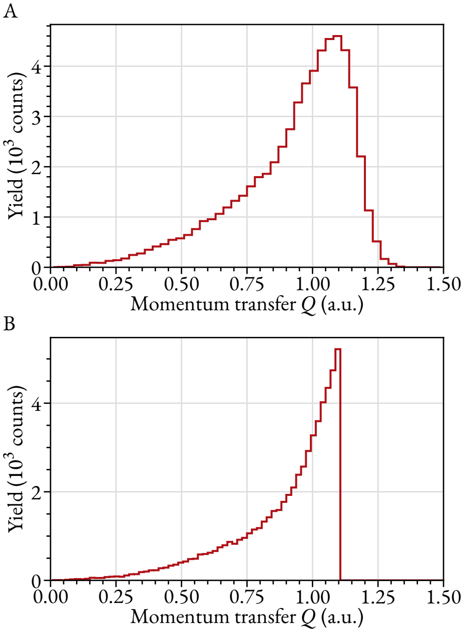

Figure 6.3: Momentum transfer of Compton scattering at helium with $\hbar\omega$ = 2.1 keV before and after scaling the photon momentum. A, Raw momentum transfer, corresponding to Figures 6.1G to 6.1I. B, Momentum transfer after scaling the calculated scattered photon momentum using Equation (6.5) such that $k'_\gamma = k_\gamma$.

This changes the distributions shown in Figures 6.1G to 6.1I to the ones shown in Figure 6.2.

For a free electron with an initial momentum $\boldsymbol{p}_e^i$, the final momentum $\boldsymbol{p}_e$ is given by

$$\boldsymbol{p}_e = \boldsymbol{k}_\gamma - \boldsymbol{k}'_\gamma + \boldsymbol{p}_e^i = \boldsymbol{Q} + \boldsymbol{p}_e^i \,. \tag{6.6}$$

$\boldsymbol{Q} \equiv \boldsymbol{k}_\gamma - \boldsymbol{k}'_\gamma$ is the momentum transfer. Figure 6.3 shows the momentum transfer before and after the scaling of the photon momentum using Equation (6.5).

Figure 6.4 shows a simulation for the final photon and electron momenta. The simulated photons scatter with a distribution given by the Klein-Nishina cross section [see Equation (2.34), Page 23], resulting in the momenta shown in Figure 6.4A. Panel B shows the corresponding simulated final electron momenta given by Equation (6.6). For the initial momentum distribution, a microcanonical distribution for a Coulomb potential with a corrected binding energy, as given by [Abr66]

$$\rho_{p_0}(\boldsymbol{p}_e^i) = \frac{8p_0^5}{\pi^2} \frac{1}{\left(p_e^{i\,2} + p_0^2\right)^4} \,, \tag{6.7}$$

was used. Here, p_e^i is the magnitude of $\boldsymbol{p}_e^i$ and p_0 is given by

$$p_0 = \sqrt{2m_e E_\text{bind}} \,. \tag{6.8}$$

Also shown in Figure 6.4B is a circle with radius p_0 centered around zero, which corresponds to the momentum of the electron necessary to overcome the ionization threshold. The majority of the electron momentum distribution is within the sphere, avowing to the fact that the impulse approximation is invalid for the chosen photon energy.

Figures 6.1D to 6.1F show the He^+ ion momenta. Within the impulse approximation, in the Compton scattering process the ion acts solely as a spectator [Sam94; Spi95]. Thus, the ion momentum distribution would be centered around zero. However, the ion momentum would not be exactly zero, since it must compensate for the initial momentum of the electron. Hence, in conditions where the impulse approximation holds true, the ion momentum reflects the initial momentum distribution of the bound electron [Kal04]. Noticeably, in Figures 6.1D to 6.1F, the momentum distributions are not centered around momentum zero, but they are shifted along the x

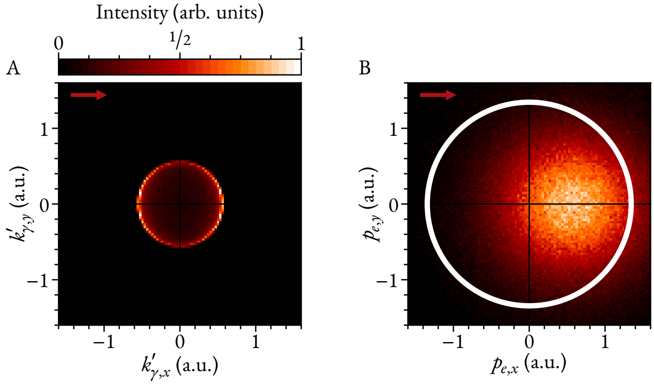

Figure 6.4: Simulation of the final photon (A) and electron (B) momenta resulting from 2.1 keV photons Compton scattering at free electrons with an initial momentum distribution given by Equation (6.7). The circle in B corresponds to the respective momentum p_0 necessary to surpass the ionization threshold of helium.

coordinate, that is, along the initial photon vector, indicating the breakdown of the impulse approximation.

The ionization threshold of He(1*s*) is 24.6 eV. The maximum energy from Compton back-scattering using Equation (6.2) is $E_{e,\text{max}} = 17.1$ eV, well below 24.6 eV. The maximum energy given by Equation (6.2) is only valid for free electrons at rest. Within the impulse approximation, the energy of the electron is given by

$$E_{e,\text{IA}} = \frac{\left|\boldsymbol{Q} + \boldsymbol{p}_e^i\right|^2}{2m_e} . \tag{6.9}$$

The average initial electron momentum, given by Equation (6.8), is about $p_0 = 1.3$ a.u. The maximum momentum transfer Q is approximately $2k_\gamma = 1.1$ a.u. With these values, assuming that momentum transfer and initial momentum are parallel, Equation (6.9) results in an electron energy of $(p_0 + 2k_\gamma)^2/(2m_e) = 78$ eV, well above 24.6 eV.

The A^2 approximation (see Section 2.4.1, Page 26) can be used to describe the system. The interaction operator for a photon interacting with an electron has a linear and quadratic dependency on the vector potential $\boldsymbol{A}$ [see Equation (2.5), Page 12]. The A^2 approximation neglects the linear contribution of $\boldsymbol{A}$. Physically it describes a two-step scenario. First, a photon scatters at one electron bound in helium. The probability of this is given by the Klein-

Nishina cross section. It describes the probability of a photon scattering at a free electron at rest. Hence, in this first "step," the binding of the electron is ignored. Following Equation (6.2), the energy transfer of a few electronvolt to the electron is small compared to the energy of the photon. Therefore, the photon energy remains approximately unchanged. The momentum of the photon, however, changes significantly. The change in photon momentum—that is, the momentum transfer $\boldsymbol{Q}$—"kicks" the helium system, displacing the electron momentum distribution in momentum space by $\boldsymbol{Q}$. Then, the initial bound-state electron wave function in momentum space changes to $\Psi_i(\boldsymbol{p}_e^i) \rightarrow \Psi_i(\boldsymbol{p}_e^i + \boldsymbol{Q})$. The wave function in momentum space is related to the wave function in position space via the Fourier transform

$$\Psi_i(\boldsymbol{p}_e^i) = \frac{1}{\sqrt{(2\pi)^3}} \int \mathrm{d}^3\boldsymbol{r}\, \Psi_i(\boldsymbol{r}) \mathrm{e}^{\mathrm{i}\boldsymbol{p}_e^i \cdot \boldsymbol{r}} \,. \tag{6.10}$$

With the momentum-boosted wave function, this becomes

$$\begin{aligned} \Psi_i(\boldsymbol{p}_e^i + \boldsymbol{Q}) &= \frac{1}{\sqrt{(2\pi)^3}} \int \mathrm{d}^3\boldsymbol{r}\, \Psi_i(\boldsymbol{r}) \mathrm{e}^{\mathrm{i}(\boldsymbol{p}_e^i + \boldsymbol{Q}) \cdot \boldsymbol{r}} \\ &= \frac{1}{\sqrt{(2\pi)^3}} \int \mathrm{d}^3\boldsymbol{r}\, \mathrm{e}^{\mathrm{i}\boldsymbol{Q}\cdot\boldsymbol{r}} \Psi_i(\boldsymbol{r}) \mathrm{e}^{\mathrm{i}\boldsymbol{p}_e^i \cdot \boldsymbol{r}} \,, \end{aligned} \tag{6.11}$$

that is, a momentum-boosted wave function $\Psi_i(\boldsymbol{p}_e^i + \boldsymbol{Q})$ in momentum space relates to the wave function $\mathrm{e}^{\mathrm{i}\boldsymbol{Q}\cdot\boldsymbol{r}} \times \Psi_i(\boldsymbol{r})$ in position space.

The projection of the momentum-boosted initial wave function onto continuum states corresponds to the probability for ionization to occur. It follows for the probability to transition into a final state $|\Psi_f\rangle$ with electron momentum $\boldsymbol{p}_e$ [Arb09]

$$\frac{\mathrm{d}P}{\mathrm{d}\boldsymbol{p}_e} = \left| \langle \Psi_f | \mathrm{e}^{\mathrm{i}\boldsymbol{Q}\cdot\boldsymbol{r}} | \Psi_i \rangle \right|^2 . \tag{6.12}$$

Classically this would mean that ionization occurs if an electron with an already "forward-pointing" momentum receives a "kick" in the same direction.

The origin of the minimum in between the binary and the recoil peak is explained by Equation (6.12). Expanding $\exp \mathrm{i}\boldsymbol{Q} \cdot \boldsymbol{r} = 1 + \mathrm{i}\boldsymbol{Q} \cdot \boldsymbol{r} + \ldots$, one can see that the leading terms correspond to a dipole transition and thus, the momentum-boosted ground state is of dipole shape in the leading term. This dipole-shaped momentum-boosted ground state wave function is then projected onto a final state, keeping the node.

Note as well that the probability given by Equation (6.12) compares to the first term of the Kramers-Heisenberg-Waller matrix element [see Equation (2.38), Page 25], which explicitly links to photon scattering processes. It emphasizes the fact that the transition probability depends on the momentum transfer $\boldsymbol{Q}$ irrespective of its origin.

The Klein-Nishina cross section $(\mathrm{d}\sigma/\mathrm{d}\Omega_{\gamma'})_{\mathrm{KN}}$ describes the probability of a certain momentum transfer Q occurring. The magnitude $Q = \left|\boldsymbol{k}_\gamma - \boldsymbol{k}'_\gamma\right|$ can be calculated using the law of cosine

$$Q^2 = k_\gamma^2 + {k'_\gamma}^2 - 2k_\gamma k'_\gamma \cos\theta_\gamma \,. \tag{6.13}$$

Under the assumption that the photon momentum magnitudes before and after the scattering process are equal—that is $k_\gamma = k'_\gamma$—and using the identity $1 - \cos\theta_\gamma = 2\sin^2(\theta_\gamma/2)$, this simplifies to

$$Q = 2k_\gamma \sin\left(\frac{\theta_\gamma}{2}\right) . \tag{6.14}$$

Hence, the Klein-Nishina cross section has a corresponding momentum transfer distribution. In Figure 6.5b, this distribution is shown by the solid light-orange line. The probability for ionization occurring after a certain momentum transfer [Equation (6.12)] is termed incoherent scattering function S, which is tabulated for helium in Reference [Hub75] and is shown by the dashed black line in Figure 6.5b. Also shown in this figure is the product of S with $(\mathrm{d}\sigma/\mathrm{d}\Omega_{\gamma'})_{\mathrm{KN}}$ (solid dark-red line), which gives the probability for ionization due to Compton scattering. Furthermore, Figure 6.5 shows theoretical and experimental scattering angle distributions and the measured momentum transfer distribution.

In Figure 6.5a, it is apparent that the forward scattering domain is strongly suppressed. The distribution of the momentum transfer is explained by the two-step picture laid out above: in the forward domain, the corresponding momentum transfer is small. Therefore, the ionization probability given by the incoherent scattering function S is small and thus, ionization is strongly suppressed. The shape of the light-orange curves in Figure 6.5 differs significantly from the experimental data—unsurprising, given the underlying assumption of a free electron for these distributions. The very simplistic two-step picture—that is, multiplying the probability of a certain momentum transfer (given by the Klein-Nishina cross section) with the probability to ionize due to this momentum transfer (given by the scattering function

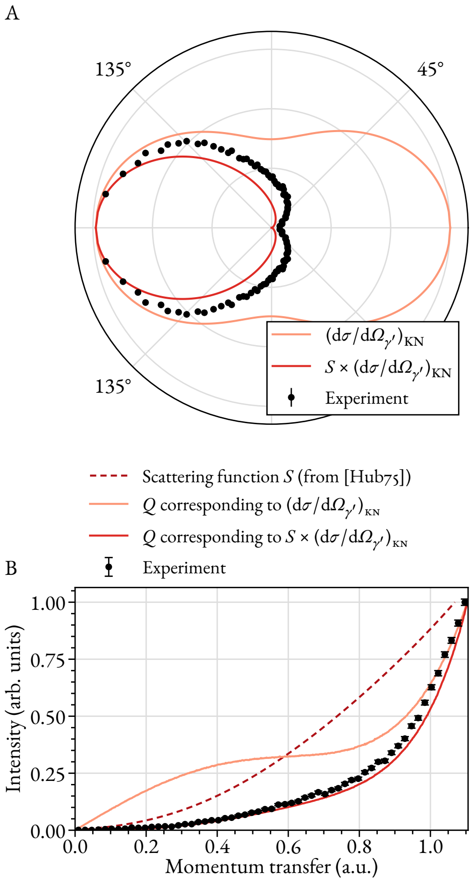

Figure 6.5: Comparison of simulated angular and momentum transfer distributions with experimental data resulting from Compton scattering at helium with $\hbar\omega = 2.1\,\mathrm{keV}$. Random photon scattering angles following the distribution of the Klein-Nishina cross section are created and the corresponding momentum transfers are calculated using Equation (6.14). A, Angular distribution of scattering angles θ_γ in polar representation. The data is mirrored horizontally. B, Distribution of the momentum transfer Q corresponding to the distributions in A (solid lines), incoherent scattering function S, (taken from [Hub75], dashed line), and experimental data (points). The normalization of the data in both panels is chosen such that the maxima of the simulated distributions match, respectively.

S)—already closes the gap between theoretical prediction and experimental data greatly. Even so, it is not a perfect description, as the experimental angular distribution appears significantly larger than the theoretical prediction.

This can be explained by the following considerations: The normalization for the experimental data is chosen such that the maxima of experimental data and theoretical prediction match. However this choice does not have any physical basis and is overall only useful to show a similar trend in theory and experiment. For example, one aspect of the experiment was not discussed so far: only electrons up to a maximum energy of 25 eV were measured with a full solid angle of 4π. This detector cutoff results in an under-representation of large photon scattering angles. Hence normalizing the experimental data to the theoretical maximum (which does not consider this aspect) enhances the overall amplitude of the experimental data. Since no absolute cross sections are measured in this experiment, it is not possible to choose a physically meaningful normalization of the data on its own merits. The comparison shown in Figure 6.5 are included here to emphasize the validity of the two-step description for low-energy Compton scattering at helium. However, in the scope of this work, a full A^2 approximation calculation was carried out, taking the present experimental parameters fully into account. The discussion thereof is presented in the following Section 6.1.

6.1 DISCUSSION OF THEORETICAL METHODS

The experimental data shown here and the theoretical calculations described in this section were published in [Kir20].

To compare experimental data with theoretical models, it is necessary to calculate cross sections of the process. For that, appropriate initial- and final-state wave functions have to be chosen for Equation (6.12). In helium, two electrons with positions $\boldsymbol{r}_1$ and $\boldsymbol{r}_2$ are bound and are described by an initial state $\Psi_i = \Psi_i(\boldsymbol{r}_1, \boldsymbol{r}_2)$. The experiment measures the final momentum $\boldsymbol{p}_e$ of the emitted electron, thus, the final-state wave function is a scattering state with one electron in the continuum while the second electron remains bound at the He$^+$ ion, that is, $\Psi_f = \Psi_f(\boldsymbol{r}_1, \boldsymbol{r}_2; \boldsymbol{p}_e)$. Then, with the kinematic conditions laid out by Equations (6.3) and (6.4) and within the A^2 approximation, the fully differential cross section can be expressed as

$$\frac{d^3\sigma}{dE_e d\Omega_e d\Omega_{\gamma'}} = r_0^2 p_e t \left| (\boldsymbol{\varepsilon} \cdot \boldsymbol{\varepsilon}') \left\langle \Psi_f \middle| \sum_{j=1}^{2} e^{i\boldsymbol{Q}\cdot\boldsymbol{r}_j} \middle| \Psi_i \right\rangle \right|^2 . \tag{6.15}$$

Here, Ω_e and $\Omega_{\gamma'}$ are the solid angles of the emitted electrons and scattered photons, respectively. r_0 is the classical electron radius and $\boldsymbol{\varepsilon}$ and $\boldsymbol{\varepsilon}'$ are the polarization vectors of the incoming and outgoing photon, respectively.

The initial and final states have to be orthogonal—that is,

$$\left\langle \Psi_i \middle| \Psi_f \right\rangle = 0\,, \tag{6.16}$$

—to ensure that for a momentum transfer of $Q = 0$, the cross section is zero. The final photon polarization $\boldsymbol{\varepsilon}'$ is not measured, which is taken into account by averaging over the initial polarization and summing up the probabilities corresponding to the two possible orthogonal polarization states. Then, Equation (6.15) becomes

$$\frac{\mathrm{d}^3\sigma}{\mathrm{d}E_e \mathrm{d}\Omega_e \mathrm{d}\Omega_{\gamma'}} = \frac{r_0^2}{2}\left(1 + \cos^2\theta_\gamma\right) p_e t \left| \left\langle \Psi_f \middle| \sum_{j=1}^{2} \mathrm{e}^{\mathrm{i}\boldsymbol{Q}\cdot\boldsymbol{r}_j} \middle| \Psi_i \right\rangle \right|^2 . \tag{6.17}$$

The factor $1/2\, r_0^2 \left(1 + \cos^2\theta_\gamma\right) = (\mathrm{d}\sigma/\mathrm{d}\Omega_{\gamma'})_{\mathrm{Th}}$ is known as the Thomson cross section. In the limit of small photon energies, Compton scattering is also referred to as Thomson scattering. For Thomson scattering, the approximation $k_\gamma = k'_\gamma$ is exact. Hence, the corresponding Thomson cross section has no dependency on the initial photon and final electron energy. From Equation (6.17), all measured physical observables can be calculated.

Introducing the angles φ_e and θ_e, it is possible to express the angular distribution of the scattered photon as [Hou20]

$$\frac{\mathrm{d}\sigma}{\mathrm{d}\Omega_{\gamma'}} = \int_0^{p_{e,\max}} p_e \mathrm{d}p_e \int_0^{2\pi} \mathrm{d}\varphi_e \int_0^{\pi} \mathrm{d}\theta_e \sin\theta_e \frac{\mathrm{d}^3\sigma}{\mathrm{d}E_e \mathrm{d}\Omega_e \mathrm{d}\Omega_{\gamma'}} . \tag{6.18}$$

φ_e is the angle between the scattering plane and the plane defined by the vectors $\boldsymbol{k}_\gamma$ and $\boldsymbol{p}_e$. The scattering plane is defined by the vectors $\boldsymbol{k}_\gamma$ and $\boldsymbol{k}'_\gamma$. θ_e is the emission angle of the electron with respect to the incoming photon direction. $p_{e,\max}$ is the maximum electron momentum magnitude.

The energy distribution of the emitted electron is [Hou20]

$$\frac{\mathrm{d}\sigma}{\mathrm{d}E_e} = 2\pi \int_0^{2\pi} \mathrm{d}\varphi_e \int_0^{\pi} \mathrm{d}\theta_\gamma \sin\theta_\gamma \int_0^{\pi} \mathrm{d}\theta_e \sin\theta_e \frac{\mathrm{d}^3\sigma}{\mathrm{d}E_e \mathrm{d}\Omega_e \mathrm{d}\Omega_{\gamma'}} . \tag{6.19}$$

To calculate the above integrals, explicit wave functions for the initial and final states in Equation (6.17) have to be chosen. Here, two complementary approaches were pursued. For the two approaches, different sets of initial-state and final-state wave functions were used:

APPROACH I Both electrons in the helium atom are treated explicitly using a correlated two-electron ground-state wave function $\Psi_i = \Psi_i(\boldsymbol{r}_1, \boldsymbol{r}_2)$. For the final state, one electron remains bound in the ionic ground state while the escaping electron's wave function is approximated by Coulomb wave functions.

APPROACH II In the initial state, only one electron is considered active while the other stays frozen at the core. For the final state, a single-active-electron effective potential is used.

6.1.1 THEORETICAL APPROACH I

For the initial state, the correlated two-electron ground-state trial wave function of form

$$\Psi_i(\boldsymbol{r}_1, \boldsymbol{r}_2) = \sum_{j=1}^{10} D_j \left(\mathrm{e}^{-\alpha_j r_1 - \beta_j r_2} + \mathrm{e}^{-\alpha_j r_2 - \beta_j r_1} \right) \mathrm{e}^{-\gamma_j r_{12}} \tag{6.20}$$

was used. D_j, α_j, β_j, and γ_j are parameters. $r_{12} = |\boldsymbol{r}_1 - \boldsymbol{r}_2|$ is the relative coordinate of the two electrons. For more details, the reader is referred to Reference [Chu06]. The ground-state wave function yields a helium ground state energy of $E_0 = -2.903\,71$ a.u., practically equal to the experimental value $E_0^{\mathrm{exp}} = -2.903\,724$ a.u. [Chu22]. For the final-state wave function

$$\Psi_f(\boldsymbol{r}_1, \boldsymbol{r}_2; \boldsymbol{p}_e) = \frac{1}{\sqrt{2}} \left(\psi^C_{\boldsymbol{p}_e}(\boldsymbol{r}_1) \psi_0^{\mathrm{He}^+}(r_2) + \psi^C_{\boldsymbol{p}_e}(\boldsymbol{r}_2) \psi_0^{\mathrm{He}^+}(r_1) \right) \tag{6.21}$$

was used [Kir20]. Here,

$$\psi_0^{\mathrm{He}^+}(r_i) = \sqrt{\frac{8}{\pi}} \mathrm{e}^{-2r_i} \tag{6.22}$$

and $\psi^C_{\boldsymbol{p}_e}(\boldsymbol{r}_i)$ are Coulomb wave functions

$$\psi^C_{\boldsymbol{p}_e}(\boldsymbol{r}_i) = \sqrt{\frac{\mathrm{e}^{-\pi\zeta}}{(2\pi)^3}}\, \Gamma(1 - \mathrm{i}\zeta) \mathrm{e}^{-\mathrm{i}\boldsymbol{p}_e \cdot \boldsymbol{r}_i}\, {}_1F_1\left(\mathrm{i}\zeta; 1; -\mathrm{i}p_e r_i - \mathrm{i}\boldsymbol{p}_e \cdot \boldsymbol{r}_i\right) \tag{6.23}$$

with $\zeta = -1/p_e$. ${}_1F_1$ is the confluent hypergeometric function. To explicitly ensure the requirement of orthogonality—that is, ensuring the condition in Equation (6.16)—the final state in Equation (6.17) is replaced by

$$\langle \Psi_f | = \langle \tilde{\Psi}_f | - \langle \tilde{\Psi}_f | \Psi_i \rangle \langle \Psi_i | \,. \tag{6.24}$$

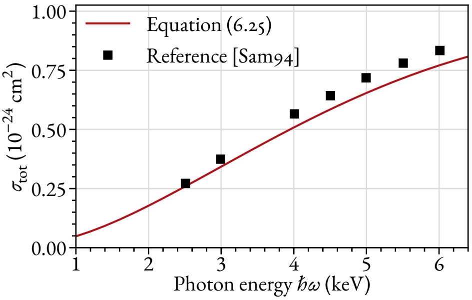

FIGURE 6.6: Total cross section for Compton scattering at helium.

As a crosscheck for this theoretical approach, the total cross section was calculated by integrating Equation (6.18) with respect to the scattering angle θ_γ, that is,

$$\sigma_{\mathrm{tot}} = 2\pi \int_0^\pi \mathrm{d}\theta_\gamma \sin\theta_\gamma \frac{\mathrm{d}\sigma}{\mathrm{d}\Omega_{\gamma'}} . \tag{6.25}$$

A comparison of Equation (6.25) with Reference [Sam94] for different initial photon energies is shown in Figure 6.6.

6.1.2 THEORETICAL APPROACH II

The first theoretical approach outlined above treats the problem with correlated initial wave functions. However, the approximation that the emitted electron escapes from a Coulomb potential created by the remaining He$^+$ ion does not properly reflect the physical nature of the process. The influence of the second remaining electron is effectively ignored. Its influence is crudely included by the fact that the emitted electron escapes a $Z = 1$ instead of a $Z = 2$ Coulomb potential. This assumption is only valid for large distances $r \longrightarrow \infty$.

In the second approach, a more sophisticated description of the final states was chosen. However, a simpler description of the initial state was used. Here, from the two electrons of the helium ground state, only one is considered "active" throughout the scattering process, while the other remains frozen at the core. The active electron receives the momentum transfer $\boldsymbol{Q}$ and, if emitted, escapes in a single-active-electron effective potential [Ton05]. As opposed to the static charge $Z = 1$ of Approach I, the influence of the inactive electron is modeled by asymptotic charges of $Z = 2$ for $r \longrightarrow 0$ and $Z = 1$ for $r \longrightarrow \infty$, that is, the inactive electron screens the helium nucleus charge effectively only for large distances.

The ground state $|\Psi_i\rangle$ and continuum state $|\Psi_f\rangle$ are calculated numerically by solving the radial Schrödinger equation [Kir20].

* * *

For both, Approach I and Approach II, two major approximations are used:

- The scattering process is not fully correlated. This manifests strongest in the low-energy regions of the recoil peak (the backward lobes in Figures 6.1A and 6.1B, Page 79). Particularly, shakeoff (ionization of the second, inactive electron due to initial-state correlations) and shakeup (excitation of the inactive electron due to initial-state correlations) processes are not fully included. Approach I includes electron-electron correlations marginally due to the orthogonalization of the final and the initial state in Equation (6.24), and Approach II by using the single-active-electron effective potential.

- In both approaches, it is assumed that the He^+ ion remains in the ground state. However, the experiment does not resolve the state of the ion, which means that in all experimental data shown excited He^+ ion states are included. The theoretical calculations could be improved by explicitly including different ionization channels, since with the presented experimental method, distinction between these ionization channels is not possible.

6.2 COMPARISON OF EXPERIMENTAL DATA WITH THEORETICAL CALCULATIONS

Figure 6.7 shows the angular distribution already presented in Figure 6.5A. Also shown are the Thomson cross section (the distribution of a low-energy photon scattering at a free electron at rest) and calculations—that is, Equation (6.18)—using Approach I, which are labeled "Theory" in the figure legend. As mentioned previously, only electrons with an energy smaller than 25 eV were measured with full solid angle 4π. Accounting for that, the solid curve in Figure 6.7 is a calculation where this detection cutoff is considered. The intensity of photon back-scattering is reduced significantly—almost by a factor of 2—compared to the calculation without detection cutoff (dashed curve). The agreement between theory and experiment is excellent. Note that the theoretical calculations are enhanced by a factor of 1.9, reflecting the fact that the cross section of Compton scattering at helium is reduced to

FIGURE 6.7: Photon scattering angle distribution of ionization by Compton scattering at helium with $\hbar\omega = 2.1\,\mathrm{keV}$. The dotted line is the Thomson cross section. The error bars are the statistical error and are smaller than the dot size. The dashed and the solid line show the A^2 approximation for all electron energies and electron energies below 25 eV, respectively. The solid and the dashed curves are multiplied by a factor 1.9. The data is horizontally mirrored and normalized to the integral of the solid line. (Modified from [Kir20].)

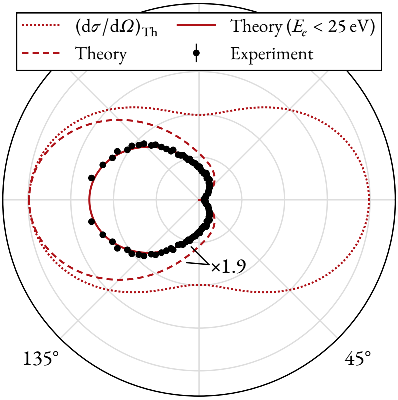

about 20% of its value of 10^{-24} cm^2 for Compton scattering at free electrons [Sam94].

In Figure 6.1 (Page 79), the electron and He$^+$ ion momentum distributions in the laboratory frame (x, y, z) are already shown. However, the laboratory frame is not ideal in representing the underlying physics of the process, since it does not account for the rotational symmetry around the incident light axis of the photon scattering angle. Thus, it is helpful to transform the momenta into a more physically representative reference frame (x', y', z'), with unit vectors $\hat{\boldsymbol{n}}_{x',y',z'}$. The incoming and outgoing photon momentum vector, $\boldsymbol{k}_\gamma$ and $\boldsymbol{k}'_\gamma$, define a scattering plane. It contains the momentum transfer $\boldsymbol{Q}$. It is useful to look at the momentum distributions within that plane. To do that, the coordinate system is defined as follows: the x' coordinate is along the $\boldsymbol{k}_\gamma$ direction, that is,

$$\hat{\boldsymbol{n}}_{x'} = \frac{\boldsymbol{k}_\gamma}{k_\gamma} . \tag{6.26}$$

The direction of the y' coordinate is defined by the outgoing photon momentum k' and is perpendicular to x'

$$\hat{\boldsymbol{n}}_{y'} = \frac{\boldsymbol{k}'_\gamma \times \hat{\boldsymbol{n}}_{x'}}{\left|\boldsymbol{k}'_\gamma \times \hat{\boldsymbol{n}}_{x'}\right|} . \tag{6.27}$$

To get a right-handed coordinate system, the z' direction is then given by

$$\hat{\boldsymbol{n}}_{z'} = \hat{\boldsymbol{n}}_{y'} \times \hat{\boldsymbol{n}}_{x'} . \tag{6.28}$$

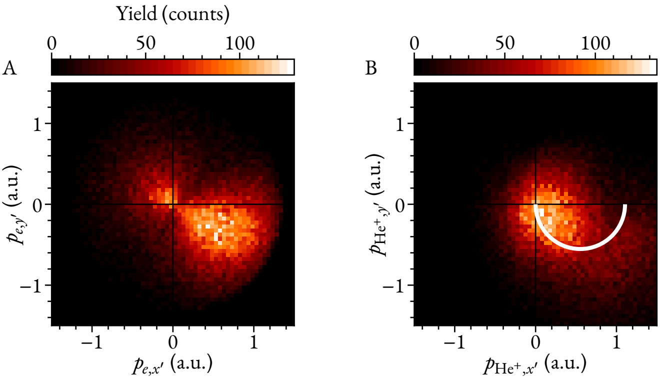

Figure 6.8: Momentum distributions of electrons (A) and He$^+$ ions (B) in the scattering plane as a result of ionization by Compton scattering with $\hbar\omega = 2.1$ keV. For both panels, $p_{x'}$ and $p_{y'}$ are the momentum components defined by Equations (6.26) to (6.28). The color scale depicts counts. See main text for an explanation of the half circle in B. (Adapted from [Kir20].)

Within the $x'y'$ plane of this coordinate frame, the outgoing photon per definition scatters into the upper-half plane and thus, the momentum transfer $\boldsymbol{Q}$ always points into the lower-right quadrant.

The electron and the He$^+$ ion momentum distributions within this coordinate system are shown in Figure 6.8. Within this reference frame, the bimodal shape of the electron momentum distribution becomes very apparent. A forward lobe pointing in the direction of the momentum transfer $\boldsymbol{Q}$ is separated by a distinct minimum at zero from a smaller backward lobe. The He$^+$ ion momentum distribution shows a corresponding (somewhat inverted) distribution, where the majority of momenta are close to the origin, while a significant amount is "smeared out" in direction of the momentum transfer, which is indicated by the half-circle drawn in the lower-right quadrant. The momentum transfer starts at a right angle (to the incoming photon vector) and magnitude zero, corresponding to the limit of the scattering angle $\theta_\gamma \to 0°$. The magnitude increases up to the maximum of $2k_\gamma$ for $\theta_\gamma = 180°$, which corresponds to a momentum transfer direction parallel to the incoming photon momentum vector. It is notable that just outside the circle, the He$^+$ ion momentum distribution shows increased intensity. The width of this increased intensity is comparable to the width of the backward lobe of the electron distribution. This supports the following explanation for the origin of the bimodal electron distribution. The forward lobe correlates with the momentum transfer, these electron momenta result from a binary encounter of electron and photon, that is, the He^+ ion is mostly a spectator and thus, the ion momentum distribution is close to zero. The backward lobe in the electron momentum distribution results from the electron back-scattering at the He^+ ion. Momentum conservation dictates that the ion has to compensate for the change of electron momentum. Then, in a pure mechanistic picture and for back-scattering, the He^+ ion momentum must be equal to the original momentum imparted onto the electron (that is, the momentum transfer) plus the final electron momentum (that is, the momenta in the backward lobe). This is exactly what is visible in Figure 6.8.

Following this reasoning, the forward lobe is termed *binary peak*, the backward lobe *recoil peak*. This is in accordance with other examples where these bimodal distributions are known from: Analogous to Compton scattering—so to say, ionization by photon impact—these bimodal distributions are known from other collision experiments, for example, ionization by electron impact [Ehr86] or ion impact [Fis03].

Figure 6.8 is integrated over all momentum transfers. To see the bimodal structure more clearly, the distributions are shown for fixed magnitudes of the momentum transfer in Figure 6.9. There, three gates for the magnitude were chosen. This corresponds to a momentum configuration of $\boldsymbol{k}_\gamma$, $\boldsymbol{k}'_\gamma$, and $\boldsymbol{Q}$ as indicated in the last column of the figure. A bimodal distribution is also visible for the He^+ ion momentum distributions. Both the electron and ion distributions' orientation follow the direction of the momentum transfer. In the He^+ ion momentum distributions the ions corresponding to the electrons in the recoil peak are situated just at the end of the momentum transfer, supporting the aforementioned mechanistic description.

In Figures 6.9a to 6.9c, the corresponding electron momentum distributions obtained from the theoretical Approach II are included. Again, theoretical predictions and experimental data are in excellent agreement.

The mechanistic description of an electron back-scattering at the helium nucleus does not explain the node between binary and recoil peak. In a classical description there would not be a minimum at zero. However, as has been discussed at the beginning of this chapter, the node is explained by the description of the A^2 approximation (see Page 83).

It is noteworthy that the theoretical predictions shown in Figures 6.9a to 6.9c do not have an explicit reference to Compton scattering. The bimodal shape originates from the alteration of the ground state due to the "kick" given by the momentum transfer. In Reference [Arb09] the same distributions are predicted for attosecond half-cycle laser pulses, shown there in Figure 2. These distributions are also predicted for neutron scattering [Pin14]. In both

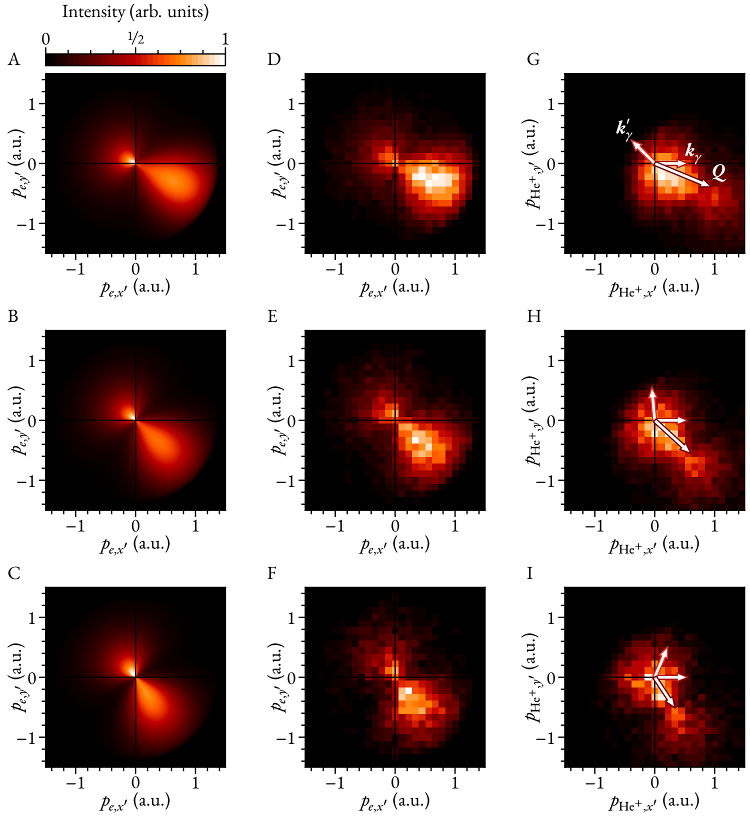

Figure 6.9: Electron and ion momentum distributions in the scattering plane for different momentum transfer gates. A–C, Electron momentum distributions obtained from modeling within the A^2 approximation. D–F, Experimental electron momentum distributions. G–I, Respective He^+ ion momentum distributions. Rows depict different momentum transfer magnitudes Q, namely, from top to bottom, Q = 0.9–1.1, 0.7–0.9, and 0.5–0.7 a.u., respectively. This results in a momentum configuration as indicated by the arrows in G to I. (Adapted from [Kir20].)

these examples ionization occurs due to a momentum kick which is the result of a neutral projectile, not, as is often the case, due to the impact of a charged projectile. For charged projectile impact, due to post collision interaction, the bimodal distribution does not follow the momentum transfer direction exactly (see, for example, Figure 2 in Reference [Gas16]).

As mentioned before, the energy of the electron is small, justifying the

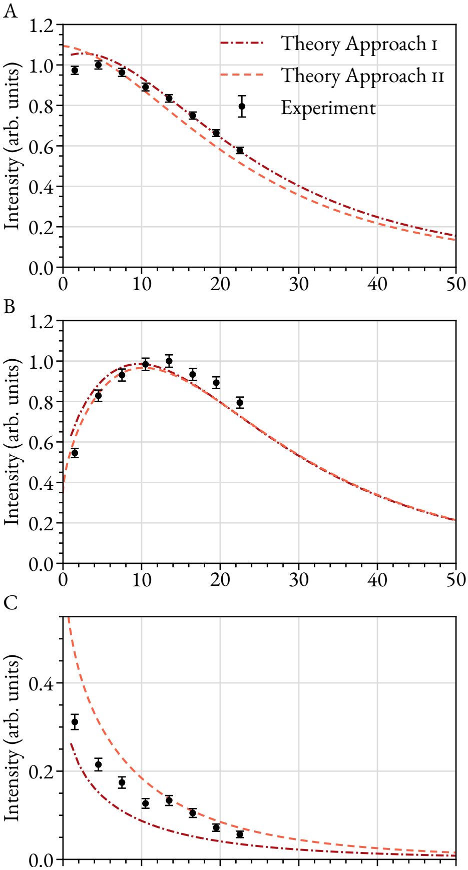

FIGURE 6.10: Electron energy distributions for different emission angles θ_e for Compton scattering at helium with $\hbar\omega = 2.1$ keV. In all panels, the photon scattering angle is restricted to $140 < \theta_\gamma < 180°$. A, Integration over all angles. B, Emission in forward direction, that is, $0 < \theta_e < 40°$. C, Emission in backward direction, that is, $140 < \theta_e < 180°$. In A and B, the experimental data is normalized such that the maximum is 1 and the theoretical predictions are normalized so the integrals of experimental data and theory curves are equal. In C, the normalization factors are equal to those in B. The legend in A applies to all panels. (Adapted from [Kir20].)

approximation that $k_\gamma = k'_\gamma$. Figure 6.10 shows the energy distributions of the electron integrated over all electron emission angles θ_e as well as for forward and backward emission only. θ_e is defined by

$$\cos\theta_e = \frac{p_{e,x}}{p_e} \,. \tag{6.29}$$

Thus, Figure 6.10 shows the total electron energy distribution, the energy distribution of the binary, and the energy distribution of the recoil peak for back-scattering photons, that is, $140 < \theta_\gamma < 180°$.

In the case of integrated electron emission angles (Figure 6.10A) the distribution has its maximum at zero and falls off exponentially. There, differences between the two theoretical approaches are visible. Approach II predicts higher intensities for low-energy electrons. This becomes even clearer in Figure 6.10C, that is, backward emission of the electron. There, the difference in both approaches is bigger than a factor of two for low-energy electrons. However, for forward scattering (Panel B), both approaches predict almost identical distributions.

This is unsurprising given the different potentials used in Approaches I and II. In Approach I, the electron escapes in a Coulomb potential, created by a static charge $Z = 1$. The effective potential of Approach II has a varying charge $Z > 1$, with $Z = 2$ for $r \to 0$. Thus, the potential well the electron escapes from is effectively deeper for Approach II than for Approach I. This explains the difference in both predictions for low-energy electrons as well as their resemblance in Figure 6.10B. For low-energy electrons the asymptotic charge of Approach II is effectively more attractive, while high-energy electrons are less affected. Mechanistically speaking, they "spend" less time close to the potential origin than low-energy electrons. This means, in Approach II, back-scattering of the electrons is more effective than in Approach I. Hence, the recoil peak intensity is enhanced.

Figure 6.11 gives further insight into the process. There, the angular distribution with respect to the momentum transfer and fixed photon scattering angle is plotted, that is, the distribution of χ, where χ is defined by

$$\cos\chi = \frac{\boldsymbol{p}_e \cdot \boldsymbol{Q}}{p_e Q} \,. \tag{6.30}$$

Figures 6.11D and 6.11E show the decreasing intensity of the recoil lobe for increasing electron energy. The same trend as observed in Figure 6.10 is visible: Approach II predicts a higher intensity of the recoil peak than Approach I while the overall shape of the curves are similar. The experimental data does not perfectly match any of the curves. However, Approach II predicts a better intensity-ratio of recoil and binary peak. In both panels D and E, Approach II predicts the intensity of the binary peak excellently while slightly overestimating the intensity of the recoil peak. Approach I predicts a binary peak almost 1.5 times higher than experimentally observed. This suggests that the dynamics in the final state must be considered appropriately and the use of simple Coulomb states—as done by Approach I—is not an adequate description of the process. However, since Approach II does overestimate the recoil peak intensity slightly, a proper description of the initial state dynamics seems necessary as well and thus, hints toward the importance of both theoretical approaches.

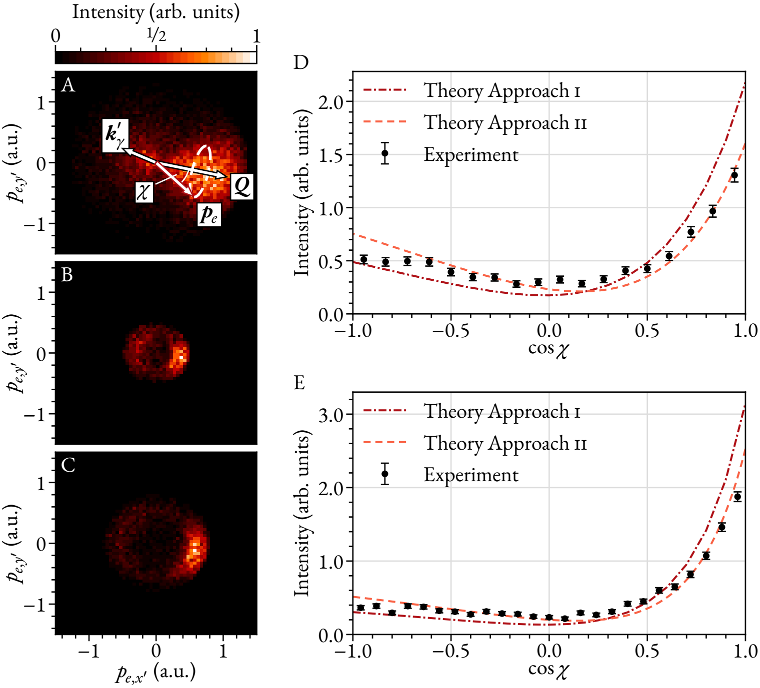

Figure 6.11: Fully differential electron angular distribution for Compton scattering at helium with $\hbar\omega = 2.1$ keV. In all panels, $130 < \theta_\gamma < 170°$. A, Electron momentum distribution in the scattering plane for a fixed momentum configuration—as shown by the black-outlined arrows ($\boldsymbol{k}'_\gamma$ and $\boldsymbol{Q}$)—with $E_e < 25$ eV. The red-outlined arrow illustrates the relation of $\boldsymbol{p}_e$ and $\boldsymbol{Q}$ with the angle χ. B,C, Same distributions as in A with $1.0 < E_e < 3.5$ eV and $3.5 < E_e < 8.5$ eV, respectively. D,E, Distributions of the angle χ for the distributions shown in B and C, respectively. In D and E, theoretical predictions and experimental data are normalized such that the integral below each curve and data, respectively, is 1. (D,E adapted from [Kir20].)

6.3 Low-energy Compton scattering in D_2

Additionally, in the same experimental run, molecular deuterium instead of helium was used as a target. By switching the target to D_2, the initial photon scatters at a system with a lower ionization threshold, namely 13.6 eV instead of 24.6 eV. Thus, for D_2, one would expect the binding energy to have less of an effect on the electron, ion, and scattered photon spectra than for helium. Furthermore, one would expect the total cross section to increase. This, however, cannot be tested by the experimental setup, since total cross sections are not measured. The experimental run with D_2 as target was also much shorter than the helium run, resulting in significantly less statistics collected for D_2. Comparisons of the two datasets are shown in Figures 6.12 to 6.14.

The comparison shows that the angular distribution of the scattered pho-

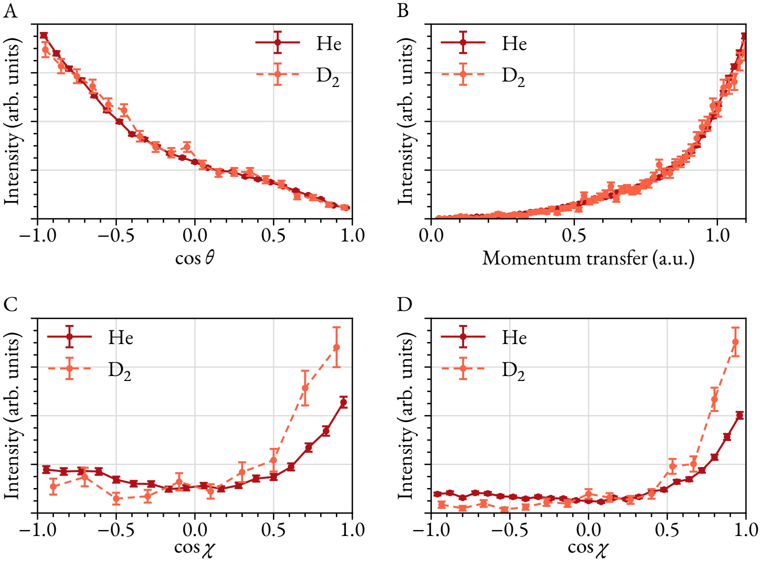

Figure 6.12: Comparison of singly differential cross sections for Compton scattering at helium and D_2 with $\hbar\omega$ = 2.1 keV. In all panels, the data is normalized such that the integral of all bins equals 1, respectively. A, Angular distribution of the scattered photon. The helium data is the same as in Figure 6.7 (Page 91). B, Magnitude of the momentum transfer. The helium data is the same as shown in Figure 6.3B (Page 80). C,D, Angular distribution of the electron around the momentum transfer vector for the same conditions as in Figures 6.11D and 6.11E, respectively. (Helium data in C,D from [Kir20].)

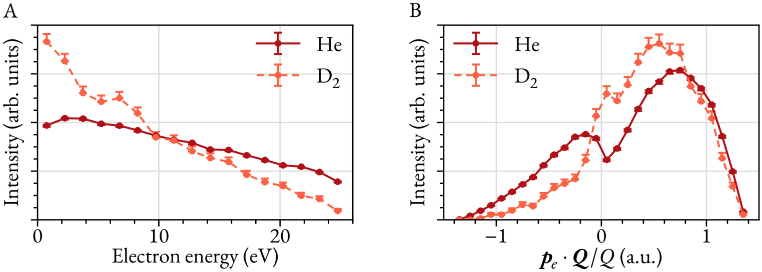

Figure 6.13: Comparison of electron energies (A) and the projection of the electron momentum onto the momentum transfer (B) for Compton scattering at helium and D_2 with $\hbar\omega = 2.1$ keV. In each panel, both datasets are normalized such that the integral of all bins equals 1, respectively.

ton and the momentum transfer is unaffected by the change of target sample. However, Figures 6.12c and 6.12d show a significant difference in intensities of the recoil and binary peaks of the electron distribution. These figures show the same distributions of the helium data seen in Figures 6.11d and 6.11e. In both panels, one can see a higher intensity for the binary peak and a lower intensity for the recoil peak as compared to the helium data. This is unsurprising, given the larger binding energy for helium, which results in lower electron energies compared to D_2, as can be seen in Figure 6.13a. This further supports the picture of the Compton electrons in the recoil peak resulting from back-scattering at the ionic core. Since the binding energy of D_2 is lower than that of helium, the electron energies are larger and thus, back-scattering at the ionic core is less efficient. In Panel b of the figure, the projection of the electron momentum vector onto the momentum transfer is shown, the shape of which supporting the same arguments.

Figure 6.14 shows the electron momentum distribution within the scattering plane. The data for helium in Figure 6.14a is the same as in Figure 6.8a. Again, one can see that for the D_2 data the recoil peak for the electrons is significantly less intense than the one for the helium data. Because of the lack of statistics for the D_2 data, no comparison of the electron momentum distributions for fixed momentum transfer (Figure 6.9, Page 94) is possible.

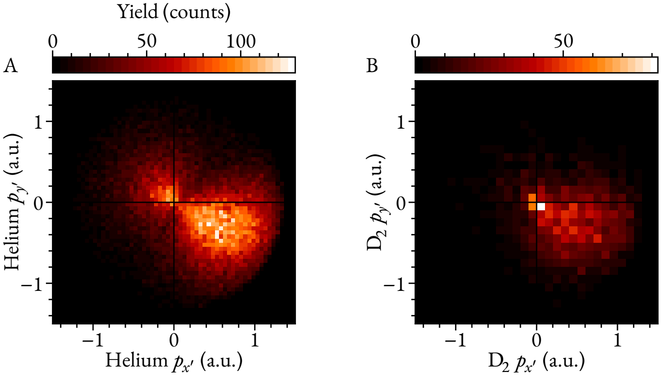

FIGURE 6.14: Comparison of the electron momentum distributions for Compton scattering at helium (A) and D_2 (B) with $\hbar\omega = 2.1$ keV. (A from [Kir20].)

6.A CALIBRATION

The electric field and the electron detector were calibrated with a measurement of photoionization of argon with photon energies of 255.5 and 265.5 eV, namely

$$\gamma + \mathrm{Ar} \rightarrow \mathrm{Ar}^+(2p_{1/2})^{-1} + e^- \,, \tag{6.31}$$

$$\gamma + \mathrm{Ar} \rightarrow \mathrm{Ar}^+(2p_{3/2})^{-1} + e^- \,. \tag{6.32}$$

The binding energies of the $2p_{1/2}$ and $2p_{3/2}$ states are 250.6 and 248.4 eV, respectively. Thus, electrons with energies 2.2 eV apart are measured for each photon energy. The corresponding spectra are shown in Figure 6.15.

The time offset t_0 was determined with a high magnetic field (see Section 5.3, Page 72). Sweeping the electron time-of-flight over several gyration nodes (see also Section 5.3) was used to determine the magnetic field. The corresponding spectra of the two runs are shown in Figure 6.16.

The ion detector was calibrated using photoionization of helium with a photon energy of 275 eV. The corresponding ion momenta are shown in Figure 6.17.

6.B EXPERIMENTAL PARAMETERS

For the ion and the electron detector alike, the x offset, that is, the offset in the direction of the incoming light, is critical. Due to rotational symmetry of Compton scattering around the incoming photon momentum vector, the Compton-scattering-momentum spectra (Figure 6.1, Page 79) have to be centered around $y = z = 0$, whereas no such assumption can be made for the x component, requiring determination of the detector x offset through a suitable calibration using photoionization of helium.

The measurement was performed at the permanent COLTRIMS endstation of beam line P04 of the PETRA III Synchrotron at DESY, Hamburg in October 2017. The synchrotron ring was operated in 40-bunch timing mode, which corresponds to a time spacing of 192 ns between photon bunches. The beam line was operated in pink-beam mode. Foil filters, namely 980 nm aluminum, 144 nm copper, and 153 nm iron, were installed in the photon beam. The experimental parameters of the COLTRIMS setup are listed in Table 6.1. A sketch of the spectrometer is shown in Figure 6.18.

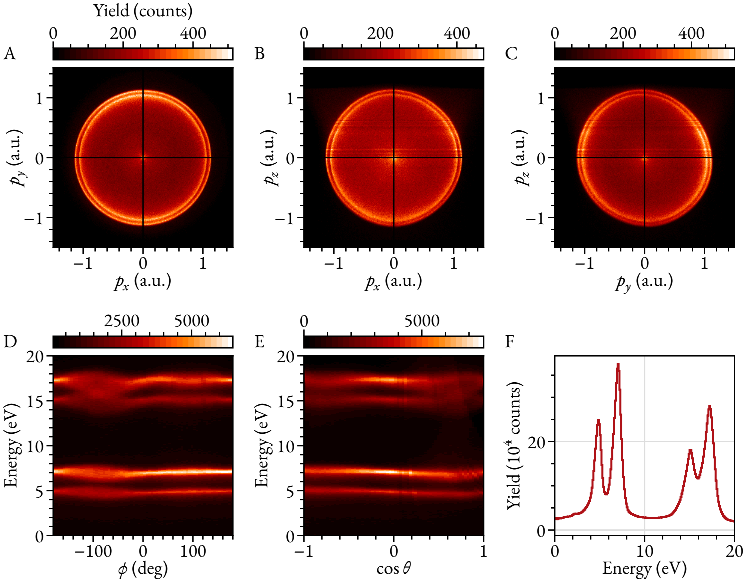

FIGURE 6.15: Spectra for photoionization of argon with $\hbar\omega = 255.5$ and 265.5 eV. A–C, Electron momenta for $\hbar\omega = 265.5$ eV. D,E, Laboratory angles ϕ and $\cos\theta$ versus the electron energy, respectively, for both $\hbar\omega = 255.5$ and 265.5 eV. F, Electron energy for both $\hbar\omega = 255.5$ and 265.5 eV. The egg-like shape of the momentum sphere in the upper half of C is due to the electrostatic lens of the spectrometer influencing electrons with a momentum vector pointing toward the ion detector. The blurred regions in D and E are also a result thereof.

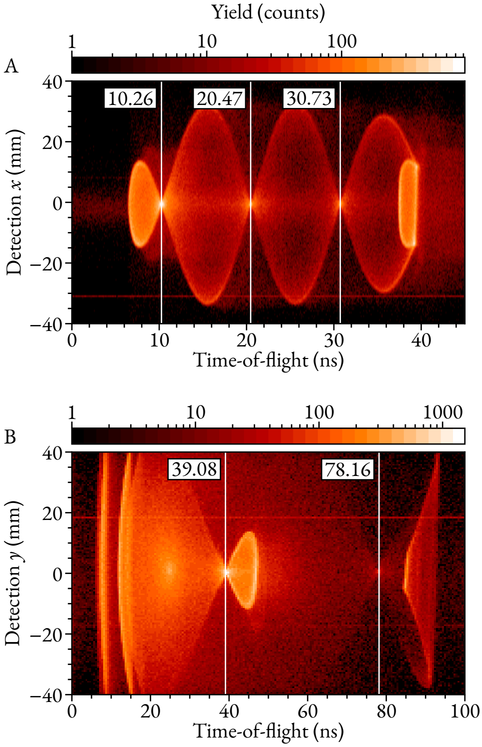

FIGURE 6.16: Time-of-flight versus detection position of electrons for t_0 measurement (A) and B-field calibration (B). The numbers left to the lines are the node positions in nanoseconds, respectively.

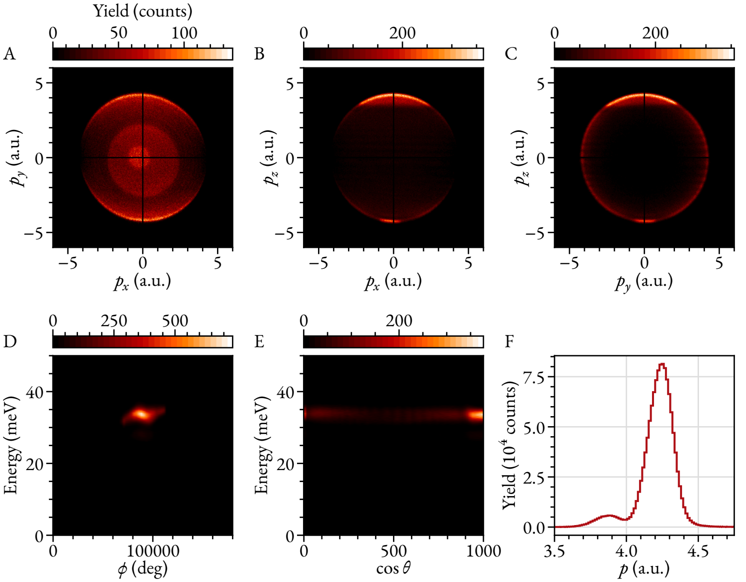

FIGURE 6.17: Spectra for photoionization of helium with $\hbar\omega = 275$ eV. A–C, He^+ ion momenta. D,E, Laboratory angles ϕ and cos θ versus the ion energy, respectively. F, Ion momentum magnitude.

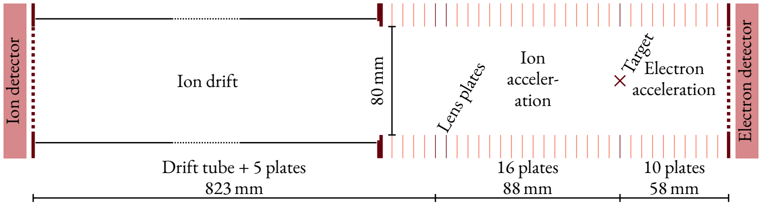

FIGURE 6.18: Sketch of the spectrometer of the beam time in October 2017 at beam line P04 of the PETRA III synchrotron at DESY, Hamburg.

Table 6.1: Experimental parameters of the experimental run of the beam time in October 2017 at beam line P04 of the PETRA III synchrotron, DESY, Hamburg, Germany.

Target			
Driving pressure	50 bar	Nozzle diameter	30 µm
Width at interaction point	≈ 1 mm	Target gas	helium
Temperature	300 K	Jetdump vacuum	1.5×10^{-7} mbar
Expansion vacuum	4.3×10^{-3} mbar		
Beam line			
Photon energy E_γ	2.1 keV	Polarization	circular
$\Delta E_\gamma / E_\gamma$	1.1%	Focus size	0.2×0.1 mm^2 (W×H)
Operation mode	40-bunch pink beam	Bunch spacing	192 ns
Filter setup	980 nm aluminum 144 nm copper 153 nm iron		
Spectrometer			
Electron arm	5.8 cm (acc.)	Ion arm	12.4 cm (acc.) 79.3 cm (drift)
E-field	18.3 V/cm	Vacuum	4×10^{-9} mbar
B-field	9.1 Gs	Lens voltage jump	187 V
		Lens position	8.8 cm from target
Voltages			
Electron detector	−50 V (front) +2687 V (signal)	Ion detector	−2454 V (front) +30 V (signal)
Spectrometer	−499 V (electron) −1151 V (ion)	Helmholtz current	44.6 A
Detectors			
Electron	80 mm	Ion	80 mm
Electron MCP	regular	Ion MCP	regular
Rates			
Electron	10–40 kHz	Ions	0.5 kHz (trigger)

7

HELIUM DOUBLE IONIZATION

The impulse approximation is a good description of Compton scattering in the hard x-ray regime. Within the impulse approximation, the electron at which the photon Compton scatters can be considered free, with an initial momentum distribution as if it was bound. Then, Compton scattering can be used to study momentum distributions of single-active-electrons in bound states of matter. Typically, this is done by measuring energy spectra of the Compton scattered photons [Kan92]. Under fixed photon scattering angles θ_γ, the energy of the photons is Doppler-broadened due to the initial momentum distribution of the target electrons. By measuring the photon distribution, one can deduce the initial momentum distribution of the electron. This is known as the Compton profile

$$J(q) = \frac{1}{2} \int_q^\infty \mathrm{d}p p \rho(p) \,. \tag{7.1}$$

Here, $\rho(p)$ is the momentum density of the bound electron and q is the projection of the electron momentum onto the incoming photon momentum. The symbol q is chosen to comply literature standards. For this work, the projection of the electron momentum onto the incoming light axis is $p_{e,x} = q$.

In this chapter, a measurement of momentum distributions for electrons and ions for Compton scattering at helium with photon energies of $\hbar\omega = 40\,\mathrm{keV}$ is presented. However, not only single ionization of helium was measured, but simultaneously, double ionization as well. The results were published in [Kir22] and confirm the reflection of the electron momentum profile in the He^{1+}-ion momentum distribution. The momentum distribution of the doubly charged He^{2+} ion is very close to the momentum distribution of the nucleus in the atomic helium ground state, underlining the role of the nucleus acting as a spectator not only in one-photon single ionization, but in one-photon double ionization as well.

For Compton scattering at photon energies of 40 keV, the mechanisms facilitating one-photon double ionization are shakeoff and knockout. In shakeoff, double ionization occurs, since the initial eigenstates have an overlap with not only the final bound eigenstates of the system, but also with the continuum. The initial eigenstates are the electronic eigenstates of the system before a first electron is emitted. The final bound electronic eigenstates correspond to the system with one electron removed. The overlap of the initial eigenstates with the continuum corresponds to a certain probability for

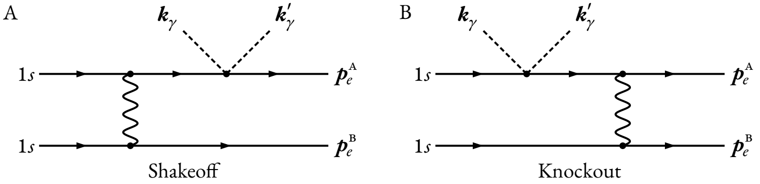

Figure 7.1: Feynman diagrams for the shakeoff (A) and the knockoff (B) process for helium. For each process, a second diagram with permuted lines for $\boldsymbol{p}_e^{\mathrm{A}}$ and $\boldsymbol{p}_e^{\mathrm{B}}$ was omitted, respectively. (Adapted from [Amu95].)

the emission of a second electron. Knockout—as the name implies—refers to the second electron being "knocked out" by the first electron [Sam90; McG97]. For a more extensive discussion of the two processes the reader is referred to Section 2.5 on Page 31. In principle, one-photon double ionization by shakeoff means double ionization due to electron-electron correlations in the initial state, whereas one-photon double ionization by knockout refers to double ionization due to electron-electron correlations in the final state. This is illustrated by the Feynman diagrams in Figure 7.1.

In both the knockout and the shakeoff mechanism the nucleus solely acts as a spectator, as can be seen in the Feynman diagrams. Hence, it is not surprising that in the case of one-photon double ionization by Compton scattering the momentum distributions of the helium nucleus is the same as the two-electron ground-state momentum distribution. To describe this process properly, nonrelativistic calculations with highly correlated initial and final states are required. In the following Section 7.1, a brief overview of those methods is provided. Note that the Feynman diagrams of Figure 7.1 are not the basis of the theoretical calculations and are included for illustrative purposes only.

Two reactions were measured, namely

$$\gamma\,(40\,\mathrm{keV}) + \mathrm{He} \rightarrow \gamma' + \mathrm{He}^{1+} + e^- \,, \tag{7.2}$$

$$\gamma\,(40\,\mathrm{keV}) + \mathrm{He} \rightarrow \gamma' + \mathrm{He}^{2+} + e^-_{\mathrm{A}} + e^-_{\mathrm{B}} \,, \tag{7.3}$$

with corresponding momenta

$$\boldsymbol{k}_\gamma + \boldsymbol{p}_{\mathrm{He}} \rightarrow \boldsymbol{k}'_\gamma + \boldsymbol{p}_{\mathrm{He}^{1+}} + \boldsymbol{p}_e \,, \tag{7.4}$$

$$\boldsymbol{k}_\gamma + \boldsymbol{p}_{\mathrm{He}} \rightarrow \boldsymbol{k}'_\gamma + \boldsymbol{p}_{\mathrm{He}^{2+}} + \boldsymbol{p}_e^{\mathrm{A}} + \boldsymbol{p}_e^{\mathrm{B}} \,. \tag{7.5}$$

Experimentally, it was only possible to measure electrons up to a maximum momentum magnitude of $p_{e,\mathrm{max}} = 1.1$ a.u. However, the majority of electron

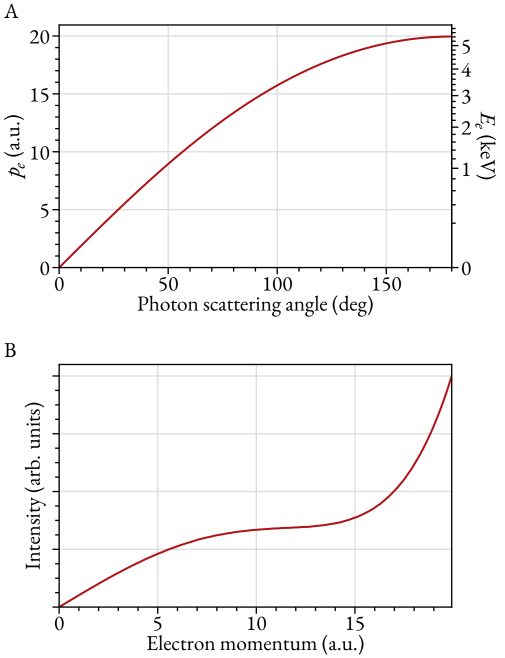

Figure 7.2: Electron momenta after Compton scattering at a free electron at rest with $\hbar\omega = 40$ keV. A, Electron momenta (left axis) and corresponding electron energies (right axis) dependent on the photon scattering angle. B, Electron momentum distribution corresponding to the distribution of photon scattering angles using the Klein-Nishina cross section.

momenta originating from Compton scattering with $\hbar\omega = 40$ keV are much higher than 1.1 a.u., as shown in Figure 7.2. (Note, this spectrum shows the electron momentum for Compton scattering at free electrons at rest and is included only to give a perspective of the electron momenta involved.) As a consequence for the case of single ionization, since all electrons originate from Compton scattering, no electrons were detected. In the case of double ionization only one electron is measured. For double ionization, it is important to note that the experiment does not distinguish between the origin of the detected electron—that is, if it originates from Compton scattering, shakeoff, or knockout. However, because of the selection of small momenta, the majority of electrons will be due to the shakeoff or knockout process.

The ion momentum magnitude is restricted to a maximum of 1.8 a.u. This is due to restrictions given by the experimental setup at beam line ID31 of the ESRF synchrotron. The chosen electric fields and spectrometer geometry resulted in a temporal and spatial overlap of background produced by He^{1+} ions and He^{2+} ions on the detector, as shown in Figure 7.14 on Page 128. To suppress this background the ion momenta had to be restricted to the aforementioned 1.8 a.u. A more extensive discussion of the ion and the electron momentum gates is included in Section 7.c at the end of this chapter.

The scattered photon is never detected.

7.1 Discussion of theoretical methods

Analogous to the theoretical calculations in the previous Chapter 6, the basis of describing this experiment theoretically is again the A^2 approximation. The momenta of two final reaction particles are measured: the momentum of the He^{2+} ion $p_{\mathrm{He}^{2+}}$ and the momentum of the electron p_e^{B}. Note that the momentum p_e^{B} is always small, whereas the momentum p_e^{A} of the other electron ranges from large to small momenta, depending on the momentum transfer $\boldsymbol{Q} = \boldsymbol{k}_\gamma - \boldsymbol{k}'_\gamma$.

Unless stated otherwise, the following equations are given in atomic units. The methods described below are published in more detail in Reference [Chu22].

The sixfold differential cross section (6dcs) is given by

$$\frac{\mathrm{d}^6\sigma}{\mathrm{d}^3\boldsymbol{p}_e^{\mathrm{B}}\,\mathrm{d}^3\boldsymbol{p}_{\mathrm{He}^{2+}}} = \frac{\alpha^2}{(2\pi)^6\hbar\omega^2}\int \mathrm{d}^3\boldsymbol{k}'_\gamma\,\frac{|M|^2}{\boldsymbol{k}'_\gamma} \tag{7.6}$$

$$\times\,\delta\left[t - \frac{k'_\gamma}{k_\gamma} - \frac{\alpha}{2k_\gamma}\left(\boldsymbol{k}_\gamma - \boldsymbol{k}'_\gamma - \boldsymbol{p}_e^{\mathrm{B}} - \boldsymbol{p}_{\mathrm{He}^{2+}}\right)^2\right]. \tag{7.7}$$

Here, α is the fine-structure constant, M is the transition matrix element, and t is defined by

$$t \equiv 1 - \frac{\hbar\omega' - E_{\mathrm{bind}}}{\hbar\omega} \approx 1\,. \tag{7.8}$$

The momentum of Electron a is expressed with $\boldsymbol{k}_\gamma - \boldsymbol{k}'_\gamma - \boldsymbol{p}_e^{\mathrm{B}} - \boldsymbol{p}_{\mathrm{He}^{2+}} = \boldsymbol{p}_e^{\mathrm{A}}$. Energy conservation is ensured by the δ function in Equation (7.7). Defining x, with $0 \le x \le 1$ and $x \equiv k'_\gamma / k_\gamma$, Equation (7.7) is rewritten to

$$\frac{\mathrm{d}^6\sigma}{\mathrm{d}^3\boldsymbol{p}_e^{\mathrm{B}}\,\mathrm{d}^3\boldsymbol{p}_{\mathrm{He}^{2+}}} = \frac{\alpha^4}{(2\pi)^6}\int_0^1 x\mathrm{d}x\int \mathrm{d}\Omega_{\gamma'}\,|M|^2$$

$$\times\,\delta\left[t - x - \frac{\alpha k_\gamma}{2}\left(\hat{\boldsymbol{n}} - \hat{\boldsymbol{n}}'x - \frac{\boldsymbol{p}_e^{\mathrm{B}} + \boldsymbol{p}_{\mathrm{He}^{2+}}}{k_\gamma}\right)^2\right] \tag{7.9}$$

where $\hat{\boldsymbol{n}}$ and $\hat{\boldsymbol{n}}'$ are the unit vectors in direction of $\boldsymbol{k}_\gamma$ and $\boldsymbol{k}'_\gamma$, respectively. Considering that $t \approx 1$, and solving the expression within the δ function with respect to x yields an approximate solution

$$x_1 = 1 - \frac{\alpha k_\gamma}{2}\left(\hat{\boldsymbol{n}} - \hat{\boldsymbol{n}}'t - \frac{\boldsymbol{p}_e^{\mathrm{B}} + \boldsymbol{p}_{\mathrm{He}^{2+}}}{k_\gamma}\right)^2 . \tag{7.10}$$

Then, the 6DCS becomes

$$\frac{\mathrm{d}^6\sigma}{\mathrm{d}^3 p_e^{\mathrm{B}} \mathrm{d}^3 p_{\mathrm{He}^{2+}}} = \frac{\alpha^4}{(2\pi)^6} \int \mathrm{d}\Omega_{\gamma'} x_1 |M|^2 . \tag{7.11}$$

Within the A^2 approximation, M is given by the electronic matrix element

$$M(\boldsymbol{p}_e^{\mathrm{A}}, \boldsymbol{p}_e^{\mathrm{B}}; \boldsymbol{\varepsilon}, \boldsymbol{\varepsilon}') = (\boldsymbol{\varepsilon} \cdot \boldsymbol{\varepsilon}') \left\langle \Psi_f(\boldsymbol{p}_e^{\mathrm{A}}, \boldsymbol{p}_e^{\mathrm{B}}) \middle| \sum_{j=1}^{N=2} \mathrm{e}^{\mathrm{i}\boldsymbol{Q}\cdot\boldsymbol{r}_j} \middle| \Psi_i \right\rangle . \tag{7.12}$$

Here, $\boldsymbol{\varepsilon}$ and $\boldsymbol{\varepsilon}'$ are the polarization vectors of the incoming and scattered photon, respectively, and fulfill the conditions $\boldsymbol{\varepsilon} \cdot \boldsymbol{k}_\gamma = \boldsymbol{\varepsilon}' \cdot \boldsymbol{k}'_\gamma = 0$. $\boldsymbol{r}_1$ and $\boldsymbol{r}_2$ are the positions of Electron A and B, respectively.

The final and the initial states are—analogously to Equation (6.24) in Chapter 6 on Page 88—explicitly orthogonalized. Since the photon polarization is not measured, initial photon polarization is averaged and the final photon polarization is summed up, giving rise to the factor $\left(1 + (\hat{\boldsymbol{n}} \cdot \hat{\boldsymbol{n}}')^2\right)$. Finally, the 6DCS becomes

$$\begin{aligned} \frac{\mathrm{d}^6\sigma}{\mathrm{d}^3 p_e^{\mathrm{B}} \mathrm{d}^3 p_{\mathrm{He}^{2+}}} = \frac{\alpha^4}{(2\pi)^6} \int & \mathrm{d}^2\hat{n}'\, x_1\left(1 + (\hat{\boldsymbol{n}} \cdot \boldsymbol{n}')^2\right) \\ & \times \left| T_1 + T_2 - 2\langle \Psi_i | \mathrm{e}^{\mathrm{i}\boldsymbol{Q}\cdot\boldsymbol{r}} | \Psi_i \rangle\, T_3 \right|^2 . \end{aligned} \tag{7.13}$$

Here, $\boldsymbol{r} = \boldsymbol{r}_1 - \boldsymbol{r}_2$, and

$$T_1 = \langle \Psi_f | \mathrm{e}^{\mathrm{i}\boldsymbol{Q}\cdot\boldsymbol{r}_1} | \Psi_i \rangle , \tag{7.14}$$

$$T_2 = \langle \Psi_f | \mathrm{e}^{\mathrm{i}\boldsymbol{Q}\cdot\boldsymbol{r}_2} | \Psi_i \rangle , \tag{7.15}$$

$$T_3 = \langle \Psi_f | \Psi_i \rangle . \tag{7.16}$$

From Equation (7.13), the singly differential cross sections that are compared to the experimental data (Section 7.2) are obtained.

A more detailed description of Equations (7.14) to (7.16) can be found in References [Chu21; Chu22], where a physical interpretation of the terms T_1 to T_3 is given. A brief discussion of the contributions to the 6DCS of Equation (7.13) of the three terms is following.

T_1 describes the direct interaction of the photon with the electron corresponding to the coordinate $\boldsymbol{r}_1$, that is, the "fast" Electron A. The electron both absorbs and emits the photon. The second Electron B is emitted via the shakeoff mechanism. Thus, since the only electron-electron interaction is in the initial state, T_1 gives information about the internal structure of the helium atom.

In T_2, the photon does not interact directly with Electron A but is scattered by Electron B which transfers the momentum to Electron A due to internal electron-electron correlations. For increasing photon scattering angles—that is, increasing momentum transfer $\boldsymbol{Q}$—this term rapidly tends to zero. This exchange term is zero without electron-electron correlations. However, for small scattering angles, the distinction of both electrons into "fast" and "slow" is arbitrary. The ramifications thereof will be discussed later in this chapter, when I compare the theoretical predictions with the experimental data.

The matrix element T_3 is artificial and a result of the non-orthogonality of the trial wave functions of the initial and final states of the helium atom. Usually, it is small over the entire range of photon scattering angles [Chu22].

7.1.1 INITIAL AND FINAL STATES

Different sets of calculations were performed to model the experiment. For the initial states, three different ground-state wave functions were chosen: a highly correlated trial wave function (CF) [Chu06] (which is the same wave function that was used in the previous Chapter 6, see Equation (6.20) on Page 88), a single-parameter Hylleraas-type wave function (HY) [Hyl28], and a simple configuration-interaction wave function (SPM) [Sil60]. Respectively, the helium ground-state energies of these wave functions are −2.85 a.u. (HY), −2.895 227 8 a.u. (SPM), and −2.903 71 a.u. (CF), compared to the experimental value of −2.903 724 a.u.

For the final state, the well-known Brauner-Briggs-Klar (BBK) wave function [Bra89] (that is, a three-body Coulomb wave function), simple Coulomb-wave (CW) wave functions, as well as a plane-wave (PW) wave functions were used. The BBK wave function is fully correlated and considers equally the electron-electron and electron-nucleus interaction. For the Coulomb wave functions, Electron A is approximated with a PW wave function, while Electron B is described using CW wave functions with $Z = 2$, that is, no electron-electron correlation exists in the final state. Finally, for the calculations only using PW wave function, both Electrons A and B are described using PW wave functions.

Treating either electron (A or B) as plane waves is the high-energy limit: for a high-energy electron, the Coulomb potential it escapes from has minimal influence on the electron wave packet. If the Compton electron is within this limit, one-photon double ionization by Compton scattering can only occur due to the shakeoff effect, since no electron-electron interactions exist in the final state: the Compton electron is effectively "instantly" removed from the helium system. This is referred to as the sudden approximation in the literature.

Multiple combinations of initial-state and final-state calculations are investigated in this work, namely

CF+BBK (correlated initial state with correlated final state),

CF+PW (correlated initial state with plane-wave approximation for the final state),

HY+CW (Hylleraas-type initial state with Coulomb wave functions for the final state), and

SPM+CW (simple configuration-interaction wave function for the initial state with Coulomb wave functions for the final state).

Multiple singly differential cross sections (SDCS) for these sets of calculations and their respective comparison to the experimental data are shown in Section 7.2.

Additionally, the momentum distributions of one electron in the ground state and the momentum distributions of the helium nucleus in the two-electron ground state were calculated. The former relates to the Compton profile and is reflected in the He^{1+}-ion momentum distribution, the latter is the momentum distribution of the He^{2+} ion. Expressing the initial wave function in momentum space, one obtains via the Fourier transform

$$\Psi_i(\boldsymbol{p}_e^{\mathrm{A}}, \boldsymbol{p}_e^{\mathrm{B}}) = \int \mathrm{d}^3\boldsymbol{r}_1 \int \mathrm{d}^3\boldsymbol{r}_2 \, \mathrm{e}^{-\mathrm{i}\boldsymbol{p}_e^{\mathrm{A}}\cdot\boldsymbol{r}_1} \mathrm{e}^{-\mathrm{i}\boldsymbol{p}_e^{\mathrm{B}}\cdot\boldsymbol{r}_2} \, \Psi_i(\boldsymbol{r}_1, \boldsymbol{r}_2) \, . \qquad (7.17)$$

Momentum in the helium ground state is obviously conserved, that is, $\boldsymbol{p}_e^{\mathrm{A}} + \boldsymbol{p}_e^{\mathrm{B}} + \boldsymbol{p}_{\mathrm{He}^{2+}} = 0$. Thus, $\Psi_i(\boldsymbol{p}_e^{\mathrm{A}}, \boldsymbol{p}_e^{\mathrm{B}}) = \Psi_i(-\boldsymbol{p}_e^{\mathrm{B}} - \boldsymbol{p}_{\mathrm{He}^{2+}}, \boldsymbol{p}_e^{\mathrm{B}})$. Then,

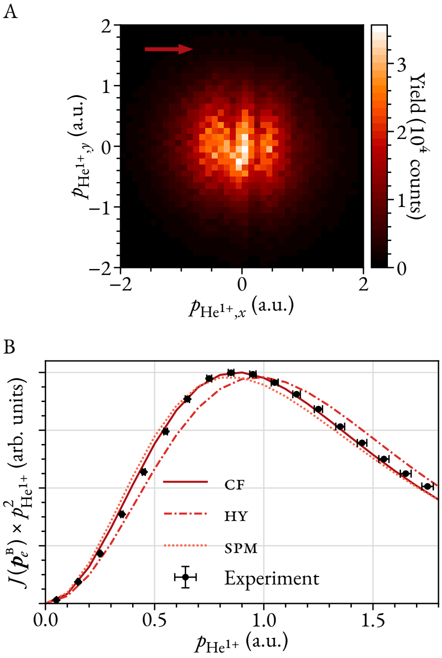

Figure 7.3: Momentum distribution of He^{1+} ions produced by Compton scattering at helium with $\hbar\omega = 40\,\mathrm{keV}$. A, Projection of the He^{1+} ion momentum onto the xy plane. The arrow in the top-left corner indicates the direction of the incident light. B, Comparison of He^{1+} momentum magnitude and theoretical predictions. The curves are based on Equation (7.18) with different initial helium ground-state wave functions. The experimental data is normalized to the integral of the solid line. The horizontal error bars are based on a 1.5% uncertainty due to the helium momentum calibration, the vertical error bars are the standard statistical error and are smaller than the dot size. The vertical stripes in A are an artifact of the ion detector and carry no physical meaning. (B adapted from [Kir22].)

the Compton profile in terms of the ion momentum distribution is

$$J(\boldsymbol{p}_e^{\mathrm{B}}) = \int \frac{\mathrm{d}^3 \boldsymbol{p}_{\mathrm{He}^{2+}}}{(2\pi)^3} \left| \Psi_i(-\boldsymbol{p}_e^{\mathrm{B}} - \boldsymbol{p}_{\mathrm{He}^{2+}}, \boldsymbol{p}_e^{\mathrm{B}}) \right|^2 , \tag{7.18}$$

and the helium nucleus momentum profile—that is, the two-electron ground state momentum distribution—is

$$J(\boldsymbol{p}_{\mathrm{He}^{2+}}) = \int \frac{\mathrm{d}^3 \boldsymbol{p}_e^{\mathrm{B}}}{(2\pi)^3} \left| \Psi_i(-\boldsymbol{p}_e^{\mathrm{B}} - \boldsymbol{p}_{\mathrm{He}^{2+}}, \boldsymbol{p}_e^{\mathrm{B}}) \right|^2 . \tag{7.19}$$

The aforementioned three different wave functions (CF, HY, and SPM) were chosen to calculate the momentum distributions of Equations (7.18) and (7.19). The results are presented in the following section.

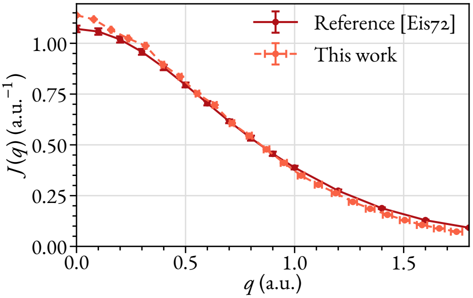

FIGURE 7.4: Comparison of Compton profiles [Equation (7.1)] obtained from the literature [Eis72] and measured in this work. The error bars of this work are the same as in Figure 7.3. The data of this work is normalized to the integral of the data from the literature.

7.2 COMPARISON OF EXPERIMENTAL DATA WITH THEORETICAL CALCULATIONS

Single ionization of helium is a well-understood process. Hence, the comparison of the momentum profiles given by Equation (7.18) and the respective experimental data are a good benchmark to check the validity of the measurement. The comparison is shown in Figure 7.3B while the momentum distribution of the He^{1+} ions in the xy plane are shown in Panel A of the figure. The vertical stripes are detection inefficiencies of the microchannel-plate detector caused by the calibration measurement. The horizontal error bars in Figure 7.3B do not correspond to the statistical standard error, but are a result of the helium momentum calibration. An ion collision experiment was used to calibrate the detector: an ion beam (instead of a photon beam) was crossed with the gas jet to create discrete and detectable helium ion momenta. The uncertainty of the longitudinal momentum of ions within the projectile beam results in an uncertainty of the momentum calibration of about 1.5%. This uncertainty corresponds to a compression or stretch of He^{1+} momenta. The details of the calibration measurements are discussed in Section 7.B.

Within the error bars, the agreement of experimental data and theoretical predictions in Figure 7.3B is excellent. One can also see that the calculations with the “best” ground-state wave function—that is, the wave function with the highest degree of electron-electron correlations—has the best agreement with the experimental data, hinting at the importance of a sophisticated treatment of the electronic ground-state in helium to get proper predictions for the electron momentum distributions.

These findings are, however, not the main focus of this work. The measurement of the one-electron Compton profile has been done before, for example, already by DuMond and Kirkpatrick in 1937 [DuM37] or by Eisenberger and Reed in 1972 [Eis72]. Figure 7.4 shows the results obtained in this work with the measurements of Eisenberger and Reed. Note that in Equations (7.18) and (7.19), the momentum profile is calculated in dependence of the full three-dimensional momentum, whereas the distributions shown in Figure 7.4 only compare the momentum profile with respect to one momentum component, namely the momentum component parallel to the incoming light axis. In this work, the incoming light is along the x axis of the laboratory frame. The data shown in Figure 7.4, however, is the y component of the He^{1+} momentum. Since the momentum distribution of a helium $1s$ electron is isotropic, the distributions along x and y are identical. Comparison with the y component was chosen, since for the x component, the detector artifacts visible in Figure 7.3A cause intensity drops in the distribution which carry no physical meaning.

However, to the best of my knowledge, a differential observation of the two-electron ground-state momentum distribution for helium double ionization by Compton scattering cannot be found in the literature. Using Compton scattering to probe the two-electron ground state has advantages over other means of ionization. Conceptually, collision experiments with charged particles (such as ions or electrons) have the advantage of much higher cross sections compared to Compton scattering. For instance, typical ion-atom collision experiments have cross sections of about 10^{-17} cm^2, compared to typical Compton scattering experiments with cross sections of about 10^{-24} cm^2 (compare Figure 6.6, Page 89). However, the final state is always influenced by the projectile charge. This *post-collision interaction* often masks the fingerprint of the ground-state wave function on the final-state observables. Collision experiments using neutrons as projectiles circumvent this problem, but neutrons create other experimental challenges (such as the inability to manipulate neutron beams with electric or magnetic fields). Ionization by photoabsorption does not have post-collision interaction effects due to a projectile charge. However, photoabsorption does not give an unbiased sampling of the full momentum distribution of the probed electron. Photoabsorption preferably selects that part of the electronic wave function which matches the final momentum of the photoelectron.

Analogously to Figure 7.3B, Figure 7.5A shows the momentum distribution of He^{2+} ions and compares the experimental data to the calculations given by Equation (7.19). The momentum profile of the He^{2+} ions match closely the helium-nucleus momentum profile. This means that the momentum of the ground-state helium nucleus is unaltered by Compton scattering one-photon-double-ionization processes: The helium nucleus is to a very good approximation only a spectator of the photon-electron interaction.

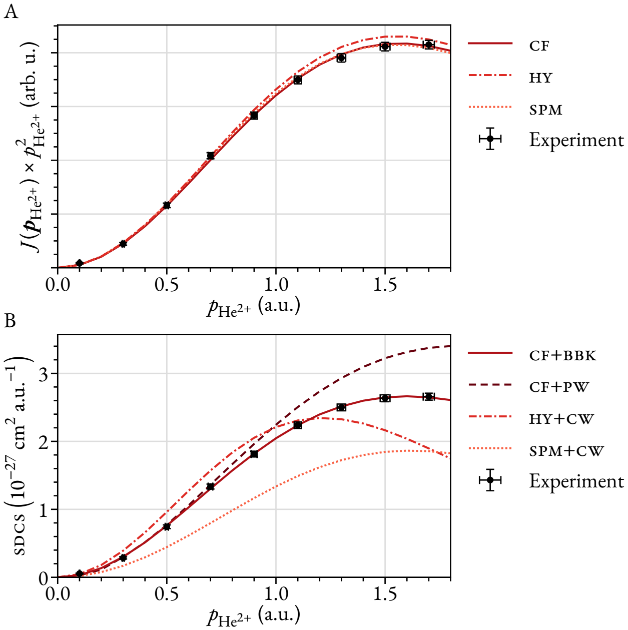

Figure 7.5: Momentum distribution of He^{2+} ions produced by Compton scattering with $\hbar\omega = 40\,\mathrm{keV}$. A, Comparison of experimental data (points) with theoretical calculations based on Equation (7.19) (lines) for different initial ground-state wave functions. B, Comparison of experimental data (points) with different sets of initial ground-state and final-state wave functions (see Page 113 for an explanation of the abbreviations). In both panels, the experimental data is normalized to the integral of the solid line. The vertical error bars correspond to the standard statistical error, the horizontal error bars are a result of the uncertainty of the momentum calibration. (Adapted from [Kir22].)

This may be surprising in the light of previous literature. For example, Shi and Lin investigate double photoionization of helium and find a dependence of the shakeoff probability on the initial-state momentum of the electron in the ground state [Shi02]. This effectively results in different asymptotic ratios of double to single ionization for Compton scattering and photoionization in the high-energy limit [Åbe70; Spi95], since Compton scattering and photoionization probe the electron momentum distribution differently. Compton scattering probes the distribution uniformly, whereas photoionization in the high-energy limit selects larger momenta of the distribution. Intuitively, a dependence of the shakeoff probability on the initial-state electron momentum suggests a dependence of the nucleus momentum distribution thereof.

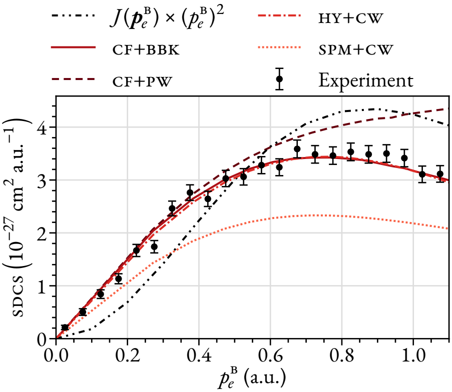

Figure 7.6: Momentum distribution of low-energy electrons produced by helium double ionization by Compton scattering with $\hbar\omega = 40$ keV. For an explanation of the abbreviations, the reader is referred to Page 113. The experimental data is normalized to the integral of the solid line. The error bars are the standard statistical error. The dash-dot-dotted line is the momentum distribution of the bound electron and correspond to Equation (7.18), Page 114. (Adapted from [Kir22].)

However, one has to consider two facts: the aforementioned uniform probing of electron momenta by Compton scattering and the dependence of the helium-nucleus momentum on the sum of both electrons in the ground state. This is also apparent in the Feynman diagrams for Compton-scattering one-photon double ionization (Figure 7.1, Page 108), where no lines for the helium nucleus are present.

Figure 7.5B shows a comparison of theoretical calculations with the experiment for different combinations of initial- and final-state wave functions. The calculations labeled "CF+BBK" show excellent agreement with the experimental data. Note that the data shown in both panels of Figure 7.5 are the same. All other sets of calculations have a smaller degree of correlation in the initial or the final state (or in both), and clearly generate results of different shape than the CF+BBK calculations. This shows that for helium double ionization by Compton scattering with $\hbar\omega = 40$ keV, the inclusion of electron-electron correlation in the initial *and* in the final states is necessary to accurately describe the process.

So far, only the imprint of electron momenta onto the nucleus were investigated. In the following, the electron momenta will be discussed directly. Figure 7.6 shows the momentum distribution of the measured electrons, that is, electrons with $p_e^B < 1.1$ a.u. Again, there is excellent agreement of the experimental data and the theoretical calculations using CF initial and BBK final states. Also overlapped in the figure is the Compton profile [Equation (7.18), Page 114; which is the same as the solid line in Figure 7.3, Page 114]. The Compton profile describes the momentum distribution of the electron in the helium ground state. Figure 7.6 shows that the measured electron momentum p_e^B is significantly smaller than the ground-state momentum distribution. This is expected, since the majority of the electrons of the distribution shown in Figure 7.6 result from the shakeoff or the knockout process, and for both processes, small energy transfers onto the secondary electron are favored. The electrons are mostly shakeoff or knockout electrons, since, following the Klein-Nishina cross section, only about 3% of the scattered photons contribute to reactions where the Compton electrons are indistinguishable in energy from shakeoff or knockout processes. To be indistinguishable, both electrons of the helium-double-ionization reaction need to have momenta below 1.1 a.u. For this to occur, the maximum energy transfer allowed is 111 eV, that is, the double-ionization threshold (79 eV) plus the energy corresponding to two electrons with $p_e = 1.1$ a.u. (2×16 eV). The maximum photon scattering angle to fulfill this condition is about 15°, corresponding to the aforementioned 3% of total scattering events. This is the motivation of the label p_e^{B} (as opposed to p_e^{A}) of the x axis. Electron A is the (allegedly) "first"—that is, Compton—electron. Then, Electron B is the knockout or the shakeoff electron. However, given the considerations above, for small photon scattering angles, this label is arbitrary.

In Figure 7.6, the dashed curve labeled "CF+PW" corresponds to calculations where no final-state electron-electron correlations are considered. This effectively "disables" the knockout mechanism. The dashed curve shows increasing discrepancies for large electron momenta, agreeing with findings of Knapp et al. [Kna02b]. There, the authors induced helium double ionization with photoabsorption in an energy regime where both the shakeoff and the knockout mechanisms have significant contributions. They find that the exclusion of the knockout mechanism in the theoretical considerations results in discrepancies between measured and predicted electron angular distributions.

Of further interest are the angular distributions of the measured low-energy electron. The investigated angle θ_e is defined by

$$\cos\theta_e = \frac{p_{e,x}^{\mathrm{B}}}{p_e^{\mathrm{B}}}\,, \tag{7.20}$$

that is, θ_e is the polar angle around the incoming light axis. The experimental angular distribution is shown in Figure 7.7 by the dots. There, an almost isotropic distribution is visible. The intensity is increased in forward direction. The electron distribution is integrated over electron momenta from 0.1 to 1.1 a.u. The lower bound is necessary, since the angular resolution for electrons with small momenta tends to infinity.

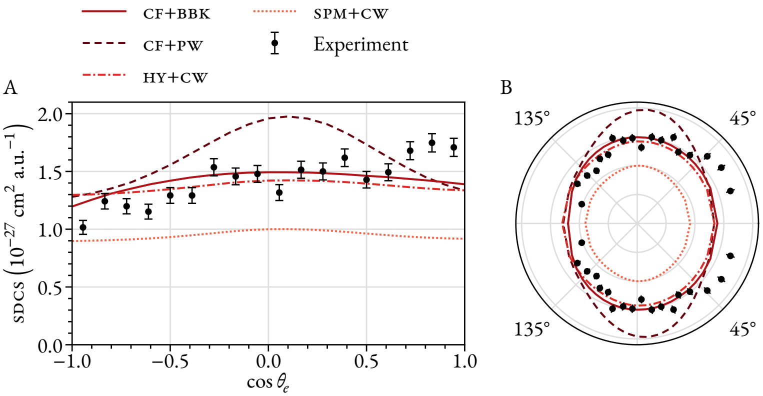

Figure 7.7: Angular distribution of low-energy electrons produced by helium double ionization by Compton scattering with $\hbar\omega$ = 40 keV. A, Comparison of the singly differential cross section of the experiment (points) and the theoretical predictions (lines). The data is normalized to the integral of the solid line. The error bars are the standard statistical error. The experimental data is integrated over electron momentum magnitudes from 0.1 to 1.1 a.u. B, Same as A, but in polar representation. The data is horizontally mirrored. (A adapted from [Kir22].)

For small scattering angles where the Compton electrons are indistinguishable from knockout or shakeoff electrons, the momentum transfer $\boldsymbol{Q}$ is almost perpendicular to the incoming photon direction. This explains the origin of the peak of the dashed line of Figure 7.7. The dashed curve results from calculations using a plane wave in the final state for the faster electron, that is, no electron-electron or electron-nucleus correlations are considered. However, these correlations distribute the electrons that would contribute to the peak in angle, as was shown by the findings of, for example, Wehlitz et al. and Knapp et al. [Weh91; Kna02a]. In their one-photon-double-ionization experiments, the authors find that low-energy electrons are not distributed strongly along the polarization axis of the photon. Therefore, they were distributed due to interactions with the second electron.

The best calculations (CF+BBK) do not explain the increased intensity of the measured distribution in forward direction. One possible explanation is an increased detection efficiency if both electrons have low energy. If the Compton electron is of high energy, it does not reach the electron detector, thus only one electron can be detected. However, if both the Compton and knockout/shakeoff electrons are low in energy, two electrons can be detected, doubling the detection efficiency. Since Compton electrons are always

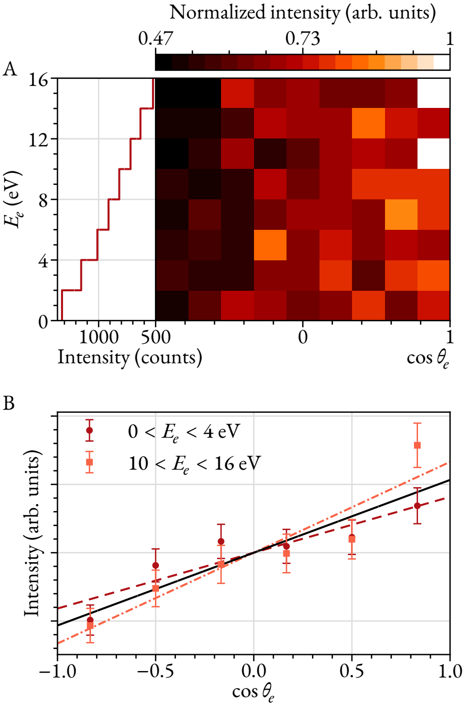

Figure 7.8: Angular distributions for different electron energies for electrons produced by Compton scattering at helium with $\hbar\omega = 40$ keV. A, Electron angular distribution versus electron energy, where each row of bins is normalized to the integral of its total counts, that is, the value of the respective bin in the (vertical) histogram to the left. B, Electron angular distribution for two energy gates. The dashed line is a linear fit of the round dots, the dash-dotted line of the squared dots, and the solid line of the experimental data shown in Figure 7.7. The error bars correspond to the standard statistical error.

forward directed, and since this fact is not accounted for in the theoretical calculations, it gives a possible explanation for the discrepancy of the CF+BBK curve and the experimental data.

Figure 7.8 shows the electron angular distribution in dependence of the electron energy. In Panel A, each row is normalized such that the integral of each row is one, that is, each row is divided by the value of the corresponding bin of the vertical histogram on the left. The two-dimensional histogram shows the forward trend persisting throughout all electron energies. In Figure 7.8B, two electron angular distributions with different energy gates are shown. Also shown is a linear fit of the data points, visualizing the strength of the forward trend. It increases for higher electron energies. This supports the argument that it may originate from Compton electrons, since those have an increasing forward trend for bigger scattering angles, that is, larger electron energies.

7.A IN- AND OUT-COUPLING OF THE SYNCHROTRON BEAM

At photon energies of several tens of kiloelectronvolts, it is not necessary to directly attach the vacuum components of the beam line and the COLTRIMS chamber to each other. Instead, the photon beam enters the experimental hutch through a beryllium window into air. At either end of the COLTRIMS setup another beryllium window is attached. The photon beam enters and exits the COLTRIMS setup through these windows. Preferably, the beryllium windows are mounted at great distance to the reaction chamber to ensure that no electrons created by photons scattering off the windows are able to enter the reaction chamber, where, with a low probability, they could be detected by the electron detector or lead to the emission of secondary electrons which could be detected as well. To ensure that only the primary synchrotron beam enters the chamber, lead shielding with a 1 mm hole at the appropriate position was installed directly in front (behind) of the beryllium entry (exit) window.

The energy of a 40 keV photon is high enough to penetrate the chamber walls (see Figure 7.9) and directly trigger the microchannel-plate detector. As a consequence, it is necessary to shield the detectors sufficiently from stray light. For this, the chamber was wrapped in about 1 mm thick lead sheets. Additionally, collimators are installed before and after the reaction chamber to cut out stray light that would otherwise hit the spectrometer copper plates. Figure 7.10 shows a photon time-of-flight spectrum, that is, the ion-detector microchannel-plate signal in reference to the bunchmarker signal of the beam line. The dashed lines show various objects where a photon can scatter at, causing respective times-of-flight of a photon. For instance, a photon scattering at the hutch entrance directly towards the ion detector has the shortest distance to travel (marked as reference in Figure 7.10 with a time-of-flight of

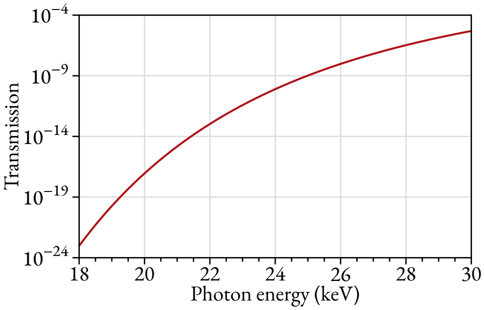

FIGURE 7.9: Transmission of x rays through 2 mm iron. Data based on Reference [Hen93].

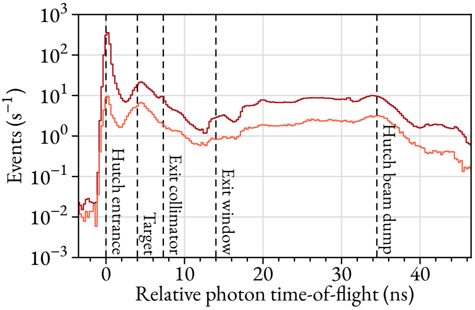

FIGURE 7.10: Photon time-of-flight spectrum. The x axis shows the relative time-of-flight, that is, the difference compared to the most direct path from hutch entrance to ion detector. The upper red curve shows the spectrum without lead shielding, the lower orange curve with shielding.

0 ns), while a photon entering and exiting the reaction chamber and finally back-scattering at the beam dump at the end of the hutch towards the ion detector has the longest time-of-flight. Various peaks in the time-of-flight spectrum can be identified with physical objects of the experimental setup. Shielding the detectors using the lead sheets and adjusting the collimators reduces the background events caused by direct photon detection by several orders of magnitudes (compare upper-red and lower-orange curves in Figure 7.10).

7.B CALIBRATION

The momentum-zero position on the detector is arbitrary, hence, a calibration is necessary. As a reminder, the laboratory frame is defined such that the initial photon beam is along the x component, the direction of the supersonic gas target is along the y component, and the z component points towards the ion detector, forming a right-handed coordinate system.

Compton scattering does not break symmetry in the yz plane, thus, in this plane, the electron and ion momentum distributions have to be mirror symmetric. This symmetry does not exist in the x direction. The momentum transfer always points in the forward direction, subsequently breaking the forward/backward symmetry. In x direction, the He^{1+} and He^{2+} ions are only centered around momentum-zero if they are truly a spectator in the photon-electron interaction. An example of experimental parameters where this is not the case was discussed in the previous Chapter 6. However, for single ionization at high photon energies as used in the present experiment, it is known that this assumption holds true [Sam94; Spi95]. Thus, the He^{1+} ion momentum distribution is centered around zero for all components, respectively.

For experiments with helium, typically, ionization by photoabsorption is used to calibrate the ion detector, as was done, for instance, for the low-energy Compton scattering experiment (see Section 6.a on Page 101). However, beam line id31 of the esrf cannot produce low photon energies to create helium ions with small-enough momenta to be measured by the utilized coltrims setup.

Because of this, an unconventional calibration method was used.

Instead of using the photon beam provided by beam line id31 for calibration, an ion-projectile beam produced by a Penning ion source was used. For this, the experimental setup was changed between the calibration measurement and the Compton-scattering measurement. For the calibration setup, the ion source was attached to the coltrims reaction chamber. Downstream the coltrims reaction chamber, He^{1+} ions and He^{0} atoms were detected with a microchannel-plate delay-line-anode detector. Note that the projectile ions and atoms trigger the microchannel-plate since the energy of the projectile is large enough. After the calibration was performed, the setup was changed. The ion source as well as the projectile-ion detector were detached from the coltrims reaction chamber and replaced with beryllium windows, respectively, used for in- and out-coupling of the synchrotron photon beam. In the setup for the Compton scattering measurement, the direction of the incoming photon beam is the opposite of the direction of the ion beam used in the calibration setup.

The single and double capture processes

$$\mathrm{He}_{\mathrm{P}}^{2+} + \mathrm{He}^{0} \rightarrow \mathrm{He}_{\mathrm{P}}^{1+} + \mathrm{He}_{\mathrm{R}}^{1+} \,, \tag{7.21}$$

$$\mathrm{He}_{\mathrm{P}}^{2+} + \mathrm{He}^{0} \rightarrow \mathrm{He}_{\mathrm{P}}^{0} + \mathrm{He}_{\mathrm{R}}^{2+} \tag{7.22}$$

produce He^{1+} and He^{2+} ions with well-defined momenta in projectile direction, respectively. Subscript P indicates the projectile ion, measured by the projectile detector; subscript R indicates the recoil ion, measured by the ion detector of the coltrims spectrometer. For projectile energies, 10 and 25 keV were chosen.

Figure 7.11 shows the x-detection position of the ion detector. For single capture, three capture lines were identified and used for calibration, for double capture, two lines are identified. They are marked in Panels a and b of the figure. The x component of the ion momentum is well-defined and can be calculated using

$$p_{\mathrm{capture},x} = -\frac{Q_c}{v_{\mathrm{P}}} - n\frac{v_{\mathrm{P}} m_e}{2} \,, \tag{7.23}$$

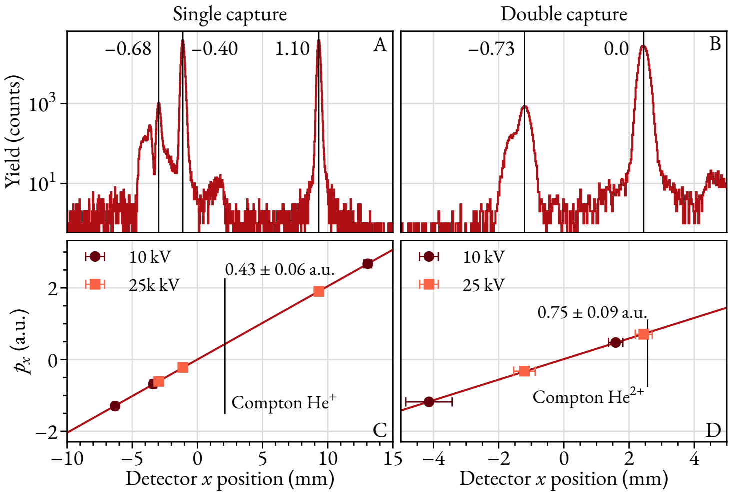

FIGURE 7.11: Calibration of the ion momentum x component for the single and the double capture process. A,B, Histogram of x-position hits on the ion detector for single and double capture, respectively, for the projectile energy of 25 keV. The vertical lines correspond to the square dots in the panels below and are the result of a gaussian fit. The numbers next to the vertical lines are the corresponding Q_c values in a.u. C,D, x position versus the expected ion momentum. The solid line is a linear fit $m(x\text{-position}) + b$ of the data points. The horizontal error bars are the full-width-half-maximum of the Gaussian fits in the upper panels. See main text for an explanation of the vertical lines. The value next to the vertical line is the y value at which it intersects with the linear fit.

with the projectile velocity v_P and the number of captured electrons n. It is solely determined by the change of the kinetic energy of the projectile ion [Scho6]. The Q_c value depends on the reaction and is determined by the energy levels of the target atom and the projectile ion, that is,

$$Q_c = (B^i_\mathrm{P} + B^i_\mathrm{R}) - (B^f_\mathrm{P} + B^f_\mathrm{R}) \,, \tag{7.24}$$

where $B^{i/f}_{\mathrm{P/R}}$ are the initial and final binding energies of the projectile and recoil ion, respectively. The first term of Equation (7.23) corresponds to the momentum change of the projectile ion due to the difference in binding energies, the second term corresponds to the energy needed to accelerate the captured electrons to projectile velocities.

The expected momenta corresponding to the Q_c-values are shown in Figures 7.11C and 7.11D as the y value. There, the x shift and x stretch of the ion detector were chosen such that the data in Panels C and D are linear, and the connecting line passes through the coordinate origin. (Note that this results in different shifts and stretches for double and single ionization, respectively.) A linear fit $m \times (x\text{-position}) + b$ was performed to confirm the linearity. The fit in Figure 7.11c yields ($m = 0.2043 \pm 0.0004$) a.u./mm and $b = (0.0027 \pm 0.0031)$ a.u., and $m = (0.287 \pm 0.002)$ a.u./mm and ($b = 0.014 \pm 0.006$) a.u. for Panel d. Note that the slope for double capture is $\sqrt{2}$ times larger than for single capture not by chance, but because the time-of-flight—and subsequently, the detection position of the ion—scales with the square root of its charge-to-mass ratio.

Also shown in Figures 7.11c and 7.11d are vertical lines corresponding to the position of the He^{1+} and He^{2+} ions produced by Compton scattering, that is, with the changed experimental setup. Following the considerations at the beginning of this section, the offset from zero is unexpected. Using the x shift resulting from the calibration measurements, the x position of the Compton He^{1+} ions is centered not around zero, but around 2.11 mm. This corresponds to ion momenta centered around 0.43 a.u., which is the intersection of the He^{1+} ion x position with the linear fit in Figure 7.11c. Analogously, in Panel d, the position of the He^{2+} is marked as well as the intersection with the linear fit.

This shift was attributed to an unwanted and uncontrolled change of the detector position between the ion beam and photon beam measurements. However, there are no physical reasons for the He^{1+} ion momentum not to be centered around zero. For this reason, for both helium single and double ionization, the unexplained shift was compensated in x direction by −2.11 mm.

The resulting ion momenta for double and single ionization of helium by Compton scattering are shown in Figure 7.12. Note that in Panels d to f the ion was measured in coincidence with one electron, while in Panels a to c, no coincidence with electrons was required, explaining the significant difference in collected statistics. The vertical lines visible in Panels a and b (as well as weakly in d and e) are detection inefficiencies resulting from the calibration measurements.

* * *

The calibration setup also allowed for electron momentum calibration and consequently, the calibration of the electric and magnetic field. The reaction

$$\mathrm{He}_{\mathrm{P}}^{2+}\,(20\,\mathrm{keV}) + \mathrm{Ne} \rightarrow \mathrm{He}_{\mathrm{P}}^{1+} + \mathrm{Ne}^{2+} + e^{-} \tag{7.25}$$

was measured. Here, the $\mathrm{He}_{\mathrm{P}}^{2+}$ projectile captures one electron of an inner shell of the neon target atom, which subsequently autoionizes, that is, it emits

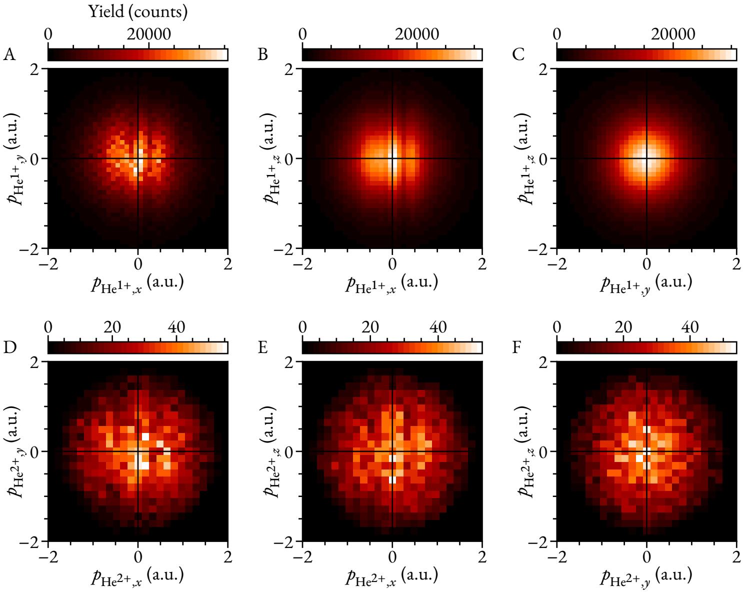

FIGURE 7.12: He^{1+} (A–C) and He^{2+} (D–F) ion momenta produced by Compton scattering at helium with $\hbar\omega = 40$ keV.

FIGURE 7.13: Electron momenta resulting from of neon autoionization and neon transfer ionization induced by Reaction (7.25). The arrow in the upper left corner indicates the direction of the $\mathrm{He}_\mathrm{p}^{2+}$ projectile beam.

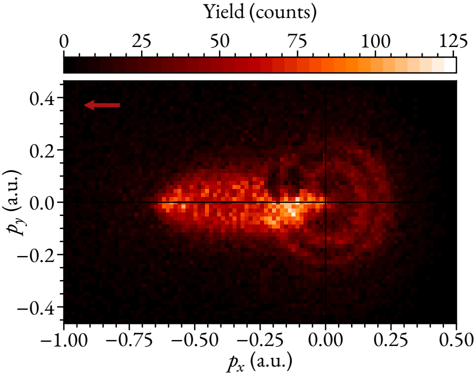

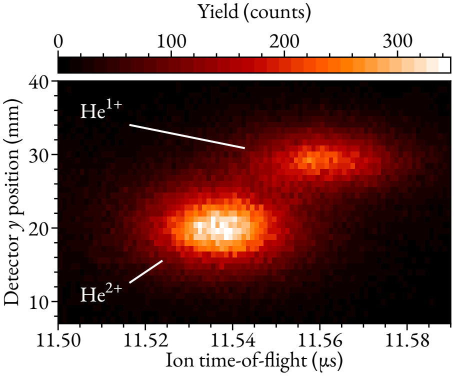

FIGURE 7.14: y-fish spectrum for helium double ionization by Compton scattering with $\hbar\omega = 40$ keV. The increased intensity labeled "He^{1+}" is background produced by singly ionized helium ions which are detected in coincidence with a background electron.

an electron with discreet energy. Figure 7.13 shows the electron momenta of Reaction (7.25). The rings correspond to electrons emitted due to the autoionizing process. The feature extending from $-0.75 < p_x < 0$ a.u. is the result of neon transfer ionization resulting from soft collisions between projectile and target. There, one electron of the neon is captured by the $\mathrm{He}_\mathrm{p}^{2+}$ projectile, while a second one is ionized.

A thorough discussion of capture and transfer ionization processes can be found in References [Schoo; Scho6].

7.C ION AND ELECTRON MOMENTUM GATES

As described more extensively in Section 5.1 on Page 69, the ion time-of-flight is calculated in reference to the detected electron. The time-of-flight of the electron is calculated in reference to the bunch-marker signal of the beam line. If a background-electron—that is, an electron not originating from the the interaction of gas-target helium and a synchrotron photon—is detected, its time-of-flight is still calculated in reference to a bunchmarker, however, a random one. Now, if a helium ion is detected in coincidence with that background-electron, a "false" time-of-flight for the helium ion will be calculated. Even so the helium ion may have resulted from a valid reaction of photon and target, its calculated time-of-flight does not correspond to a meaningful momentum p_z. This results in background data, which is repeated periodically in time with the bunchmarker spacing. In this experiment, the mean time-of-flight for He^{1+} and He^{2+} ions were 16.31 μs and 11.54 μs, respectively. The bunchmarker spacing of the beam line was 176 ns. The modulo of the He^{1+} and He^{2+} times-of-flight with the bunchmarker spacing

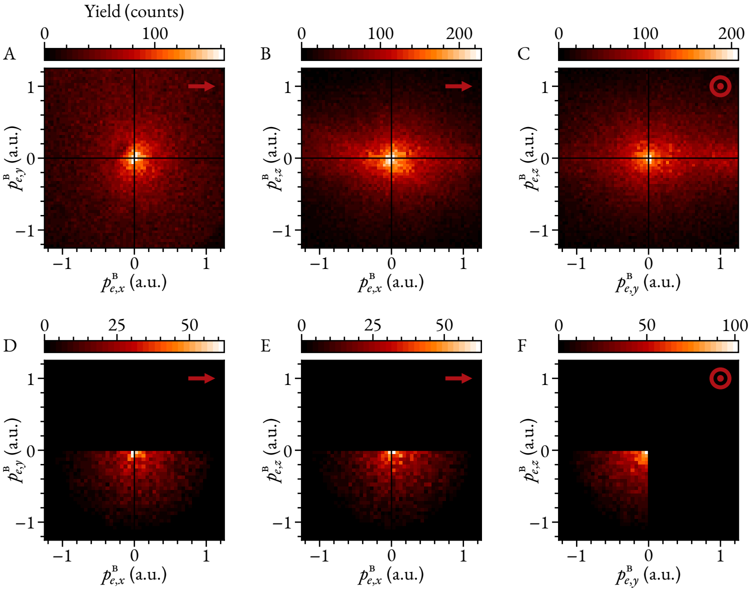

FIGURE 7.15: Measured electron momenta for helium double ionization by Compton scattering with $\hbar\omega = 40$ keV. A–C, Electron momenta of electrons measured in coincidence with He^{2+} ions without any further momentum gates. D–F, Electron momenta after the gates listed in Equation (7.26) were applied. The direction of the incoming photons are indicated in the upper-left corner of each panel, respectively.

overlap. Further, a spatial overlap between the two charge states was present (see Figure 7.14). This problem is avoidable by altering the electric field of the spectrometer slightly while observing the times-of-flight of the ions until the periodic background of the different charge states do not overlap. For this experiment, however, this was not an option, since the electric field was calibrated using an ion-collision process—that is, not using the synchrotron light of beam line ID31—and hence, the ion time-of-flight calculation did not include the bunchmarker signal of the beam line.

The measured electron momenta are shown in Figure 7.15. In the upper-left quadrant of Figure 7.15A, a detection inefficiency of the microchannel-plate detector is visible. Thus, electron momenta within the upper-half-plane were removed. This is viable, since Compton scattering is isotropic around the incoming light axis—here, the yz plane of the laboratory frame. Because of this, the z component of the electron momentum can also be, and was, restricted. A constant background of false electron momenta becomes quadratically more dramatic for larger momentum magnitudes. Thus, the total electron momentum magnitudes were restricted. The final gates were

$$p^{\mathrm{B}}_{e,y} \leq 0\,\text{a.u.}, \quad p^{\mathrm{B}}_{e,z} \leq 0\,\text{a.u.}, \quad p^{\mathrm{B}}_{e} \leq 1.1\,\text{a.u.} \tag{7.26}$$

7.D EXPERIMENTAL PARAMETERS

For a more general description of the ensuing components, see Section 4.2. A summary of the experimental parameters is given in Table 7.1. The ion beam line of the calibration setup is sketched in Figure 7.16. A sketch of the spectrometer setup as a whole is given in Figure 7.17, while a detailed sketch of the spectrometer is given in Figure 7.18. The used COLTRIMS setup was modified from the setup described in Reference [Kas14].

The observations presented in this chapter required good momentum resolution of the helium ions. For this, an electrostatic lens and a time-of-flight-focusing geometry was employed for the ion arm of the spectrometer. This extended its length beyond the reaction chamber height. To achieve this experimental setup, the upper and lower part of the spectrometer had to be separable. The ion arm consisted of an acceleration region ending with the electrostatic lens which transitioned into the drift region. The field-free drift region was created using an aluminum tube with an inner diameter of 105 mm and an outer diameter of 110 mm that was separable from the main spectrometer. For this, the copper plates of the main spectrometer were mounted on stainless steel rods which were mounted on a CF300-to-CF250 adapter flange. The aluminum drift tube was placed at the end of the main spectrometer and housed within CF250 vacuum tubes. An 80 mm MCP with delay-line anode detector was mounted at the end of the drift tube. The ions did not gain enough energy in the acceleration region of the spectrometer which is why they had to be further accelerated to efficiently trigger the MCP. To separate the acceleration field from the drift region, a fine metal mesh with a transmission of 78% was placed at the end of the drift tube and in front of the MCP.

The electron arm of the spectrometer consisted of an acceleration and a drift region to achieve time-of-flight focusing as well. A 120 mm MCP was employed for electron detection. The drift region was separated using a 78%-transmission metallic mesh. Another mesh with the same transmission was placed between the end of the spectrometer and the MCP for the same reasons as in the ion arm.

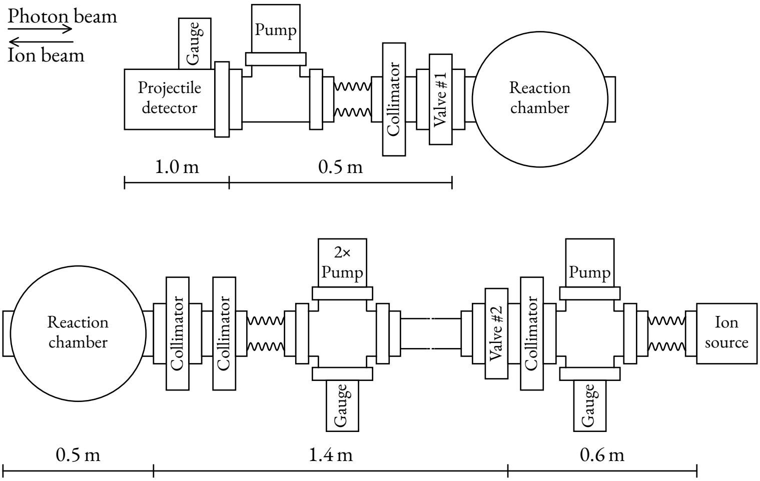

Figure 7.16: Calibration setup of the beam time in April 2018 at beam line ID31 of the ESRF, Grenoble France. For the measurement setup with synchrotron light, Valve #1 and Valve #2 were closed and vacuum tubes with attached beryllium windows were installed. Note that the improved experimental setup of the following beam time resulted in much fewer background events (see Figure 8.11, Page 152).

Steerer plates to manipulate the ion beam during the calibration measurements were installed in front and behind the spectrometer. An up/down steerer is placed in front of the spectrometer to clean the initial ion beam. It removes projectiles that changed charge states due to interaction with the residual gas of the projectile beam line from the ion beam. The left/right steerer after the spectrometer analyzes the projectile by steering different projectile charge states onto different spots of the projectile detector.

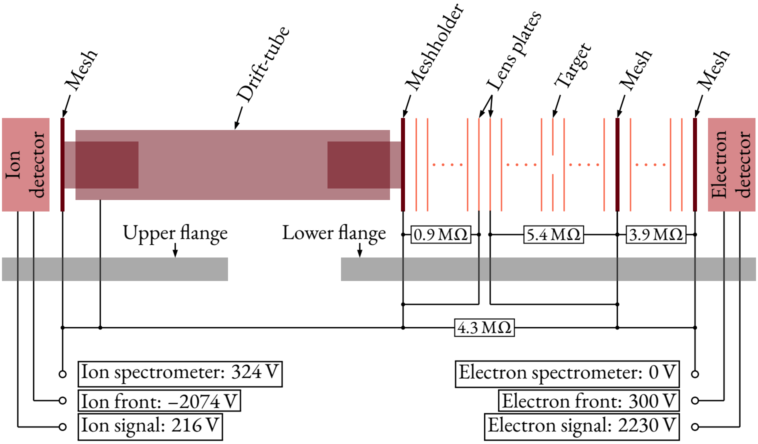

Figure 7.17: Sketch of the spectrometer setup of the beam time in April 2018 at beam line ID31 of the ESRF, Grenoble. The resistances drawn directly below the copper plates are the combined resistances of 100 kΩ connecting each subsequent copper plate.

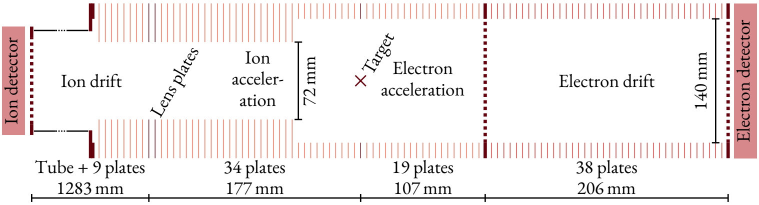

Figure 7.18: Detailed sketch of the spectrometer of the beam time in April 2018 at beam line ID31 of the ESRF, Grenoble France. The number of plates drawn corresponds to the actual numbers of plates mounted in the spectrometer. Note that in actuality, the ion drift tube is longer than the spectrometer section with copper plates.

Table 7.1: Experimental parameters of the experimental run of the beam time in April 2018 at beam line ID31 of the ESRF, Grenoble, France.

Target			
Driving pressure	42 bar	Nozzle diameter	60 μm
Width at interaction point	≈ 1 mm		(calculated 45 μm)
Temperature	300 K	Target gas	helium
Expansion vacuum	4.6×10^{-3} mbar	Jetdump vacuum	1.3×10^{-7} mbar
Beam line			
Photon energy E_γ	40 keV	Polarization	99% horizontal
$\Delta E_\gamma / E_\gamma$	1.1%	Focus size	0.4×0.1 mm^2 (W×H)
Operation mode	16-bunch	Bunch rate	5.68 MHz
Bunch spacing	176.0375 ns	Photon flux	≈ 8.4×10^{14} photons/s
Spectrometer			
Electron arm	10.4 cm (acc.) 20.8 cm (drift)	Ion arm	17.1 cm (acc.) 128.8 cm (drift)
E-field	6.6 V/cm	Vacuum	4.5×10^{-9} mbar
B-field	6.4 Gs	Lens voltage jump	145.6 V
Voltages			
Electron detector	+300 V (front) +2230 V (signal)	Ion detector	−2074 V (front) +216 V (signal)
Spectrometer	+0 V (electron)	Helmholtz current	36.6 A
	−324 V (ion)	Correction coils	off
Detectors			
Electron	120 mm	Ion	80 mm
Electron MCP	regular	Ion MCP	regular
Rates			
Electron	20–30 kHz	Ions	1.1 kHz (trigger)
Acquisition time	120 h		

COMPTON SCATTERING IN MOLECULES 8

So far, the results of two beam times investigating the helium atom were presented; one at PETRA III, Hamburg, investigating low-energy Compton scattering and one at ESRF, Grenoble, investigating helium double ionization. Resolving the Compton process differentially is experimentally challenging, explaining the scarcity of experiments performed in such a manner and the interest in such investigations [Roy04].

Given the success of the previous measurements, a next step is to carry the investigation to more complex systems. For this work, molecular nitrogen was investigated. The experiment was carried out at the same beam line ID31, at ESRF, Grenoble, utilized in the experiment discussed in the previous Chapter 7. For the photon energy, again, 40 keV was chosen. In this chapter, the following two reactions will be discussed

$$\gamma(40\,\mathrm{keV}) + \mathrm{N}_2 \rightarrow \gamma' + \mathrm{N}_2^+(n^{-1}) + e_\mathrm{C} \quad (n > 1) \tag{8.1}$$

$$\gamma(40\,\mathrm{keV}) + \mathrm{N}_2 \rightarrow \gamma' + \mathrm{N}_2^+(1s^{-1}) + e_\mathrm{C} \rightarrow \gamma' + \mathrm{N}^+ + \mathrm{N}^+ + e_\mathrm{C} + e_\mathrm{A}\,, \tag{8.2}$$

that is, Compton scattering at a valence shell, and Compton scattering at a core shell with subsequent Auger decay. In the former reaction, the N_2^+ ion was measured in coincidence with the Compton electron e_C. In the latter, the two N^+ ions and the Auger electron e_A were measured, also in coincidence.

8.1 VALENCE-SHELL COMPTON SCATTERING

Besides the photon energy and the target sample, this reaction is in principle the same as the low-energy Compton scattering at helium experiment discussed in Chapter 6. That is, the molecular nature of N_2 is neglectable if the initial photon interacts with a valence electron. However, opposed to the low-energy analogue, at $\hbar\omega = 40\,\mathrm{keV}$ the binding energy of $\mathrm{N}_2\,(2s)$ compared to the energy transfer of the photon is (mostly) irrelevant, and (mostly) the impulse approximation is valid. Only for very small photon scattering angles—smaller than about 10°—is the energy transfer comparable to the binding energy of $\mathrm{N}_2\,(2s)$ of 37.3 eV.

Then, the interaction of photon and electron is binary, and the final electron momentum $\boldsymbol{p}_e$ is along the momentum transfer $\boldsymbol{Q} = \boldsymbol{k}_\gamma - \boldsymbol{k}'_\gamma$, that is, the difference between the incoming and the outgoing photon momen-

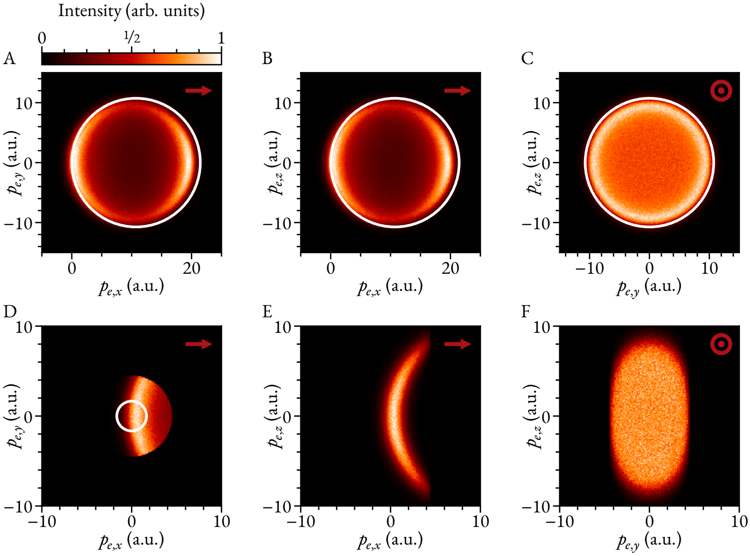

Figure 8.1: Simulated electron momenta for valence-shell Compton scattering at N_2 with $\hbar\omega = 40\,\text{keV}$. A–C, Simulation without detector cutoff. D–F, Simulation including a detector cutoff, that is, $p_{e,x}^2 + p_{e,y}^2 \leq (4.5\,\text{a.u.})^2$. The direction of the incoming photon is indicated in the upper right corner of each panel, respectively. See main text for an explanation of the circles in A–D.

tum. Ignoring that the electron is bound in N_2, this would result in electron momenta as shown in Figures 8.1a to 8.1c.

There, the final electron momenta from a binary encounter with a photon are simulated. The simulated photons scatter with a distribution given by the Klein-Nishina cross section (see Section 2.4, Page 21). The electron momentum is equal to the resulting momentum transfer. Ignoring the initial ground-state momentum distribution of the electron, the final electron momenta would be sharp. Analogously to the simulations shown for low-energy Compton scattering (see Figure 6.4, Page 82), the initial momentum distribution of the bound electron was taken into account by folding the final electron momentum distribution with a distribution given by [Abr66]—the same as has been used in Chapter 6 [Equation (6.7), Page 81]:

$$\rho_{p_0}(\boldsymbol{p}_e^i) = \frac{8p_0^5}{\pi^2} \frac{1}{\left(p_e^{i\,2} + p_0^2\right)^4}\,, \tag{8.3}$$

Here, $E_{\mathrm{bind}} = 37.3\,\mathrm{eV}$ is the binding energy of $N_2\,(2s)$. This distribution is related to the Compton profile insofar that it approximates the momentum distribution of the initial-state electron. As will be seen by the comparison of the simulation and experiment, this approximation is sufficient for a qualitative comparison.

Specifically, the simulation was performed with the following Monte-Carlo procedure: A distribution of events with electron and photon momenta was generated with a random generator such that the distribution of photon scattering angles θ_γ was given by the Klein-Nishina distribution [Equation (2.34), Page 23], the photon azimuth angle was isotropic and the electron momentum distribution resembles a microcanonical distribution as given by Equation (8.3). The final electron momentum was calculated as $\boldsymbol{p}_e = \boldsymbol{p}_e^i + \boldsymbol{Q}$. The panels in Figure 8.1 show two-dimensional histograms of two components of $\boldsymbol{p}_e$, respectively.

Without the broadening due to the initial electron momentum distribution, the final electron momenta would be perfectly situated on the surface of an almost-sphere. In the low-energy limit of Compton scattering, also referred to as Thomson scattering, it would be a perfect sphere, since there, the photon does not lose energy (in Chapter 6, this approximation was used). Then, the momentum transfer $\boldsymbol{Q}$ is solely due to the change of the photon's momentum vector direction, not its magnitude. Unlike Compton scattering with $\hbar\omega = 2.1\,\mathrm{keV}$, discussed in Chapter 6, this approximation breaks down for Compton scattering with $\hbar\omega = 40\,\mathrm{keV}$. For instance, in the case of backscattering, the photon loses about 15% of its initial energy. In this case, the maximum momentum transfer Q is not equal to twice the incoming photon momentum magnitude (as would be the case for Thomson scattering). The circles in Figures 8.1A to 8.1C emphasize this. The simulated events are clearly deviating from the circles, which correspond to a sphere with radius k_γ centered around $(x, y, z) = (k_\gamma, 0, 0)$.

The bottom row of Figure 8.1 (Panels D to F) show the same distribution as the top row with an additional detector cutoff: the momenta in the xy plane are restricted to 4.5 a.u., that is, $p_{e,x}^2 + p_{e,y}^2 \leq (4.5\ \mathrm{a.u})^2$.

The histograms in Figure 8.1 ignore—in spirit of the impulse approximation—the binding of the electron. If the energy transfer in the scattering process is smaller than the binding energy, this is obviously not viable. The circle in Figure 8.1D indicates the momentum $(2m_eE_{\mathrm{bind}})^{1/2}$ corresponding to the binding energy of $N_2\,(2s)$. Photon scattering angles of about less than 10° result in events within this circle. To take the ionization threshold

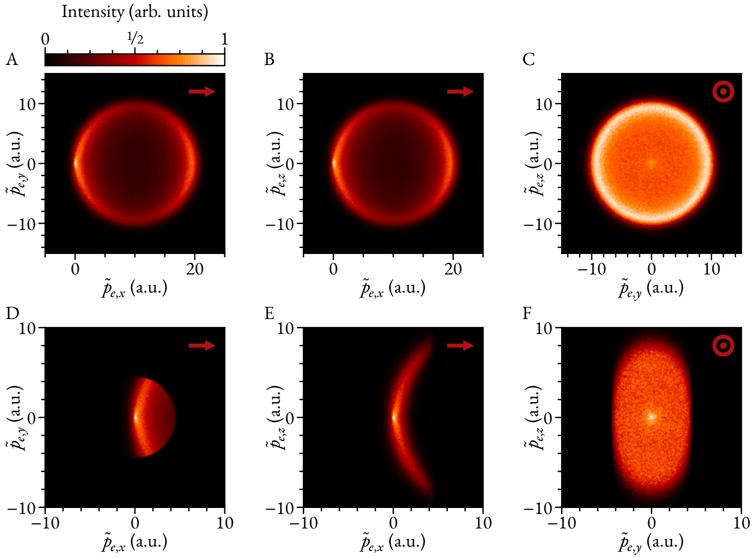

FIGURE 8.2: Same as Figure 8.1, except the effects of the binding energy of N_2 (2*s*) were taken into account.

in a first approximation into account, the electron momentum vector was modified after the interaction with the photon: The electron-momentum-vector direction and magnitude is determined using the process laid out above (that is, $\boldsymbol{p}_e = \boldsymbol{p}_e^i + \boldsymbol{Q}$). Then, the energy corresponding to the electron momentum is reduced by the binding energy and the magnitude of the corrected electron momentum $\tilde{\boldsymbol{p}}_e$ is determined, that is,

$$\tilde{p}_e = \sqrt{2 \times \left(\frac{p_e^2}{2m_e} - E_{\text{bind}} \right)}. \tag{8.4}$$

While the magnitude is reduced this way, the emission direction is kept the same.

The results thereof are shown in Figure 8.2. There, one can see a peak appearing at zero. Using the approximation of simply reducing the electron momentum magnitude, this is to be expected. With this method, all the events on the sphere indicated by the circle in Figure 8.1D are "sucked back" by the Coulomb potential of the N_2^+ ion to momentum zero, causing a spike in intensity. However, this is a flawed method of accounting for the binding energy. Given the insight gained from the low-energy Compton scattering

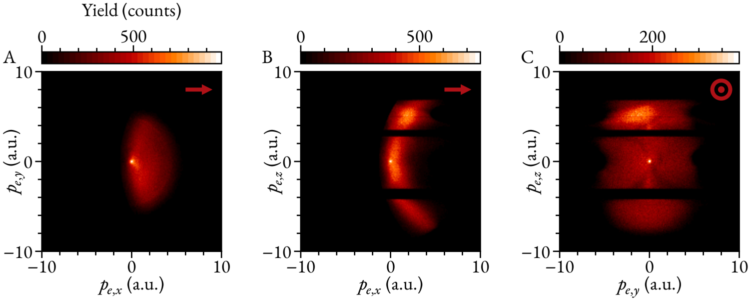

FIGURE 8.3: Two dimensional momentum distributions for electrons produced by valence-shell Compton scattering at N_2 with $\hbar\omega$ = 40 keV. The horizontal cutouts in A and B are to remove the wiggle nodes (see Section 4.2.2, Page 63). In each panel, the direction of the incoming light is indicated in the upper-right corner.

experiment discussed in Chapter 6, simply subtracting the binding energy from the electron momentum is invalid. In this low-energy-transfer regime, one cannot treat the problem simply in a billiard-type fashion, as is the case by using this approximation.

Further, by simply reducing the electron's energy by the subtraction of a constant binding energy corresponding to $N_2\,(2s)$, one treats the electron as if it is fixed at a constant position within the nitrogen molecule. However, this is invalid. In quantum mechanics, only the total energy of the electron—that is, the sum of its kinetic and potential energy—is an eigenvalue of the system. In the simulation, every electron has a fixed kinetic energy corresponding to its initial momentum $\boldsymbol{p}_e^i$. Due to Heisenberg's uncertainty principle, a fixed kinetic energy results in an uncertainty of the electron's position within the system and thus, an uncertainty of its potential energy (which depends on the electron's position). By subtracting a constant binding energy, this fact is ignored.

Despite these considerations, comparing the two simulations to the actual experimental data, one can see a strong resemblance in the qualitative features of both distributions. Figure 8.3 shows the electron momenta measured in the experiment for valence-shell Compton scattering. These distributions are very comparable to the simulation where effects of the N_2^+ Coulomb potential were ignored (Figure 8.1). However, a peak at momentum zero is visible in the experimental data. Figure 8.2 suggests that this increase in intensity of low-momentum electrons may be due to the Coulomb potential of the ion. For a definite conclusion and a more quantitative comparison, a proper theoretical treatment is necessary.

* * *

The goal of this experiment was to investigate Compton scattering in a molecular system. Compton scattering at the valence shell of N_2, however, does not result in a molecular breakup. Without a molecular breakup, the orientation of the N_2 molecule is not accessible by the COLTRIMS technique, which is why the valence-shell Compton scattering reaction channel is not investigated further. Nonetheless, the basic results shown here already point toward interesting physics. It seems that even at 40 keV photon energy, the impulse approximation breaks down for a significant portion of Compton scattering events even for ionization thresholds of only a few tens of electronvolts.

Compton scattering at the core shell results in a molecular breakup, and thus, reveals the molecular orientation. The discussion thereof follows in the next section.

8.2 CORE-SHELL COMPTON SCATTERING

Here, I will present the findings of Compton scattering at $1s$ electrons of N_2, that is, the reaction

$$\gamma(40\,\mathrm{keV}) + \mathrm{N}_2 \rightarrow \gamma' + \mathrm{N}_2^+(1s^{-1}) + e_\mathrm{C} \rightarrow \gamma' + \mathrm{N}^+ + \mathrm{N}^+ + e_\mathrm{C} + e_\mathrm{A} \quad (8.5)$$

was measured: The photon scatters at a core-shell electron of N_2, ionizing it and leaving a vacancy ($1s^{-1}$). The excited intermediate state Auger decays, emitting an Auger electron e_A. The unstable N_2^{2+} ion Coulomb explodes, resulting in two N^+ ions. Electrons with a momentum of up to 6 a.u. are measured with full solid angle. Therefore, Auger electrons (with a momentum of 4.97 a.u.) are measured with full solid angle. The Auger electrons overlap with the Compton electrons which, qualitatively, have the same distribution as the ones shown in the previous section. Both N^+ ions are measured, giving insight into the molecular orientation at reaction time via the relative momentum

$$\boldsymbol{p}_\mathrm{rel} = \frac{\boldsymbol{p}^\mathrm{A}_{\mathrm{N}^+} - \boldsymbol{p}^\mathrm{B}_{\mathrm{N}^+}}{2}\,. \quad (8.6)$$

If the N_2 molecule is not rotating quickly, the direction of $\boldsymbol{p}_\mathrm{rel}$ corresponds to the molecular axis [Web01; Zar72].

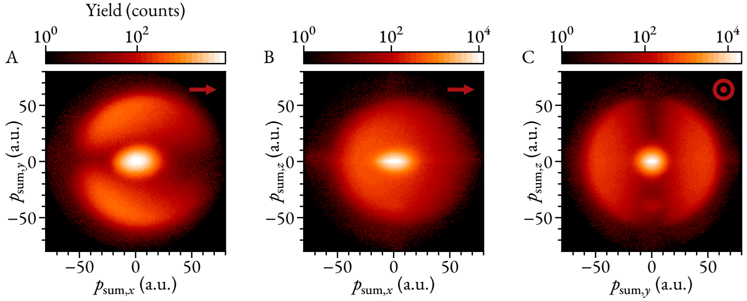

Figure 8.4: Sum momenta of two N^+ ions for core-shell photoreactions at N_2 with $\hbar\omega$ = 40 keV. Note that the color scale is logarithmic. In each panel, the direction of the incoming light is indicated in the upper-right corner.

In the Coulomb explosion of N_2^{2+}, the two N^+ ions repel each other back-to-back and, because of momentum conservation, the sum momentum

$$\boldsymbol{p}_{\mathrm{sum}} = \boldsymbol{p}_{\mathrm{N}^+}^{\mathrm{A}} + \boldsymbol{p}_{\mathrm{N}^+}^{\mathrm{B}} \tag{8.7}$$

—where $\boldsymbol{p}_{\mathrm{N}^+}^{\mathrm{A/B}}$ are measured in the center of mass system—must be zero, unless it has to balance other momenta. Within the impulse approximation the photon-electron interaction is a binary encounter. Thus, the sum momentum does not have to balance the final Compton electron momentum, but it has to balance its initial momentum. The momentum of the Auger electron, however, has to be balanced by the N^+/N^+ sum momentum.

This gives the possibility to distinguish between Compton scattering at the core shell and photoionization, that is,

$$\gamma(40\,\mathrm{keV}) + \mathrm{N}_2 \rightarrow \mathrm{N}_2^+(1s^{-1}) + e_\gamma \rightarrow \mathrm{N}^+ + \mathrm{N}^+ + e_\gamma + e_\mathrm{A}\,. \tag{8.8}$$

(Note that at 40 keV photon energy, the cross section for photoionization at the valence shell is neglectable.) Since neither the scattered photon nor most of the Compton electrons or photoelectrons are measured, Reactions (8.5) and (8.8) are indistinguishable by the reaction particles alone. However, for photoionization, the final photoelectron momentum of about 54 a.u. must be balanced by the sum momentum. By gating on the inner or outer part of the sum momentum, one can distinguish between the two reaction channels.

The sum momenta for both Compton scattering and photoionization combined are shown in Figure 8.4. Throughout the remainder of this chapter, only sum momenta with $p_{\mathrm{sum}} \leq 15$ a.u. are considered.

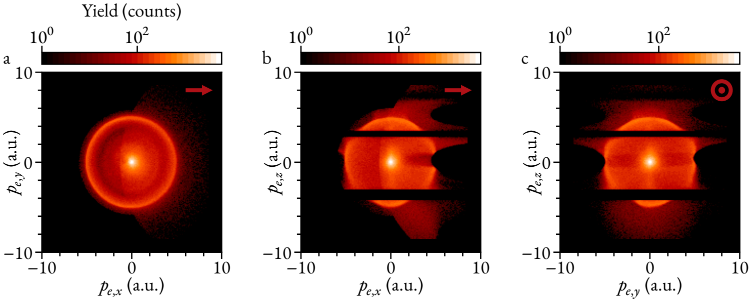

Figure 8.5: Two dimensional momentum distributions for electrons produced by core-shell Compton scattering at N_2 with $\hbar\omega$ = 40 keV. In all panels, the color scale is logarithmic. Gates are applied to only display Auger and Compton electrons. The horizontal cutouts in A and B are to remove detection nodes caused by the magnetic field (see Section 4.2.2, Page 63). The direction of the incoming light is indicated in the upper-right corner of each panel.

The particular shape of the photoelectron momentum distribution imprinted onto the sum momenta shown in Figure 8.4 is very intriguing and will be discussed in later chapters of this work.

Concretely, Reaction (8.5) is experimentally identified by detecting two N^+ molecules and one electron in coincidence, where $p_{\text{sum}} \leq 15$ a.u. This effectively removes the Photoionization reaction (8.8) from the data set. Electrons with $4 < p_e \equiv p_{eA} < 6$ a.u. are identified as Auger electrons. Electrons with momenta in forward direction (as seen in Figure 8.3 on Page 139) are identified as Compton electrons with momentum $\boldsymbol{p}_{eC}$. For the majority of events, only either the Auger *or* the Compton electron is detected. Figure 8.5 shows the sum of both electron momentum distributions.

In the histograms, an increased intensity at momentum zero is visible, as has been seen in the case for valence-shell Compton scattering as well. Just like in the case for valence-shell, for core-shell Compton scattering this increased intensity may be the result of the non-zero binding energy of $N_2(1s)$. The ionization threshold for core-shell electrons of 409.9 eV is much bigger than that of outer-shell electrons (37.3 eV). Thus, it is reasonable to expect a larger peak at momentum zero, as is observed. However, no full theoretical modeling is currently available and the true origin of the peak at momentum zero is not identified, especially in view of the following considerations.

If no Auger electron ($4 < p_{eA} < 6$ a.u.) is detected, N_2 double ionization by valence-shell Compton scattering due to the shakeoff or knockout mechanism (see Section 2.5, Page 31) possibly results in the same reaction

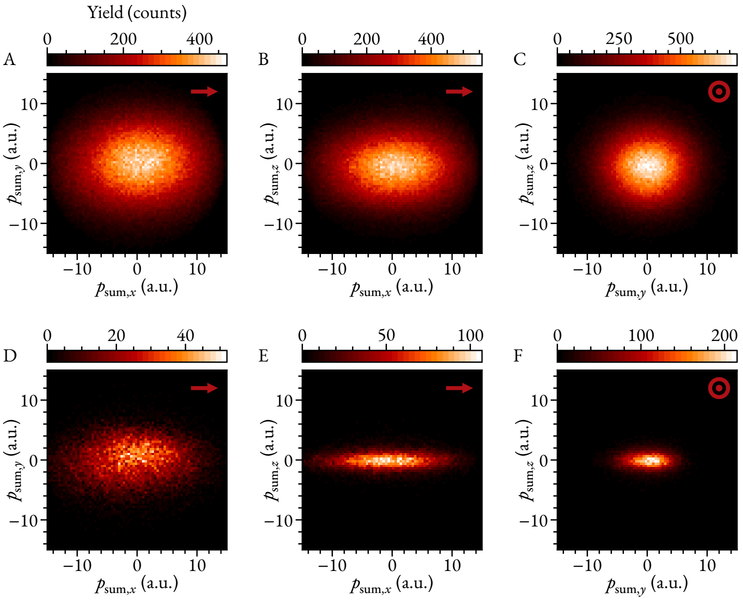

FIGURE 8.6: Sum momenta of two N^+ ions for Compton scattering at N_2 with $\hbar\omega = 40$ keV. A–C, Sum momenta with a gate on the electron momentum of $4 < p_{eA} < 6$ a.u. D–F, Sum momenta with a gate on the electron energy of $E_e < 1$ eV. In all panels, the color scale depicts counts and the direction of the incoming light is indicated in the upper-right corner.

particles being detected as core-shell Compton scattering—namely two N^+ ions and one small-momentum electron. The difference is that for core-shell Compton scattering, a (relatively) large-momentum Auger electron is emitted, the momentum of which has to be balanced by the sum momentum of the two N^+ ions. Figure 8.6 shows the sum momentum for different electron momenta. Panels A to C show the sum momentum for detected Auger electrons, Panels D to F for low-energy electrons with $E_e < 1$ a.u. If all events shown in Figure 8.5 with momentum close to zero were the result of core-shell Compton scattering, the histograms of Figure 8.6 would show a similar shape. This, however, is not the case. Thus, a significant portion of the electrons in Figure 8.5 with small momentum is not necessarily the result of core-shell Compton scattering.

With sufficiently good momentum resolution for the measured N^+-ion momentum, one can distinguish between the two processes. This can be seen in Figure 8.7. There, a Monte-Carlo simulation of the sum momentum

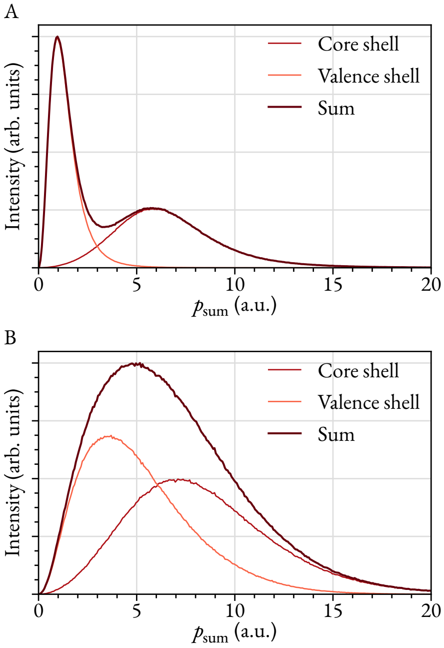

FIGURE 8.7: Simulation of p_{sum} for core-shell Compton scattering with subsequent Auger decay and valence-shell Compton scattering with a subsequent shakeoff or knockout process. In B, the data of A is smeared out with a Gaussian to simulate the finite momentum resolution of the experimental setup.

p_{sum} resulting from core-shell Compton scattering with subsequent Auger decay and valence-shell Compton scattering with a subsequent one-photon double-ionization process is shown. The sum momenta are simulated as

$$\boldsymbol{p}_{\mathrm{sum}} = -\boldsymbol{p}_e^i - \boldsymbol{p}_{e\mathrm{A}} \qquad \text{(core shell)}, \tag{8.9}$$

$$\boldsymbol{p}_{\mathrm{sum}} = -\boldsymbol{p}_e^i \qquad \text{(valence shell)}, \tag{8.10}$$

where the initial electron momentum $\boldsymbol{p}_e^i$ is simulated using the same procedure laid out in the beginning of Section 8.1 [see Equation (8.3), Page 136]. The Auger electrons are simulated with an isotropic distribution with a momentum magnitude of 4.97 a.u.

In Panel A of Figure 8.7, the two reaction channels are clearly distinguishable by their imprint on the sum momentum. However, with the experimental setup used for the presented experiment, the momentum resolution was not sufficient enough to enable this distinction. As can already be seen in Figure 8.6, the momentum resolution in x and y direction is much worse than the momentum resolution in z direction. The resolution in x direction is limited by the width of the gas jet at the interaction region (about 1 mm); in

y direction it is limited by the width of the photon beam (about 0.4 mm). A time-focusing geometry in the spectrometer was used, resulting in the much better momentum resolution in z direction. In Figure 8.7B, the effect of a finite momentum resolution was simulated. There, a Gaussian with full-width half-maximum of 5, 2.5 and 0.5 a.u. for $p_{\mathrm{sum},x}$, $p_{\mathrm{sum},y}$, and $p_{\mathrm{sum},z}$, respectively, was folded with the core- and valence-shell distributions of Panel A. Clearly, Compton scattering at a core shell and Compton scattering at a valence shell are not distinguishable anymore.

If the sum momentum and the momentum of the Auger electron are independent of the Compton reaction, one can gate on the sum momentum without influencing the distributions of the Compton electron. Thus, it is possible to remove the events with a N^+ sum momentum that correspond to a reaction without Auger decay, even though the lacking resolution does not allow full distinction of these events from reactions where Auger decay took place . For the spectra shown throughout the remainder of this chapter, the events with the following sum momenta—unless stated otherwise—were removed:

$$|p_{\mathrm{sum},x}| \leq 10\,\mathrm{a.u.}, \quad |p_{\mathrm{sum},y}| \leq 5\,\mathrm{a.u.}, \quad |p_{\mathrm{sum},z}| \leq 2\,\mathrm{a.u.} \qquad (8.11)$$

8.2.1 MOLECULAR-FRAME COMPTON-ELECTRON ANGULAR DISTRIBUTIONS

Investigation of molecular frame photoelectron angular distributions (MFPADs) is a well-established scientific field. Specifically using the COLTRIMS technique, MFPADs are accessed by measuring the molecular fragments and the photoelectron in coincidence after the photoabsorption reaction is induced. For diatomic molecules, the relative momentum of the molecular fragments $\boldsymbol{p}_{\mathrm{rel}}$ [Equation (8.6), Page 140] corresponds to the molecular axis. Thus, the momentum distribution of the photoelectron in the laboratory frame can be transformed into the momentum distributions in the molecular frame.

Since the photoelectron is multiply scattered by the molecular potential, MFPADs are influenced by the molecular potential of the parent molecule as well as the initial-state wave function of the photoelectron and the polarization of the photon. Depending on the energy of the photoelectron, the influence of the molecular potential on the MFPAD varies. In the upper limit of an instantaneous removal of the photoelectron, the anisotropic molecular potential has no influence on the angular distributions. The influence of

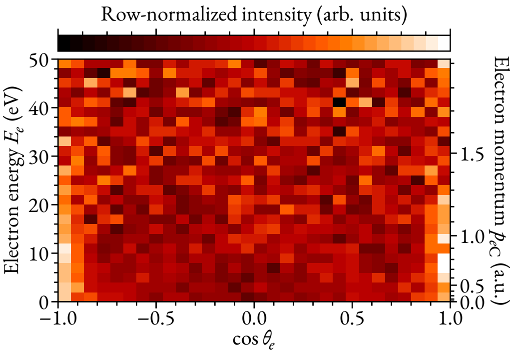

Figure 8.8: Electron angular distribution versus electron energy for core-shell Compton scattering at N_2 with $\hbar\omega = 40\,\text{keV}$. Each row is normalized to its integral, respectively.

the molecular potential on MFPADs and other effects caused by it are studied extensively; for some examples, the reader is referred to References [Pia99; Che00; Lan01].

The energy of the photoelectron produced by the photoabsorption reaction is fixed by the energy of the initial photon and the ionization threshold. Thus, the transition from an anisotropic molecular potential to an effective isotropic (that is, atomic) potential can only be observed by changing the initial photon energy.

Instead of the photoabsorption reaction, the molecule can be ionized by Compton scattering. For Compton scattering, the energy of the Compton electron varies and therefore, the interaction strength of the electron with the molecular potential changes. Thus, by measuring molecular frame Compton electron angular distributions (MFCADs) for different electron energies, one can observe the influence of the molecular potential vanishing. This can be observed well in Figure 8.8. There, the electron angular distribution is shown depending on the electron energy. θ_e is defined by

$$\cos\theta_e = \frac{\boldsymbol{p}_{\text{rel}} \cdot \boldsymbol{p}_{e\text{C}}}{p_{\text{rel}}\, p_{e\text{C}}} . \tag{8.12}$$

For low electron energies, one can see increased intensities at $\cos\theta_e = \pm 1$—that is, along the molecular axis—whereas for increasing energies the angular distribution becomes more isotropic: A “slow” electron is influenced “stronger” by the molecular potential of N_2 than a “fast” one. Since the direction of the momentum transfer of the Compton scattering process—which, within the impulse approximation, corresponds to the final Compton-electron momentum—is random within the molecular frame (since the molecules are randomly oriented with respect to the incident light), the

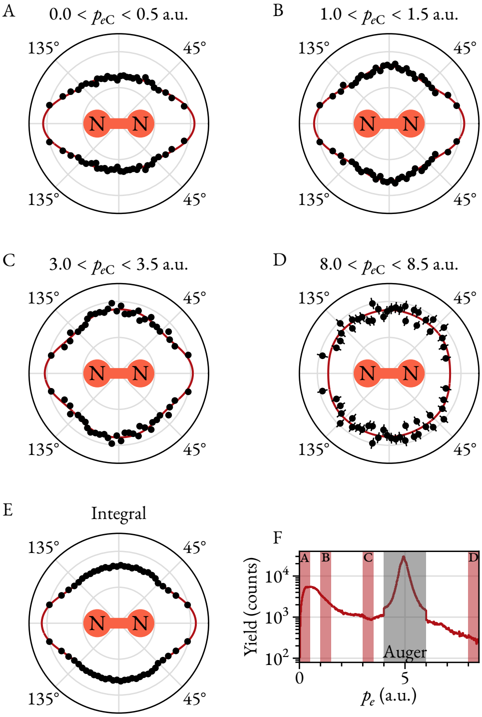

Figure 8.9: MFCADs for inner-shell Compton scattering at N_2 with $\hbar\omega = 40$ keV. A–E, MFCADs in polar representation for different gates on the electron momentum p_{eC}. The points show experimental data; the error bars are the standard statistical error. The lines are Legendre polynomials of degree six. The gates for A to D are shown in F as the red (thin) rectangles, respectively. The data in E is integrated over all electron momenta, excluding those identified as Auger electron momenta. F, Electron momentum distribution. The electrons with momenta marked by the gray (wide) rectangle are identified as Auger electrons.

initial electron emission direction is isotropic. Only the molecular potential breaks the symmetric emission pattern, the influence thereof disappearing for large electron energies.

Figure 8.9 shows the same angular distribution in polar representation for different magnitudes of the electron momentum. From Panels A to D, the electron momenta increase from $p_{eC} = 0.25, 1.25, 3.25, 8.25 \pm 0.25$ a.u., respectively. In each panel, the data was fitted to a Legendre polynomial of sixth degree. Again, one can observe how the electron angular distribution increasingly stops aligning with the N_2 molecular orientation, which is shown in the center of each polar plot. Integrating over all Compton electron momenta yields the angular distribution shown in Figure 8.9E. In Panel F, the momentum distribution of all electrons is shown. Every electron with momentum within the gray (wide) shaded area is identified as an Auger electron, since there is no identifier other than the electron's energy to distinguish Compton and Auger electrons. This means, some Compton electrons are wrongly labeled Auger electrons. However, this Compton-electron background in the Auger-electron distribution is small. Note that the distinct step at the edges of the Auger electron momentum distribution of Figure 8.9F are due to cuts in the two-dimensional momentum distribution of the electrons (Figure 8.5, Page 142). Electrons with a significant momentum component opposite of the incident light direction ($-x$) that are not identified as Auger electrons are identified as background and removed. This removes background only from the Compton electron momentum distribution and not from the Auger electron, resulting in the steps visible.

8.3 COMPTON PROFILES OF CORE- AND VALENCE-SHELL ELECTRONS

The fact that for Compton scattering the N_2^+ ion is only a spectator in the photon-electron interaction (excluding very small photon scattering angles) results in the initial electron momentum being imprinted onto the ion momentum [Kal04]. Thus, for valence-shell Compton scattering, the initial electron momentum distribution of a valence electron is mirrored in the N_2^+ ion momentum distribution.

For core-shell Compton scattering, it is mirrored in the sum momentum distribution of the two N^+ ions, as long as the recoil of the Auger electron is removed. Therefore, the sum momentum, the initial Compton electron's momentum, and the Auger electron's momentum are connected by

$$\boldsymbol{p}_{\text{sum}} + \boldsymbol{p}^{i}_{e\text{C}} + \boldsymbol{p}_{e\text{A}} = 0\,, \tag{8.13}$$

and

$$\left|-\boldsymbol{p}_{\text{sum}} - \boldsymbol{p}_{e\text{A}}\right| = \left|\boldsymbol{p}^{i}_{e\text{C}}\right| = p^{i}_{e\text{C}} \tag{8.14}$$

reflects the one-dimensional initial momentum distribution of the Compton electron for core-shell Compton scattering.

By measuring the Compton or Auger electron in coincidence with measuring one N_2^+ ion or two N^+ ions, one can distinguish between the electron momentum distribution of valence- and core-shell electrons, respectively.

The distributions of Figure 8.10 show directly the unbiased momentum distributions of the different shells. As expected, the momentum distribution for core-shell electrons is larger than the one of valence-shell electrons, while the sum distribution of both core- and valence-shell electrons significantly differs from both.

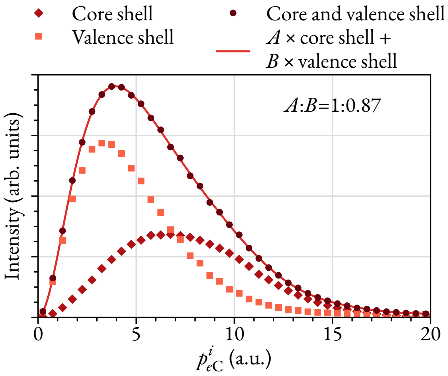

Figure 8.10: Core- and valence-shell electron momentum distribution for N_2. The data of the sum of core- and valence-shell (dots) is normalized such that its integral equals one. The data of both core- (diamonds) and valence-shell (squares) is normalized such that the integral of the sum of both equals one. See main text for an explanation of the line and the ratio A:B.

Theoretically, the integral of the sum-distribution of both valence and core shell electrons should be the integral of either, weighted by the total Compton scattering cross section for each shell. For atomic nitrogen, these cross sections have been calculated by Rao et al. [Rao04]. The ratio of the cross sections for $\mathrm{N}(1s^2)$ to $\mathrm{N}(2s^2)$ and $\mathrm{N}(2p^3)$ is about 1:2.95. If the scattering cross sections for each subshell were constant per electron, the aforementioned ratio would be given by the number of electrons within each subshell (that is, 2:5). At $\hbar\omega = 40$ keV, this is not the case for atomic nitrogen (see Figure 2 of Reference [Rao04]).

To compare the expected ratio with the measurement, the detection efficiencies for the different reaction channels have to be taken into account. Core-shell Compton scattering is identified by the detection of two N^+ ions and one Auger electron ($4 < p_{eA} < 6$ a.u.); valence-shell Compton scattering by the detection of one N_2^+ ion and one Compton electron.

Since for core-shell scattering two instead of one ion has to be detected, the relative detection efficiency is reduced to about $0.78 \times 0.9 \approx 72\%$. This reduction is caused by the transmission through the mesh in front of the ion detector and the active-surface percentage of the utilized funnel microchannel-plate detector (see Sections 4.2.2 and 4.2.3, Page 63). The detection efficiency is increased by the possibility that the Compton electron has the same energy as an Auger electron. However, the number of such Compton electrons is small compared to the total number of Compton events. One can see this in Figure 8.9f, where the momentum magnitude distribution for both Compton and Auger electron is shown. The Auger electron's distribution is on top of a Compton electron "background," which only constitutes to a few percent in total.

For valence-shell Compton scattering, the detection efficiency is dramatically reduced since, due to the detector cutoff, only a fraction of Compton electrons can be detected. Based on the simulations shown in Figure 8.2 (Page 138), only about 15% of all valence-shell Compton events are detected. This value is obtained by comparing the total number of simulated events in the upper row of Figure 8.2 with the total number of events in the lower row.

Correcting the expected ratio by these detection efficiencies results in an expected ratio of 1:0.63. In the measurement, the ratio was found to be 1:0.87. It was obtained by fitting a polynomial of degree ten to the core and valence shell distributions, respectively, then, fitting the distribution of the sum of both resulting polynomials, weighted by fitting parameters A and B. The latter fit is shown in in Figure 8.10 by the red line. The relative yield of valence-shell Compton scattering is about 40% larger than expected. However, the true relative detection efficiency between the two reaction channels is not measured in the experiment. The estimation that only 15% of the total valence-shell Compton scattering reaction channel is measured is based on the simple model laid out in the beginning of Section 8.1. The detection of the funnel microchannel-plate detector is also only estimated as well. With a reasonable uncertainty in the estimated detection efficiencies of 16%, the uncertainty of the expected ratio would overlap with the experimental results.

However, the experimentally obtained distributions in Figure 8.10 demonstrate that ionization by Compton scattering with coincidence detection of the emitted electrons and of the ion(s) using the COLTRIMS technique can be a method of spectroscopy of dynamical properties. Coincidence detection methods for Compton scattering to distinguish between different subshells are not a novel experimental approach (see, for example, References [Fuk72; Rol89]). Already in his pioneering work of 1933, DuMond shows the theoretical contribution of K and L electrons to his observed Compton peak (see Figure 12 in [DuM33]).

However, such $(\gamma, e\gamma)$ studies remain rare [Pra14]. The fact that the initial momentum distribution of the active Compton electron is reflected in the measured momenta of the ion(s) removes the necessity to detect the scattered photons. Removing the need to detect photons makes full solid angle measurements feasible, since electric and magnetic fields can project the complete sphere of the momenta of the ionic fragments onto the two-dimensional detector. The coincident detection of Auger electrons gives access to the information, at which electronic shell Compton scattering occurred.

The above is only valid within the impulse approximation. Only within the impulse approximation is the electron's initial momentum distribution directly reflected in the momentum distribution of the measured ion(s), that is, the ion has to be a spectator-only in the Compton reaction.

8.A IN- AND OUT-COUPLING OF THE SYNCHROTRON BEAM

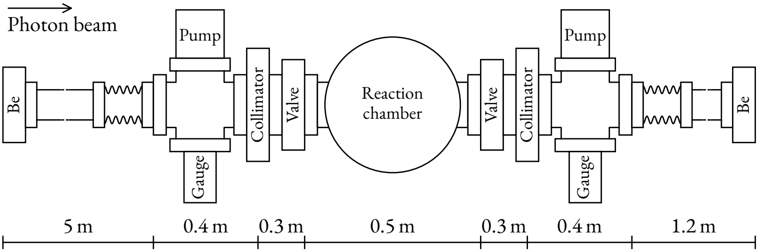

FIGURE 8.11: Sketch of the COLTRIMS beam line of the beam time at ESRF, August 2018. The distances given are approximate values. The collimators in front and behind the chamber were used in combination with pinholes, dividing the beam line into three differentially pumped sections which could be separated by valves. Note that the sketch is not to scale.

The in- and out-coupling of the x-ray beam through the COLTRIMS setup was modified compared to the setup utilized at the previous beam time in April 2018, which was discussed in the appendix of the previous Chapter 7. Since no ion collision calibration measurement was performed, the beam line setup was simplified (compare to Figure 7.16, Page 131). A sketch thereof is given in Figure 8.11. The most significant change is the movement of the entry window as close as possible toward the hutch entrance, that is, as far away as possible from the reaction chamber. Collimators in front and behind the reaction chamber were installed, where the collimator in front was controllable by step motors from outside the experimental hutch. The respective distances are specified in Figure 8.11. The collimator behind the reaction chamber was fully opened. Similarly to the beam time in April 2018, lead shielding with a 1 mm hole at the appropriate position was installed directly in front (behind) of the beryllium entry (exit) window.

Note that it is also possible to directly connect the COLTRIMS beam line to the end of beam line ID31 [Drn22], removing two beryllium windows within the photon beam path (one at the COLTRIMS setup, one at the entry point of the experimental hutch). For this work, this was not done.

8.B CALIBRATION

As opposed to the previous experiments presented in this work, no measurements beside the detection of the core-shell Compton-scattering reaction at

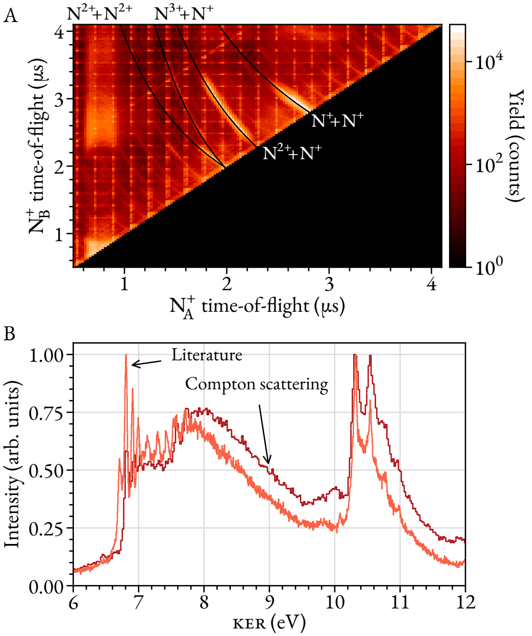

Figure 8.12: Ion-ion coincidence histogram (A) and kinetic energy release (B) for ionization of N_2 by photons with $\hbar\omega = 40$ keV. In A, no selection of specific reaction channels is done. In B, only the KER for Compton scattering at the core shell is displayed, the literature is from [Sem10], and both literature and experiment are normalized to their maximum, respectively.

N_2 is necessary to calibrate the electric field of the spectrometer. Detection of the two N^+ ions and the Auger electron enable the calibration for both the ion and the electron detector.

The momenta of the two N^+ ions are correlated: ignoring the recoil of the emitted electrons, the momenta are antiparallel. Reconstructing the momenta in time-of-flight (z) direction includes knowledge of the electric field (see Section 5.2, Page 71). Since the momenta of the first and second N^+ ion are correlated component-wise and are corresponding to the time-of-flight, plotting the times-of-flight of Ion A and Ion B in a two-dimensional coincidence histogram results in them being positioned on a curved line, as shown in Figure 8.12A. The position and slope of this line depends, among other things, on the electric field of the spectrometer, allowing the calibration of the electric field. The lines were calculated by determining the momentum component p_z of the first particle for all relevant times-of-flight using a Newton method. The z component of the momentum of the second particle is then $-p_z$, which translates back to a certain time-of-flight. Alternatively, Equation (5.7) of Reference [Ulr05] can be used if only one electric field is used in the ion arm of the spectrometer.

In Figure 8.12, the N_A^+ ion is the *first* detected ion and N_B^+ the *second*. Thus, no events are situated below the principal diagonal.

The ion detector was calibrated using the relative momentum, the sum momentum $\boldsymbol{p}_{\text{sum}}$ and the kinetic energy release (KER) of N_2. For Compton scattering, the sum momentum is centered around zero, allowing calibration of the x and y detector offset. The KER includes multiple sharp peaks at fixed energies. Thus, the stretch of x and y is fixed as well. The literature values are obtained from Reference [Sem10], which, in turn, are calibrated to the KER spectra obtained from Reference [Lun96].

The electron detector was calibrated using the Auger electrons shown in Figure 8.5 on Page 142. The momenta of the Auger electrons are on a sphere centered around momentum-zero with a radius of 4.97 a.u.

The results presented in the following Chapter 9 are obtained by the same experimental run as the ones in this chapter and thus, the calibration is the same as presented here.

8.C EXPERIMENTAL PARAMETERS

The experiment was performed at the same beam line as the experimental run presented in the previous chapter. Therefore, the beam line parameters can be found in Table 7.1 on Page 133. For the majority of acquisition time, a photon energy of 40 keV was utilized. In addition, data with lower-energy photons ($\hbar\omega$ = 12, 20, and 28 keV) was acquired, the results of which are discussed in Section 9.4 of Chapter 9. The results discussed there are obtained in the same experimental run as the ones of this chapter with identical experimental parameters. They are summarized in Table 8.1. A sketch of the spectrometer is shown in Figure 8.13. The used COLTRIMS setup was modified from the setup described in Reference [Kas14].

Table 8.1: Experimental parameters of the experimental run of the beam time in August 2018 at beam line ID31 of the ESRF, Grenoble, France. The beam line parameters can be found in Table 7.1 on Page 133.

Target			
Driving pressure	22 bar	Nozzle diameter	30 μm
Width at interaction point	≈ 1 mm	Target gas	N_2
Temperature	300 K	Jetdump vacuum	8.6×10^{-8} mbar
Expansion vacuum	2.1×10^{-3} mbar		
Spectrometer			
Electron arm	27.8 cm (acc.)	Ion arm	13.4 cm (acc.)
E-field	51.7 V/cm	Vacuum	2.5×10^{-9} mbar
B-field	21.1 Gs		
Voltages			
Electron detector	+1042 V (front) +3003 V (signal)	Ion detector	−2303 V (front) +100 V (signal)
Spectrometer	+1000 V (electron) −1000 V (ion)	Helmholtz current Correction coils	121.5 A off
Detectors			
Electron	120 mm	Ion	80 mm
Electron MCP	regular	Ion MCP	funnel
Rates			
Electron	25–30 kHz	Ions	5.4 kHz (trigger)
Acquisition times			
80 h (40 keV) 2 h (28 keV) 2 h (20 keV) 11 h (12 keV)			

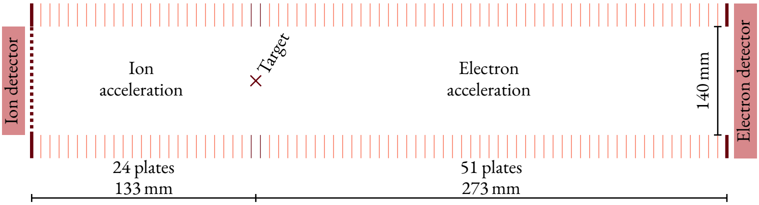

Figure 8.13: Sketch of the spectrometer of the beam time in August 2018 at beam line ID31 at the ESRF, Grenoble. Note that two target plates instead of one were used to ensure that the synchrotron beam does not collide with the spectrometer plates.

9

PHOTON-MOMENTUM-INDUCED MOLECULAR DYNAMICS

In photoionization, the momentum of the emitted electron has to be balanced solely by the remaining ion, or, in case of a molecular break-up, the ionic fragments. For the latter case, the electron's momentum is compensated by the sum momenta of all ionic fragments. Since the photon is absorbed, its momentum has to be balanced by the sum momentum of the total system. Due to the mass ratio of ion to electron (which is of the order of 10^4) the photon momentum is effectively transferred to the remaining ion(s). For typical photoionization energies, however, the photon momentum is small compared to the other momenta involved, which is the reason it is often neglected. For examples of studies beyond the dipole approximation, see References [Hem97; Krä02; Hem04; Gru18]. For studies of non-dipole effects in multi-photon photoionization, see, for example, References [Sme11; Har19; Mau21; Lin22].

If the ionic fragments Coulomb-explode, the magnitude of the ions' momenta (and therefore its kinetic energy) will be majorly the result of the Coulomb explosion. The kinetic energy release (KER) is the result of the potential energy curves and the dynamics involved in the ionization process. As such, large momenta of the photoelectron (and therefore, the recoil onto the molecular system) may significantly alter the KER distribution. Analogously, if the photon momentum is big enough, its "kick" is big enough to have an influence as well. This recoil effect is extensively studied for rotational and vibrational excitation which manifests in a reduced energy of the photoelectron [Dom78; Kuk05; Tho11; Sim14; Kuk18].

By neglecting the linear photon momentum and only considering its momentum magnitude (that is, its energy), one effectively describes the problem within the dipole approximation (see Section 2.3.1, Page 16). This approximation breaks down for big photon momenta.

In the scope of this work, these briefly introduced effects are investigated. Three distinct results will be presented in this chapter:

- the influence of the photon and photoelectron "kick" onto the molecular dynamics, the results of which are published in [Kir19a], discussed in Sections 9.1 and 9.2,
- a recoil-induced asymmetry in the molecular frame photoelectron angular distributions, published in [Kir19b], discussed in Section 9.3,

- the observation of a backwards emission of the N^+ ions with respect to the light direction, published in [Gru20a] and discussed in Section 9.4.

All of these results were obtained in one experiment of one beam time at beam line ID31 at the ESRF, Grenoble, in August 2018, the same experiment that yielded the results of the previous Chapter 8.

The following reaction was measured:

$$\gamma(40\,\text{keV}) + \text{N}_2 \rightarrow \text{N}_2^+(1s^{-1}) + e_\gamma \rightarrow \text{N}^+ + \text{N}^+ + e_\gamma + e_\text{A}\,, \tag{9.1}$$

that is, a $E_\gamma = 40$ keV photon with momentum $\boldsymbol{k}_\gamma$ induces core-shell photoionization of a N_2 molecule. A photoelectron e_γ with momentum $\boldsymbol{p}_{e\gamma}$ is emitted. The N_2^+ system subsequently Auger decays onto a dissipating N^+/N^+ state, emitting an Auger electron e_A with momentum $\boldsymbol{p}_{e\text{A}}$. The two positively charged N^+ ions Coulomb explode, resulting in momenta $\boldsymbol{p}^\text{A}_{\text{N}^+}$ and $\boldsymbol{p}^\text{B}_{\text{N}^+}$. The momenta of the Auger electron and the two N^+ ions are detected in coincidence. The momentum of the photoelectron is calculated exploiting momentum conservation.

Figure 9.1 shows the measured momenta $\boldsymbol{p}_{e\text{A}}$ of the Auger electrons, the sum momenta $\boldsymbol{p}_\text{sum} = \boldsymbol{p}^\text{A}_{\text{N}^+} + \boldsymbol{p}^\text{B}_{\text{N}^+}$, and the relative momenta $\boldsymbol{p}_\text{rel} = 1/2(\boldsymbol{p}^\text{A}_{\text{N}^+} - \boldsymbol{p}^\text{B}_{\text{N}^+})$. The histograms in Panels A to C and D to F are in principal the same as those shown in Figures 8.4 and 8.5 (Page 141), respectively, except that a gate is applied for the electron momenta, only accepting Auger electrons (that is, $4 < \boldsymbol{p}_{e\text{A}} < 6$ a.u.) and that small ion sum momenta $\boldsymbol{p}_\text{sum} < 30$ a.u. are excluded, consequently gating on core-shell photoionization while excluding Compton scattering. The horizontal cutouts in Panels B and C exist to remove the nodes caused by the gyration of the electrons due to the magnetic field (see Section 4.2.2, Page 63). The z component of the relative momentum $\boldsymbol{p}_\text{rel}$ is by definition positive only. The first detected N^+_A ion (which is the first ion to reach the detector) is the one with a momentum $p^\text{A}_{\text{N}^+,z}$ pointing towards the ion detector—that is, $p^\text{A}_{\text{N}^+,z} > 0$. Since in the center-of-mass system, the two ion fragments have back-to-back momenta, $p^\text{B}_{\text{N}^+,z}$ then points away from the ion detector, that is, $p^\text{B}_{\text{N}^+,z} < 0$. Thus, the relative momentum is larger than zero per definition. If the two N^+ ions are indistinguishable, one could switch Ions A and B randomly to get a full momentum sphere instead of only the upper half. This was not done in the following analysis.

The circle in Figure 9.1D has a radius of 54.9 a.u., which is the magnitude of the photoelectron momentum for core-shell photoionization of N_2 with $\hbar\omega = 40$ keV. This momentum is compensated by the sum momentum of the ions. Notice that the distribution of $\boldsymbol{p}_\text{sum}$ is clearly shifted in the direction

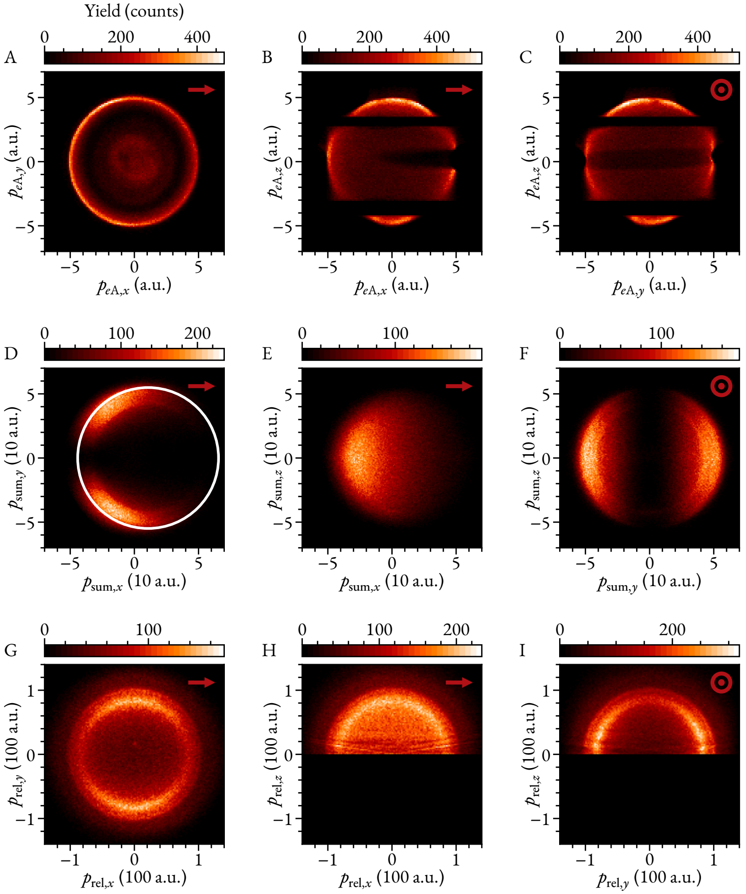

FIGURE 9.1: Momenta of the Auger electron (A–C) and the sum (D–F) and relative (G–I) momenta of N^+ ions produced by core-shell photoionization of N_2 with $\hbar\omega$ = 40 keV. In all panels, the color scale depicts counts and the direction of the incident photon is implicated in the upper right corner. See main text for an explanation of the circle in D.

of the incoming light. In fact, it is shifted by the magnitude of the incoming photon's momentum $k_\gamma = 10.7$ a.u. This is dictated by momentum conservation; however, the shift is not the focus of this chapter. It will be discussed in Section 9.4. Further, the distribution is not symmetric with respect to the polarization direction of the incoming photon, but is bend in backward direction with respect to the incoming light. This will also be discussed in the subsequent sections of this chapter.

9.1 INFLUENCE OF THE PHOTON MOMENTUM ON THE KINETIC ENERGY RELEASE

Figure 9.1D shows that at $\hbar\omega = 40$ keV, the linear photon momentum plays a large role in photoionization and cannot be neglected, as is typically the case by using the dipole approximation. In this section, the influence of the linear photon momentum k_γ on the molecular dynamics of N_2 photoionization—particularly, the KER—will be discussed. The KER is obtained in the center-of-mass system, that is,

$$\text{KER} = \frac{1}{2\mu}\frac{\left|\boldsymbol{p}^{\text{A}}_{\text{N}^+} - \boldsymbol{p}^{\text{B}}_{\text{N}^+}\right|^2}{4} = \frac{p^2_{\text{rel}}}{2\mu} \tag{9.2}$$

with the reduced mass $\mu = m_\text{N} m_\text{N}/(m_\text{N} + m_\text{N}) = {}^1\!/2 m_\text{N}$. m_N is the mass of one nitrogen atom.

One can directly compare the difference of the KER resulting from photoionization with a KER that is free of the influence of k_γ. In the presented experiment, Compton scattering and photoionization are both measured simultaneously. As discussed in previous chapters of this work, within the impulse approximation the ionic fragments are only a spectator in the Compton-scattering reaction. Thus, the KER is uninfluenced. The comparison of both

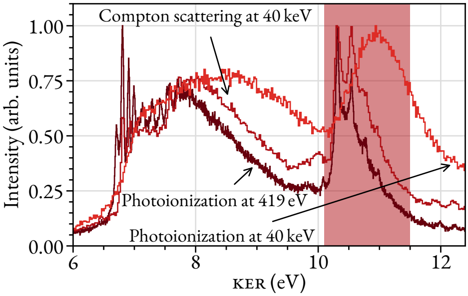

FIGURE 9.2: KER comparison of different photoreactions. All data is normalized to the highest peak. The data for photoionization at $\hbar\omega = 419$ eV is taken from [Sem10]. The peaks within the shaded area are of special interest and are discussed in the main text of Section 9.1.1. (Adapted from [Kir19a].)

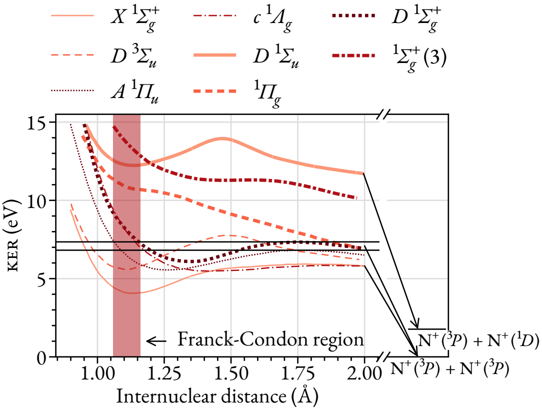

Figure 9.3: Potential energy curves for N_2^{2+}. The curves are taken from References [Lun96; Deh75; Thu75]. The y axis shows the KER corresponding to the dissociation limit of the N_2^{2+} onto the measured N^+/N^+ ion states. (Adapted from [Sem10].)

KERs is shown in Figure 9.2. There, photoionization with $\hbar\omega = 40$ keV and 419 eV as well as ionization by Compton scattering at 40 keV are shown. Note that the two sharp peaks of the low-energy photoionization and the Compton scattering KER within the shaded area correspond to the two rings visible in Figures 9.1g to 9.1i. The data for photoionization at 419 eV is taken from the literature [Sem10] and is used for the calibration (see Section 8.b, Page 152). The respective peak for photoionization at $\hbar\omega = 40$ keV is shifted significantly towards higher KER. It is worth mentioning that, since we measure ionization by Compton scattering and photoionization *simultaneously*, the observed shift must be due to the different underlying ionization processes and cannot be due to a systematic error of the experimental setup.

In Figure 9.2, the shift of the peak position within the shaded area is the only difference between the different processes. The relative intensity of the distinct features are significantly different, most notably the sharp peaks around 6.8 eV for photoionization at 419 eV, and the falling slopes at 8 to 10 eV for all spectra. The KER distribution is determined by the potential energy curves of the N_2^+ intermediate state and the dicationic N_2^{2+} states within the Franck-Condon region. The Franck-Condon *principle* gives the probability of the transition from one molecular state onto another. The Franck-Condon *region* is given by the extent of the initial state in position space. If the transition processes (here, photoionization and Auger decay) are fast compared to the nuclear motion, only transitions within the Franck-Condon region contribute to the doubly charged N_2^{2+} state. Several potential energy curves for N_2^{2+} are shown in Figure 9.3. The position of the peaks in Figure 9.2 is fixed by the potential energy curves (insofar one neglects the impact of the photon's momentum and the electron's momentum recoil). While the peaks' positions are fixed, their relative intensities are not. These depend on the underlying process responsible for the decay. The experimental resolution has another impact on the relative intensity of the peaks. It does not affect the intensity directly, nonetheless a finite experimental resolution smears out intense sharp peaks over an energy range corresponding to the energy resolution, reducing their relative height.

Precisely what originates the disparity of peak intensity between the Compton scattering KER distribution and the photoionization KER distribution? Since for these measurements the influence of the photon and electron momenta are neglectable, it must be due to a different population of the final state. For photoionization, the final state results from Auger decay onto the dissociating N^+/N^+ state, whereas for Compton scattering, another decay is possible, explaining the differences in the distributions. The Compton scattering distribution results from two processes: (1) the photon scatters at the core shell, creating a vacancy at the core which relaxes via Auger decay, and (2) the photon scatters at the outer valence shell, with double ionization occurring due to a knockout or shakeoff process (see Section 2.5, Page 31). The latter processes are similar to electron-impact double ionization, of which a KER spectrum can be found in Reference [Lun96].

The most prominent and sharpest feature of all KER distributions are the peaks within the shaded area of Figure 9.2. In the following section, the shift of those peaks is discussed in a quantitative way.

9.1.1 MAGNITUDE OF THE KINETIC-ENERGY-RELEASE SHIFT

The aforementioned peaks result from an Auger decay of the $N_2^+(1s^{-1})$ intermediate state onto the $(2\sigma_u)^{-1}(1\pi_u)^{-1}\ {}^1\Pi_g$, the $(1\pi_u)^{-2}\ {}^1\Sigma_g^+$, and the $(3\sigma_g)^{-1}(2\sigma_u)^{-1}\ {}^1\Sigma_u$ states of the Coulomb exploding N_2^{2+}. The last one is responsible for the sharp narrow peaks visible in the Compton-scattering-induced KER distribution [Sem10; Kir19a]. Since in the case of Compton scattering the $N_2^+(1s^{-1})$ molecular ion is only a spectator in the reaction, it remains mostly in the ground and lowest vibrational states [Her04].

In the case of photoionization with a 40 keV photon, all momenta are relevant for the molecular dynamics—that is, the momentum of the photon, the momentum of the photoelectron (more so, its recoil onto the molecular system), and the momentum of the Auger electron. Other than for Compton scattering, the momentum of the photon is absorbed and its momentum has to be compensated by the nuclei, meaning the $N_2^+(1s^{-1})$ molecular ion is an “active participant” in the reaction. The recoil of the photoelectron momentum $-\boldsymbol{p}_{e\gamma}$ is transferred locally to one of the nitrogen atoms. This local deposit of energy leads to a relative motion between the nuclei. The kinetic energies of the measured N^+ ions are calculated in the center-of-mass reference frame, where the sum momentum $\boldsymbol{p}_{\text{sum}}$ of the two ions equals zero. Since N_2 is a homonuclear molecule, if the photoelectron momentum recoil $-p_{e\gamma}$ is deposited locally to one nucleus, it follows that the relative motion within this reference frame is half of $p_{e\gamma}$. This deposition leads to internal rotational and vibrational excitation [Dom78; Fel05], resulting in the observed KER shift. In turn, the photoelectron energy is reduced [Dom78; Tho11; Sim14; Mat05; Tho08; Kuk18]. For the present case of a 40 keV photon the energy of the photoelectron is approximately 39.6 keV. Note that at these high energies, one has to take special relativity into account when calculating the photoelectron momentum, where,

$$p_{e\gamma} = c^{-1}\sqrt{\left(m_e c^2 + \hbar\omega - E_{\text{bind}}\right)^2 - m_e^2 c^4} \approx 54.9\,\text{a.u.} \tag{9.3}$$

Here, $c = 137\,\text{a.u.}$ is the speed of light, $\hbar\omega = 40\,\text{keV}$ is the energy of the photon, $E_{\text{bind}} = 410\,\text{eV}$ is the ionization threshold for core-shell photoionization of N_2, and $m_e = 1\,\text{a.u.}$ is the electron mass. Consequently, since half of this momentum recoil goes into vibrational and rotational excitation, the corresponding KER increase is $(-p_{e\gamma}/2)^2/(2\mu) \approx 0.79\,\text{eV}$.

Of course, in the observed reaction, the photoelectron momentum is not the only momentum involved (however, the largest). Naturally, the question arises whether only the photoelectron momentum has an influence on the KER increase. Investigating the KER distribution for fixed momentum configurations, namely, the orientation of the three vectors $\boldsymbol{k}_\gamma$, $\boldsymbol{p}_{e\gamma}$, and $\boldsymbol{p}_{e\text{A}}$, gives an answer to this question. Two configurations, described by the angles ϑ_1 and ϑ_2, were chosen:

- ϑ_1 is the angle between the incoming photon momentum $\boldsymbol{k}_\gamma$ and the photoelectron momentum $\boldsymbol{p}_{e\gamma}$. Since the scenario is rotationally symmetric around the light axis, this angle is a polar angle, that is, it is defined as $\cos\vartheta_1 = \boldsymbol{p}_{e\gamma}\cdot\boldsymbol{k}_\gamma/(p_{e\gamma}\,k)$. For this configuration, the Auger electron emission direction is integrated over all angles.

- ϑ_2 is the angle between the Auger electron momentum and the sum momentum $\boldsymbol{p}_{e+\gamma} = \boldsymbol{p}_{e\gamma} + \boldsymbol{k}_\gamma$, where the angle ϑ_1 is fixed at $45 \pm 10°$. Analogously to ϑ_1, ϑ_2 is defined as $\cos\vartheta_2 = \boldsymbol{p}_{e\text{A}}\cdot\boldsymbol{p}_{e+\gamma}/(p_{e\text{A}}\,p_{e+\gamma})$.

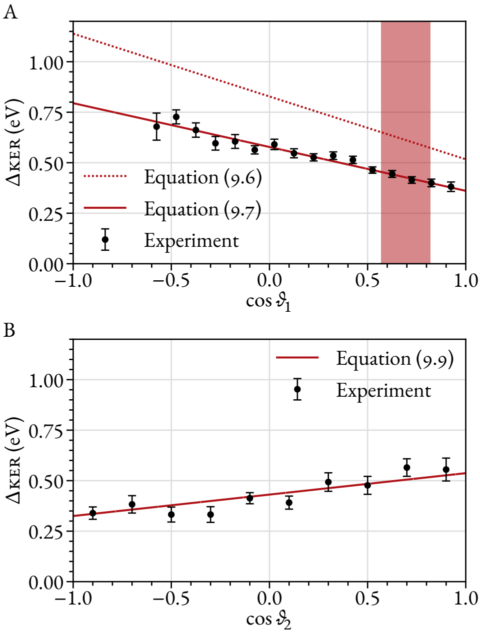

Figure 9.4: KER shift dependency on the momentum configuration of $\boldsymbol{k}_\gamma$, $\boldsymbol{p}_{e\gamma}$, and $\boldsymbol{p}_{e\mathrm{A}}$. A, Different configurations of the photoelectron and photon momentum. B, Different configurations of the Auger electron and the sum momentum $\boldsymbol{p}_{e+\gamma}$, where the configuration $(\boldsymbol{p}_{e\gamma},\boldsymbol{k}_\gamma)$ is fixed within the shaded area of A. In both panels, the data points are the KER shift as obtained by the fit given by Equation (9.4) and the error bars are the standard deviation resulting from these fits. (Adapted from [Kir19a].)

For the different momenta orientations, $\mathrm{KER}_{e\gamma}$—that is, the position of the peak in the shaded area of Figure 9.2 (Page 160) of the curve resulting from photoionization at $\hbar\omega = 40\,\mathrm{keV}$—was determined using the fit function

$$f(\mathrm{KER}) = A\exp(-B\times\mathrm{KER}) + C\exp\left(-\frac{(\mathrm{KER}-\mathrm{KER}_{e\gamma})^2}{2\sigma^2}\right). \tag{9.4}$$

It was fitted for a KER in-between 8.5 and 13 eV for both angles ϑ_1 and ϑ_2, respectively. The resulting fits are shown in the appendix of this chapter in Figures 9.13 and 9.14 on Pages 183 and 184, respectively.

Figure 9.4 shows the difference of the KER peak positions resulting from ionization by Compton scattering and by photoabsorption, that is,

$$\Delta\mathrm{KER} = \mathrm{KER}_{e\gamma} - \mathrm{KER}_{\mathrm{C}}\,. \tag{9.5}$$

$\mathrm{KER}_{\mathrm{C}}$ is the peak position of the KER resulting from ionization by Compton scattering. It was obtained by using the same fit function f from Equation (9.4). Since for photoionization the KER shift smears out the two sharp vibrational peaks, the Compton scattering KER was convoluted with a 0.15 eV width Gaussian to smear out those vibrational peaks as well. The resulting fit is shown in the appendix of this chapter in Figure 9.15 on Page 184. The fit yields $\mathrm{KER}_\mathrm{C} = 10.57\,\mathrm{eV}$, which would be situated at $\Delta\mathrm{KER} = 0$ in Figure 9.4.

To quantify the shift ΔKER in Figure 9.4A, we follow the aforementioned consideration that half the momentum "kick" goes into vibrational and rotational excitation [Fel05]. The recoil onto the $\mathrm{N}_2^+(1s^{-1})$ molecular ion is $1/2\left[\boldsymbol{k}_\gamma + (-\boldsymbol{p}_{e\gamma})\right]$. This increase of energy of the molecular system can then be distributed amongst the other reaction particles: the two N^+ ions and the Auger electron. Assuming none of the energy is transferred to the Auger electron, one can easily model the maximum energy shift $\Delta\mathrm{KER}_\mathrm{max}$ [Kir19a]:

$$\begin{aligned}\Delta\mathrm{KER}_\mathrm{max}(\cos\vartheta_1) &= \frac{1}{2\mu}\frac{\left|\boldsymbol{k}_\gamma - \boldsymbol{p}_{e\gamma}\right|^2}{4}\\ &= \frac{k_\gamma^2 + p_{e\gamma}^2}{8\mu} - \frac{k_\gamma p_{e\gamma}}{4\mu}\cos\vartheta_1\,. \end{aligned} \tag{9.6}$$

This maximum shift is shown in Figure 9.4A by the dotted red line. The black dots are the experimental data, the error bars are the standard deviation resulting from the fit. It is apparent that the experimental data is significantly below the maximal shift given by Equation (9.6). However, the data shows unambiguously that for photon energies of several tens of kiloelectronvolts the photon momentum plays a significant role in the molecular dynamics of ionization of N_2 by photoabsorption. If the photon momentum were to be neglectable, the data presented in Figure 9.4A would be flat, but, for parallel and antiparallel orientation of $\boldsymbol{k}_\gamma$ to $\boldsymbol{p}_{e\gamma}$ (that is, $\cos\vartheta_1 = \pm 1$), the corresponding KER differs by approximately 0.4 eV. This means that for parallel momenta $\boldsymbol{p}_{e\gamma}$ and $\boldsymbol{k}_\gamma$ ($\cos\vartheta_1 = 1$), the recoil of the photoelectron $-p_{e\gamma}$ is opposite to the momentum "kick" of the photon, and the overall KER shift is smaller than in the opposite case, where $\boldsymbol{p}_{e\gamma}$ and $\boldsymbol{k}_\gamma$ are antiparallel ($\cos\vartheta_1 = -1$).

The simple considerations of Equation (9.6) clearly do not explain the experimental findings. A smaller KER shift than $\mathrm{KER}_\mathrm{max}$ of the experimental data hints towards an energy transfer not only into vibrational and rotational excitation but also an energy transfer to the only other particle involved: the Auger electron. To get an understanding what part of the energy transfer goes into excitation and what part is transferred onto the Auger electron, the experimental data was fitted with

$$\Delta\mathrm{KER}_{e\gamma}(\cos\vartheta_1) = c \times \Delta\mathrm{KER}_\mathrm{max}(\cos\vartheta_1) \tag{9.7}$$

yielding a fraction $c = 0.7$, that is, 70% of the momentum "kick" is transferred into vibrational and rotational excitation. The solid line in Figure 9.4a shows this fit. Since the only other particle involved in the reaction is the Auger electron, the remaining 30% result in an increase of its energy. However, this increase is only several millielectronvolts, while the energy of the Auger electron is of several hundred electronvolts. The chosen COLTRIMS spectrometer is not able to detect this shift.

What are possible explanations for the 70/30 ratio? To answer this, consider the following simplified thought notion: For diatomic molecules, 2/3 of the internal energy leads to rotational excitation, a consequence of the rotational (2) and vibrational (1) degrees of freedom of diatomic molecules. Rotational excitation does not couple to the Auger electron [Kir19a]. Meanwhile, the combined momentum transfer $\boldsymbol{k}_\gamma - \boldsymbol{p}_{e\gamma}$ yields a momentum component along the molecular bond direction, leading to compression or stretching of the molecule. Due to the compression/stretching of the molecular bond length, the Auger decay does not solely occur at the average N_2^+ bond length. The Auger electron's energy depends on the initial and final potential energy surface, which, in turn, depends on the molecular bond length. This gives a possible mechanism how the Auger electron's energy is increased. However, T. Thomas demonstrates that only an anisotropic distribution of the recoil momentum $\boldsymbol{k}_\gamma - \boldsymbol{p}_{e\gamma}$ with respect to the molecular axis can result in an Auger energy increase of the observed 30% [Tho20]. However, this is in contrast to previous findings [Tho09; Tho10; Kuk17; Kuk18]. As of yet, a quantitative explanation of the 70/30 ratio has not been achieved.

Figure 9.4b reveals the influence of the recoil of the Auger electron onto the molecular dynamics. There, the angle between the incident photon and the photoelectron is fixed to 45 ± 10°, indicated by the shaded area of Figure 9.4a. For this configuration the effective momentum "kick" p_{eff} is 33.5 a.u. This *effective* momentum considers the empirical fraction $c = 0.7$ of Equation (9.7), that is,

$$p_{\text{eff}} = c \times \left| \boldsymbol{p}_{e\gamma} + \boldsymbol{k}_\gamma \right| . \qquad (9.8)$$

Using this effective momentum, analogously to Equation (9.6), one can calculate the expected KER shift due to p_{eff} and the momentum recoil of the Auger electron

$$\Delta\text{KER}_{e+\gamma,\text{A}}(\cos\vartheta_2) = \frac{p_{\text{eff}}^2 + p_{e\text{A}}^2}{8\mu} - \frac{p_{\text{eff}}\, p_{e\text{A}}}{4\mu} \cos\vartheta_2 \qquad (9.9)$$

As opposed to the KER shift resulting from the photoelectron momentum $\boldsymbol{p}_{e\gamma}$ and the photon momentum $\boldsymbol{k}_{\gamma}$, the recoil momentum of the Auger electron adds to the KER shift in full, and thus, Equation (9.9) accurately describes the experimental findings. Note that for this accuracy it is necessary to consider the effective momentum p_{eff} instead of the photoelectron and photon sum momentum $p_{e+\gamma}$, further backing up the validity of the empirical fraction c.

The slopes in Figures 9.4A and 9.4B are of opposite sign because in Panel A, the momentum transferred to the molecule by the photon is parallel to $\boldsymbol{k}_{\gamma}$, whereas the momentum imparted on the molecule by the photoelectron is its recoil, which points in opposite direction. The same applies for the Auger electron. From the definitions of ϑ_1 and ϑ_2 (Page 163), it then follows that the sign of $\cos\vartheta_1$ is positive while the sign of $\cos\vartheta_2$ is negative and therefore, the signs of the slopes in Figures 9.4A and 9.4B flip.

Describing the effect of the Auger electron recoil onto the molecular system by Equation (9.9) implies that the recoil acts on the same molecular center as the effective momentum p_{eff}, that is, the same center that the photon and the photoelectron act upon. It is plausible to assume that the photon and the photoelectron act essentially on the same nitrogen atom. This is because the core hole may be thought of as localized, even though both nitrogen atoms in N_2 are equivalent [Sny70]. Note, however, that the photoelectron and Auger electron are in an entangled Bell state. The question if the core hole is localized or delocalized is not trivially answered and depends on what exactly is measured. For a more detailed discussion thereof, the reader is referred to Reference [Sch08]. The removal of a core electron initiates charge migration in the valence shells [Kul16]. Due to fast charge migration driven by electron correlation, it is also possible for the initially localized core hole to migrate within the molecular system [Ced99], and thus, it is not predetermined that the Auger decay is linked to the same atomic core where photoionization occurred. In homonuclear diatomic molecules, the hopping time is given by the energy splitting of the gerade and ungerade states. In N_2 the energy splitting is about 100 meV [Kir19a; Her04; Eha06], which corresponds to about 20 fs hopping time. Comparing this to the average lifetime of the $N_2^+(1s)$ hole state of about 7 fs, the hole state Auger decays in most cases before charge migration takes place and thus, it is plausible to assume that the Auger electron recoil acts upon the same atomic center as the photoelectron recoil. This is further backed up by the good agreement of the classical considerations given by Equation (9.9) and the experimental data.

In that regard, one can speculate further why the Auger electron momentum recoil acts localized on one center, even though the orbital of which the

Auger electron originates from is delocalized over the molecule. However, no proper calculations were performed here to support the following assumptions. The speculation is as follows: The matrix element for Auger decay contains, (1) the $N_2^+(1s)$ hole state, which is tightly localized at one of the two nuclei, (2) the orbital of the valence electron filling the core hole, and (3) the orbital of the emitted Auger electron. The necessary electron-electron interaction is also part of the matrix element. It is given by the Coulomb term of the two, which depends inversely on the distance between the two electrons. Therefore, the biggest contribution to the Auger matrix element comes from the spatial region close to the two nuclei.

9.2 ROTATIONAL MOTION OF THE MOLECULAR ION

Under the assumption that no photon momentum and electron recoil acts upon the N_2 molecule, no rotation of the molecule is induced by the photoreaction. This fact was used in the previous chapter to determine the molecular axis, since without rotation, the measured relative momentum $\boldsymbol{p}_{\text{rel}}$ is pointing along the internuclear axis, and thus, one can investigate observables in the molecular frame.

However, as shown by the results presented in the previous sections, the photon momentum and electron recoils cannot be ignored. In fact, they induce a rotational excitation of the $N_2^+(1s^{-1})$ intermediate state. Thus, the molecule rotates after the emission of the photoelectron and the final orientation after Auger decay and subsequent fragmentation are not identical to the orientation at the instant of the photoreaction. That the photoelectron momentum recoil indeed influences the molecular rotational motion is visible in Figure 9.5. There, the two-dimensional distribution of the relative momentum is shown, where in each panel the emission direction of the photoelectron is fixed, as indicated by the dashed white lines, and as such, each panel of Figure 9.5 is a subset of Figure 9.1G (Page 159). Instead of an isotropic distribution of $\boldsymbol{p}_{\text{rel}}$, one can clearly see correlation of the distribution of the relative momentum and the photoelectron emission angle. Since in the reaction, the N_2 molecule is randomly oriented, one would expect a random—that is, isotropic—distribution of $\boldsymbol{p}_{\text{rel}}$, as is seen in Figures 9.1G to 9.1I. However, the regions *almost* perpendicular to the photoelectron emission angle are depleted, while the distribution peaks *almost* along the parallel direction. It is important to note that the relative-momentum distribution is *not* entirely aligned along the photoelectron emission direction.

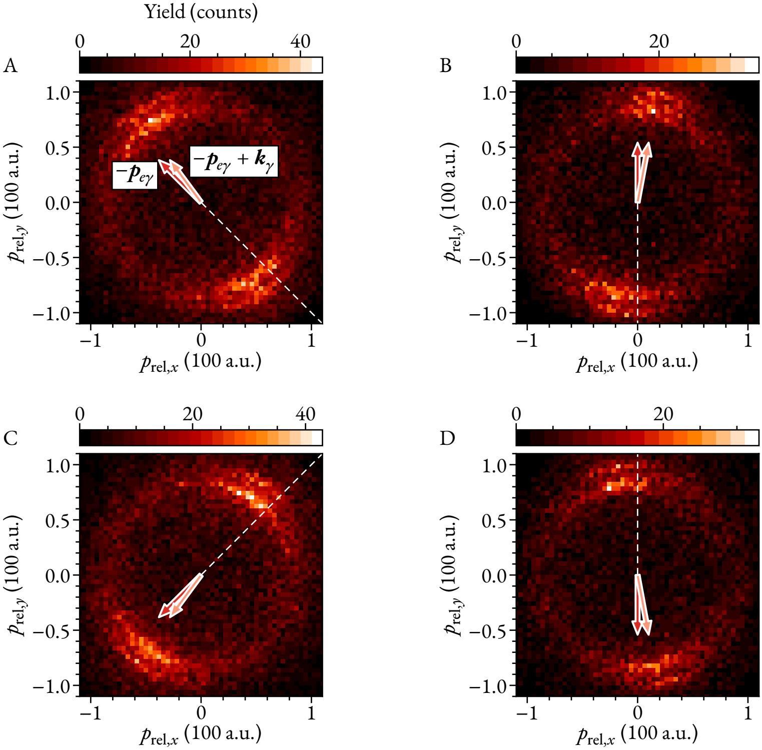

FIGURE 9.5: Relative momenta of the N^+ ions produced by core-shell photoionization of N_2 with $\hbar\omega = 40$ keV for fixed photoelectron emission angles. From A to D, the photoelectron emission direction within the plane is fixed at $\phi_e = -45, -90, 45$, and $90 \pm 10°$, respectively, while the out-of-plane angle is ±10°. In each panel, the dashed-white line indicates the angle ϕ_e, and the arrows are the recoil of the photoelectron and the combined recoil of photon and photoelectron, as labeled in A. (Adapted from [Kir19a].)

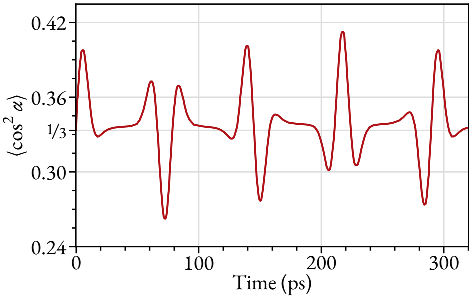

FIGURE 9.6: Rotational state population of the argon dimer. α is the angle between the dimer axis and the laser field polarization. (Taken from [Wu11].)

The reason for this is immediately apparent if one considers the combined momentum transfer of the photon momentum and the photoelectron recoil onto the molecular system. In Figure 9.5, the photon direction is always along positive x. Thus, the combined recoil $-\boldsymbol{p}_{e\gamma} + \boldsymbol{k}_{\gamma}$ is different from the photoelectron recoil $-\boldsymbol{p}_{e\gamma}$ alone. The arrows in each panel represent both recoil momentum vectors. The distribution of $\boldsymbol{p}_{\mathrm{rel}}$ is aligned to that combined recoil, emphasizing the importance of the linear photon momentum in addition to the photoelectron momentum.

The alignment is caused by the rotation of the $N_2^+(1s^{-1})$ intermediate state. At the instant of photoionization, a rotational wave packet is initialized. The wave packet evolves in time, that is, the $N_2^+(1s^{-1})$ rotates. This rotation is quenched by the Auger decay transition of the $N_2^+(1s^{-1})$ intermediate state onto a N_2^{2+} state which eventually Coulomb-explodes and dissociates. Without the Auger decay and the subsequent separation of the two N^+ ions, the rotation would continue and revivals of molecular alignment would show. They are a consequence of the quantization of the angular momentum transfer onto the molecule and are known from nonadiabatic alignment of molecules by strong nonresonant laser pulses. A detailed review of this field is given in Reference [Sta03]. Figure 9.6 shows the periodic alignment and anti-alignment revival structure of argon dimers as simulated by Wu et al. [Wu11]. There, $\langle\cos^2\alpha\rangle$ gives a quantitative degree of alignment. An isotropic distribution corresponds to $\langle\cos^2\alpha\rangle = 1/3$, for values greater than 1/3, the molecule is aligned along the driving laser field polarization. For values lesser than 1/3 the molecule is aligned perpendicular to the polarization [Kun21].

However, from laser based experiments it is known that the revival time for N_2 is with 58.462 ps [Doo03] much longer than the Auger lifetime; all the while an abrupt alignment shortly after the laser pulse is observable, causing the observed alignment in Figure 9.5.

The magnitude of the KER is determined by the potential energy curves

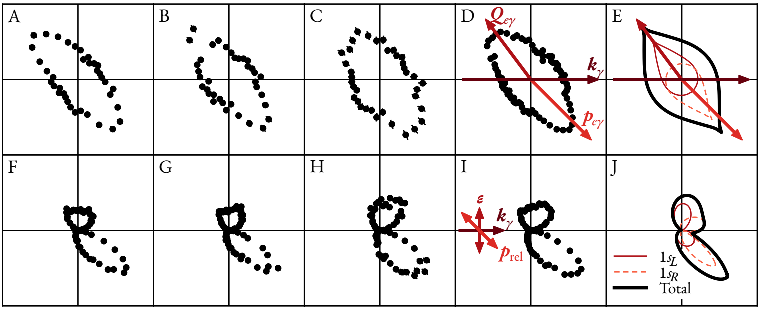

FIGURE 9.7: Polar representation of the angular distributions for the relative and the photoelectron momenta for electrons and N^+ ions produced by photoionization of N_2 with $\hbar\omega = 40$ keV. A–C, Distribution of $\boldsymbol{p}_{\mathrm{rel}}$ for fixed electron emission angles (the same emission angles applied in Figure 9.5A) and different regions of the KER for each panel. F–H, Distributions of $\boldsymbol{p}_{e\gamma}$ for fixed configurations of $\boldsymbol{p}_{\mathrm{rel}}$ and the same KER gates as the panel above, respectively. D,E, Experimental and theoretical distributions of $\boldsymbol{p}_{\mathrm{rel}}$ integrated over all KER, respectively. I,J, Experimental and theoretical distributions of $\boldsymbol{p}_{e\gamma}$ integrated over all KER, respectively. The error bars of the experimental data represent the standard statistical error. The arrows in D and E represent the orientation of $\boldsymbol{k}_\gamma$, $\boldsymbol{p}_{e\gamma}$, and $\boldsymbol{Q}_{e\gamma}$ and apply to each panel in the top row; the arrows in I represent the orientation of $\boldsymbol{k}_\gamma$, $\boldsymbol{\varepsilon}$ and $\boldsymbol{p}_{\mathrm{rel}}$ and apply to each panel in the bottom row. The legend in J applies to E as well. See main of text Section 9.3 for an explanation of the labels therein. (Adapted from [Kir19b].)

of the N_2^{2+} dicationic state (see Figure 9.3, Page 161), and it depends on the internuclear distance R—that is, for small R, the final momenta of the two N^+ ions are large and vice versa. Within the reflection approximation, the internuclear distance and the KER are inversely proportional, that is, $R\,(\mathrm{a.u.}) = 1/\mathrm{KER}\,(\mathrm{a.u.})$ [Gis73]. For a fixed electron emission angle, the momentum transfer $\boldsymbol{Q}_{e\gamma} = -\boldsymbol{p}_{e\gamma} + \boldsymbol{k}_\gamma$ onto the molecular system is constant. Classically, it is then expected that the relative influence of $\boldsymbol{Q}_{e\gamma}$ changes depending on the KER.

In Figure 9.7, this effect is observable. In Panels A to C, the angular distribution of the relative momentum $\boldsymbol{p}_{\mathrm{rel}}$ for a fixed electron emission angle is shown. They are in principal the same distributions as in Figure 9.5A, but in polar representation and with different regions of the KER for each panel. For Panels A to C, the KER ranges from small to large, respectively. Panel D is the data of Figure 9.5A in polar representation without any further gates on the KER. One can observe an elongated distribution for smaller KER and a wider distribution for larger KER. This means that the molecular alignment with respect to the momentum transfer $\boldsymbol{Q}_{e\gamma}$ is less pronounced for breakups with larger KER, that is,

$$\left(\frac{p_{\mathrm{rel}}}{Q_{e\gamma}}\right)_{\text{large KER}} \geq \left(\frac{p_{\mathrm{rel}}}{Q_{e\gamma}}\right)_{\text{small KER}} . \tag{9.10}$$

Figure 9.7D shows—indicated by the arrows—the momentum configuration of the photon and the photoelectron momenta. One can observe again that the angular distribution is not symmetrical with respect to the photoelectron momentum vector but symmetrical with respect to $\boldsymbol{Q}_{e\gamma}$, emphasizing again the relevance of the linear photon momentum.

Panels F to I of Figure 9.7 show the angular distribution of the photoelectron for the same KER gates as the row above and for a fixed direction of $\boldsymbol{p}_{\mathrm{rel}}$. For linearly polarized light and within the dipole approximation (that is, for small photon momenta where the linear momentum k_γ is neglectable), a $(1s)$ photoelectron has a dipole distribution along the polarization direction. No such straight-forward dipole distribution is visible in Figures 9.7F to 9.7I, but a significant forward trend (that is, a trend in photon momentum direction) is visible, as well as a huge up/down asymmetry. These two phenomena are not trivial and will be extensively discussed in the next section. Regardless of these details, one can observe that the asymmetry is the strongest for small KERs and weaker for large KERs. This hints toward the fact, that the asymmetry of the photoelectron angular distribution originates due to the influence of $\boldsymbol{Q}_{e\gamma}$ onto the molecular system.

Theoretical calculations for the angular distributions of Panels D and I are given in Panels E and J, respectively. They accurately describe the experimental results, and details thereof will also be discussed in the following section.

9.3 RECOIL-INDUCED ASYMMETRIES IN MOLECULAR-FRAME PHOTOELECTRON ANGULAR DISTRIBUTIONS

The interaction Hamiltonian describing the interaction of photon and electron includes the term $\exp \mathrm{i}\boldsymbol{k}_\gamma \cdot \boldsymbol{r}$ representing the plane wave of the ionizing field of the photon (see Section 2.3.1, Page 16). Here, $\boldsymbol{r}$ is the position of the electron. Within the dipole approximation, this term is approximated by unity, which neglects the photon momentum [see Equation (2.12), Page 15]. Then, the angular distribution of a photoelectron originating from a $N_2\,(1s)$ shell is a dipole distribution along the direction of $\boldsymbol{\varepsilon}$, the polarization vector of the incident light.

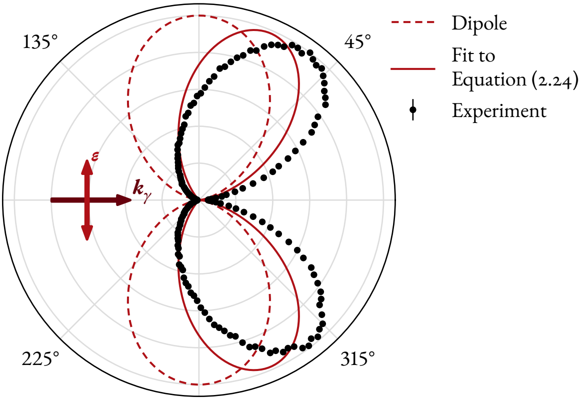

Figure 9.8: Angular distribution of the $N_2(1s)$ photoelectron with $\hbar\omega = 40$ keV in polar representation. The points show the measured photoelectron emission distribution with respect to the photon momentum vector (forward pointing arrow), that is, the distribution of the azimuth angle given by $\arctan2(p_{e\gamma,y}, p_{e\gamma,x})$. The standard statistical error results in error bars smaller than the dot size. The dashed line shows the emission distribution resulting from the dipole approximation, normalized to the maximum of the experimental data. The solid line is a fit of the experimental data to Equation (2.24) with $\phi_{e,\gamma} = 0$, $\beta = 2$, and $\delta = 0$ (see Page 20).

Figure 9.8 shows the angular distribution measured in this experiment (points) overlaid with the expectation where the photon momentum would be neglectable (line). One can clearly see the striking difference: the electron distribution is significantly "bend" in forward direction, that is, the direction of the incident photon momentum vector. The lines shown in Figure 9.8 correspond to dipole (dashed) as well as dipole and quadrupole (solid) transitions. The experimental data is not properly described by these transitions, showing that at $\hbar\omega = 40$ keV, higher-order transitions cannot be neglected to properly describe the experimental findings. This aspect will be more extensively discussed in Section 9.4, starting on Page 178

In Figure 9.8, the molecule is randomly oriented, that is, the orientation of the vector $\boldsymbol{p}_{\text{rel}}$ is isotropic (see Figure 9.1, Page 159). Within the axial recoil approximation the direction of $\boldsymbol{p}_{\text{rel}}$ corresponds to the orientation of the molecule [Zar72; Web01] and thus, by knowledge of $\boldsymbol{p}_{\text{rel}}$ one gains access to the molecular-frame photoelectron angular distributions (MFPADs).

However, Figure 9.9 shows that the axial recoil approximation is not valid for the present experimental conditions, and the ramifications thereof originate the structure visible in the figure. In the figure, Panels K to O show

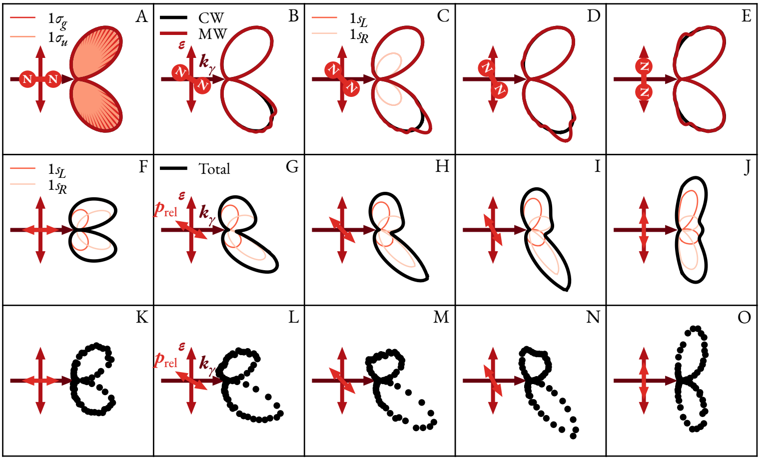

Figure 9.9: Polar representation of the molecular-frame angular distributions of the 1s photoelectrons of N_2 induced by $\hbar\omega = 40$ keV for fixed orientation of N_2 or fixed orientation of $\boldsymbol{p}_{\mathrm{rel}}$. A–E, Calculations using Coulomb wave (cw) and accurate molecular wave (mw) functions (see legend in B), where in each panel the molecular orientation is different (and indicated by the inset). In A and C, the partial cw contributions of the $1\sigma_{g/u}$ and the $1s_{R/L}$ orbitals are shown, respectively. (R/L indicate the *left* or *right* nitrogen molecule.) The contributions of $1s_{R/L}$ are both identical. F–J, Theoretical simulations considering the combined impact of $\boldsymbol{Q}_{e\gamma} = -\boldsymbol{p}_{e\gamma} + \boldsymbol{k}_\gamma$ (see legend in F and G), where in each panel the $\boldsymbol{p}_{\mathrm{rel}}$ is fixed as indicated by the insets. K–O, Experimental results. The error bars represent the standard statistical error. In each panel, the photon polarization vector is indicated by the up/down double arrow, and the photon momentum direction is indicated by the right-pointing arrow. (Taken from [Kir19b].)

the electron angular distribution for different orientations of $\boldsymbol{p}_{\mathrm{rel}}$. Panels A to E and Panels F to J show different theoretical approaches to explain the experimental results, respectively. Note that the theoretical considerations in Panels A to E fix the molecular orientation at the instant of the photoreaction, while all other panels fix the orientation of the finally measured relative momentum $\boldsymbol{p}_{\mathrm{rel}}$. The orientation is indicated by the insets of each panel, respectively. For the experimental data the out-of-plane angle of $\boldsymbol{p}_{\mathrm{rel}}$ is restricted to ±20°.

First, let us discuss the experimental results of Figures 9.9K to 9.9O. There, the same angular distribution as in Figure 9.8 is shown, the difference being the selection of $\boldsymbol{p}_{\mathrm{rel}}$. The distributions are significantly different. For instance, in the case of parallel (Panel K) and perpendicular (Panel O) orientation of $\boldsymbol{p}_{\mathrm{rel}}$ with $\boldsymbol{k}_\gamma$, the distribution is compressed or elongated, respectively. This means, the forward/backward asymmetry is stronger for parallel orientation of $\boldsymbol{p}_{\text{rel}}$ and $\boldsymbol{k}_\gamma$ as compared to perpendicular orientation. In Panels L to N, the angles between $\boldsymbol{p}_{\text{rel}}$ and $\boldsymbol{k}_\gamma$ are 120, 135, and 170 ± 10°, respectively. Huge up/down asymmetries are observable. No such asymmetry is observable for randomly oriented molecules.

What is the origin of this symmetry breaking? The homonuclearity of N_2 hides the origin of the photoelectron and therefore, it is unknown if the photoelectron was emitted from the forward (in direction of the incoming photon) or backward pointing nitrogen atom. Then, the probability that the electron was emitted from the up-pointing nitrogen atom or the down-pointing nitrogen atom is equal. Consequently, one would expect the emission direction to be symmetric with respect to the up/down direction.

The molecular potential influences the MFPADs. However, at high photoelectron energies the effect of the molecular potential vanishes. This was observed in the molecular-frame Compton electron angular distributions (MFCADs) shown in Figure 8.9 (Page 147). There, the MFCADs are elongated along the molecular axis for small Compton electron momenta. However, already at momentum magnitudes of 8 a.u., the influence of the molecular potential practically vanishes. The photoelectron, however, has a much larger momentum of 54.9 a.u. For these high momenta the Born approximation describing the outgoing electron by a plane wave without the modifications by the potential should be very accurate, and the different orientations of the N_2 molecule would explain the huge up/down asymmetry. Another possible source are asymmetries in the spatially oriented, localized electronic initial states.

Both these possible origins for the up/down asymmetry are tested by the calculations shown in Figures 9.9A to 9.9E. There, calculations within the stationary single center method [Dem11] are performed. The first employed set of calculations describes the outgoing electron by a Coulomb wave (CW). There, the initial $1\sigma_{g/u}$ or $1s_{R/L} = {}^1\!/\!\sqrt{2}(1\sigma_g \mp 1\sigma_u)$ orbitals were calculated in the molecular field. For the final continuum states, Coulomb waves of energy $E_{e\gamma} = 39.59$ keV, momentum $p_{e\gamma} = 54.9$ a.u., and effective charge $Z = 1$ were chosen [Kir19b]. Note that at these photoelectron energies, the electron has relativistic velocities. Choosing Coulomb waves for the final states eliminates the influence of the molecular potential on the photoelectron, and thus, one can observe a potential influence of the spatially oriented, localized initial states. No such influence is observable in Figures 9.9A to 9.9E; the CW calculations are virtually identical in every panel. The nondipole effects were considered by the inclusion of partial electron waves with momentum quantum numbers $\ell \leq 90$ and $|m| \leq 6$. The final photoelectron angular distribution is the sum of the two contributing initial states. As an example, the $1\sigma_{g/u}$ contributions are shown in Figure 9.9A and the $1s_{L/R}$ contributions in Figure 9.9C. The CW calculations show a strong backward/forward asymmetry and accurately describe the photoelectron angular distribution for randomly oriented molecules (Figure 9.8).

Next, the influence of the molecular potential—which is asymmetric with respect to the photon up/down direction—is tested in a second set of calculations, shown by the thick solid red line in Figures 9.9A to 9.9E. There, the nonspherical potential of the molecular ion is mixed with the partial photoelectron waves using the stationary single-center method as well [Kir19b]. Using these accurate molecular wave (MW) functions results in a significant modification of the MFPADs, most prominent in the forward-direction nitrogen atom (see Panels C and D). However, these asymmetries are far from explaining the asymmetries observable in the experimental distributions.

The spectra already shown in Figure 9.7 on Page 171 give a lead on the origin of the asymmetry. There, one could observe a dependence of the strength of the asymmetry on the KER, as long as one fixes the electron emission direction. We also learned that the photoelectron and photon momentum recoil cause a rotation of the molecular N_2^+ ion. Then it is clear that the axial recoil approximation is invalid and one cannot determine the molecular orientation at the instant of the photoreaction by measuring the final relative momentum $\boldsymbol{p}_{\text{rel}}$.

Intuitively, one can describe the kinematics of the problem as follows: The photon is absorbed locally by one nitrogen atom and a photoelectron is emitted. The recoil of the photoelectron as well as the momentum of the photon, that is,

$$\boldsymbol{Q}_{e\gamma} = -\boldsymbol{p}_{e\gamma} + \boldsymbol{k}_{\gamma}, \tag{9.11}$$

transfer angular momentum and induce a rotation of the $N_2^+(1s^{-1})$ intermediate state, which eventually Auger decays onto a N_2^{2+} state and ultimately Coulomb-explodes. The angular momentum transfer ranges from $0\hbar$ ($\boldsymbol{Q}_{e\gamma}$ parallel to the molecular axis) to about $68\hbar$ ($\boldsymbol{Q}_{e\gamma}$ perpendicular to the molecular axis) [Kir19b]. This assumes an equilibrium internuclear distance of the N_2 ground state of 2.074 a.u. and a maximum recoil of $Q_{e\gamma} \approx 66$ a.u. Thus, the theoretical angular distributions of Figures 9.9A to 9.9E—which are calculated within the axial recoil approximation, that is, with respect to the molecular axis before the instant of photoabsorption—must be corrected depending on (1) the relative orientation of $\boldsymbol{Q}_{e\gamma}$ and the molecular axis, (2) the KER value, and (3) the instant of the Auger decay. The angular momentum transfer depends on (1) and (2), while the instant of the molecular breakup depends on (3).

The experimentally measured value of $\boldsymbol{p}_{\mathrm{rel}}$ includes half of the locally transferred momentum recoil $\boldsymbol{Q}_{e\gamma}$ [a consequence of the definition of $\boldsymbol{p}_{\mathrm{rel}} \equiv 1/2(\boldsymbol{p}^{\mathrm{A}}_{\mathrm{N}^+} - \boldsymbol{p}^{\mathrm{B}}_{\mathrm{N}^+})$]. Additionally, a larger KER corresponds to a smaller internuclear distance and thus, the angular momentum transfer by $\boldsymbol{Q}_{e\gamma}$ is smaller. Similarly, for smaller KER (that is, larger internuclear distances), the angular momentum transfer is larger. After the angular momentum transfer, the molecule rotates until the N_2^+ molecule Auger decays. For instance, at the equilibrium internuclear distance and for maximal angular momentum transfer ($\boldsymbol{Q}_{e\gamma}$ perpendicular to the molecular axis) the molecule rotates about 19° during the average Auger lifetime of about 7 fs. For the corrections, (3) was considered by weighing the distributions after corrections, (1) and (2) by the exponential distribution of Auger decay times. The resulting spectra are shown in Figures 9.9F to 9.9J. These accurately predict the experimental distributions of Panels K to O.

Following the underlying model outlined above, what is the origin of the observed asymmetry?

To explain it, let us consider an example configuration where the angle between the incident photon and the molecular axis is 135°. For a qualitative explanation, the effect of the photon momentum $\boldsymbol{k}_\gamma$ can be ignored. The photoelectron angular distribution is then given by the MW calculations of Figure 9.9C. The recoil of the photoelectron induces a rotation, which, due to the forward/backward asymmetry, is directed in the backward direction in the majority of cases. The recoil results in an angular momentum transfer and rotation of the molecule, where upward emitted photoelectrons induce a counterclockwise rotation and downward emitted photoelectrons a clockwise rotation. However, the magnitude of the angular momentum transfer differs for upward and downward emitted photoelectrons due to the orientation of molecular axis. For instance, the most likely emission direction results in a perpendicular emission direction for upward emitted photoelectrons and a parallel emission direction for downward emitted ones.

Thus, for upward directed photoelectron emissions the molecule will rotate counterclockwise, resulting in measured relative momenta $\boldsymbol{p}_{\mathrm{rel}}$ larger than 135°. Then, by measuring the photoelectron angular distribution with respect to $\boldsymbol{p}_{\mathrm{rel}}$, where $\boldsymbol{p}_{\mathrm{rel}}$ is fixed in space at 135° (Figures 9.9H and 9.9M), the orientation of the actual molecular axis was smaller than 135°, and, on average, the angle $\angle(\boldsymbol{p}_{e\gamma}, \boldsymbol{p}_{\mathrm{rel}})$ is bigger than $\angle(\boldsymbol{p}_{e\gamma}$, molecular axis$)$. Then, the anisotropy of the photoelectron angular distribution, in particular—the forward/backward asymmetry—result in a depletion of intensity of photoelectrons emitted upward.

For the other case, that is, the photoelectron is emitted downward, the most likely emission direction does not induce a molecular rotation and the measured relative momentum $\boldsymbol{p}_{\mathrm{rel}}$ corresponds with the molecular axis. Then, no depletion of the intensity takes place.

Finally, following the same considerations (1) to (3), the theoretical predictions of Figure 9.7E (Page 171) are calculated with an average value of KER = 10 eV. The distributions shown in Figures 9.7I and 9.7J are the same as shown in Figures 9.9H and 9.9M, respectively.

9.4 PHOTON-MOMENTUM IMPACT ON ELECTRON AND ION EMISSION PATTERNS

The last phenomenon of photoionization of N_2 discussed here investigates the effect of the photon momentum on the ions' and the photoelectron's momentum distributions. Momentum conservation for the photoreaction reads

$$\boldsymbol{k}_{\gamma} + \boldsymbol{p}_{\mathrm{N}_2} = \boldsymbol{p}^{\mathrm{A}}_{\mathrm{N}^+} + \boldsymbol{p}^{\mathrm{B}}_{\mathrm{N}^+} + \boldsymbol{p}_{e\gamma} + \boldsymbol{p}_{e\mathrm{A}} \,. \tag{9.12}$$

Since the photon is absorbed, its momentum has to be compensated by the sum momentum of all final reaction particles. Initially, the nitrogen molecule is at rest ($\boldsymbol{p}_{\mathrm{N}_2} = 0$ a.u.). Thus, the momentum within the center-of-mass system of all particles must be zero. Due to the much larger mass of the two nitrogen atoms compared to the two electrons, the center-of-mass system of all particles is virtually identical with the center-of-mass system of the two N^+ ions. It follows that the photon momentum is compensated by $\boldsymbol{p}_{\mathrm{sum}} \equiv \boldsymbol{p}^{\mathrm{A}}_{\mathrm{N}^+} + \boldsymbol{p}^{\mathrm{B}}_{\mathrm{N}^+}$. Further, the recoil of both electrons is reflected in $\boldsymbol{p}_{\mathrm{sum}}$. This results in the shift observable in Figure 9.10A (note that this is the same distribution shown in Figure 9.1D on Page 159). Since the Auger electron is measured and using Equation (9.12), one can calculate the photoelectron's momentum, which is shown in Figure 9.10B.

Panels C and D of Figure 9.10 show a projection of the above spectra onto the x direction, that is, the direction of the incident photon. Naïvely, since the photon momentum is compensated by $\boldsymbol{p}_{\mathrm{sum}}$, one would expect the sum

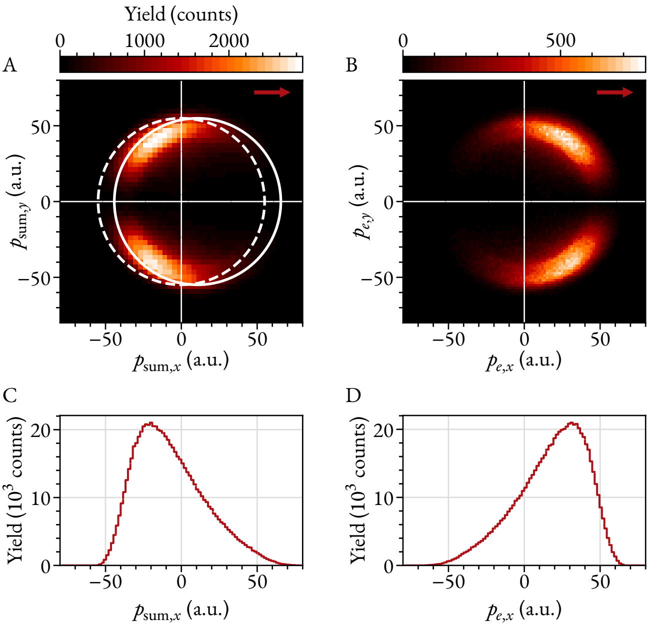

FIGURE 9.10: Ion sum and photoelectron momenta produced by photoionization of N_2 with $\hbar\omega = 40$ keV. A,B, Sum momenta and photoelectron momenta within the xy plane, respectively. In the sum momentum, the effect of the Auger electron's recoil has already been compensated. The direction of the incident photon is indicated by the top-right arrow. C,D, Projection of A and B onto the x axis, respectively. See main text for an explanation of the circles in A.

momentum to be shifted forward by the amount k_γ. However, as can clearly be seen, the momentum distribution in Figure 9.10C leans *toward* the photon direction, as if the radiation pressure of the photon *attracts* the ions. To quantize this, the mean sum momentum in photon direction is caluclated, that is,

$$\langle p_x \rangle = \frac{1}{\sum_{i=1}^{N} N_i} \sum_{i=1}^{N} p_{x_i} N_i \,, \tag{9.13}$$

where p_{x_i} is the momentum value and N_i the counts of the ith bin of the histogram in Figure 9.10C. This results in a mean sum momentum $\langle p_{\text{sum},x} \rangle = -7.07$ a.u. To guide the eye, a solid-line circle is overlaid on the distribution of Figure 9.10A. The radius of that circle is given by the photoelectron's momentum of 54.9 a.u. It is not centered around zero, but shifted by the photon momentum k_γ. The dashed-line circle has the same radius but is centered around zero. One can clearly see that the distribution of $\boldsymbol{p}_{\text{sum}}$ is following the shifted circle, which means that, indeed, the photon's momentum is transferred on the ionic fragments, as momentum conservation dictates. However, in the singly differential spectrum of Figure 9.10a this fact is obfuscated.

The backward shift of $\langle p_{\text{sum},x} \rangle$ requires a forward shift of the corresponding photoelectron mean momentum $\langle p_{e\gamma,x} \rangle$, that is, in fact, larger than the momentum of the photon. This peculiar property of the photoelectron was already observed but left unexplained in 1927 by Auger and Perrin [Aug27]. A first explanation was given by Sommerfeld and Schur in 1930, [Som30]. 2014, Chelkowski, Bandrauk, and Corkum derived a relationship between the photon momentum, and the ion's sum and photoelectron's mean momentum [Che14]:

$$\langle p_{\text{sum},x} \rangle = -\frac{3}{5}\frac{E_\gamma - E_{\text{bind}}}{c} + \frac{E_{\text{bind}}}{c} = -\frac{3}{5}k_\gamma \bigg|_{E_{\text{bind}}=0} , \qquad (9.14)$$

$$\langle p_{e\gamma,x} \rangle = \frac{8}{5}\frac{E_\gamma - E_{\text{bind}}}{c} = \frac{8}{5}k_\gamma \bigg|_{E_{\text{bind}}=0} . \qquad (9.15)$$

Here, E_{bind} is the ionization threshold of $N_2(1s)$, which can be ignored since $\hbar\omega \gg E_{\text{bind}}$. To observe the relations of Equations (9.14) and (9.15), multiple experimental runs with varying photon energy where performed, namely $\hbar\omega = 12, 20, 28$, and 40 keV, which corresponds to $k_\gamma = 3.3, 5.5, 7.5$, and 10.7 a.u., respectively.

Figure 9.11 shows the doubly and singly differential distributions of the sum momentum for each run. Note that Figures 9.11d and 9.11h are the same spectra of Figures 9.10a and 9.10c, respectively. For each run, the photoelectron momentum distribution is calculated and $\langle p_{e\gamma,x} \rangle$ is determined. The results are summed up in Figure 9.12. There, the excellent agreement of the expectations of Equations (9.14) and (9.15) and the experimental data confirm quantitatively the long-lasting, counterintuitive backward emission of photoions and the large forward-directed photoelectron. The emission of the photoion toward the incident light direction is a result of the recoil of the photoelectron, which, due to nondipole effects, is forward directed.

The experimental data presented here ranges from photon energies of 12 to 40 keV and are published in Reference [Gru20a]. There, the scaling effect of Equations (9.14) and (9.15) are also observed for photon energies ranging from 600 to 1775 eV in an experiment, where photoionization of

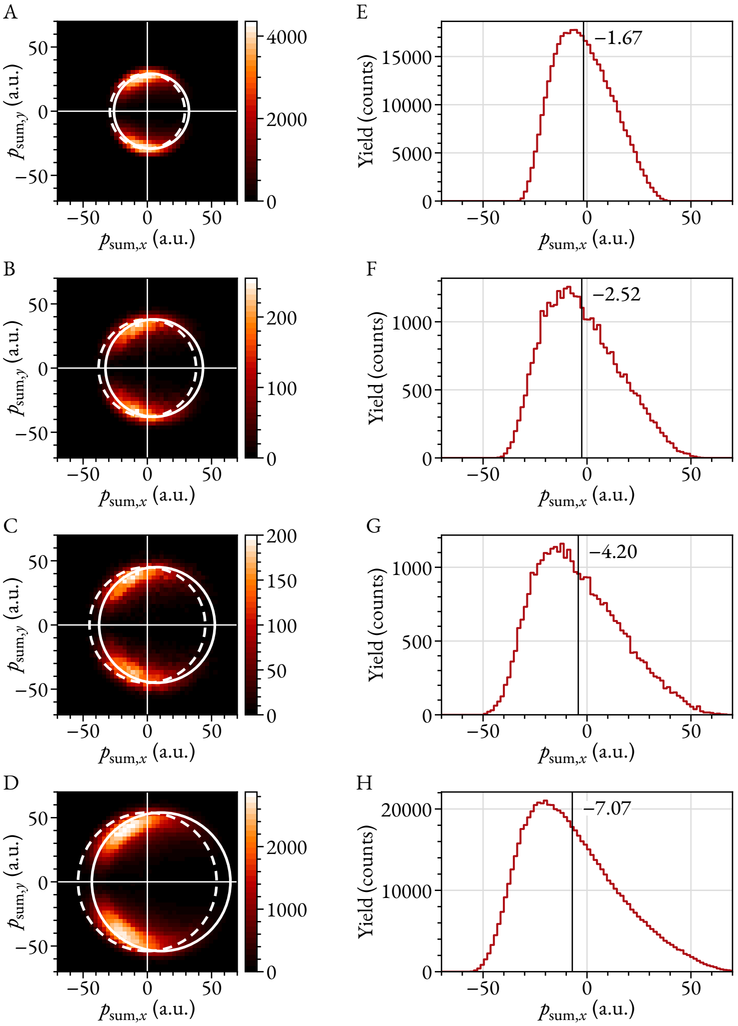

FIGURE 9.11: Histograms of N^+ ion sum momenta for different photon momenta k_γ. From the top to the bottom row, the photon momenta are 3.3, 5.5, 7.5, and 10.7 a.u., respectively. A–D, Sum momenta in the plane spanned by the incoming light (x) and the polarization vector (y). The dashed circles are centered around zero with a radius $p_e \approx (2\hbar\omega - E_{\mathrm{bind}})^{1/2}$. The solid circles are the dashed circles shifted by the photon momentum k_γ. The color scale depicts counts. E–H, Histogram of $p_{\mathrm{sum},x}$. The vertical line marks the expectation value $\langle p_{\mathrm{sum},x} \rangle$, calculated using Equation (9.13). The number next to it is its numerical value in atomic units.

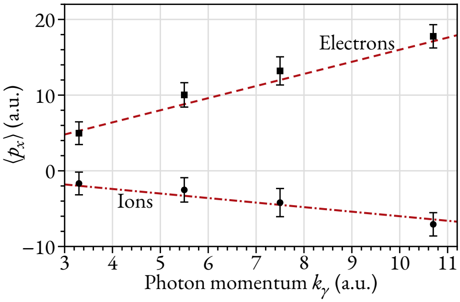

FIGURE 9.12: Photon momentum versus mean momentum in light direction. The upper and lower lines are $8/5k_\gamma$ and $-3/5k_\gamma$, respectively [Equations (9.14) and (9.15)]. (Adapted from [Gru20a].)

helium was measured and therefore, combined with the data presented here, the theoretical predictions are confirmed over an enormous photon energy range.

9.A EXPERIMENTAL FITS OF FIGURE 9.4

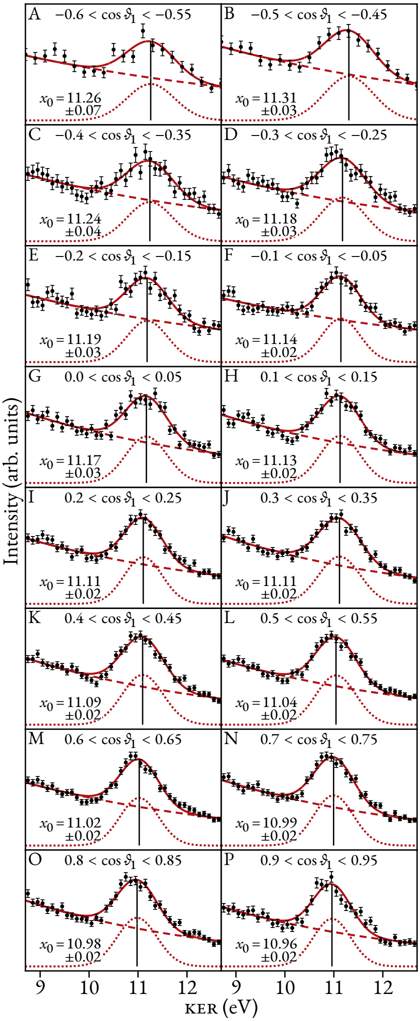

FIGURE 9.13: Experimental fits to obtain the KER peak position for different configurations of the photoelectron and photon momentum for photoionization of N_2 at $\hbar\omega = 40$ keV. For each panel, ϑ_1 is the emission angle of the photoelectron with respect to the incoming light axis. A Gaussian (dotted line) overlapped with an exponential function (dashed line) [see Equation (9.4), Page 164] is used to fit the experimental data (points). The solid line is the resulting fit. In each panel, x_0 is the expectation value of the Gauss function as obtained by the fit and as marked by the vertical line.

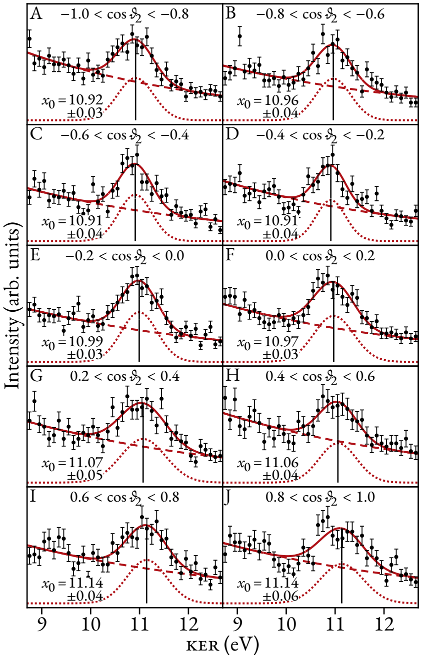

Figure 9.14: Experimental fits to obtain the KER peak position for different configurations of the Auger electron momentum and the sum of photoelectron and photon momentum for photoionization of N_2 at $\hbar\omega = 40$ keV. For each panel, ϑ_2 is the emission angle of the photoelectron in respect to the incoming light axis. A Gaussian (dotted line) overlapped with an exponential function (dashed line) [see Equation (9.4), Page 164] is used to fit the experimental data (points). The solid line is the resulting fit. In each panel, the bottom-left number is the expectation value x_0 of the Gauss function as obtained by the fit as marked by the vertical line.

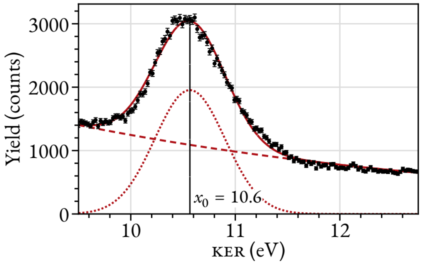

Figure 9.15: Fit to determine the peak position of the KER distribution resulting from Compton scattering at $\hbar\omega = 40$ keV at N_2. A Gaussian (dotted line) overlapped with an exponential function (dashed line) [see Equation (9.4), Page 164] is used to fit the experimental data (points). The solid line is the resulting fit. $x_0 = 10.566 \pm 0.004$ eV is the expectation value of the Gauss function, as obtained by the fit.

9.B CALIBRATION AND EXPERIMENTAL PARAMETERS

The same calibration of Chapter 8 was used and, since the results were recorded simultaneously, the experimental parameters are identical as well (see Sections 8.B and 8.C).

The Philosopher
You know so much about nothing at all

Ch. Schuldiner

Part III

CONCLUSIONS

SUMMARY AND OUTLOOK 10

In summary, this work investigated the kinematics of Compton scattering at gaseous, internally-cool helium and molecular nitrogen targets in the high-energy ($\hbar\omega = 40\,\mathrm{keV}$) and the low-energy ($\hbar\omega = 2.1\,\mathrm{keV}$) regime. Additionally, photoionization at molecular nitrogen with high-energy photons was investigated. These experimental regimes were previously inaccessible due to the extremely small cross sections involved. Nowadays, the third- and fourth-generation synchrotron machines produce sufficient photon flux, enabling the investigation of the above processes. The utilized cold-target recoil-ion momentum spectroscopy (COLTRIMS) technique further increases the detection efficiency of the observed processes, since it enables full-solid-angle detection by exploiting momentum conservation.

Compton scattering was investigated at photon energies of $\hbar\omega = 2.1$ (helium) and 40 keV (helium and N_2). In the high-energy regime, the impulse approximation is mostly valid, which is not the case for the low-energy regime. The impulse approximation assumes that the Compton-scattering process takes place at a free electron with a momentum distribution as if it was bound, thus ignoring the binding energy of the system.

Photoionization of N_2 was investigated at photon energies of $\hbar\omega = 40\,\mathrm{keV}$. At 40 keV, the linear photon momentum $\boldsymbol{k}_\gamma = \boldsymbol{p}_\gamma/\hbar$ cannot be neglected, as is the fashion of the commonly used dipole approximation.

Part I introduces the necessary theoretical and experimental background necessary in order to understand the results of this work. In Chapter 2, inelastic x-ray scattering and photoabsorption processes are introduced, including the dipole approximation (photoabsorption) and the impulse and A^2 approximation (Compton scattering). In Chapter 3, atoms and molecules as described in quantum mechanics are discussed. Chapter 4 introduces the experimental setup, including the discussion of synchrotron radiation and an overview of the COLTRIMS technique. Chapter 5 briefly introduces the necessary steps of the offline data analysis.

The results of this work are presented in Part II. Chapters 6 to 8 present the results of the investigation of the Compton scattering process; Chapter 9 the results of high-energy photoionization.

Chapter 6 presents the results of the low-energy Compton scattering experiment. Helium in the gas-phase was investigated with photons of $\hbar\omega = 2.1\,\mathrm{keV}$. The experiment was performed in October 2017 at beam line P04 of the PETRA III synchrotron at DESY, Hamburg. At photon energies of $\hbar\omega = 2.1\,\mathrm{keV}$, the impulse approximation is invalid. This is emphasized by the following simple consideration: at $\hbar\omega = 2.1$ keV, the energy transfer corresponding to the maximum momentum transfer—the result of photon back-scattering—is about 17.1 eV, which is well below the the ionization threshold of helium of 24.6 eV. The experimental findings were compared with theoretical calculations within the A^2 approximation specifically performed for this work. The agreement of theoretical calculations and experiment is excellent. The spectra obtained by the experiment resemble predictions for neutron scattering [Pin14] or attosecond half-cycle laser pulses [Arb09] and are qualitatively already known from ionization by electron [Ehr86] or ion [Fis03] impact. It shows that in this energy regime (where the A^2 approximation is valid), photon scattering can be pictured as a two-step process. In the first step, the photon scatters at the target electrons, resulting in a sudden momentum transfer onto the target system. In the second step, the sudden momentum transfer results in a finite probability for target ionization. The origin of the momentum transfer (be it photon scattering, or some other scattering process) is not explicitly necessary for a qualitative description of the process.

Chapter 7 presents the results of the high-energy ($\hbar\omega = 40$ keV) Compton scattering experiment at gas-phase helium. The experiment was performed in April 2018 at beam line ID31 of the ESRF, Grenoble and observed helium double ionization as result of the single Compton scattering event. The double ionization of helium is solely the result of electron-electron correlations. At $\hbar\omega = 40$ keV, both final-state electron-electron or initial-state electron-electron correlations are responsible for the double ionization process, as is confirmed by multiple sets of theoretical calculations which were performed to model the experimental results. Excellent agreement of experimental data and theoretical calculations is achieved, with the additional insight that excluding either initial-state or final-state electron-electron correlations results in a worse agreement of theory and experiment. The experiment also shows that helium double ionization by Compton scattering does not alter the momentum distribution of the helium nucleus in the ground state, since the helium nucleus is only a spectator in the photon/electron interaction. Thus, the helium nucleus momentum profile reflects the two-electron momentum profile of the helium ground state.

Chapter 8 presents the results of a Compton scattering experiment with a molecular target. The experiment was performed in August 2018 at beam line ID31 of the ESRF, Grenoble, where Compton scattering at gas-phase N_2 at $\hbar\omega = 40$ keV was observed. With the chosen target and at the chosen photon energy, core- and valence-shell ionization by Compton scattering were detected. Valence-shell Compton scattering ignores the molecular nature of the gas target, while in the case of core-shell Compton scattering, the subsequent Auger decay and molecular breakup give access to the molecular axis at reaction time. Since the N_2 target is in its rotational and vibrational ground state, the measured momenta of the two N^+ cations correspond to the molecular axis. Access to the molecular axis enables the transformation of the electron's emission direction from the laboratory frame into the molecular frame. This way, the first molecular-frame Compton-electron angular distributions have been observed and presented in this work. Further, the identification of the involved subshell at which Compton scattering occurred via the detection of the Auger electron enables the measurement of the electron's momentum distributions for each subshell distinctively.

Chapter 9 presents the results of photoionization of N_2 at $\hbar\omega = 40$ keV. In this hard x-ray regime, the dipole approximation is invalid, which is observed in a drastic forward/backward asymmetry of the photoelectron emission pattern. At these photon energies, the photon momentum as well as the photoelectron's momentum recoil influence the molecular dynamics. This is directly observed in the kinetic energy release (KER) which is altered by the ionization process. The KER is shifted toward larger energies. The shift depends on the configuration of all momenta involved: the configuration given by the molecular axis, the photoelectron, the Auger electron, as well as the photon. The recoil of the photoelectron also causes a rotation of the molecule, which consequently breaks the assumptions of the axial recoil approximation. Hence the orientation of the molecule at reaction time does not coincide with the direction of the relative momentum of both nitrogen cations. This causes huge asymmetries in the molecular-frame photoelectron angular distributions, as has been observed and theoretically explained in this work. Further, the linear photon momentum results in a forward shift of the photoelectron's mean momentum larger than the magnitude of the photon momentum. This results in a backward shift of the photoion's mean momentum, seemingly causing an attraction of the photoion toward the incident light. The photoelectron's mean-momentum shift is quantitatively described by $8/5 \times k_\gamma$ while for the photoion, the shift equals $-3/5 \times k_\gamma$, ensuring momentum conservation—that is, the large forward shift of the photoelectron is compensated by the backward shift of the photoion.

* * *

In conclusion, this work demonstrates that although Compton scattering is a well-known effect of quantum dynamics, the first experimental proof of the existence of the photon momentum, and an entry-level example of quantum dynamics at the high-school level, that Compton scattering yet is an entrancing field of modern science. The small cross section of the process eluded a dynamically-complete observation of the process until modern photon sources and detection techniques were—as demonstrated here—able to shine light onto up to now experimentally unobserved phenomena.

The research on Compton scattering—particularly the research utilizing the COLTRIMS technique—is far from exhausted. An outlook on potential future research is listed in the following.

For high-energy Compton scattering at N_2, an increased intensity of electrons with a momentum close to zero has been measured (see Figure 8.3, Page 139 and Figure 8.5, Page 142). The origin thereof stays unanswered by this work. Here, it has been speculated that it may be an effect of the binding energy of N_2. However, the simulations performed (see Figure 8.2, Page 138) were based on a quite possibly much too simplistic model, as has been discussed in Section 8.1. Further, in the case of core-shell Compton scattering at N_2, the experimental setup utilized for this work was not able to sufficiently distinguish between all reaction channels that result in electrons with a momentum close to zero. The experimental shortfall could be addressed with an adjusted spectrometer with increased momentum resolution on the ionic fragments, which is necessary to accurately distinguish between the reaction channels; namely, Compton scattering at a core-shell electron with small scattering angles and with subsequent Auger decay and Compton scattering at a valence-shell electron with a subsequent shakeoff or knockout process. Both reactions result in a molecular breakup with two N^+ cations and an electron with small momentum. They are distinguishable by the Auger electron's recoil onto the sum momentum of the ionic fragments. Further, proper theoretical calculations for the experimental parameters could be performed to confidently identify the origin of the low-momentum electrons.

The complete kinematics of Compton scattering at helium were observed in the performed low-energy ($\hbar\omega$ = 2.1 keV) experiment. At these photon energies, the final Compton electron's energy was detectable with (almost) full solid angle. For large photon energies, the complete kinematics could not be observed since the energy of the final Compton electron is too large to be detectable for the majority of scattering angles. However, performing an experiment at large photon energies—that is, photon energies large enough that the impulse approximation is valid for at least a portion of photon scattering angles—promises interesting results. Such an experiment would bridge the two energetic regions that have been investigated in this work. If one were able to detect all charged reaction particles with full solid angle resulting from

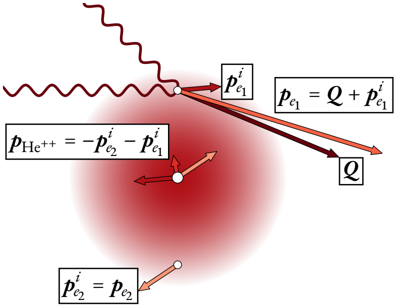

Figure 10.1: Sketch of helium double ionization by Compton scattering with large momentum transfers. The photon scatters at Electron e_1 (wiggly lines), transferring the momentum $\boldsymbol{Q}$. Due to the shakeoff mechanism double ionization occurs. Only the momenta $\boldsymbol{p}_{\mathrm{He}^{++}}$ of the helium nucleus and $\boldsymbol{p}^{e_2}_f$ of the shakeoff electron are measured in coincidence. The final momentum of the shakeoff electron corresponds to its initial bound-state momentum. The initial momentum of the Compton electron can be calculated via $\boldsymbol{p}^{e_1}_i = -\boldsymbol{p}_{\mathrm{He}^{++}} - \boldsymbol{p}^{e_2}_f$. These considerations are only valid within the impulse approximation and under the assumption that no knockout process occurs.

electronic shells with a relatively large binding energy [for example, Ne(1*s*) with $E_{\mathrm{bind}} = 870.2\,\mathrm{eV}$] at sufficiently large photon energies (for example, $\hbar\omega = 20\,\mathrm{keV}$), one could observe the kinematics of Compton reactions that transition from energetic regions where the impulse approximation is invalid to a region where it is.

Compton scattering at molecular targets is another interesting subject to study further. To the best of my knowledge, Compton scattering in a molecular reference frame has not been investigated experimentally up to this point. The angular distribution of the Compton electron in the molecular frame has been unobserved to this point. The distributions obtained in this work (Figure 8.9, Page 147) lack a proper theoretical comparison, which could be the subject of future work. Directional Compton profiles in molecules, that is, the electron momentum distribution parallel or perpendicular to the molecular axis, have been calculated theoretically [Kai76; Tha86]. Accurate measurements of the N_2 Compton profile have been performed by Kobayashi et al. [Kob11], however, not the Compton profile in reference to the molecular axis.

The results presented in Chapter 7 show that at $\hbar\omega = 40\,\mathrm{keV}$, the electron momentum distributions produced by double ionization of helium are influenced to a significant degree by final-state electron-electron correlations (that is, double ionization due to the knockout mechanism). As has been demonstrated in Reference [Chu22], helium double ionization by Compton scattering can be a method of dynamical spectroscopy of the ground-state electron-electron correlations. The results presented in this work fail to do this, as at the chosen photon energy, double ionization is not solely the result of initial-state electron-electron correlations (that is, double ionization due to the shakeoff mechanism). Double ionization due to the knockout mechanism is only significant for scattering angles smaller 40°, since the probability of knockout drops for increasing energy of the Compton electron. Increasing the photon energy to reduce the scattering events that contribute to double ionization by knockout or utilizing a photon detector to detect photons with small scattering angles, thus rejecting double ionization events by knockout, could remove the influence of final-state electron-electron correlations. Then, the detection of the shakeoff electron in coincidence with the He^{2+} nucleus directly gives access to an experimental image of the square of the correlated two-electron ground-state wave function $\Psi(\boldsymbol{p}_i^{e_1}, \boldsymbol{p}_i^{e_2})$. Figure 10.1 sketches the principle behind this idea.

DEUTSCHE ZUSAMMENFASSUNG

11

Im Rahmen dieser Arbeit wurde der Compton-Effekt an gasförmigem Helium und molekularem Stickstoff bei niedrigen ($\hbar\omega = 2.1$ keV) sowie hohen ($\hbar\omega = 40$ keV) Photonenenergien untersucht. Der Compton-Effekt bezeichnet die inelastische Streuung eines Photons an einem freien oder gebundenen Elektron. Im Falle eines gebundenen Elektrons ist der Energieübertrag in der Streuung ausreichend, um das System, in dem es gebunden ist, zu ionisieren. Zusätzlich wurde Photoionisation von molekularem Stickstoff bei hohen Photonenenergien untersucht.

Die vorgestellten Experimente geben Einsicht in die kinematischen Eigenschaften der Compton-Streuung. Insbesondere im Falle der Niedrigenergieexperimente an Helium wurde die *vollständige* Kinematik beobachtet, was in dieser Form erstmalig realisiert werden konnte. Im Gegensatz zu typischen Experimenten zur Untersuchung des Compton-Effekts, bei denen das gestreute Photon (manchmal in Koinzidenz mit dem emittierten Elektron) detektiert wird, wurde für diese Arbeit die Experimentiertechnik COLTRIMS (cold-target recoil-ion momentum spectroscopy) verwendet. Hierbei werden anstatt des gestreuten Photons die Impulse des Compton-Elektrons und des Compton-Ions koinzident detektiert. Der Nachteil dieser Experimentiertechnik ist, dass aufgrund der Notwendigkeit eines kalten, lokalisierten Targetgases die Targetdichte relativ gering ist, was in Kombination mit den kleinen Streuquerschnitten des Compton-Effekts dessen Untersuchung experimentell sehr anspruchsvoll gestaltet. Generell sind Compton-Experimente mit gasförmigen Targets wegen des kleinen Streuquerschnitts rar. Erst die Weiterentwicklung von Synchrotronanlagen in den letzten Jahrzehnten, und die daraus resultierenden erreichbaren Photonendichten ermöglichen eine differenzielle Untersuchung der Kinematik des Compton-Effekts mittels der COLTRIMS-Technik. Moderne Synchrotronanlagen der dritten und vierten Generation ermöglichen hinreichend große Photonenflüsse von bis zu 10^{15} Photonen/s. Da bei der eingesetzten COLTRIMS-Messmethode nicht die gestreuten Photonen, sondern die Impulse der Compton-Ionen und Elektronen gemessen werden, eröffnet sich die Möglichkeit, die Compton-Reaktion unter Abdeckung des vollen Raumwinkels zu vermessen. Die geladenen Reaktionsteilchen werden mittels elektrischer und magnetischer Felder (erzeugt durch ein Spektrometer) auf zwei Detektoren geführt. Aus der Geometrie des Spektrometers sowie den Auftrefforten und Flugzeiten der Teilchen lassen sich dann ihre dreidimensionalen Impulsvektoren zum Reaktionszeitpunkt bestimmen. Die Impulse des gestreuten Photons werden unter Ausnutzung der Impulserhaltung bestimmt, wodurch eine direkte Detektion des Photons überflüssig wird.

Der Compton-Effekt wurde bei Photonenenergien von $\hbar\omega = 2.1$ (Helium) und 40 keV (Helium und N_2) untersucht. Für hohe Photonenenergien ist die „Impulse Approximation“ (aus dem englischen: impulse, Impuls; approximation, Näherung) größtenteils anwendbar. Dies ist für Niedrigenergiephotonen nicht der Fall. Die Impulse Approximation besagt, dass die Bindung des streuenden Elektrons vernachlässigt werden kann, insofern man diese nur berücksichtigt, indem man das streuende Elektron nicht in Ruhe sondern mit einer Impulsverteilung des gebundenen Zustands annimmt.

Die Photoionisation von N_2 wurde bei Photonenenergien von 12 bis 40 keV untersucht. Bei solch hohen Photonenenergien ist die häufig angewandte Dipolnäherung nicht mehr gültig. Innerhalb der Dipolnäherung wird der lineare Photonenimpuls $\boldsymbol{k}_\gamma = \boldsymbol{p}_\gamma / \hbar$ vernachlässigt.

Teil I dieser Arbeit führt die relevanten, theoretischen und experimentellen Grundlagen, welche notwendig sind, um die vorgestellten Ergebnisse zu verstehen, ein. In Kapitel 2 wird inelastische Photonenstreuung und Photoabsorption vorgestellt. Dies inkludiert die oben erwähnte Impulse Approximation und die Dipolnäherung. In Kapitel 3 werden atomare und molekulare Systeme eingeführt, insbesondere ihre Beschreibung im Rahmen der Quantenmechanik. Kapitel 4 stellt die verwendete Coltrims-Technik sowie Synchrotronstrahlung vor. In Kapitel 5 wird die offline-Datenanalyse erläutert.

In Teil II werden die Ergebnisse dieser Arbeit vorgestellt. Dabei behandeln die Kapitel 6 bis 8 die Messungen bezüglich des Compton-Effekts und Kapitel 9 die Untersuchungen bezüglich der Photoionisation.

Kapitel 6 behandelt die Ergebnisse des Niedrigenergieexperiments an gasförmigem Helium, welches im Oktober 2017 am Strahlrohr P04 des Petra III Synchrotrons (Desy, Hamburg) durchgeführt und in Referenz [Kir20] veröffentlicht wurde. Im hier gewählten Energiebereich ist die Impulse Approximation nicht mehr anwendbar; sie wäre nur anwendbar falls, der Energieübertrag auf das Elektron wesentlich größer wäre als die Bindungsenergie. Bei einem einlaufenden Photon mit $\hbar\omega = 2.1$ keV ist jedoch der maximale Energieübertrag (welcher dem maximalen Impulsübertrag durch Photonenrückstreuung entspricht) auf ein freies Elektron in Ruhe etwa 17.1 eV und somit deutlich unterhalb der Ionisationsschwelle von Helium von 24.6 eV. Die experimentellen Ergebnisse wurden mit theoretischen Berechnungen innerhalb der A^2-Näherung verglichen und zeigen hervorragende Übereinstimmung mit diesen. Innerhalb der A^2-Näherung wird nur der quadratische

Term des Vektorpotentials $\boldsymbol{A}$ des Wechselwirkungshamiltonoperators berücksichtigt. Die beobachteten und berechneten Spektren sind vergleichbar mit Spektren aus Streuexperimenten mit Neutronen [Pin14], ultrakurzen Laser-Pulsen [Arb09] und Elektron- [Ehr86] oder Ionstreuexperimenten [Fis03]. Die Ergebnisse verdeutlichen, dass innerhalb des gewählten Energiebereichs der Photonenstreuprozess zweistufig interpretiert werden kann: Im ersten Schritt streut das Photon am gebundenen Elektron, wodurch das System einen abrupten Impulsübertrag erfährt. Diesem Impulsübertrag entspricht eine gewisse Wahrscheinlichkeit, dass das System in einem zweiten Schritt ionisiert wird. Es zeigt sich, dass für eine qualitative Beschreibung der Ursprung dieses Impulsübertrags (sei er von Photonenstreuung oder einem anderen Experiment) von sekundärer Bedeutung ist.

In Kapitel 7 werden die Ergebnisse eines Hochenergieexperiments ($\hbar\omega = 40\,\mathrm{keV}$), ebenfalls an Helium, vorgestellt. Das Experiment wurde am Strahlrohr ID31 des ESRF, Grenoble, im April 2018 durchgeführt und die Ergebnisse in Referenz [Kir22] veröffentlicht. Es wurde die Doppelionisation von Helium durch ein einzelnes Compton-Streuereignis untersucht. Hierbei ist die Doppelionisation von Helium einzig der Wechselwirkung beider Elektronen untereinander geschuldet. Es zeigt sich, dass im gewählten Energiebereich die Korrelation und die Wechselwirkung im Anfangs- sowie Endzustand der Elektronen für die Doppelionisation verantwortlich sind. Dies wurde über mehrere theoretischen Vorhersagen, mit welchen die experimentellen Daten verglichen wurden, bestätigt. Eine Übereinstimmung von Experiment und Theorie ist nur dann zu erreichen, wenn die theoretischen Modelle sowohl Anfangs- wie auch Endzustandskorrelationen berücksichtigen. Wird eine der beiden vernachlässigt, weichen experimentelle und theoretische Spektren stark voneinander ab. Weiter zeigt sich, dass bei Doppelionisation durch Compton-Streuung die Grundzustandsimpulsverteilung des Heliumkerns unbeeinflusst vom Streuprozess bleibt, da in diesem der Kern lediglich ein inaktiver Beobachter der Compton-Reaktion ist. Folglich ist die Zweielektronengrundzustandsimpulsverteilung über die Impulsverteilung des Heliumkerns nach der Reaktion messbar.

In Kapitel 8 wird ein Compton-Streuexperiment an einem molekularen Target, N_2, vorgestellt. Das Experiment ist am Strahlrohr ID31 des ESRF im August 2018 durchgeführt worden. Die gewählte Photonenenergie war ebenfalls $\hbar\omega = 40\,\mathrm{keV}$. In diesem Energiebereich ist die Innerschalen- und Valenzschalen-Ionisation beobachtbar. Bei der Messung von Compton-Streuung an der Valenzschale spielt die molekulare Natur des N_2 weitgehend keine Rolle. Bei der Streuung an den innenliegenden Schalen des N_2 jedoch erfolgt eine Abregung des angeregten Zwischenzustandes $N_2^+(1s^{-1})$ meist über den Auger-Zerfall, was einen Aufbruch des Moleküls nach sich zieht. Durch die Detektion der beiden resultierenden N^+-Ionen erhält man Aufschluss über die molekulare Orientierung zum Reaktionszeitpunkt. Dadurch wiederum lässt sich die Emissionsrichtung des Compton-Elektrons im molekularen Bezugssystem bestimmen. Solche molekülfesten Emissionsverteilungen wurden erstmals im Rahmen dieser Arbeit gemessen und präsentiert. Da die in der Compton-Streuung involvierten Elektronenschalen experimentell identifiziert werden konnten, und sich die elektronischen Anfangszustandsimpulsverteilungen in den gemessenen Impulsverteilungen widerspiegeln, war es möglich, die Impulsverteilungen der gebundenen Elektronen differenziert für die einzelnen Schalen zu messen.

Kapitel 9 behandelt die Ergebnisse für Photoionisation von N_2 durch hochenergetische Photonen. Dabei wurden die Messdaten simultan zu der oben vorgestellten Messung des Compton-Effekts an N_2 aufgenommen. Die Ergebnisse dieses Kapitels wurden teilweise in den Referenzen [Kir19a; Kir19b; Gru20a] veröffentlicht. Für die gewählten Photonenenergien von $\hbar\omega = 12$ bis 40 keV ist die häufig angewandte Dipolnäherung nicht mehr gültig, was sich in einer starken vorwärts/rückwärts-Asymmetrie der Photoelektronenemissionswinkelverteilung auszeichnet. Weiter beeinflussen der Photonenimpuls als auch der Rückstoß des Photoelektrons auf das Molekül die Dynamik des Prozesses. Dies spiegelt sich direkt in der kinetischen Energie (KER, aus dem englischen *kinetic energy release*) der Molekülfragmente wider. Durch den Photonenimpuls und den Photoelektronenrückstoß verschiebt sich der KER hin zu größeren Energien. Die Stärke dieser Verschiebung hängt von der relativen Emissionsrichtung des Photons und des Photoelektrons zur Molekülachse ab. Weiter verursacht der Rückstoß des Photoelektrons eine Rotation des Moleküls. Diese Rotation verhindert, dass man die Molekülorientierung zur Reaktionszeit aus der Messung der ionischen Relativimpulse bestimmen kann. Dadurch entstehen enorme Asymmetrien in den molekülfesten Winkelverteilungen des Photoelektrons, wie sie im Rahmen dieser Arbeit beobachtet wurden. Außerdem verursacht der lineare Photonenimpuls k_γ eine Vorwärtsverschiebung des mittleren Elektronenimpulses, welche in der Tat größer ist als k_γ. Aufgrund von Impulserhaltung zieht dies einen entgegengesetzten Ionenimpuls (also hin zum einlaufenden Photon) nach sich. Die Verschiebungen der mittleren Elektronen- und Ionenimpulse sind quantitativ jeweils über $8/5 \times k_\gamma$ und $-3/5 \times k_\gamma$ gegeben. Dieser Zusammenhang wurde anhand mehrerer Photonenenergien im Rahmen dieser Arbeit bestätigt.

And ever somewhere lost inside you
There's a child that smiles

C. H. Van Eeckhout

ADDENDUM

Atomic units

While working with systems of atomic size, it is useful to use a unit system reflecting the atomic magnitude. Within atomic units (a.u.)—also called Hartree atomic units, named after the physicist Douglas Hartree—the reduced Planck constant $\hbar$, the elementary charge e, the Bohr radius $a_0 = 4\pi\varepsilon_0\hbar^2 m_e^{-1} e,^{-2}$ and the electron mass m_e are set to unity. In Table 1, various derived physical quantities are listed.

Table 1: Various physical quantities in atomic units.

Elemental charge	e	1 a.u. = 1.6022×10^{-19} A s
Electron mass	m_e	1 a.u. = 9.1096×10^{-31} kg
Planck constant	h	2π a.u. = 6.6262×10^{-31} kg m^2 s^{-2}
Vacuum speed of light	c	137 a.u. = 299 792 458 m s^{-1}
Bohr radius	a_0	1 a.u. = 5.2918×10^{-11} m
Hartree energy	E_H	1 a.u. = 27.2 eV = 4.3597×10^{-18} J s
Time		1 a.u. = 2.4189×10^{-17} s
Velocity		1 a.u. = 2.1877×10^{6} m s^{-1}
Momentum		1 a.u. = 1.9929×10^{-24} kg m s^{-1}
Electric potential		1 a.u. = 27.2114 V
Electric field		1 a.u. = 5.1422 V m^{-1}

BIBLIOGRAPHY

[Åbe70] T. Åberg. "Asymptotic Double-Photoexcitation Cross Sections of the Helium Atom" *Physical Review A* 2 (1970), 1726–1729. DOI: 10.1103/PhysRevA.2.1726 (cited on Page 117).

[Åbe85] T. Åberg and J. Tulkki. "Inelastic X-Ray Scattering Including Resonance Phenomena" *Atomic Inner-Shell Physics*. Edited by Bernd Crasemann. New York: Plenum Press, 1985. ISBN: 0-306-41847-9. DOI: 10.1007/978-1-4613-2417-1 (cited on Pages 12, 28).

[Abr66] R. Abrines and I. C. Percival. "Classical theory of charge transfer and ionization of hydrogen atoms by protons" *Proceedings of the Physical Society* 88 (1966), 861–872. DOI: 10.1088/0370-1328/88/4/306 (cited on Pages 81, 136).

[Ala05] M. Alagia et al. "Core level ionization dynamics in small molecules studied by x-ray-emission threshold-electron coincidence spectroscopy" *Physical Review A* 71 (2005), 012506. DOI: 10.1103/PhysRevA.71.012506 (cited on Page 46).

[Amu75] M. Ya. Amusia, E. G. Drukarev, V. G. Gorshkov, and M. O. Kazachkov. "Two-electron photoionization of helium" *Journal of Physics B: Atomic and Molecular Physics* 8 (1975), 1248–1266. DOI: 10.1088/0022-3700/8/8/016 (cited on Pages 32, 33).

[Amu95] M. Ya. Amusia and A. I. Mikhailov. "Double electron ionization in Compton scattering of high energy photons by helium atoms" *Journal of Physics B: Atomic, Molecular and Optical Physics* 28 (1995), 1723–1734. DOI: 10.1088/0953-4075/28/9/011 (cited on Page 108).

[And94] L. Andersson and J. Burgdörfer. "Excitation-ionization and double ionization of helium by Compton scattering" *Physical Review A* 50 (1994), R2810–R2813. DOI: 10.1103/PhysRevA.50.R2810 (cited on Page 33).

[Arb09] D. G. Arbó, K. Tőkési, and J. E. Miraglia. "Atomic ionization by a sudden momentum transfer" *Nuclear Instruments and Methods in Physics Research Section B: Beam Interactions with Materials and Atoms* 267 (2009), 382–385. DOI: 10.1016/j.nimb.2008.10.086 (cited on Pages 83, 93, 190, 199).

[Aug27] P. Auger and F. Perrin. "La répartition dans l'espace des directions d'émission des photoélectrons" *Journal de Physique et Le Radium* 8 (1927), 93–112. DOI: 10.1051/jphysrad:019270080209300 (cited on Page 180).

[Bac14] H. Bachau, M. Dondera, and V. Florescu. “Stimulated Compton Scattering in Two-Color Ionization of Hydrogen with keV Electromagnetic Fields” *Physical Review Letters* 112 (2014), 073001. DOI: 10.1103/PhysRevLett.112.073001 (cited on Page 21).

[Bac21] H. Bachau and M. Dieng. “Compton scattering of keV photons at helium near the $He^+(1s)$ threshold for small momentum transfer” *The European Physical Journal D* 75 (2021), 34. DOI: 10.1140/epjd/s10053-021-00048-0 (cited on Page 30).

[Bar12] M. Barr, K. M. O’Donnell, A. Fahy, W. Allison, and P. C. Dastoor. “A desktop supersonic free-jet beam source for a scanning helium microscope (SHeM)” 23 (2012), 105901. DOI: 10.1088/0957-0233/23/10/105901 (cited on Page 60).

[Bel90] F. Bell, A. J. Rollason, J. R. Schneider, and W. Drube. “Determination of electron momentum densities by a (γ,eγ) experiment” *Physical Review B* 41 (1990), 4887–4890. DOI: 10.1103/PhysRevB.41.4887 (cited on Page 4).

[Bel91] F. Bell, T. Tschentscher, J. R. Schneider, and A. J. Rollason. “The triple differential cross section for deep inelastic photon scattering: a $(\gamma, e\gamma')$ experiment” *Journal of Physics B: Atomic, Molecular and Optical Physics* 24 (1991), L533–L538. DOI: 10.1088/0953-4075/24/22/001 (cited on Page 4).

[Ber93] P. M. Bergstrom, T. Surić, K. Pisk, and R. H. Pratt. “Compton scattering of photons from bound electrons: Full relativistic independent-particle-approximation calculations” *Physical Review A* 48 (1993), 1134–1162. DOI: 10.1103/PhysRevA.48.1134 (cited on Pages 25–27).

[Ber97] P.M. Bergstrom and R.H. Pratt. “An overview of the theories used in compton scattering calculations” *Radiation Physics and Chemistry* 50 (1997), 3–29. DOI: 10.1016/S0969-806X(97)00022-4 (cited on Pages 3, 4, 26).

[Bet04] K. Bethge, G. Gruber, and T. Stöhlker. “Physik der Atome und Moleküle: Eine Einführung” 2nd ed. Weinheim: Wiley-VCH, 2004 (cited on Page 51).

[Big75] F. Biggs, L. B. Mendelsohn, and J. B. Mann. “Hartree-Fock Compton profiles for the elements” *Atomic Data and Nuclear Data Tables* 16 (1975), 201–309. DOI: 10.1016/0092-640X(75)90030-3 (cited on Page 27).

[Blo34] F. Bloch. “Contribution to the Theory of the Compton-Line” *Physical Review* 46 (1934), 674–687. DOI: 10.1103/PhysRev.46.674 (cited on Page 3).

[Bor26] M. Born. “Quantenmechanik der Stoßvorgänge” *Zeitschrift für Physik* 38 (1926), 803–827. DOI: 10.1007/BF01397184 (cited on Page 16).

[Bot25] W. Bothe and H. Geiger. “Über das Wesen des Comptoneffekts; ein experimenteller Beitrag zur Theorie der Strahlung” *Zeitschrift für Physik* 32 (1925), 639–663. DOI: 10.1007/BF01331702 (cited on Page 4).

[Bra89] M. Brauner, J. S. Briggs, and H. Klar. “Triply-differential cross sections for ionisation of hydrogen atoms by electrons and positrons” *Journal of Physics B: Atomic, Molecular and Optical Physics* 22 (1989), 2265. DOI: 10.1088/0953-4075/22/14/010 (cited on Page 112).

[Bri99] J. S. Briggs and V. Schmidt. “Differential cross sections for photo-double-ionization of the helium atom” *Journal of Physics B: Atomic, Molecular and Optical Physics* 33 (1999), R1–R48. DOI: 10.1088/0953-4075/33/1/201 (cited on Page 31).

[Bru02] L. W. Bruch, W. Schöllkopf, and J. P. Toennies. “The formation of dimers and trimers in free jet ^{4}He cryogenic expansions” *The Journal of Chemical Physics* 117 (2002), 1544–1566. DOI: 10.1063/1.1486442 (cited on Page 61).

[CoB] RoentDek Handels GmbH. “COBOLD program package” URL: https://www.roentdek.com/software/ (visited on 07/18/2022) (cited on Page 66).

[Ced99] L. S. Cederbaum and J. Zobeley. “Ultrafast charge migration by electron correlation” *Chemical Physics Letters* 307 (1999), 205–210. DOI: 10.1016/S0009-2614(99)00508-4 (cited on Page 167).

[Cha06] B. K. Chatterjee, L. A. LaJohn, and S. C. Roy. “Investigations on compton scattering: New directions” *Radiation Physics and Chemistry* 75 (2006), 2165–2173. DOI: 10.1016/j.radphyschem.2006.03.073 (cited on Page 25).

[Che00] N. A. Cherepkov et al. “K-shell photoionization of CO: II. Determination of dipole matrix elements and phase differences” *Journal of Physics B: Atomic, Molecular and Optical Physics* 33 (2000), 4213–4236. DOI: 10.1088/0953-4075/33/20/302 (cited on Page 146).

[Che14] S. Chelkowski, A. D. Bandrauk, and P. B. Corkum. “Photon Momentum Sharing between an Electron and an Ion in Photoionization: From One-Photon (Photoelectric Effect) to Multiphoton Absorption” *Physical Review Letters* 113 (2014), 263005. DOI: 10.1103/PhysRevLett.113.263005 (cited on Page 180).

[Chu06] O. Chuluunbaatar et al. “Role of the cusp conditions in electron-helium double ionization” *Physical Review A* 74 (2006), 014703. DOI: 10.1103/PhysRevA.74.014703 (cited on Pages 88, 112).

[Chu21] O. Chuluunbaatar et al. "Compton ionization of atoms as a method of dynamical spectroscopy" *Journal of Quantative Spectroscopy & Radiative Transfer* 272 (2021), 107820. DOI: 10.1016/j.jqsrt.2021.107820 (cited on Page 112).

[Chu22] O. Chuluunbaatar et al. "Compton double ionization of the helium atom: Can it be a method of dynamical spectroscopy of ground state electron correlation?" *Journal of Quantitative Spectroscopy & Radiative Transfer* 278 (2022), 108020. DOI: j.jqsrt.2021.108020 (cited on Pages 88, 110, 112, 193).

[Com23a] A. H. Compton. "A Quantum Theory of the Scattering of X-rays by Light Elements" *Physical Review* 21 (1923), 483–502. DOI: 10.1103/PhysRev.21.483 (cited on Pages 2, 22).

[Com23b] A. H. Compton. "The Spectrum of Scattered X-Rays" *Physical Review* 22 (1923), 409–413. DOI: 10.1103/PhysRev.22.409 (cited on Page 3).

[Coo69] J. W. Cooper and S. T. Manson. "Photo-Ionization in the Soft X-Ray Range: Angular Distributions of Photoelectrons and Interpretation in Terms of Subshell Structure" *Physical Review* 177 (1969), 157–163. DOI: 10.1103/PhysRev.177.157 (cited on Pages 17, 18).

[Coo77] M. J. Cooper. "Compton scattering and electron momentum" *Contemporary Physics* 18 (1977), 489–517. DOI: 10.1080/00107517708231504 (cited on Pages 2–4, 21).

[Coo85] M. J. Cooper. "Compton scattering and electron momentum determination" *Reports on Progress in Physics* 48 (1985), 415–481. DOI: 10.1088/0034-4885/48/4/001 (cited on Pages 4, 30).

[Coo90] J. W. Cooper. "Multipole corrections to the angular distribution of photoelectrons at low energies" *Physical Review A* 42 (1990), 6942–6945. DOI: 10.1103/PhysRevA.42.6942 (cited on Page 18).

[Cro50] W. G. Cross and N. F. Ramsey. "The Conservation of Energy and Momentum in Compton Scattering" *Physical Review* 80 (1950), 929–936. DOI: 10.1103/PhysRev.80.929 (cited on Page 4).

[Cul89] D. E. Cullen et al. "Tables and graphs of photon-interaction cross sections from 10 eV to 100 GeV derived from the LLNL Evaluated Photon Data Library (EPDL)" (1989). URL: https://www.osti.gov/biblio/6901928 (cited on Page 3).

[Cur71] R. Currat, P. D. DeCicco, and R. J. Weiss. "Impulse Approximation in Compton Scattering" *Physical Review B* 4 (1971), 4256–4261. DOI: 10.1103/PhysRevB.4.4256 (cited on Page 4).

[Deh75] J. L. Dehmer and D. Dill. “Shape Resonances in K-Shell Photoionization of Diatomic Molecules” *Physical Review Letters* 35 (1975), 213–215. DOI: 10.1103/PhysRevLett.35.213 (cited on Page 161).

[Dem09] W. Demtröder. “Experimentalphysik 2: Elektrizität und Optik” 5th ed. Springer, 2009. ISBN: 978-3-540-68210-3. DOI: 10.1007/978-3-540-68219-6 (cited on Pages 51, 52).

[Dem11] Ph. V. Demekhin, A. Ehresmann, and V. L. Sukhorukov. “Single center method: A computational tool for ionization and electronic excitation studies of molecules” *Journal of Chemical Physics* 134 (2011), 024113. DOI: 10.1063/1.3526026 (cited on Page 175).

[Dem16] W. Demtröder. “Experimentalphysik 3: Atome, Moleküle und Festkörper” 5th ed. Springer, 2016. ISBN: 978-3-662-49093-8. DOI: 10.1007/978-3-662-49094-5 (cited on Page 36).

[Der99] A. Derevianko, W. R. Johnson, and K. T. Cheng. “Non-dipole effects in photoelectron angular distributions for rare gas atoms” *Atomic Data and Nuclear Data Tables* 73.2 (1999), 153–211. DOI: 10.1006/adnd.1999.0818 (cited on Page 20).

[Dom78] W. Domcke and L. S. Cederbaum. “Electronic recoil effects in high-energy photoelectron spectroscopy” *Journal of Electron Spectroscopy and Related Phenomena* 13 (1978), 161–173. DOI: 10.1016/0368-2048(78)85024-5 (cited on Pages 157, 163).

[Doo03] P. W. Dooley et al. “Direct imaging of rotational wave-packet dynamics of diatomic molecules” *Physical Review A* 68 (2003), 023406. DOI: 10.1103/PhysRevA.68.023406 (cited on Page 170).

[Drn22] J. Drnec. Private communication. 2022 (cited on Pages 58, 152).

[DuM29] J. W. M. DuMond. “Compton Modified Line Structure and its Relation to the Electron Theory of Solid Bodies” *Physical Review* 33 (1929), 643–658. DOI: 10.1103/PhysRev.33.643 (cited on Pages 2, 26, 77).

[DuM33] J. W. M. DuMond. “The Linear Momenta of Electrons in Atoms and in Solid Bodies as Revealed by X-Ray Scattering” *Reviews of Modern Physics* 5 (1933), 1–33. DOI: 10.1103/RevModPhys.5.1 (cited on Pages 3, 150).

[DuM37] J. W. M. DuMond and H. A. Kirkpatrick. “A Direct Spectrum of the Structure and Shift of the Compton Line with Helium Gas as the Scatterer” *Physical Review* 52 (1937), 419–436. DOI: 10.1103/PhysRev.52.419 (cited on Pages 3, 5, 115).

[Eha06] M. Ehara et al. “Symmetry-dependent vibrational excitation in N 1*s* photoionization of N_2: Experiment and theory” *Journal of Chemical Physics* 124 (2006), 124311. DOI: 10.1063/1.2181144 (cited on Pages 47, 167).

[Ehr86] H. Ehrhardt, K. Jung, G. Knoth, and P. Schlemmer. “Differential cross section of direct single electron impact ionization” *Zeitschrift für Physik D – Atoms, Molecules and Clusters* 1 (1986), 3–32. DOI: 10.1007/BF01384654 (cited on Pages 93, 190, 199).

[Eic20] U. Eichmann et al. “Photon-recoil imaging: Expanding the view of nonlinear x-ray physics” *Science* 369 (2020), 1630–1633. DOI: 10.1126/science.abc2622 (cited on Page 21).

[Ein05] A. Einstein. “Über einen die Erzeugung und Verwandlung des Lichtes betreffenden heuristischen Gesichtspunkt” *Annalen der Physik* 322.6 (1905), 132–148. DOI: 10.1002/andp.19053220607 (cited on Page 6).

[Eis70] P. Eisenberger and P. M. Platzman. “Compton Scattering of X Rays from Bound Electrons” *Physical Review A* 2 (1970), 415–423. DOI: 10.1103/PhysRevA.2.415 (cited on Pages 4, 28).

[Eis72] P. Eisenberger and W. A. Reed. “Gamma-Ray Compton Scattering: Experimental Compton Profiles for He, N_2, Ar, and Kr” *Physical Review A* 5 (1972), 2085–2094. DOI: 10.1103/PhysRevA.5.2085 (cited on Page 115).

[Feh18] K. Fehre et al. “Absolute ion detection efficiencies of microchannel plates and funnel microchannel plates for multi-coincidence detection” *Review of Scientific Instruments* 89 (2018), 045112. DOI: 10.1063/1.5022564 (cited on Page 66).

[Fel05] V. C. Felicíssimo, F. F. Guimarães, and F. Gel’mukhanov. “Enhancement of the recoil effect in x-ray photoelectron spectra of molecules driven by a strong ir field” *Physical Review A* 72 (2005), 023414. DOI: 10.1103/PhysRevA.72.023414 (cited on Pages 163, 165).

[Fis03] D. Fischer, R. Moshammer, M. Schulz, A. Voitkiv, and J. Ullrich. “Fully differential cross section for the single ionization of helium by ion impact” *Journal of Physics B: Atomic, Molecular and Optical Physics* 36 (2003), 3555–3567. DOI: 10.1088/0953-4075/36/17/301 (cited on Pages 93, 190, 199).

[Fou03] L. Foucar. “Ionisation und Anregung von Wasserstoff- und Deuteriummolekülen mit Synchrotronstrahlung” Diplomarbeit. Johann Wolfgang Goethe-Universität Frankfurt, 2003. URN: urn:nbn:de:hebis:30-5715 (cited on Page 71).

[Fuk72] T. Fukamachi and S. Hosoya. "Separate measurement of compton profile due to 1s electrons in Fe, Ni and Cu by coincidence method" *Physics Letters A* 38 (1972), 341–342. DOI: 10.1016/0375-9601(72)90150-8 (cited on Page 150).

[Gas16] H. Gassert et al. "Agreement of Experiment and Theory on the Single Ionization of Helium by Fast Proton Impact" *Physical Review Letters* 116 (2016), 073201. DOI: 10.1103/PhysRevLett.116.073201 (cited on Page 94).

[Gil65] F. R. Gilmore. "Potential energy curves for N_2, NO, O_2 and corresponding ions" *Journal of Quantitative Spectroscopy and Radiative Transfer* 5 (1965), 369–IN3. ISSN: 0022-4073. DOI: 10.1016/0022-4073(65)90072-5 (cited on Pages 46, 47).

[Gis73] E. A. Gislason. "Series expansions for Franck-Condon factors. I. Linear potential and the reflection approximation" *The Journal of Chemical Physics* 58 (1973), 3702–3707. DOI: 10.1063/1.1679721 (cited on Page 171).

[Gra20] J.A. Gray. "The scattering of x- and γ-rays" *Journal of the Franklin Institute* 190 (1920), 633–655. DOI: 10.1016/S0016-0032(20)90858-X (cited on Page 22).

[Gru18] S. Grundmann et al. "Separating Dipole and Quadrupole Contributions to Single-Photon Double Ionization" *Physical Review Letters* 121 (2018), 173003. DOI: 10.1103/PhysRevLett.121.173003 (cited on Pages 18, 157).

[Gru20a] S. Grundmann et al. "Observation of Photoion Backward Emission in Photoionization of He and N_2" *Physical Review Letters* 124 (2020), 233201. DOI: 10.1103/PhysRevLett.124.233201 (cited on Pages 18, 158, 180, 182, 200).

[Gru20b] S. Grundmann et al. "Revealing the two-electron cusp in the ground states of He and H_2 via quasifree double photoionization" *Physical Review Research* 2 (2020), 033080. DOI: 10.1103/PhysRevResearch.2.033080 (cited on Page 18).

[Gru22] S. Grundmann. "Nondipolar Photoionization of Atoms and Molecules" Dissertation. Johann Wolfgang Goethe-Universität Frankfurt, 2022. URN: urn:nbn:de:hebis:30:3-676957 (cited on Pages 15, 18, 33).

[Har19] A. Hartung et al. "Magnetic fields alter strong-field ionization" *Nature Physics* 15 (2019), 1222–1226. DOI: 10.1038/s41567-019-0653-y (cited on Page 157).

[Hei54] W. Heitler. "The Quantum Theory of Radiation" 3rd ed. Oxford: Claredon Press, 1954 (cited on Pages 23, 24).

[Hem04] O. Hemmers, R. Guillemin, and D. W. Lindle. “Nondipole effects in soft X-ray photoemission” *Radiation Physics and Chemistry* 70 (2004), 123–147. DOI: 10.1016/j.radphyschem.2003.12.009 (cited on Page 157).

[Hem97] O. Hemmers et al. “Beyond the dipole approximation: angular-distribution effects in valence photoemission” *Journal of Physics B: Atomic, Molecular and Optical Physics* 30 (1997), L727. DOI: 10.1088/0953-4075/30/21/003 (cited on Page 157).

[Hen93] B. L. Henke, E. M. Gullikson, and J. C. Davis. “X-ray interactions: photoabsorbtion, scattering, transmission and reflection at E=50–30 000 eV, Z=1–92” *Atomic Data and Nuclear Data Tables* 54 (1993), 181–342. DOI: 10.1006/adnd.1993.1013. Online resource: https://henke.lbl.gov/optical_constants/filter2.html, (visited on 09/26/2022). (Cited on Pages 56, 57, 122).

[Her01] U. Hergenhahn, O. Kugeler, A. Rüdel, E. E. Rennie, and A. M. Bradshaw. “Symmetry-Selective Observation of the N 1s Shape Resonance in N_2” *The Journal of Physical Chemistry A* 105 (2001), 5704–5708. DOI: 10.1021/jp0038456 (cited on Page 47).

[Her04] U. Hergenhahn. “Vibrational structure in inner shell photoionization of molecules” *Journal of Physics B: Atomic, Molecular and Optical Physics* 37 (2004), R89–R135. DOI: 10.1088/0953-4075/37/12/R01 (cited on Pages 162, 167).

[Her10] I. V. Hertel and C.-P. Schulz. “Atome, Moleküle und optische Physik 2” Springer, 2010. ISBN: 978-3-642-11972-9. DOI: 10.1007/978-3-642-11973-6 (cited on Pages 38, 41–44).

[Her17] I. V. Hertel and C.-P. Schulz. “Atome, Moleküle und optische Physik 1” 2nd ed. Springer, 2017. ISBN: 978-3-662-53103-7. DOI: 10.1007/978-3-662-53104-4 (cited on Pages 12, 17, 37, 38, 50, 52).

[Hil06] R. N. Hill. “Hydrogenic Wave Functions” *Handbook of Atomic, Molecular, and Optical Physics*. Edited by G. W. F. Drake. New York: Springer Science+Business Media, Inc., 2006. ISBN: 978-0-387-20802-2. DOI: 10.1007/978-0-387-26308-3 (cited on Page 15).

[Hoh02] O. Hohn. “Hochdruckmikroentladungen mit hohem Gasfluss: Eine Quelle zur Erzeugung von Ionen und spinpolarisierten metastabilen Atomen” Dissertation. Johann Wolfgang Goethe-Universität Frankfurt, 2002. URN: urn:nbn:de:hebis:30-0000001539 (cited on Page 60).

[Hou20] S. Houamer, O. Chuluunbaatar, I. P. Volobuev, and Y. V. Popov. "Compton ionization of hydrogen atom near threshold by photons in the energy range of a few keV: nonrelativistic approach" *The European Physical Journal D* 74 (2020), 81. DOI: 10.1140/epjd/e2020-100572-1 (cited on Page 87).

[Hub75] J. H. Hubbell et al. "Atomic form factors, incoherent scattering functions, and photon scattering cross sections" *Journal of Physical and Chemical Reference Data* 4 (1975), 471–538. DOI: 10.1063/1.555523 (cited on Pages 28, 84, 85).

[Hyl28] E. A. Hylleraas. "Über den Grundzustand des Heliumatoms" *Zeitschrift für Physik* 48 (1928), 469–494. DOI: 10.1007/BF01340013 (cited on Pages 36, 37, 112).

[Hyl29] E. A. Hylleraas. "Neue Berechnung der Energie des Heliums im Grundzustande, sowie des tiefsten Terms von Ortho-Helium" *Zeitschrift für Physik* 54 (1929), 347–366. DOI: 10.1007/BF01375457 (cited on Page 37).

[Jag02] O. Jagutzki et al. "Multiple hit readout of a microchannel plate detector with a three-layer delay-line anode" *IEEE Transactions on Nuclear Science* 49 (2002), 2477–2483. DOI: 10.1109/TNS.2002.803889 (cited on Pages 58, 65, 69).

[Jau25] G. E. M. Jauncey. "Quantum Theory of the Unmodified Spectrum Line in the Compton Effect" *Physical Review* 25 (1925), 314–321. DOI: 10.1103/PhysRev.25.314 (cited on Page 3).

[Kai76] P. Kaijser and V. H. Smith Jr. "Directional compton profiles for molecular systems: N2" *Molecular Physics* 31 (1976), 1557–1568. DOI: 10.1080/00268977600101231 (cited on Page 193).

[Kal04] Z. Kaliman and K. Pisk. "Compton cross-section calculations in terms of recoil-ion momentum observables" *Radiation Physics and Chemistry* 71 (2004), 633–635. DOI: 10.1016/j.radphyschem.2004.04.035 (cited on Pages 5, 31, 81, 148).

[Kan92] P. P. Kane. "Inelastic scattering of X-rays and gamma rays by inner shell electrons" *Physics Reports* 218 (1992), 67–139. ISSN: 0370-1573. DOI: 10.1016/0370-1573(92)90050-A (cited on Pages 4, 107).

[Kap36] H. Kappeler. "Messung der Form und Breite der Comptonlinie für die Gase Ne, O2, N2 und für die festen Stoffe Li, C und NaF" *Annalen der Physik* 419 (1936), 129–168. DOI: 10.1002/andp.19364190206 (cited on Page 3).

[Kas14] G. Kastirke. “Konstruktion und Aufbau einer UHV-tauglichen COLTRIMS-Kammer” Masterarbeit. Johann Wolfgang Goethe-Universität Frankfurt, 2014. URN: urn:nbn:de:hebis:30:3-347395 (cited on Pages 130, 154).

[Kas20] G. Kastirke. “Angeregt und abgefragt: Moleküle im Reaktionsmikroskop” Dissertation. Johann Wolfgang Goethe-Universität Frankfurt, 2020. URN: urn:nbn:de:hebis:30:3-560575 (cited on Page 49).

[Kem96] B. Kempgens et al. “A high-resolution N 1s photoionization study of the N_2 molecule in the near-threshold region” *Journal of Physics B: Atomic, Molecular and Optical Physics* 29 (1996), 5389. DOI: 10.1088/0953-4075/29/22/016 (cited on Page 47).

[Kim84] K. J. Kim. “A synchrotron radiation source with arbitrarily adjustable elliptical polarization” *Nuclear Instruments and Methods in Physics Research* 219 (1984), 425–429. DOI: 10.1016/0167-5087(84)90354-5 (cited on Page 53).

[Kir19a] M. Kircher et al. “Photon-Momentum-Induced Molecular Dynamics in Photoionization of N_2 at $h\nu = 40\,\mathrm{keV}$” *Physical Review Letters* 123 (2019), 193001. DOI: 10.1103/PhysRevLett.123.193001 (cited on Pages 157, 160, 162, 164–167, 169, 200).

[Kir19b] M. Kircher et al. “Recoil-Induced Asymmetry of Nondipole Molecular Frame Photoelectron Angular Distributions in the Hard X-ray Regime” *Physical Review Letters* 123 (2019), 243201. DOI: 10.1103/PhysRevLett.123.243201 (cited on Pages 157, 171, 174–176, 200).

[Kir20] M. Kircher et al. “Kinematically complete experimental study of Compton scattering at helium atoms near the threshold” *Nature Physics* 16 (2020), 756–760. DOI: 10.1038/s41567-020-0880-2 (cited on Pages 31, 86, 88, 90–92, 94, 95, 97, 98, 100, 198).

[Kir22] M. Kircher et al. “Ion and Electron Momentum Distributions from Single and Double Ionization of Helium Induced by Comopton Scattering” *Physical Review Letters* 128 (2022), 053001. DOI: 10.1103/PhysRevLett.128.053001 (cited on Pages 31, 107, 114, 117, 118, 120, 199).

[Kle29] O. Klein and Y. Nishina. “Über die Streuung von Strahlung durch freie Elektronen nach der neuen relativistischen Quantendynamik von Dirac” *Zeitschrift für Physik* 52 (1929), 853–868. DOI: 10.1007/BF01366453 (cited on Pages 2, 23).

[Kna02a] A. Knapp et al. “Energy sharing and asymmetry parameters for photo double ionization of helium 100 eV above threshold in single-particle and Jacobi coordinates” *Journal of Physics B: Atomic, Molecular and Optical Physics* 35 (2002), L521–L526. DOI: 10.1088/0953-4075/35/23/103 (cited on Page 120).

[Kna02b] A. Knapp et al. “Mechanisms of Photo Double Ionization of Helium by 530 eV Photons” *Physical Review Letters* 89 (2002), 033004. DOI: 10.1103/PhysRevLett.89.033004 (cited on Page 119).

[Kob11] K. Kobayashi et al. “Accurate Compton scattering measurements for N_2 molecules” *Journal of Physics B: Atomic, Molecular and Optical Physics* 44 (2011), 115102. DOI: 10.1088/0953-4075/44/11/115102 (cited on Page 193).

[Krä02] B. Krässig et al. “Photoexcitation of a Dipole-Forbidden Resonance in Helium” *Physical Review Letters* 88 (2002), 203002. DOI: 10.1103/PhysRevLett.88.203002 (cited on Page 157).

[Kra25] H. A. Kramers and W. Heisenberg. “Über die Streuung von Strahlung durch Atome” *Zeitschrift für Physik* 31 (1925), 681–708. DOI: 10.1007/BF02980624 (cited on Page 25).

[Krä95] B. Krässig et al. “Nondipolar Asymmetries of Photoelectron Angular Distributions” *Physical Review Letters* 75 (1995), 4736–4739. DOI: 10.1103/PhysRevLett.75.4736 (cited on Page 18).

[Kuk05] E. Kukk et al. “Violation of the Franck-Condon Principle due to Recoil Effects in High Energy Molecular Core-Level Photoionization” *Physical Review Letters* 95 (2005), 133001. DOI: 10.1103/PhysRevLett.95.133001 (cited on Page 157).

[Kuk17] E. Kukk et al. “Photoelectron recoil in CO in the x-ray region up to 7 keV” *Physical Review A* 95 (2017), 042509. DOI: 10.1103/PhysRevA.95.042509 (cited on Page 166).

[Kuk18] E. Kukk et al. “Energy Transfer into Molecular Vibrations and Rotations by Recoil in Inner-Shell Photoemission” *Physical Review Letters* 121 (2018), 073002. DOI: 10.1103/PhysRevLett.121.073002 (cited on Pages 157, 163, 166).

[Kul16] A. I. Kuleff, N. V. Kryzhevoi, M. Pernpointner, and L. S. Cederbaum. “Core Ionization Initiates Subfemtosecond Charge Migration in the Valence Shell of Molecules” *Physical Review Letters* 117 (2016), 093002. DOI: 10.1103/PhysRevLett.117.093002 (cited on Page 167).

[Kun21] M. Kunitski et al. “Ultrafast manipulation of the weakly bound helium dimer” *Nature Physics* 17 (2021), 174–178. DOI: 10.1038/s41567-020-01081-3 (cited on Page 170).

[Lan01] A. Landers et al. “Photoelectron Diffraction Mapping: Molecules Illuminated from Within” *Physical Review Letters* 87 (2001), 013002. DOI: 10.1103/PhysRevLett.87.013002 (cited on Page 146).

[Leb02] M. Lebech, J. C. Houver, and D. Dowek. “Ion-electron velocity vector correlations in dissociative photoionization of simple molecules using electrostatic lenses” *Review of Scientific Instruments* 73 (2002), 1866–1874. DOI: 10.1063/1.1458063 (cited on Page 65).

[Lev81] D. H. Levy. “The Spectroscopy of Very Cold Gases” *Science* 214 (1981), 263–269. DOI: 10.1126/science.214.4518.263 (cited on Page 59).

[Lin22] K. Lin et al. “Photoelectron energy peaks shift against the radiation pressure in strong-field ionization” *Science Advances* 8 (2022), eabn7386. DOI: 10.1126/sciadv.abn7386 (cited on Page 157).

[Lof77] A. Lofthus and P. H. Krupenie. “The spectrum of molecular nitrogen” *Journal of Physical and Chemical Reference Data* 6 (1977), 113–307. DOI: 10.1063/1.555546 (cited on Page 46).

[Lun96] M. Lundqvist, D. Edvardsson, P. Baltzer, and B. Wannberg. “Doppler-free kinetic energy release spectrum of N_2^{2+}” *Journal of Physics B: Atomic, Molecular and Optical Physics* 29 (1996), 1489–1499. DOI: 10.1088/0953-4075/29/8/013 (cited on Pages 154, 161, 162).

[Mat05] D. N. Matsukevich et al. “Entanglement of a Photon and a Collective Atomic Excitation” *Physical Review Letters* 95 (2005), 040405. DOI: 10.1103/PhysRevLett.95.040405 (cited on Page 163).

[Mau21] J. Maurer and U. Keller. “Ionization in intense laser fields beyond the electric dipole approximation: concepts, methods, achievements and future directions” *Journal of Physics B: Atomic, Molecular and Optical Physics* 54 (2021), 094001. DOI: 10.1088/1361-6455/abf731 (cited on Page 157).

[McG97] J. H. McGuire. “Electron Correlation Dynamics in Atomic Collisions” Cambridge, England: Cambridge University Press, 1997 (cited on Page 108).

[Mil88] D. R. Miller. “Free jet sources” *Atomic and Molecular Beam Methods* 1 (1988). Edited by G. Scoles (cited on Page 61).

[Mor29] P. M. Morse. “Diatomic Molecules According to the Wave Mechanics. II. Vibrational Levels” *Physical Review* 34 (1929), 57–64. DOI: 10.1103/PhysRev.34.57 (cited on Page 45).

[Pal06] J. Paldus. “Perturbation Theory” *Handbook of Atomic, Molecular, and Optical Physics*. Edited by G. W. F. Drake. New York: Springer Science+Business Media, Inc., 2006. ISBN: 978-0-387-20802-2. DOI: 10.1007/978-0-387-26308-3 (cited on Page 14).

[Pia99] M. N. Piancastelli. “The neverending story of shape resonances” *Journal of Electron Spectroscopy and Related Phenomena* 100 (1999), 167–190. DOI: 10.1016/S0368-2048(99)00046-8 (cited on Page 146).

[Pin14] M. S. Pindzola et al. “Neutron-impact ionization of He” *Journal of Physics B: Atomic, Molecular and Optical Physics* 47 (2014), 195202. DOI: 10.1088/0953-4075/47/19/195202 (cited on Pages 93, 190, 199).

[Pla65] P. M. Platzman and N. Tzoar. “X-Ray Scattering from an Electron Gas” *Physical Review* 139 (1965), A410–A413. DOI: 10.1103/PhysRev.139.A410 (cited on Page 4).

[Pra10] R. H. Pratt et al. “Compton scattering revisited” *Radiation Physics and Chemistry* 79 (2010), 124–131. DOI: 10.1016/j.radphyschem.2009.04.035 (cited on Pages 25, 28–30).

[Pra14] R.H. Pratt. “Photon absorption and photon scattering—What we do not know and why it matters” *Radiation Physics and Chemistry* 95 (2014), 4–13. DOI: 10.1016/j.radphyschem.2013.10.018 (cited on Pages 4, 31, 150).

[Rao04] D.V. Rao, S.M. Seltzer, and P.M. Bergstrom. “Compton scattering cross-sections for individual subshells for a few elements of biological interest in the energy region 5keV–10MeV” *Radiation Physics and Chemistry* 70 (2004), 479–489. DOI: 10.1016/j.radphyschem.2003.12.026 (cited on Page 149).

[RDek] RoentDek Handels GmbH. “MCP Delay Line Detector Manual” URL: https://www.roentdek.com/manuals/MCP%20Delay%20Line%20manual.pdf (visited on 07/18/2022) (cited on Pages 66, 69).

[Rol05] D. Rolles et al. “Isotope-induced partial localization of core electrons in the homonuclear molecule N_2” *Nature* 437 (2005), 711–715. DOI: 10.1038/nature04040 (cited on Page 47).

[Rol89] A. J. Rollason, F. Bell, J. R. Schneider, and W. Drube. “Electron momentum densities by inelastic gamma ray-recoil electron scattering: A (γ, eγ) experiment” *Solid State Communications* 72 (1989), 297–300. DOI: 10.1016/0038-1098(89)90813-2 (cited on Pages 4, 150).

[Ros34] P. A. Ross and P. Kirkpatrick. “Effect of Electron Binding upon the Magnitude of the Compton Shift” *Physical Review* 46 (1934), 668–673. DOI: 10.1103/PhysRev.46.668 (cited on Page 3).

[Roy04] S. C. Roy and R. H. Pratt. “Need for further inelastic scattering measurements at X-ray energies” *Radiation Physics and Chemistry* 69 (2004), 193–197. DOI: 10.1016/S0969-806X(03)00465-1 (cited on Page 135).

[Sam90] J. A. R. Samson. “Proportionality of electron-impact ionization to double photoionization” *Physical Review Letters* 65 (1990), 2861–2864. DOI: 10.1103/PhysRevLett.65.2861 (cited on Page 108).

[Sam94] J. A. R. Samson, Z. X. He, R. J. Bartlett, and M. Sagurton. "Direct measurement of He^+ ions produced by Compton scattering between 2.5 and 5.5 keV" *Physical Review Letters* 72 (1994), 3329–3331. DOI: 10.1103/PhysRevLett.72.3329 (cited on Pages 5, 31, 81, 89, 91, 123).

[Sch00] L. Schmidt. "Effekte molekularer Symmetrien in der Elektronenemission bei langsamen He^{2+}-He-Stößen: Eine kinematisch vollständige experimentelle Untersuchung" Dissertation. Johann Wolfgang Goethe-Universität Frankfurt, 2000. URN: urn:nbn:de:hebis:30-0000001418 (cited on Page 128).

[Sch02] M. S. Schöffler. "Entwicklung und Aufbau eines Abbildungssystems zur Messung von Elektronen jenseits niedriger Energien" Diplomarbeit. Johann Wolfgang Goethe-Universität Frankfurt, 2002. URN: urn:nbn:de:hebis:30-21129 (cited on Page 72).

[Sch06] M. S. Schöffler. "Grundzustandskorrelationen und dynamische Prozesse untersucht in Ion-Helium-Stößen" Dissertation. Johann Wolfgang Goethe-Universität Frankfurt, 2006. URN: urn:nbn:de:hebis:30-35365 (cited on Pages 125, 128).

[Sch08] M. S. Schöffler et al. "Ultrafast Probing of Core Hole Localization in N_2" *Science* 320 (2008), 920–923. DOI: 10.1126/science.1154989 (cited on Page 167).

[Sch13] M. S. Schöffler et al. "Ejection of Quasi-Free-Electron Pairs from the Helium-Atom Ground State by Single-Photon Absorption" *Physical Review Letters* 111 (2013), 013003. DOI: 10.1103/PhysRevLett.111.013003 (cited on Page 33).

[Sem10] S. K. Semenov et al. "Auger decay of $1\sigma_g$ and $1\sigma_u$ hole states of the N_2 molecule: Disentangling decay routes from coincidence measurements" *Physical Review A* 81 (2010), 043426. DOI: 10.1103/PhysRevA.81.043426 (cited on Pages 47, 153, 154, 160–162).

[Shi02] T. Y. Shi and C. D. Lin. "Double Photoionization and Transfer Ionization of He: Shakeoff Theory Revisited" *Physical Review Letters* 89 (2002), 163202. DOI: 10.1103/PhysRevLett.89.163202 (cited on Page 117).

[Sil60] J. N. Silverman, O. Platas, and F. A. Matsen. "Simple Configuration-Interaction Wave Functions. I: Two-Electron Ions: A Numerical Study" *The Journal of Chemical Physics* 32 (1960), 1402. DOI: 10.1063/1.1730930 (cited on Page 112).

[Sim14] M. Simon et al. "Atomic Auger Doppler effects upon emission of fast photoelectrons" *Nature Communications* 5 (2014), 4069. DOI: 10.1038/ncomms5069 (cited on Pages 157, 163).

[Sme11] C. T. L. Smeenk et al. "Partitioning of the Linear Photon Momentum in Multiphoton Ionization" *Physical Review Letters* 106 (2011), 193002. DOI: 10.1103/PhysRevLett.106.193002 (cited on Page 157).

[Sny70] L. C. Snyder. "Core-Electron Binding Energies and Slater Atomic Shielding Constants" *Journal of Chemical Physics* 55 (1970), 95–99. DOI: 10.1063/1.1675565 (cited on Page 167).

[Som30] A. Sommerfeld and G. Schur. "Über den Photoeffekt in der *K*-Schale der Atome, insbesondere über die Voreilung der Photoelektronen" *Annalen der Physik* 396.4 (1930), 409–432. DOI: 10.1002/andp.19303960402 (cited on Page 180).

[Spa74] C. J. Sparks. "Inelastic Resonance Emission of X Rays: Anomalous Scattering Associated with Anomalous Dispersion" *Physical Review Letters* 33 (1974), 262–265. DOI: 10.1103/PhysRevLett.33.262 (cited on Page 26).

[Spi95] L. Spielberger et al. "Separation of Photoabsorption and Compton Scattering Contributionsto He Single and Double Ionization" *Physical Review Letters* 74 (1995), 4615–4618. DOI: 10.1103/PhysRevLett.74.4615 (cited on Pages 5, 31, 33, 81, 117, 123).

[Spi96] L. Spielberger et al. "Double and Single Ionization of Helium by 58-keV X Rays" *Physical Review Letters* 76 (1996), 4685–4688. DOI: 10.1103/PhysRevLett.76.4685 (cited on Pages 5, 31, 33).

[Spi99] L. Spielberger et al. "Cross-section ratio of double to single ionization of helium by Compton scattering of 40–100-keV x rays" *Physical Review A* 59 (1999), 371–379. DOI: 10.1103/PhysRevA.59.371 (cited on Pages 5, 31, 33).

[Sta03] H. Stapelfeldt and T. Seideman. "Colloquium: Aligning molecules with strong laser pulses" *Reviews of Modern Physics* 75 (2003), 543–557. DOI: 10.1103/RevModPhys.75.543 (cited on Page 170).

[Sta06] A. F. Starace. "Photoionization of Atoms" *Handbook of Atomic, Molecular, and Optical Physics*. Edited by G. W. F. Drake. New York: Springer Science+Business Media, Inc., 2006. ISBN: 978-0-387-20802-2. DOI: 10.1007/978-0-387-26308-3 (cited on Page 14).

[Ste63] A. L. Stewart and T. G. Webb. "Photo-ionization of Helium and Ionized Lithium" *Proceedings of the Physical Society* 82 (1963), 532. DOI: 10.1088/0370-1328/82/4/308 (cited on Page 37).

[Tha86] A. J. Thakkar, J. W. Liu, and W. J. Stevens. "Compton profiles and other momentum-space properties of N_2" *Physical Review A* 34 (1986), 4695–4703. DOI: 10.1103/PhysRevA.34.4695 (cited on Page 193).

[Tho08] T. D. Thomas et al. “Recoil excitation of vibrational structure in the carbon 1*s* photoelectrum spectrum of CF_4” *Journal of Chemical Physics* 128 (2008), 144311. DOI: 10.1063/1.2897756 (cited on Page 163).

[Tho09] T. D. Thomas et al. “Photoelectron-recoil-induced rotational excitation of the $B^2\Sigma_u^+$ state in N_2^+” *Physical Review A* 79 (2009), 022506. DOI: 10.1103/PhysRevA.79.022506 (cited on Page 166).

[Tho10] T. D. Thomas et al. “Valence photoelectron spectroscopy of N_2 and CO: Recoil-induced rotational excitation, relative intensities, and atomic orbital composition of molecular orbitals” *The Journal of Chemical Physics* 133 (2010), 174312. DOI: 10.1063/1.3503658 (cited on Page 166).

[Tho11] T. D. Thomas et al. “Experimental Observation of Rotational Doppler Broadening in a Molecular System” *Physical Review Letters* 106 (2011), 193009. DOI: 10.1103/PhysRevLett.106.193009 (cited on Pages 157, 163).

[Tho20] T. D. Thomas. “Effect of recoil-induced internal excitation on the Auger transition energy” *Physical Review A* 101 (2020), 043415. DOI: 10.1103/PhysRevA.101.043415 (cited on Page 166).

[Thu75] E. W. Thulstrup and A. Andersen. “Configuration interaction studies of bound, low-lying states of N_2^-, N_2, N_2^+, N_2^{2+}” *Journal of Physics B: Atomic and Molecular Physics* 8 (1975), 965–976. DOI: 10.1088/0022-3700/8/6/023 (cited on Page 161).

[Ton05] X. M. Tong and C. D. Lin. “Empirical formula for static field ionization rates of atoms and molecules by lasers in the barrier-suppression regime” *Journal of Physics B: Atomic, Molecular and Optical Physics* 38 (2005), 2593–2600. DOI: 10.1088/0953-4075/38/15/001 (cited on Page 89).

[Ull03] J. Ullrich et al. “Recoil-ion and electron momentum spectroscopy: reaction microscopes” *Reports on Progress in Physics* 66 (2003), 1463–1545. DOI: 10.1088/0034-4885/66/9/203 (cited on Page 49).

[Ulr05] B. Ulrich. “Pump-Probe Experimente zur Ionisation von diatomaren Molekülen : H_2, D_2, O_2, N_2 in ultrakurzen, hochintensiven Laserpulsen” Diplomarbeit. Johann Wolfgang Goethe-Universität Frankfurt, 2005. URN: urn:nbn:de:hebis:30-21118 (cited on Page 153).

[Vau11] G. B. M. Vaughan et al. “X-ray transfocators: focusing devices based on compound refractive lenses” *Journal of Synchrotron Radiation* 18 (2011), 125–133. DOI: 10.1107/S0909049510044365 (cited on Page 55).

[Vie13] J. Viefhaus et al. "The Variable Polarization XUV Beamline P04 at PETRA III: Optics, mechanics and their performance" *Nuclear Instruments and Methods in Physics Research Section A: Accelerators, Spectrometers, Detectors and Associated Equipment* 710 (2013), 151–154. DOI: 10.1016/j.nima.2012.10.110 (cited on Pages 53, 54).

[Vos01] M. Vos. "Observing atom motion by electron-atom Compton scattering" *Physical Review A* 65 (2001), 012703. DOI: 10.1103/PhysRevA.65.012703 (cited on Page 21).

[Wal29] I. Waller, D. R. Hartree, and R. H. Fowler. "On the intensity of total scattering of X-rays" *Proceedings of the Royal Society of London. Series A, Containing Papers of a Mathematical and Physical Character* 124 (1929), 119–142. DOI: 10.1098/rspa.1929.0101 (cited on Page 25).

[Web01] Th. Weber et al. "K-shell photoionization of CO and N_2: is there a link between the photoelectron angular distribution and the molecular decay dynamics?" *Journal of Physics B: Atomic, Molecular and Optical Physics* 34 (2001), 3669–3678. DOI: 10.1088/0953-4075/34/18/305 (cited on Pages 140, 173).

[Weh91] R. Wehlitz et al. "Electron-energy and -angular distributions in the double photoionization of helium" *Physical Review Letters* 67 (1991), 3764–3767. DOI: 10.1103/PhysRevLett.67.3764 (cited on Page 120).

[Wei77] R. J. Weiss, M. J. Cooper, and R. S. Holt. "The Compton defect" *The Philosophical Magazine: A Journal of Theoretical Experimental and Applied Physics* 36 (1977), 193–200. DOI: 10.1080/00318087708244457 (cited on Page 4).

[Wel20] M. Weller. "Der Auger-Effekt in kleinen Molekülen" Dissertation. Johann Wolfgang Goethe-Universität Frankfurt, 2020. URN: urn:nbn:de:hebis:30:3-581166 (cited on Page 38).

[Wil55] W. C. Wiley and I. H. McLaren. "Time-of-Flight Mass Spectrometer with Improved Resolution" *Review of Scientific Instruments* 26 (1955), 1150–1157. DOI: 10.1063/1.1715212 (cited on Page 64).

[Wu11] J. Wu et al. "Nonadiabatic alignment of van der Waals-force-bound argon dimers by femtosecond laser pulses" *Physical Review A* 83 (2011), 061403. DOI: 10.1103/PhysRevA.83.061403 (cited on Page 170).

[Yar06] D. R. Yarkony. "Molecular Structure" *Handbook of Atomic, Molecular, and Optical Physics*. Edited by G. W. F. Drake. New York: Springer Science+Business Media, Inc., 2006. ISBN: 978-0-387-20802-2. DOI: 10.1007/978-0-387-26308-3 (cited on Page 39).

[Zar72] R. N. Zare. "Photoejection Dynamics" *Mol. Photochem* 4 (1972), 1–37. URL: https://scholar.google.com/citations?user=NWIMAqIAAAAJ (cited on Pages 140, 173).

DANKSAGUNG

Die Danksagung ist in der digitalen Version nicht enthalten.

OWN PUBLICATIONS

Physical Review Letters 128 (2022), 053001

Ion and Electron Momentum Distributions from Single and Double Ionization of Helium Induced by Compton Scattering

Max Kircher, F. Trinter, S. Grundmann, G. Kastirke, M. Weller, I. Vela-Perez, A. Khan, Ch. Janke, M. Waitz, S. Zeller, T. Mletzko, D. Kirchner, V. Honkimäki, S. Houamer, O. Chuluunbaatar, Yu. V. Popov, I. P. Volobuev, M. Schöffler, L. Ph. H. Schmidt, T. Jahnke, and R. Dörner

Nature Physics 16 (2020), 756–760

Kinematically complete experimental study of Compton scattering at helium atoms near the threshold

Max Kircher, F. Trinter, S. Grundmann, I. Vela-Perez, S. Brennecke, N. Eicke, J. Rist, S. Eckart, S. Houamer, O. Chuluunbaatar, Y. V. Popov, I. P. Volobuev, K. Bagschik, M. N. Piancastelli, M. Lein, T. Jahnke, M. S. Schöffler, and R. Dörner

Physical Review Letters 123 (2019), 243201

Recoil-Induced Asymmetry of Nondipole Molecular Frame Photoelectron Angular Distributions in the Hard X-ray Regime

Max Kircher, J. Rist, F. Trinter, S. Grundmann, M. Waitz, N. Melzer, I. Vela-Perez, T. Mletzko, A. Pier, N. Strenger, J. Siebert, R. Janssen, L. Ph. H. Schmidt, A. N. Artemyev, M. S. Schöffler, T. Jahnke, R. Dörner, and Ph. V. Demekhin

Physical Review Letters 123 (2019), 193001

Photon-Momentum-Induced Molecular Dynamics in Photoionization of N_2 at $h\nu = 40$ keV

Max Kircher, J. Rist, F. Trinter, S. Grundmann, M. Waitz, N. Melzer, I. Vela-Perez, T. Mletzko, A. Pier, N. Strenger, J. Siebert, R. Janssen, V. Honkimäki, J. Drnec, Ph. V. Demekhin, L. Ph. H. Schmidt, M. S. Schöffler, T. Jahnke, and R. Dörner

Physical Review Research, accepted
Mechanisms of one-photon two-site double ionization after resonant inner-valence excitation in Ne clusters
A. Hans, F. Trinter, P. Schmidt, S. Eckart, S. Grundmann, G. Hartmann, X. Holzapfel, C. Honisch, G. Kastirke, Max Kircher, N. Melzer, C. Ozga, C. Richter, J. Rist, M. S. Schöffler, D. Trabert, I. Vela-Perez, J. H. Viehmann, M. Weller, R. Dörner, U. Hergenhahn, A. Ehresmann, A. Knie, K. Gokhberg, A. Ghosh, and T. Jahnke

Physical Review Research 5 (2023), 013021
Molecular-frame differential photoelectron circular dichroism of O1s-photoelectrons of trifluoromethyloxirane
G. Nalin, N. M. Novikovskiy, K. Fehre, N. Anders, D. Trabert, S. Grundmann, Max Kircher, A. Khan, R. Tomar, M. Hofmann, M. Waitz, I. Vela-Perez, G. Kastirke, J. Siebert, D. Tsitsonis, C. Küstner-Wetekam, L. Marder, J. Viehmann, F. Trinter, H. Fukuzawa, K. Ueda, J. Williams, A. Knie, R. Dörner, M. S. Schöffler, T. Jahnke, Ph. V. Demekhin

Physical Review Letters 129 (2022), 253201
Observation of Nondipole-Induced Asymmetry in the Angular Emission Distribution of Photoelectrons from Fixed-in-Space CO Molecules
D. V. Rezvan, K. Klyssek, S. Grundmann, A. Pier, N. M. Novikovskiy, N. Strenger, D. Tsitsonis, Max Kircher, I. Vela-Perez, K. Fehre, F. Trinter, M. S. Schöffler, T. Jahnke, R. Dörner, and Ph. V. Demekhin

Physical Chemistry Chemical Physics 24 (2022), 27121–27127
Investigating charge-up and fragmentation dynamics of oxygen molecules after interaction with strong X-ray free-electron laser pulses
G. Kastirke, F. Ota, D. V. Rezvan, M. S. Schöffler, M. Weller, J. Rist, R. Boll, N. Anders, T. M. Baumann, S. Eckart, B. Erk, A. De Fanis, K. Fehre, A. Gatton, S. Grundmann, P. Grychtol, A. Hartung, M. Hofmann, M. Ilchen, Ch. Janke, Max Kircher, M. Kunitski, X. Li, T. Mazza, N. Melzer, J. Montano, V. Music, G. Nalin, Y. Ovcharenko, A. Pier, N. Rennhack, D. E. Rivas, R. Dörner, D. Rolles, A. Rudenko, Ph. Schmidt, J. Siebert, N. Strenger, D. Trabert, I. Vela-Perez, R. Wagner, Th. Weber, J. B. Williams, P. Ziolkowski, L. Ph. H. Schmidt, A. Czasch, Y. Tamura, N. Hara, K. Yamazaki, K. Hatada, F. Trinter, M. Meyer, K. Ueda, Ph. V. Demekhin, and T. Jahnke

Physical Chemistry Chemical Physics 24 (2022), 26458–26465
A new route for enantio-sensitive structure determination by photoelectron scattering on molecules in the gas phase
K. Fehre, N. M. Novikosvskiy, S. Grundmann, G. Kastirke, S. Eckart, F. Trinter, J. Rist, A. Hartung, D. Trabert, Ch. Janke, M. Pitzer, S. Zeller, F. Wiegandt, M. Weller, Max Kircher, G. Nalin, M. Hofmann, L. Ph. H. Schmidt, A. Knie, A. Hans, L. B. Ltaief, A. Ehresmann, R. Berger, H. Fukuzawa, K. Ueda, H. Schmidt-Böcking, J. B. Williams, T. Jahnke, R. Dörner, Ph. V. Demekhin, and M. S. Schöffler

Atoms 10 (2022), 68
Resonance-enhanced x-ray multiple ionization of a polyatomic molecule
S. Grundmann, F. Trinter, Y.-K. Fang, K. Fehre, N. Strenger, A. Pier, L. Kaiser, Max Kircher, L.-Y. Peng, T. Jahnke, R. Dörner, and M. S. Schöffler

Physical Review A 105 (2022), 053102
Resonance-enhanced x-ray multiple ionization of a polyatomic molecule
X. Li, A. Rudenko, T. Mazza, A. Rörig, N. Anders, Th. M. Baumann, S. Eckart, B. Erk, A. De Fanis, K. Fehre, R. Dörner, L. Foucar, S. Grundmann, P. Grychtol, A. Hartung, M. Hofmann, M. Ilchen, Ch. Janke, G. Kastirke, Max Kircher, K. Kubicek, M. Kunitski, S. Meister, N. Melzer, J. Montano, V. Music, G. Nalin, Y. Ovcharenko, Ch. Passow, A. Pier, N. Rennhack, J. Rist, D. E. Rivas, I. Schlichting, L. Ph. H. Schmidt, Ph. Schmidt, M. S. Schöffler, J. Siebert, N. Strenger, D. Trabert, F. Trinter, I. Vela-Perez, R. Wagner, P. Walter, M. Weller, P. Ziolkowski, A. Czasch, M. Meyer, T. Jahnke, D. Rolles, and R. Boll

Nature Physics 18 (2022), 423–428
X-ray multiphoton-induced Coulomb explosion images complex single molecules
R. Boll, J. M. Schäfer, B. Richard, K. Fehre, G. Kastirke, Z. Jurek, M. S. Schöffler, M. M. Abdullah, N. Anders, T. M. Baumann, S. Eckart, B. Erk, A. De Fanis, R. Dörner, S. Grundmann, P. Grychtol, A. Hartung, M. Hofmann, M. Ilchen, L. Inhester, Ch. Janke, R. Jin, Max Kircher, K. Kubicek, M. Kunitski, X. Li, T. Mazza, S. Meister, N. Melzer, J. Montano, V. Music, G. Nalin, Y. Ovcharenko, C. Passow, A. Pier, N. Rennhack, J. Rist, D. E. Rivas, D. Rolles, I. Schlichting, L. Ph. H. Schmidt, P. Schmidt, J. Siebert, N. Strenger, D. Trabert, F. Trinter, I. Vela-Perez, R. Wagner, P. Walter, M. Weller, P. Ziolkowski, S.-K. Son, A. Rudenko, M. Meyer, R. Santra, and T. Jahnke

Physical Review Research 4 (2022), 013029
Coulomb explosion imaging of small polyatomic molecules with ultrashort x-ray pulses
X. Li, A. Rudenko, M. S. Schöffler, N. Anders, Th. M. Baumann, S. Eckart, B. Erk, A. De Fanis, K. Fehre, R. Dörner, L. Foucar, S. Grundmann, P. Grychtol, A. Hartung, M. Hofmann, M. Ilchen, Ch. Janke, G. Kastirke, Max Kircher, K. Kubicek, M. Kunitski, T. Mazza, S. Meister, N. Melzer, J. Montano, V. Music, G. Nalin, Y. Ovcharenko, Ch. Passow, A. Pier, N. Rennhack, J. Rist, D. E. Rivas, I. Schlichting, L. Ph. H. Schmidt, Ph. Schmidt, J. Siebert, N. Strenger, D. Trabert, F. Trinter, I. Vela-Perez, R. Wagner, P. Walter, M. Weller, P. Ziolkowski, A. Czasch, D. Rolles, M. Meyer, T. Jahnke, and R. Boll

Journal of Quantitative Spectroscopy & Radiative Transfer 278 (2022), 108020
Compton double ionization of the helium atom: Can it be a method of dynamical spectroscopy of ground state electron correlation?
O. Chuluunbaatar, S. Houamer, Yu. V. Popov, I.P. Volobuev, Max Kircher, and R. Dörner

Physical Review X 11 (2021), 041044
Inner-Shell-Ionization-Induced Femtosecond Structural Dynamics of Water Molecules Imaged at an X-Ray Free-Electron Laser
T. Jahnke, R. Guillemin, L. Inhester, S.-K. Son, G. Kastirke, M. Ilchen, J. Rist, D. Trabert, N. Melzer, N. Anders, T. Mazza, R. Boll, A. De Fanis, V. Music, Th. Weber, M. Weller, S. Eckart, K. Fehre, S. Grundmann, A. Hartung, M. Hofmann, Ch. Janke, Max Kircher, G. Nalin, A. Pier, J. Siebert, N. Strenger, I. Vela-Perez, T. M. Baumann, P. Grychtol, J. Montano, Y. Ovcharenko, N. Rennhack, D. E. Rivas, R. Wagner, P. Ziolkowski, P. Schmidt, T. Marchenko, O. Travnikova, L. Journel, I. Ismail, E. Kukk, J. Niskanen, F. Trinter, C. Vozzi, M. Devetta, S. Stagira, M. Gisselbrecht, A. L. Jäger, X. Li, Y. Malakar, M. Martins, R. Feifel, L. Ph. H. Schmidt, A. Czasch, G. Sansone, D. Rolles, A. Rudenko, R. Moshammer, R. Dörner, M. Meyer, T. Pfeifer, M. S. Schöffler, R. Santra, M. Simon, and M. N. Piancastelli

Nature Communications 12 (2021), 6657
Measuring the photoelectron emission delay in the molecular frame
J. Rist, K. Klyssek, N. M. Novikovskiy, Max Kircher, I. Vela-Perez, D. Trabert, S. Grundmann, D. Tsitsonis, J. Siebert, A. Geyer, N. Melzer, Ch. Schwarz, N. Anders, L. Kaiser, K. Fehre, A. Hartung, S. Eckart, L. Ph. H. Schmidt, M. S. Schöffler, V. T. Davis, J. B. Williams, F. Trinter, R. Dörner, Ph. V. Demekhin, and T. Jahnke

Physical Chemistry Chemical Physics 32 (2021), 17248
Photoelectron circular dichroism of O 1*s*-photoelectrons of uniaxially oriented trifluoromethyloxirane: energy dependence and sensitivity to molecular configuration
G. Nalin, K. Fehre, F. Trinter, N. M. Novikovskiy, N. Anders, D. Trabert, S. Grundmann, Max Kircher, A. Khan, R. Tomar, M. Hofmann, M. Waitz, I. Vela-Perez, G. Kastirke, J. Siebert, D. Tsitsonis, H. Fukuzawa, K. Ueda, J. B. Williams, D. Kargin, M. Maurer, C. Küstner-Wetekam, L. Marder, J. Viehmann, A. Knie, T. Jahnke, M. Ilchen, R. Dörner, R. Pietschnig, P. V. Demekhin, and M. S. Schöffler

Physical Review Letters 127 (2021), 103201
Fourfold Differential Photoelectron Circular Dichroism
K. Fehre, N. M. Novikovskiy, S. Grundmann, G. Kastirke, S. Eckart, F. Trinter, J. Rist, A. Hartung, D. Trabert, Ch. Janke, G. Nalin, M. Pitzer, S. Zeller, F. Wiegandt, M. Weller, Max Kircher, M. Hofmann, L. Ph. H. Schmidt, A. Knie, A. Hans, L. Ben Ltaief, A. Ehresmann, R. Berger, H. Fukuzawa, K. Ueda, H. Schmidt-Böcking, J. B. Williams, T. Jahnke R. Dörner M. S. Schöffler, and Ph. V. Demekhin

Journal of Quantitative Spectroscopy & Radiative Transfer 272 (2021), 107820
Compton ionization of atoms as a method of dynamical spectroscopy
O. Chuluunbaatar, S. Houamer, Yu. V. Popov, I. P. Volobuev, Max Kircher, and R. Dörner

Physical Review Letters 125 (2020), 163201

Double Core-Hole Generation in O_2 Molecules Using an X-Ray Free-Electron Laser: Molecular-Frame Photoelectron Angular Distributions

G. Kastirke, M. S. Schöffler, M. Weller, J. Rist, R. Boll, N. Anders, Th. M. Baumann, S. Eckart, B. Erk, A. De Fanis, K. Fehre, A. Gatton, S. Grundmann, P. Grychtol, A. Hartung, M. Hofmann, M. Ilchen, Ch. Janke, Max Kircher, M. Kunitski, X. Li, T. Mazza, N. Melzer, J. Montano, V. Music, G. Nalin, Y. Ovcharenko, A. Pier, N. Rennhack, D. E. Rivas, R. Dörner, D. Rolles, A. Rudenko, Ph. Schmidt, J. Siebert, N. Strenger, D. Trabert, I. Vela-Perez, R. Wagner, Th. Weber, J. B. Williams, P. Ziolkowski, L. Ph. H. Schmidt, A. Czasch, K. Ueda, F. Trinter, M. Meyer, Ph. V. Demekhin, and T. Jahnke

Science 370 (2020), 339–341

Zeptosecond birth time delay in molecular photoionization

S. Grundmann, D. Trabert, K. Fehre, N. Strenger, A. Pier, L. Kaiser, Max Kircher, M. Weller, S. Eckart, L. Ph. H. Schmidt, F. Trinter, T. Jahnke, M. S. Schöffler, and R. Dörner

Physical Review Research 2 (2020), 033209

Chiral photoelectron angular distributions from ionization of achiral atomic and molecular species

A. Pier, K. Fehre, S. Grundmann, I. Vela-Perez, N. Strenger, Max Kircher, D. Tsitsonis, J.B. Williams, A. Senftleben, T. Baumert, M. S. Schöffler, P. Demekhin, F. Trinter, T. Jahnke, and R. Dörner

Physical Review Research 2 (2020), 033080

Revealing the two-electron cusp in the ground states of He and H_2 via quasifree double photoionization

S. Grundmann, V. Serov, F. Trinter, K. Fehre, N. Strenger, A. Pier, Max Kircher, D. Trabert, M. Weller, J. Rist, L. Kaiser, A. Bray, L. Ph. H. Schmidt, J. Williams, T. Jahnke, R. Dörner, M. S. Schöffler, and A. Kheifets

Physical Review X 10 (2020), 021052
Photoelectron Diffraction Imaging of a Molecular Breakup Using an X-Ray Free-Electron Laser
G. Kastirke, M. S. Schöffler, M. Weller, J. Rist, R. Boll, N. Anders, Th. M. Baumann, S. Eckart, B. Erk, A. De Fanis, K. Fehre, A. Gatton, S. Grundmann, P. Grychtol, A. Hartung, M. Hofmann, M. Ilchen, Ch. Janke, Max Kircher, M. Kunitski, X. Li, T. Mazza, N. Melzer, J. Montano, V. Music, G. Nalin, Y. Ovcharenk, A. Pier, N. Rennhack, D. E. Rivas, R. Dörner, D. Rolles, A. Rudenko, Ph. Schmidt, J. Siebert, N. Strenger, D. Trabert, I. Vela-Perez, R. Wagner, Th. Weber, J. B. Williams, P. Ziolkowski, L. Ph. H. Schmidt, A. Czasch, F. Trinter, M. Meyer, K. Ueda, Ph. V. Demekhin, and T. Jahnke

Physical Review Letters 124 (2020), 233201
Observation of Photoion Backward Emission in Photoionization of He and N_2
S. Grundmann, Max Kircher, I. Vela-Perez, G. Nalin, D. Trabert, N. Anders, N. Melzer, J. Rist, A. Pier, N. Strenger, J. Siebert, Ph. V. Demekhin, L. Ph. H. Schmidt, F. Trinter, M. S. Schöffler, T. Jahnke, and R. Dörner

Physical Review Letters 121 (2018), 243002
Breakdown of the Spectator Concept in Low-Electron-Energy Resonant Decay Processes
A. Mhamdi, J. Rist, D. Aslitürk, M. Weller, N. Melzer, D. Trabert, Max Kircher, I. Vela-Perez, J. Siebert, S. Eckart, S. Grundmann, G. Kastirke, M. Waitz, A. Khan, M. S. Schöffler, F. Trinter, R. Dörner, T. Jahnke, and Ph. V. Demekhin

Physical Review A 98 (2018), 050701(R)
Frustrated Coulomb explosion of small helium clusters
S. Kazandjian, J. Rist, M. Weller, F. Wiegandt, D. Aslitürk, S. Grundmann, Max Kircher, G. Nalin, D. Pitters, I. Vela-Perez, M. Waitz, G. Schiwietz, B. Griffin, J. B. Williams, R. Dörner, M. S. Schöffler, T. Miteva, F. Trinter, T. Jahnke, and N. Sisourat

Journal of Physical Chemistry Letters 8 (2017), 2780–2786

Observation of Enhanced Chiral Asymmetries in the Inner-Shell Photoionization of Uniaxially Oriented Methyloxirane Enantiomers

M. Tia, M. Pitzer, G. Kastirke, J. Gatzke, H.-K. Kim, F. Trinter, J. Rist, A. Hartung, D. Trabert, J. Siebert, K. Henrichs, J. Becht, S. Zeller, H. Gassert, F. Wiegandt, R. Wallauer, A. Kuhlins, C. Schober, T. Bauer, N. Wechselberger, P. Burzynski, J. Neff, M. Weller, D. Metz, Max Kircher, M. Waitz, J. B. Williams, L. Ph. H. Schmidt, A. D. Müller, A. Knie, A. Hans, L. B. Ltaief, A. Ehresmann, R. Berger, H. Fukuzawa, K. Ueda, H. Schmidt-Böcking, R. Dörner, T. Jahnke, Ph. V. Demekhin, and M. S. Schöffler

CONTRIBUTION TO CONFERENCES AND SEMINARS

2022/06 Conference, MPS 2022, Turku, Finland. Poster presentations: “Kinematically complete experimental study of Compton scattering at helium atoms near the threshold” and “Ion and electron momentum distributions from single and double ionization of helium induced by Compton scattering.”

2021/07 Virtual conference, ViCPEAC 2021. Poster presentation: “Gas-phase helium double ionization induced by Compton scattering.”

2021/07 Virtual conference, ISIAC 2021. Talk: “A kinematically complete experiment on Compton scattering.”

2019/10 Seminar, Lomonosov University, Moscow, Russia. Talk: “Compton scattering on helium below threshold.”

2019/07 Conference, ICPEAC 2019, Deauville, France. Poster presentation: “Fully differential measurements of low-energy Compton scattering in the gas phase.”

2019/05 Conference, ECAMP 2019, Florence, Italy. Poster presentation: “Fully differential measuremnts of low-energy Compton scattering in the gas phase.”

2017/07 Conference, ICPEAC 2017, Cairns, Australia. Poster preparation (presented by Florian Trinter): “Time-resolved measurement of interatomic Coulombic decay in small helium clusters.”

2016/09 Conference, ECAMP 2016, Frankfurt, Germany. Aid in conference preparation.

EXPERIENCE IN PRACTICAL SCIENTIFIC RESEARCH

2022/08 ESRF, Grenoble, France. Beamtime, 1 week.

2021/11 BESSY II, HZB, Berlin, Germany. Beamtime, 1 week.

2021/09 PETRA III, DESY, Hamburg, Germany. Beamtime, 1 week.

2021/06 European XFEL, Hamburg, Germany. Beamtime, 1 week.

2021/02 GANIL, Caen, France. Beamtime, 3 weeks.

2021/02 PETRA III, DESY, Hamburg, Germany. Upgrade of the COLTRIMS-chamber, 1 week.

2020/02 BESSY II, HZB, Berlin, Germany. Beamtime, 1 week

2019/10 PETRA III, DESY, Hamburg, Germany. Beamtime, 1 week.

2019/06 BESSY II, HZB, Berlin, Germany. Beamtime, 1 week.

2019/02 European XFEL, Hamburg, Germany. Beamtime, 1 week.

2018/11 PETRA III, DESY, Hamburg, Germany. Beamtime, 1 week.

2018/08 ESRF, Grenoble, France. Beamtime, 3 weeks.

2018/09 PETRA III, DESY, Hamburg, Germany. Beamtime, 1 week.

2018/09 SOLEIL, Paris, France. Beamtime, 1 week.

2018/05 BESSY II, HZB, Berlin, Germany. Beamtime, 1 week.

2018/04 ESRF, Grenoble, France. Beamtime, 3 weeks.

2018/02 BESSY II, HZB, Berlin, Germany. Beamtime, 1 week.

2017/10 PETRA III, DESY, Hamburg, Germany. Beamtime, 2 weeks.

2017/06 BESSY II, HZB, Berlin, Germany. Beamtime, 1 week.

2017/02 BESSY II, HZB, Berlin, Germany. Beamtime, 1 week.

2016/06 BESSY II, HZB, Berlin, Germany. Beamtime, 1 week.

2016/02 BESSY II, HZB, Berlin, Germany. Beamtime, 1 week.

Akademischer Lebenslauf

Der Lebenslauf ist in der digitalen Version nicht enthalten.